The Pennsylvania State University
The Graduate School
Intercollege Graduate Program in Materials

OPTICAL, ELECTRICAL AND ELASTIC PROPERTIES OF FERROELECTRIC DOMAIN WALLS IN $LiNbO_3$ AND $LiTaO_3$

A Thesis in
Materials
by
Sungwon kim

Submitted in Partial Fulfillment
of the Requirements
for the Degree of

Doctor of Philosophy

December 2003

We approve the thesis of Sungwon kim.

Date of Signature

Venkatraman Gopalan
Assistant Professor of Materials Science and Engineering
Thesis Adviser
Chair of Committee

Robert E. Newnham
Professor of Materials Science and Engineering

Long Qing Chen
Professor of Materials Science and Engineering

Iam Choon Khoo
Professor of Electrical Engineering

Barbara A. Shaw
Associate Professor of Engineering Science and Mechanics
Head of the Department of Intercollege Graduate Program in Materials

Abstract

Ferroelectric $LiNbO_3$ and $LiTaO_3$ crystals have developed, over the last 50 years as key materials for integrated and nonlinear optics due to their large electro-optic and nonlinear optical coefficients and a broad transparency range from 0.4 μm - 4.5 μm wavelengths. Applications include high speed optical modulation and switching in 40GHz range, second harmonic generation, optical parametric amplification, pulse compression and so on. Ferroelectric domain microengineering has led to electro-optic scanners, dynamic focusing lenses, total internal reflection switches, and quasi-phase matched (QPM) frequency doublers. Most of these applications have so far been on non-stoichiometric compositions of these crystals.

Recent breakthroughs in crystal growth have however opened up an entirely new window of opportunity from both scientific and technological viewpoint. The growth of stoichiometric composition crystals has led to the discovery of many fascinating effects arising from the presence or absence of atomic defects, such as an order of magnitude changes in coercive fields, internal fields, domain backswitching and stabilization phenomenon. On the nanoscale, *unexpected* features such as the presence of wide regions of optical contrast and strain have been discovered at 180° domain walls. Such strong influence of small amounts of nonstoichiometric defects on material properties has led to new device applications, particularly those involving domain patterning and shaping such as QPM devices in thick bulk crystals and improved photorefractive damage compositions.

The central focus of this dissertation is to explore the role of nonsotichiometry and its precise influence on macroscale and nanoscale properties in lithium niobate and tantalate. Macroscale properties are studied using a combination of in-situ and high-speed electro-optic imaging microscopy and electrical switching experiments. Local static and dynamic strain properties at individual domain walls is studied using X-ray synchrotron imaging with and without in-situ electric fields. Nanoscale optical properties are studied using Near Field Scanning Optical Microscopy(NSOM). Finite

Difference Time Domain(FDTD) codes, Beam Propagation Method(BPM) codes and X-ray tracing codes have been developed to successfully simulate NSOM images and X-ray topography images to extract the local optical and strain properties, respectively. A 3-D ferroelectric domain simulation code based on Time Dependent Ginzburg Landau(TDGL) theory and group theory has been developed to understand the nature of these local wall strains and the preferred wall orientations. By combining these experimental and numerical tools, We have also proposed a defect-dipole model and a mechanism by which the defect interacts with the domain walls. This thesis has thus built a more comprehensive picture of the influence of defects on domain walls on nanoscale and macroscale, and raises new scientific questions about the exact nature of domain walls-defect interactions. Besides the specific problem of ferroelectrics, the experimental and simulation tools, developed in this thesis will have wider application in the area of materials science.

Table of Contents

List of Tables

List of Figures

Acknowledgments

During my four year's of Ph.D study in Penn state University, I can enjoy my reseach and personal life in every day because of the all the people who gave endless support to me. First of all, I am most grateful to my academic adviser Dr. Venkatraman Gopalan for the most invaluable academic guidance. I am also grateful to the other thesis committee members for their time and insightful comments on this work. I also thank my fellow graduate students for their friendships and enlightening discussion on my research and other topics. My parents and in-laws deserve my profound gratitude for their support, encouragement and prayer. Finally, I would like to thank my loving little son, and lovely wife for making this work enjoyable.

Chapter 1

Introduction

1.1 Overview

The phenomenon of ferroelectricity was discovered in 1920 by Valasek on Rochelle salt. During 1935 and 1938, a series of ferroelectric crystals were produced in Zurich by Busch and Scherrer [6]. Potassium dihyddrogen phosphate, (KH_2PO_4 KDP), and ammonium salts ($NH_4H_2PO_4$, APD) were developed at that time. Because of the high electromechanical coupling ratio, APD replaced underwater sound transducer and submarine detectors in World War II. After the discovery of the KDP series there was no breakthrough in the ferroelectrics area for a little while. In 1945, barium titanate ceramic was discovered, with high dielectric constants up to 3000 at room temperature. It was the first ferroelectric without hydrogen bond and with a non-piezoelectric prototype. Later on ferroelectricity was discovered in $KNbO_3$, $KTaO_3$ [4], $LiNbO_3$ [2] [3] [26] and $LiTaO_3$ [5], and in $PbTiO_3$ [14]. Based on these new ferroelectric materials, Anderson [20] and Cochran [27] introduced the lattice mode (or 'soft' mode) model, involving the ionic motion of all constituent atoms to describe the displacive lattice instability. A macroscopic theory was also developed. For example, in terms of the thermodynamical framework of displacive or order-disorder phase transitions, the concepts of long or short range interaction, and ionic or electronic displacements were introduced [18] [19]. Ginzburg and Devonshire [10]introduced the elastic energy, electrostrictive coupling energy, and polarization gradient energy terms into the total free energy for a ferroelectric. This theory will be explained and applied to lithium niobate and lithium tantalate in Ch. 3. Since 1960s, lattice dynamical or soft-mode description of ferroelectricity developed rapidly. Based on this theory, new experimental tools were developed, primarily, scattering or resonance experiments involving X-ray, neutron, light, and ultrasound.

A crystal is called a *ferroelectric* when it has two or more orientational states in the absence of an external electric field and can be transformed from one of these states to another by an external electric field. Any two of the orientation states are identical in their crystal structure and differ only in the direction of their electric polarization vector, $\mathbf{P_s}$. The highest symmetry phase compatible with the ferroelectric structure is termed as the *prototype phase*. Although this prototype phase need not necessarily be of non-polar character, such is the case for a great majority of the known ferroelectrics. Since the ferroelectric phase evolves as a result of small structural displacements from a non-polar prototype. A typical ferroelectric possesses a spontaneous polarization $\mathbf{P_s}$ with units of charge per unit area or total dipole moment per unit volume. A ferroelectric phase change represents a special class of structural phase transitions denoted by the appearance of spontaneous polarization. The higher temperature prototype phase is typically the *paraelectric phase* and it transforms to the low temperature *ferroelectric phase* at the *Curie temperature*. Cooling from above the Curie temperature, T_c, at which the paraelectric to ferroelectric phase transition occurs, the approaching transition is often signaled by diverging differential dielectric response or permittivity which follows the Curie-Weiss law, given by ϵ=C/(T-$T_\circ$), where $T_\circ$ is the Curie-Weiss temperature which is equal to the Curie temperature T_c, and C is Curie constant. In the ferroelectric phase, the presence of bulk spontaneous polarization results in positively and negatively charged surfaces in the crystal. These surface, whose maximum density is equal to $\mathbf{P_s}$, cause a *depolarizing field* that oppose the bulk spontaneous polarization and hence make them unstable. In order to minimize the depolarizing fields, these surfaces need to be made neutral. On of the ways this is achieved by a ferroelectric crystal is by creating multi-domain structures. Within each *domain*, the spontaneous polarization in the crystal lattice points in the same direction.

If the paraelectric-to-ferroelectric transition is *continuous* in terms of order parameter (spontaneous polarization, $\mathbf{P_s}$), it is called a *second order* phase transition. It is called a first order phase transition if the polarization, $\mathbf{P_s}$ changes discontinuously across the phase transition. The Landau free energy, F, of a ferroelectric can be expressed as a power series of the spontaneous polarization value P [7].

$$F(P;T,E) = -EP + g_0 + \frac{1}{2}g_2P^2 + \frac{1}{4}P^4 + \frac{1}{6}g_6P^6 \tag{1.1}$$

where g_n is the temperature dependent constant. The minimum value of F gives the spontaneous polarization value $\mathbf{P_s}$. The equilibrium polarization value under an applied electric field E satisfies

$$\frac{\partial F}{\partial P} = 0 = -E + g_2P + g_4P^3 + g_6P^5 + ... \tag{1.2}$$

To obtain a ferroelectric state, g_2 must pass through zero at some temperature $T_\circ$.

$$g_2 = \gamma(T - T_\circ)$$

A small positive value of g_2 means that the lattice is soft and is close to instability. A negative value of g_2 means that the unpolarized lattice is unstable. If g_4 in Eqn. 1.1 is positive, it becomes a second order phase transition. By using Eqn. 1.2 P_s will be either 0 or $(\gamma/g_4)^{1/2}(T_\circ - T)^{1/2}$. For T$\geq T_\circ$ only P_s=0 is allowed. For T< $T_\circ$,

$$|P_s| = (\gamma/g_4)^{1/2}(T_\circ - T)^{1/2}$$

As can be seem in Fig. 1.1, this polarization goes to zero at the critical temperature in a continuous fashion. If g_4 is negative, the transition becomes first order. The term g_6 should be positive to restrain F from going to negative infinity. By using equilibrium Eqn. 1.2, $\mathbf{P_s}$ will be 0 or $\gamma(T - T_\circ) - |g_4| P_s^2 + g_6P_s^4 = 0$. Figure 1.2 shows how the free energy varies with temperature. It is clear that polarization change is discontinuous at the Curie temperature.

1.2 Lithium Niobate ($LiNbO_3$) and Lithium Tantalate ($LiTaO_3$)

With the development of the lasers and optical communications, materials with large electro-optic, and large nonlinear optical responses are required. It is well known that large nonlinear polarizability can be achieved in materials which have a large linear

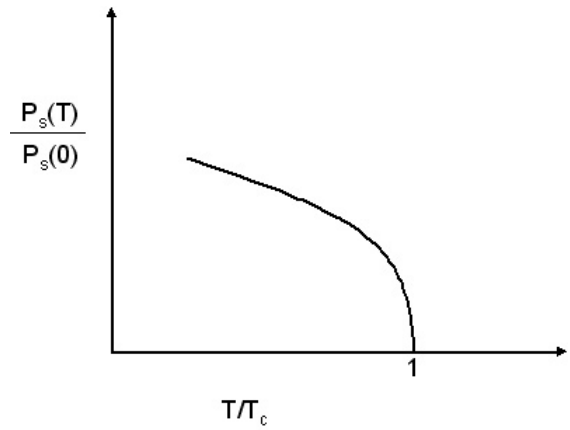

Fig. 1.1. Spontaneous polarization versus temperature, for a second order phase transition

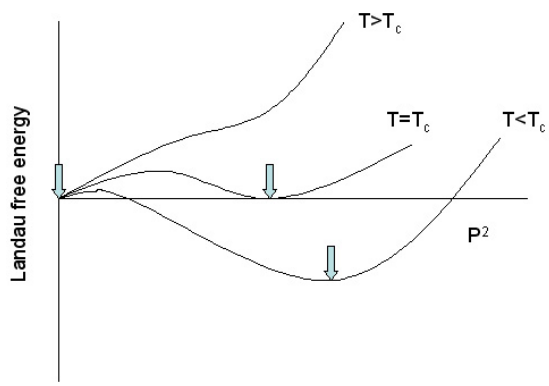

Fig. 1.2. Landau free energy function. At T_C Landau free energy has minimum in 0 and finite P at the same time. Below T_C minimum will be large finite P value.

polarizability. Naturally ferroelectric materials receive attention. Among them, $LiNbO_3$ and $LiTaO_3$ received intense attention, because of their large linear and nonlinear optical coefficients, a fast electro optical response (> 100GHz) and a large transparency window from 0.4 μm - 4.5 μm wavelengths. These materials are uniaxial in all temperature ranges, with only a single structural phase transition that corresponds to the Curie temperature,

and exibit second order (or close to the second order) phase transition. Because of the high Curie temperature (≈620 °C for $LiTaO_3$ and ≈1200 °C for $LiNbO_3$), complex optical modes of lattice vibration complicate the lattice dynamical picture of these systems. Although $LiNbO_3$ and $LiTaO_3$ do not have the perovskite structure they are ABO_3 lattices, with adjacent oxygen octahedral BO_6 sharing common faces. Fig 1.3 shows the basic room temperature ferroelectric state structure. Within the oxygen cages, the cation appears in the sequence ... [Nb(Ta), vacancy, Li]... where the bracketed sequence repeats along the uniaxial c (also called z) axis, and the spontaneous lattice polarization, $\mathbf{P_s}$, points here from left to right. The room temperature positions of the cations within the oxygen cages are known by X-ray and neutron measurements [23], [25], [22]. Because of the large offset of the cations from possible non-polar positions is quite large, they have a high spontaneous polarization value (≈55μCcm^{-2} for $LiTaO_3$, ≈75μCcm^{-2} for $LiNbO_3$). At room temperature, for $LiNbO_3$ the coordinate of atoms are showed in Table 1.1. Lattice constant of hexagonal axis a is 5.14829 $\dot{A}$, and c is 13.8631 $\dot{A}$. $LiTaO_3$ also has a distorted cation position like $LiNbO_3$.

Atom	x	y	z
Nb	0	0	0
O	0.0492±0.0004	0.3446±0.0005	0.0647±0.0004
Li	0	0	0.2829±0.0023

Table 1.1. Coordinate of the atoms in the $LiNbO_3$ at 297 K [24]

Two domain states exist in lithium niobate and tantalate, either $+\mathbf{P_s}$ (*up* domain) or $-\mathbf{P_s}$ (*down* domain), pointing along +c and -c uniaxial directions, respectively. The separation between two domains is called a domain wall, which in this case is a 180°

domain wall, since it separates two ferroelectric polarizations that are antiparallel to each other.

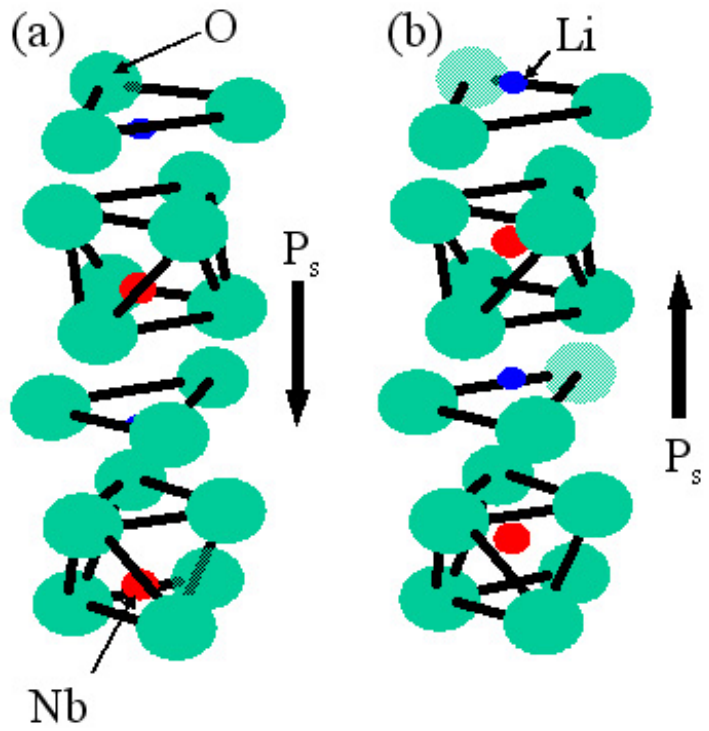

Fig. 1.3. Two possible ferroelectric state structures in $LiNbO_3$ crystal. Denpending on cation location compared to oxygen plae determined dwon(a) or up(b) domain state.

Dielectric, thermal, and phyroelectric measurements on $LiNbO_3$ and $LiTaO_3$ establish that the phase transitions are of second order. The observed Curie constant, C, for $LiNbO_3$ and $LiTaO_3$ are of the order of 10^5K and are typical for systems of broadly displacive character. The detailed characterization of the physical properties of both $LiNbO_3$ and $LiTaO_3$ is complicated by crystal-chemistry considerations. Since 1965, when Ballman [1] reported the successful growth of single crystals by the Czochralski

technique, considerable research was carried out on crystal growth and physical properties. After 1967, most work was devoted to the improvement of material quality. The very large influence of compositional variation of $LiNbO_3$ on its physical properties had been established, and the successful growth of very homogeneous material from the congruent melt was achieved. Figure 1.4 shows the phase diagram of the system $Li_2O - Ta_2O_5$ and $Li_2O - Nb_2O_5$ phase diagram. Both $LiNbO_3$ and $LiTaO_3$ has close congruent composition, but only congruent melting point is different.

Slight deficiency of the Li, and an accompanying excess of Nb or Ta makes a significant difference to the structure and physical properties. Among the various changes due to slight Li-deficiency, domain kinetics is very significant and important for applications. The direct interaction between microscopic defect configuration and macroscopic domain wall structure dramatically changes the coercive fields, creates large defect related internal fields, and gives rise to wall stabilization time, wall gradient energy, and different wall shapes. These effects on macroscale properties are detailed in Ch. 2 and Ch. 3. In addition, the local nanoscale structre of a ferroelectric domain wall changes, with additional long range strains and optical index differences across a 180° wall. These are explored in detail in Chapters 4 and 5.

1.3 Optical applications of ferroelectric domain walls

$LiNbO_3$ and $LiTaO_3$ crystals have become the workhorse materials for integrated acoustic, integrated optical and nonlinear optical devices. Examples include Mach-Zender interferometric switches [15], optical holography [11], and surface acoustic wave devices [16]. However, presently, a majority of the commercial devices based on $LiNbO_3$ crystals simply use a single domain state without any domain wall structure.

Recently, domain *microengineering* of $LiNbO_3$ and $LiTaO_3$ crystals has been applied to realize a new class of efficient linear and nonlinear optical devices. By domain microengineering is meant shaping of ferroelectric domains and domain walls into diverse shapes and sizes to create optical elements such as gratings, lenses, prisms etc. Examples include quasi-phase matched frequency converters [21], electro-optic scanners [9], dynamic focusing lenses [17], total internal reflection mirrors, etc. Most of the

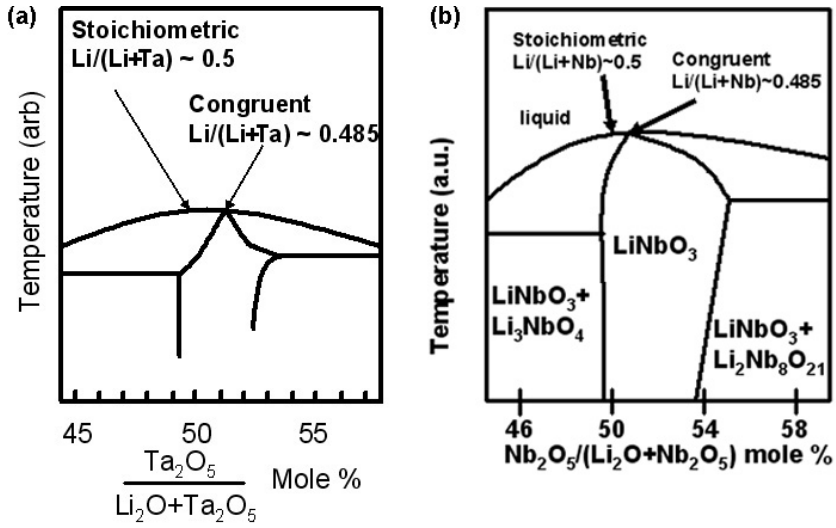

Fig. 1.4. (a) Phase diagram of $Li_2O - Ta_2O_5$ system. (b) $Nb_2O_5 - Li_2O$ phase diagram. Congruent point is off set from stoichiometric composition in both (a) and (b).

recent ferroelectric domain engineered devices are second harmonic generators or parametric oscillators for nonlinear frequency conversion application. A second harmonic generator converts light of frequency of ω to light of frequency 2 ω using a domain grating. This is schematically shown in Figure 1.5 (a), where the period of the domain grating is chosen to be twice the coherence length, $2l_c$, where coherence length is the length over which the two frequencies of light (ω and 2ω) go π out-of-phase with each other. A domain reversal after every coherence length resets this phase shift by providing an additional phase shift of π. Recently, pulse shaping, and pulse squeezing devices have been made by using periodically domain inverted $LiNbO_3$ (PPLN) crystals.

In addition to these domain engineered nonlinear optical devices,*electro-optics* based integrated optical devices are made in $LiNbO_3$ and $LiTaO_3$ crystals [13] [8]. [12]. Electro-optic refers to the change in the refractive index in a material when an external electric field is applied. For $LiNbO_3$, an electric field E_3 along the polarization direction $+c$ (also referred to by subscript 3), changes the extraordinary index n_{33}=n_e by an amount $\Delta\ n_e = -(1/2)n_e^3 r_{33} E_3$. The index decreases by this amount when the electric

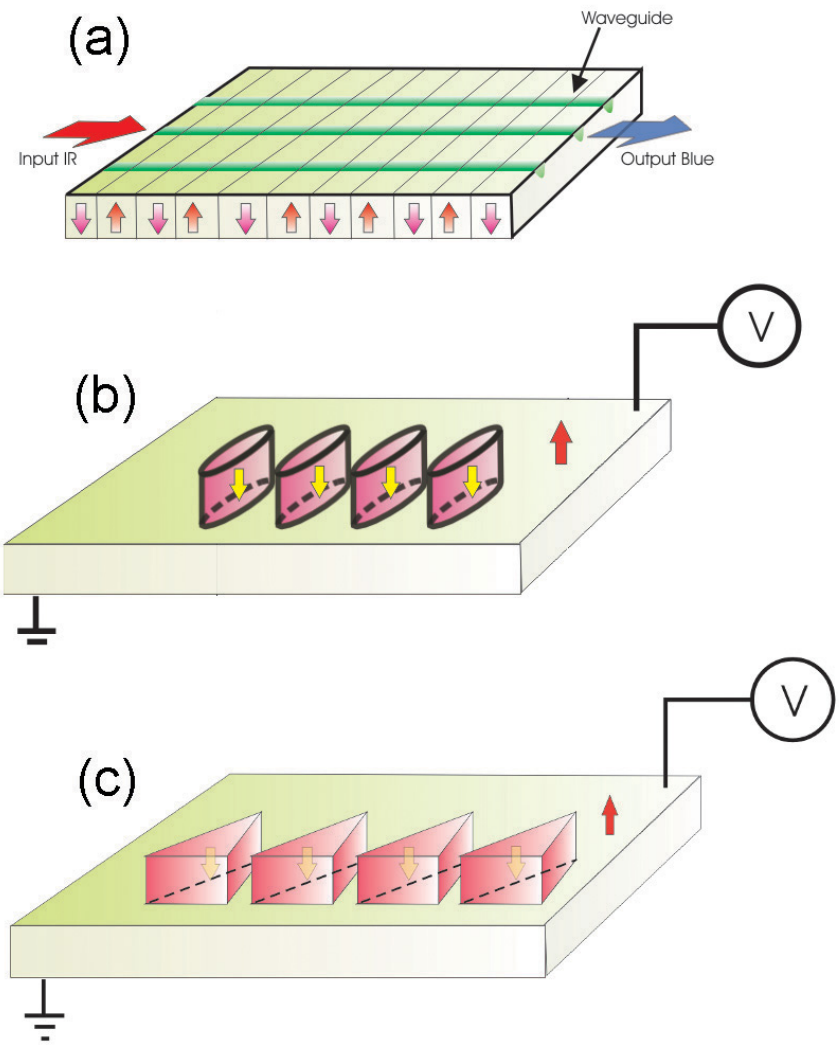

Fig. 1.5. Domain engineered micro optical devices. (a) frequency converter, (b) dynamic focusing electro-optic lens stacks, and (c) dynamical beam deflectors stack. Arrows inside the crystal indictae domain orientation.

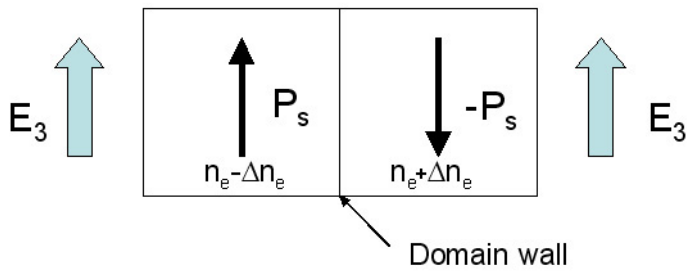

Fig. 1.6. Schematic shwoing principle of electro-optic effect.

field is parallel to the polarization direction, and increases when it is antiparallel to the polarization direction. Therefore, when a uniform electric field is applied across a domain wall as shown in Fig. 1.6, an index change of $2 \cdot \Delta n_e$ is created across the wall, which is linearly electric field tunable. This can be used to create electro-optic tunable devices. Figure 1.5 shows some such examples of electro optical devices made by domain microengineering. The dynamic focusing lens shaped domains in Figure 1.5 (b) can focus and defocus light under varying polarities and magnitudes of external electric fields [17]. The prism shaped Figure 1.5 (c) can scan light beams under external electric fields [9]. These integrated electro-optical devices have many advantages compared to the traditional optical devices. They can be integrated in a small single crystal, and can operate in the 100GHz range.

These are just some of the examples of numerous optical devices that can be designed by the ability to arbitrarily shape ferroelectric domain walls. In domain engineered nonlinear optical devices and electro-optical devices, *micro domain* engineering is a key technology. As device shrinks, domain patterning becomes more challenging. For example domain patterning below 5 μm sizes is a real challenge today. It is clear that a detailed understanding of the domain wall properties will push the technological limitations farther beyond. In order to do this, one has to understand the static and dynamic structure of domain walls in lithium niobate and tantalate. This is the primary focus of this thesis work.

1.4 Research Objectives

It is the objective of my thesis work to shed light on one of the most fundamental questions relating to these fascinating materials: How do the rich spectrum of electrical, elastic and optical properties of ferroelectrics on nanoscale to macroscale depend on atomic defects?

I focus on two prototypical ferroelectric materials, Lithium Niobate ($LiNbO_3$) and Lithium Tantalate ($LiTaO_3$). In my dissertation, I have made a number of discoveries that show that very small amount of point defects (missing atoms) in these crystals can change the macroscopic properties (such a fields required to reorient domains), often dramatically by an order of magnitude. The key bridge between these vastly different length scales (atoms to bulk) is the mesoscale phenomenon of ferroelectric domains and domain walls on nanometer length scales that mediate the influences from atomic defects to macroscale properties. I have conducted experimental and theoretical investigations of domains and domain walls on nano-to-micrometer length scales towards developing this bridge. These experiments include dynamic properties of domain walls under external fields, probing the local strain around domain walls using synchrotron X-ray imaging, and probing local optical properties near domain walls using Near-field Optical Microscopy (NSOM). My theoretical work involves modeling and simulation of domain wall structure and motion using Time-Dependent Ginzburg-Landau (TDGL) theory, and developing point defect models on atomic scales, simulating local strain effects observed in X-ray experiments using dynamic theory of X-ray scattering, and developing a Finite-Difference-Time-Domain(FDTD) simulation, and Beam Propagation Method(BPM) code to simulate local optical effects observed using NSOM. Putting all these efforts together, when the local electrical, elastic and optical effects at domain walls are thoroughly understood at this level of detail and depth, a more general framework can evolve for understanding ferroelectrics and the influence of atomic scale structure on their properties. This work will hopefully shift our approach to technologies based on these materials from an empirical trial-and-error method to a science-based approach.

1.5 Thesis Organization

To investigate domains and domain walls on macroscales, I have studied in-situ electrical field induced domain reversal experiments using optical microscopy as detailed in chapter 2. I have employed the time dependent Ginzburg-landau (TDGL) theory to understand the shape and dynamics of domains evolving in these crystal systems under equilibrium and under external fields. Chapter 3 includes all detailed derivations and simuation results from this TDGL analysis. To investigate the local structure of domain wall strains, I've carried out static and dynamic synchrotron X-ray topography experiments and simulated experimental images by using dynamical X-ray scattering theory (Ch. 4). To study the nanoscale optical properties of a domain wall that cannot be imaged by diffraction limited optical microscopy, I have employed Near Field Optical Microscopy (NSOM). To analyze these NSOM images, I have developed a new Finite Difference Time Domain based approach for calculating Optical Transfer Function(OTF) of the NSOM tip. Using this analysis, in combination with Beam Propagation method, I have quantitatively extracted the local optical index structure at a domain wall. All these experimental and numerical NSOM studies are explained in chapters 5. Finally all these experimental and theoretical results on different length scales are compared and linked together in chapter 6.

References

[1] A. A. Ballman. *J. Am. Ceram. Soc.*, 48:112, 1965.

[2] A. M. Prokhorov and Y. S. Kuzminov. *Physics and Chemistry of Crsytalline lithium niobate*. Hilger, Bristol, 1990.

[3] A. Rauber. *Chemistry and Physics of lithium niobate, current topics in Materials Scinece (E. Kaldis, Ed.)*. North Holland, New York, 1978.

[4] B. T. Matthias. *Phys. Rev.*, 75:1771, 1949.

[5] B. T. Matthias and J. P. Remeika. *Phys. Rev.*, 103:262, 1949.

[6] Scherrer. P Busch. G. *Naturwissenschaft*, 23:737, 1935.

[7] C. Kittel. *Introduction to Solid State Physics*. John Wiley and Sons, Inc.

[8] V. Gopalan K. T. Gahagan R. Sander J. M. Robinson F. Muhammad P. Chandramani F. Kiamilev D. A. Scrymgeour, A. Sharan. *Appl. Phys. Lett*, 81:3140, 2002.

[9] V. Gopalan K. T. Gahagan R. Sander J. M. Robinson F. Muhammad P. Chandramani F. Kiamilev David A. Scrymgeour, A. Sharan. *Appl. Phys. Lett*, 81:3140, 2002.

[10] Devonshire. A. F. *Phil. Mag.*, 40:1040, 1949.

[11] D.Psaltis and G.W.Burr. *Computer*, 31:52, 1998.

[12] J. Ekman F. Kiamilev D. Scrymgeour V. Gopalan E. Moore M. Weiler F. Muhammad, P. Chandramani. Multi-channel 1.1kv arbitrary waveform generator for beam steering using ferroelectric device. *IEEE Photonics Technology Letters*, 14:1605, 2002.

[13] H. Neumann G. Arlt. *Ferroelectrics*, 87:109, 1998.

[14] K. Suzuki G. Shrane, S. Hoshino. *Phys. Rev.*, 80:1105, 1950.

[15] H. F. Taylor. *J. Lightwave Technol.*, 17:1875, 1999.

[16] A. Ballato J. G. Gualtieri, J. A. Kosinski. *IEEE Trans. Ultrason. Ferroelectr. Freq. Control*, 41:53, 1994.

[17] Joanna L. Casson J. M. Robinson V. Gopalan K. T. Gahagan, David A. Scrymgeour. *Applied Optics*, 81:3140, 2002.

[18] Muller. H. *Phys. Rev.*, 57:829, 1940.

[19] Muller. H. *Phys. Rev.*, 58:565, 1940.

[20] P. W. Anderson. *In Fizika Dielectrikov*. Akad. Nauk. SSSR, Moscow, 1960.

[21] M. M. Fejer R. L. Byer R. G. Batchko, V. Y. Shur. *Appl. Phys. Lett.*, 75:1673, 1999.

[22] A. Sequeira S. C. Abrahams, W. C. Hamilton. *J. Phys. Chem. Solids*, 28:1693, 1967.

[23] J. L. Bernstein S. C. Abrahams, J. M. Reddy. *J. Phys. Chem. Solids*, 27:997, 1966.

[24] J. M. Reddy S. C. Abrahams, C. W. Hamilton. *Phys. Chem. Solids*, 27:1013, 1966.

[25] J. M. Reddy S. C. Abrahams, W. C. Hamilton. *J. Phys. Chem. Solids*, 27:1013, 1966.

[26] J. A. Aust K. Kitamura Y. Furukawa V. Gopalan, N. A. Sanford. *Crystal growth, characterization, and domain studies in lithium niobate and lithium tantalate ferroelectrics," handbook of advanced electronic and photonic materials and devices, edited by H. S. Nalwa, Vol 4: ferroelectrics and Dielectrics*. Academic Press, 2001.

[27] W. Cochran. *Adv. Phys*, 9:387, 1960.

Chapter 2

Macroscale Domain Structure and Dynamics and the Role of Non-Stoichiometric Defects

As explained in Ch. 1, ferroelectric lithium tantalate ($LiTaO_3$) and lithium niobate ($LiNbO_3$) have emerged as key optical materials in nonlinear frequency conversion [1], electro-optics [2], and holography [3]. Manipulation of ferroelectric domains into diverse shapes such as gratings, lenses, prisms, and other shapes are key to many of these applications. This is primarily achieved by the application of an external electric field. Recent discoveries [4], [5] show that the threshold coercive fields required for domain reversal change dramatically in these crystals with changes in lithium non-stoichiometry. Lithium non-stoichiometry also strongly affects the optical, electrical, and elastic properties of crystal lattice near domain walls, and the dynamics of domain nucleation and growth as recently reviewed in detail in a handbook chapter [6]. While the domain reversal properties of the lithium-deficient *congruent* composition (C=Li/(Li+Ta,Nb)=0.485) have been widely reported (see Ref. [6] and references therein), limited information is available so far regarding domain reversal properties of stoichiometric (C=0.5) or near-stoichiometric crystals [4], [5]. Any systematic understanding of the role of point defects in domain reversal characteristics is also lacking at present.This chapter attempts to address these two issues as follows. A systematic study of domain reversal characteristics of near-stoichiometric (C=0.498) crystals of $LiTaO_3$ is presented. Real-time experiments are presented which track individual domain walls and their motion in real time on time scales as small as 0.5 ms. The phenomena of domain stabilization time, domain "back-switching," the changes in threshold coercive field with repeated cycling of external electric field at different frequencies, the switching times, wall mobilities, and pinning times are investigated. These results are then contrasted with those of congruent composition crystals of $LiTaO_3$. Finally, we propose a qualitative defect model to interpret

some of the observed phenomena, such as internal fields, domain backswitching and stabilization times, and dependence of threshold coercive fields on polarization cycling.

Stoichiometric crystals of $LiTaO_3$ were grown by the double crucible Czochralski (DCCZ) technique as described in detail elsewhere. [5], [7] Here we briefly describe the salient facts. In order to grow stoichiometric crystals, a lithium rich melt (60 mol percent Li_2O) is required. The double crucible geometry consists of an inner and an outer iridium crucible connected by holes in the wall of the inner crucible. This allows the growth melt to be replenished with material in the outer crucible, in exact proportion to the weight of the crystal grown from the inner melt. This is done in real-time using an automatic weighing and powder supply system. The crystals grown along the crystallographic y axis (lying in the $(11\bar{2}0)$ mirror plane) were transparent and crack-free. The Curie temperature was measured as 685±1 °C, which is very close to the Curie temperature of 690±1 °C for sintered stoichiometric $LiTaO_3$ powder. Assuming a linear relationship between Curie temperature and crystal composition [7], the crystal composition Li/(Li+Ta) is estimated to be 0.4977-0.4992, which is quite close to the stoichiometric composition of 0.5. We will, however, show that this deviation from stoichiometry is nonetheless significant enough to introduce defect fields and influence the physical properties of these crystals. An impurity concentration of 0.9 wt ppm Fe was measured. Copper and chromium were less than 0.1 and 0.2 wt ppm, respectively. The as-grown crystals were observed to be multi-domain. The lattice papameters of congruent $LiTaO_3$ are 5.1543($\dot{A}$) and 13.7808($\dot{A}$) for a_o and b_o, respectively. In stoichiometric crystal case, lattice parameters a_o and b_o are 5.1516($\dot{A}$) and 13.7744($\dot{A}$), respectively. In stochiometric $LiTaO_3$ crystal case, crystals show no growth striations and have small refractive index chnages less than 10^{-5} throughout the $1cm^3$ cubic sample. The crystal was cut into a z-cut block, which was annealed in air at 750 °C, and subsequently cooled down at a rate of 2 °C/ min to room temperature under a dc electric field along the z direction. These blocks were cut into z-cut plates of 10×10×0.25 mm, and optically polished, resulting in plates which were single crystal and single domain, though some microdomains of 50 μm or less size were also observed. This starting state

of the crystal will be referred to in the rest of this article as the "virgin state" with a ferroelectric polarization of -P_s .

2.1 Real-time observation of domain wall motion in near-stoichiometric composition

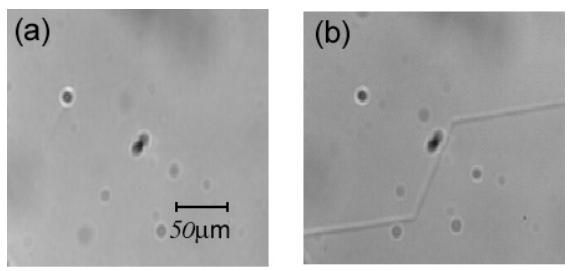

Fig. 2.1. Optical microscope image, in unpolarized transmitted light, of a 180° domain wall in z-cut near-stoichiometric $LiTaO_3$. (a) No electric field applied. The wall is not visible. (b) An electric field of 10 kV/cm applied to the crystal along the z axis, rendering the wall visible through the electro-optic effect. The polarization is normal to the image plane.

Starting from the virgin state of a 0.25 mm thick z-cut crystal, electric field is applied across the z faces to reverse the ferroelectric polarization at room temperature. Tap water is used as electrodes, with no dissolved salts, since dissolution of KNO_3 salt, for example, to any saturation level did not appear to change the observed results. The application of an electric field E_3 parallel to the z axis also gives rise to an index difference $2\Delta n_{23} = n_0^3 r_{23} E_3$ across a 180° domain wall where r_{23} is the electro-optic coefficient and n_o the ordinary index. This index difference gives rise to scattering of light at the wall which is optically imaged [8]. For example, the domain wall is not visible in Fig. 2.1(a), but becomes visible in 2.1(b), when an electric field of 10 kV/cm (which is less than the field required for wall motion) is applied along the z-axis of the

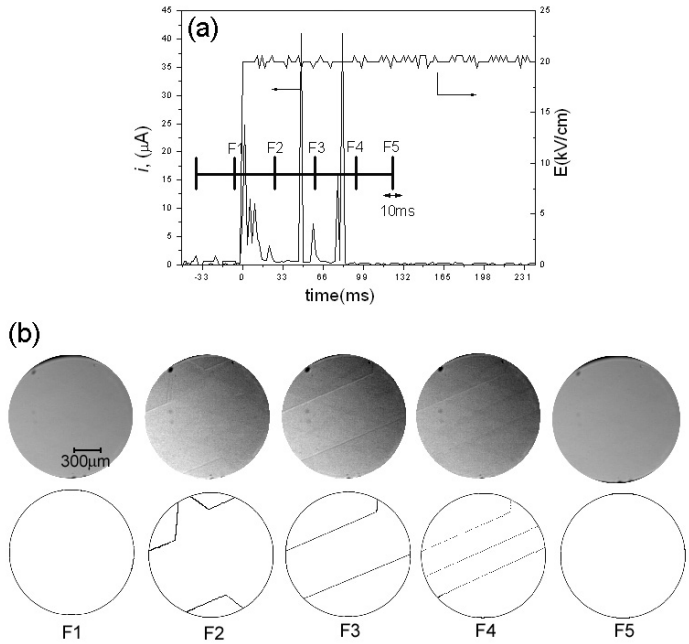

Fig. 2.2. Tracking domain wall motion under external field in a z-cut near-stoichiometric $LiTaO_3$ crystal. Electrode area was 1.2 mm^2. (a) The applied step field of ≈20 kV/cm and the corresponding transient current response, and (b) the corresponding optical images of the moving wall recorded with a video camera (33 frames/s). The time instants of the five frames shown in (b) are marked by F1F5 in (a).

crystal. Since the electric field employed for domain reversal can also aid in optically imaging the domain wall, we can study the real-time motion of domain walls under electric fields. The real-time movie was recorded using either a standard video recorder with 30 frames/s or a high-speed camera (Kodak Ektapro) with 2000 frames/s. The frames were then digitally extracted from the recorded movie using computer software.

Figure 2.2(a) shows a series of selected optical images showing the progression of domain wall creation and motion under an electric field. Also shown in Fig. 2.2(a) is the corresponding transient current, i, observed during domain reversal where $i=dq/dt=d/dt(2P_sA)$. Here A is the area of reversed domain regions, P_s is the spontaneous polarization, q the charge, and t the time. The transient currents are in the form of spikes, suggesting a very fast domain wall motion within a few milliseconds

followed by no domain motion and so on. The video frames shown here, with only a resolution of 33 ms per frame, nonetheless show the net domain motion corresponding to the transient current spikes observed in the interval between two frames. F1 shows no domain walls. After one frame interval(33 ms) corresponding to F2, three small domains have nucleated, corresponding most likely to the first three main current spikes seen in Fig. 2.2(b). The domain merging process is observed between frames F2 and F3, and therefore frame F3 shows two big merged domains. Finally these two remaining domains merge between frames F3 and F4. It is interesting to note that even though domain reversal is complete in frame F4, a faint trace of the original domain wall position in F3 is still retained in F4. After ≈33 ms this contrast disappears resulting in frame F5. This is the faint residual optical contrast at a location of a domain wall after the wall has moved away. It arises from residual strains at the domain wall which in turn arise from a small amount of lithium nonstoichiometry in the crystal and induce optical contrast through elasto-optic effect as well as through coupled piezoelectric and electro-optic effects [6]. Though faint, and difficult to observe under bright illumination conditions [such as in Fig.2.1(a)], under careful observation, this contrast is visible at a wall in near-stoichiometric crystals. The total time to reverse a domain in a given area is called the switching time, t_S , which in Fig. 2.2(a) is 80 ms as determined from the transient current data.

2.2 Domain switching kinetics

Under an electric field, the first polarization reversal (or poling) of a virgin crystal from the *virgin state* to a *domain reversed state* is termed forward poling (denoted by symbol f1), and the second reversal back to virgin state is called reverse poling (denoted by symbol r1). Subsequent forward and reverse poling operations are then successively labeled f2, f3, f4,...,etc. and r1, r2, r3,...,etc., respectively. The polarization hysteresis loop is measured by linearly ramping the electric field and tracking the transient currents created during domain reversal. When the spontaneous polarization reverses from $+P_S$ to $-P_S$ (or vice versa), the total charge q, observed under the transient current i, is $q=\int idt = 2P_SA$, where A is the electrode area and t the time. The threshold coercive

field is arbitrarily chosen as the electric field value at which the integrated charge under the transient current peak is 1 percent of the total integrated charge q under the peak. The domain switching times are typically greater than 30 min at these measured threshold coercive fields. This definition was chosen over the conventional definition of coercive field at 50 percent domain reversed area, since we wanted to measure the lowest threshold coercive fields at which reversal begins. In order to study the effect of repeated cycling of ferroelectric polarization between $+P_s$ and $-P_s$, another experimental variable was introduced called the cycling time gap, $t_{g,j}$, where j=f(for forward poling) or j=r (for reverse poling). This time gap is a measure of the time gap allowed between the beginning of one domain reversal sequence (as monitored by the transient current peak) and the beginning of another. For example, $t_{g,r}$ is the time gap between the beginning of f1 and the beginning of a successive r1, and $t_{g,f}$ is the time gap between the beginning of r1 and the beginning of a successive f2. In other words, $t_{g,r}$ is the longest time period that any part of the crystal under the electrode stays in domain state $+P_s$ (after its creation) before being reverse poled into the $-P_s$ state. Similarly, $t_{g,f}$ is the longest time period that a domain stays in the $-P_s$ state (after its creation) before being forward poled into the $+P_s$ state.

2.2.1 Threshold coercive fields

Figure 2.3 shows the hysteresis loops of polarization versus electric field for $t_{g,j}$=300 and 60 s. The observed threshold coercive fields for $t_{g,j}$=300 s are $E_{c,f}$ 16.7 kV/cm and $E_{c,r}$ 14.5 kV/cm. For $t_{g,j}$=60 s, the threshold coercive fields decrease to $E_{c,f}$=13.6 kV/cm and $E_{c,r}$=12.3 kV/ cm. The internal field, $E_{int}=(E_{c,f}-E_{c,r})/2$" 1.1 kV/cm for $t_{g,j}$=300s and 0.7 kV/cm for $t_{g,j}$=60s. In both cases, the offset of the hysteresis loop is along the positive (forward poling) field axis. For $t_{g,j}$=300s the threshold coercive field shows a sharp decrease. Figures 2.4(a) and 2.4(b), respectively, show the forward ($E_{c,f}$) and reverse ($E_{c,r}$) threshold coercive fields as a function of total cycling time $t_{g,j}$. The data corresponding to the shortest time gap, $t_{g,j}$, was obtained by measuring the stabilization time, $t_{stab,j}$, for forward and reverse poling. By the definition of stabilization time (as explained in the following section), when $t_{g,r}=t_{stab,j}$, $E_{c,r}$=0; and

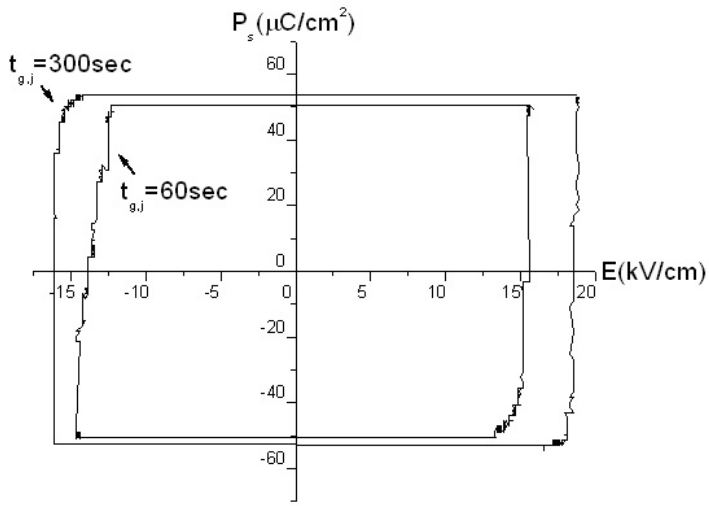

Fig. 2.3. The polarization hysteresis loops of near-stoichiometric z-cut $LiTaO_3$ crystals. The outer and inner loops are measured for time gaps $t_{g,j}$ spent in any domain state before successive polarization reversal of 300 and 60 s, respectively. Lower time gaps reduce the coercive fields as well as the saturation polarizations $\pm P_s$.

similarly, at $t_{g,f}=t_{stab,r}$, $E_{c,f}=0$. The solid line fits to the measurements (for $t_{g,j} > t_{stab,j'}$) are based on a double exponential function of the form

$$E_{c,j} = \Sigma_i E_{i,j}[exp(-t_{stab,j'}/\tau_{i,j}) - exp(-t_{g,j}/\tau_{i,j})] \tag{2.1}$$

where i=1,2 and (j,j')=(f,r) or (r,f), referring to forward (f) or reverse (r) poling directions. Table I lists the time constants $\tau_{i,j}$, $t_{stab,j'}$, and the preexponents $E_{i,j}$. Note that by definition, at $t_{g,j}=t_{stab,j'}$, $E_{c,j}=0$. The relaxation times $\tau_{i,j}$ are very similar for forward and reverse poling suggesting similar relaxation mechanisms. An important aspect of this figure is the presence of negative threshold coercive fields when $t_{g,j} < t_{stab,j'}$. The presence of negative threshold coercive fields in Figs. 2.4(a) and 2.4(b) appear counterintuitive, but are physically real. In this regime the negative threshold coercive field refers to the minimum baseline voltage that should be applied following the end of

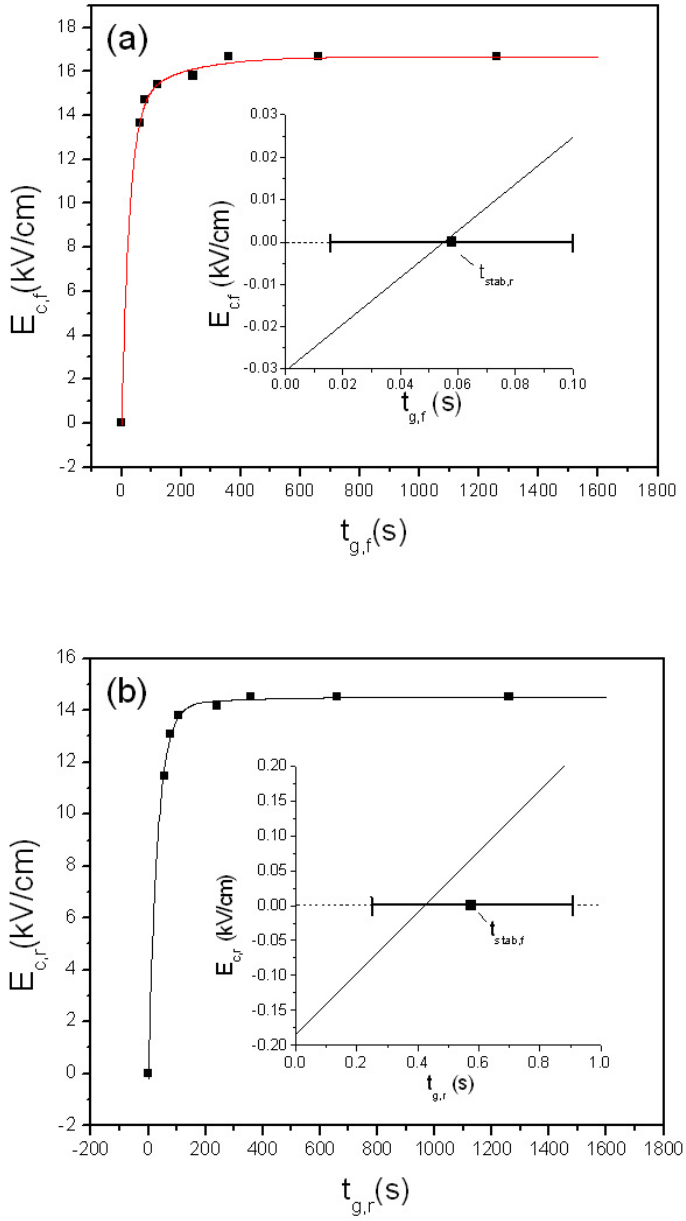

Fig. 2.4. The dependence of coercive field $E_{c,j}$ on the cycling time gap $t_{g,j}$ for (a) forward poling (j=f) and (b) reverse poling (j=r) for z-cut nearstoichiometric $LiTaO_3$. The time axis crossings at $E_{c,j}$=0 are equal to the measured stabilization times of $t_{stab,j'}$, where (j,j′)=(f,r) or (r,f). These are shown more clearly in the insets. The solid lines are double exponential fits as described by Eq. (1). The fitting parameters are given in Table 2.1. A single data point in the negative coercive field range as shown was measured for both forward and reverse poling.

the original pulse of width $t_{g,j}$ in order to prevent domain backswitching after the pulse. Such baseline voltages are often used to stabilize domains created by short pulses while fabricating domain microengineered devices [1]. The behavior of threshold coercive fields with time gap, $t_{g,j}$, appears in general to follow a different exponential time constant for time gaps shorter and longer than the stabilization time, $t_{stab,j'}$. The functional form for this behavior for $t_{g,j} < t_{stab,j'}$ is the same as Eq. 2.1. In near-stoichiometric crystals, only one data point could be obtained for the negative threshold coercive field regime due to the short times scales over which they occur. However, for congruent crystals, negative threshold coercive fields show a clear trend with at least one exponential (j=1) with a corresponding time constant, τ_{ij} (see Table I). Negative threshold coercive fields are discussed further in the following section.

$LiTaO_3$ composition Poling direction	$E_{1,j}$(kV/cm)	$\tau_{1,j}(s)$	$E_{2,j}$	$\tau_{2,j}(s)$	$t_{stab,j'}(s)$
near-stoichiometric forward poling(f) $t_{g,j} > t_{stab,j'}; (j, j') = (f, r)$	14.50 ± 1.50	26.4 ± 6	2.21 ± 1.49	177.5 ± 104	0.058 ± 0.043
near-stoichiometric reverse poling(f) $t_{g,j} > t_{stab,j'}; (j, j') = (r, f)$	14.38 ± 0.55	32.4 ± 2.6	0.33 ± 0.14	310.3 ± 200	0.55 ± 0.43
congruent forward poling(f) $t_{g,j} > t_{stab,j'}; (j, j') = (f, r)$	175.66 ± 3.80	20.3 ± 0.9	31.29 ± 3.23	399.6 ± 68	0.05 ± 0.03
congruent forward poling(f) $t_{g,j} < t_{stab,j'}; (j, j') = (f, r)$	−37.78 ± 1.06	0.0027 ± 0.006			0.05 ± 0.03
congruent reverse poling(r) $t_{g,j} > t_{stab,j'}; (j, j') = (r, f)$	100.37 ± 8.25	26.5 ± 3.9	19.80 ± 7.83	316 ± 179	0.7 ± 0.2
congruent reverse poling(r) $t_{g,j} < t_{stab,j'}; (j, j') = (r, f)$	−104.06 ± 4.19	0.06 ± 0.006			0.7 ± 0.2

Table 2.1. The fitting parameters in Eq. 2.1 describing the experimental dependence of coercive fields $E_{c,j}$ on the time gap $t_{g,j}$ spent in the previous domain state as given in Figs. 2.4 and 2.10.

2.2.2 Domain backswitching and stabilization time

Domain backswitching and stabilization processes in congruent $LiTaO_3$ crystals have been previously reported [6]. A domain created by the application of an electric field needs a certain minimum amount of time for which the electric field that created it should remain and stabilize it. This time is called the stabilization time, or $t_{stab,j}$, for the domain and subscript j=(f,r) refers, respectively, to forward or reverse poling. If the electric field is removed in a time $t_{g,j} < t_{stab,j'}$, where (j,j')=(f,r) or (r,f), then the newly created domain shrinks and reverts back to the original domain configuration that existed before the application of the field. This reversible domain wall motion is called domain backswitching. In reality, a range of stabilization times is found such that when, for example, $t_{g,f} < (t_{stab,r})_{start}$, complete domain backswitching is observed. When $t_{g,f} > (t_{stab,r})_{end}$, no domain backswitching is observed. In the intermediate pulse widths, partial domain backswitching is observed. The stabilization time was measured by applying square electric field pulses with varying pulse widths and electric field magnitudes and observing the transient currents.

Figure 2.5(a) shows the negative transient current response during domain backswitching on application of a voltage pulse of 60 kV/cm and 10 ms duration. Figure 2.5(b) shows the corresponding optical images of the domain walls during the backswitching process. These images were taken with a high-speed camera capable of 2000 frames/s. The time resolution was therefore 0.5 ms between frames, and the time instant starting from the beginning of the voltage pulse at t=0 is indicated on each frame. Domain reversal takes place until the first 10 ms, when the voltage pulse is on, followed by backswitching after the pulse disappears. In this case, the backswitching time was > 60 ms. When the external pulse is shorter, back switching time is ≈1-10 ms. If the external pulse time is close to stabilization time, back switching time increases to several hundred milliseconds. Figure 2.6(a) shows stabilization times $(t_{stab,j})_{start}$ and $(t_{stab,j})_{end}$ as a function of electric field. Many interesting aspects can be observed. The stabilization time decreases rapidly as the electric field exceeds the threshold coercive field for domain reversal. If the external field exceeds 20 kV/cm in the forward poling and 17 kV/cm in reverse poling, the stabilization times are relatively insensitive to the electric

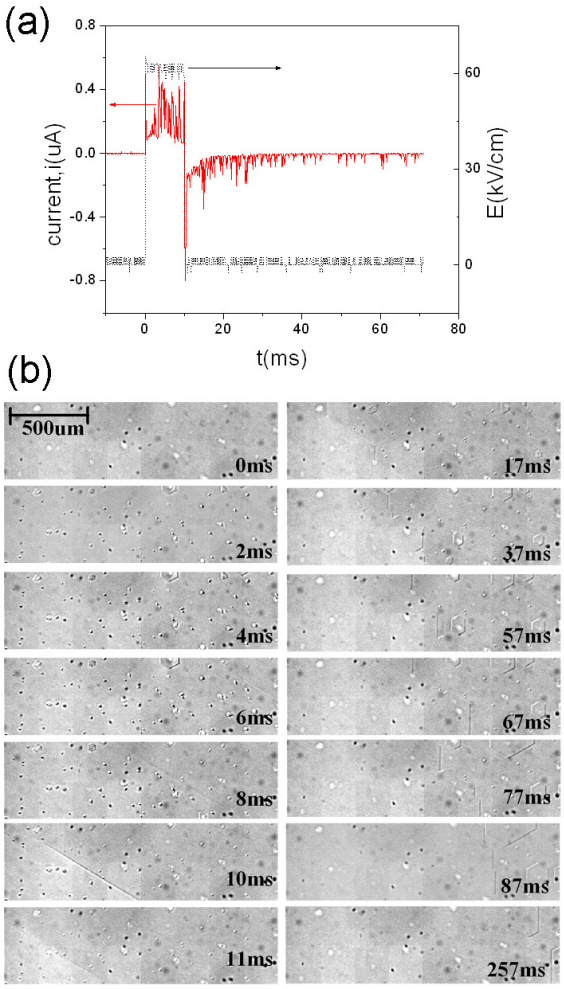

Fig. 2.5. Tracking domain backswitching phenomenon in z-cut nearstoichiometric $LiTaO_3$ following the application of a forward poling electric field pulse of 60 kV/cm and 10 ms width at time t=0 ms. Electrode area was 20 mm^2. (a) Voltage (broken line) and transient current (solid line). (b) The corresponding selected video frames using a 2000 frames/s camera. The first six frames of optical microscope images show forward switching domain motion. A large domain wall sweeps away smaller domain nucleations starting from the top right corner to bottom left corner. After a 10 ms frame, domain backswitching is captured starting from the bottom left corner. The time elapsed from the start of the voltage pulse for each frame is marked.

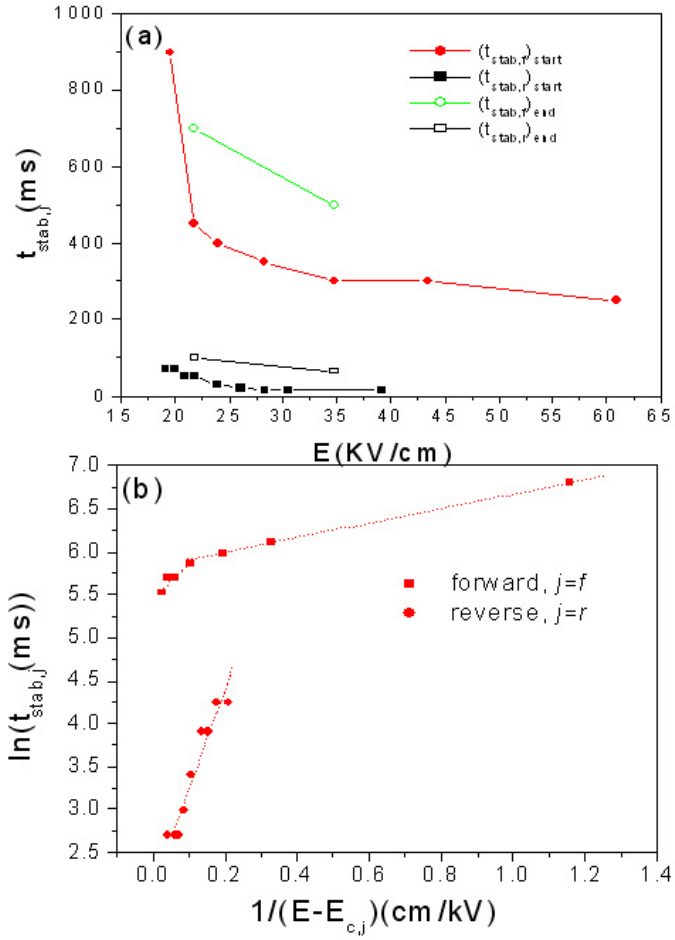

Fig. 2.6. (a) The forward and reverse stabilization times $t_{stab,j}$ where j=f for forward poling and j=r for reverse poling in near-stoichiometric z-cut $LiTaO_3$ crystals. The subscript start refers to the time gap $t_{g,j}=t_{stab,j'}$, (j,j′)=(f,r) or (r,f) below which complete domain backswitching is observed, and end refers to the time gap above which no backswitching occurs. (b) A log plot of the same information as in (a), linear fits are according to Eq. 2.3. The coercive fields $E_{c,f}$=18.7kV/cm and $E_{c,r}$=14.4kV/cm.

field magnitude and are approximately $(t_{stab,f})_{start}$ ≈300 ms, and $(t_{stab,r})_{start}$ ≈30 ms. The stabilization time in forward poling is ≈10 times higher than in reverse poling at the same electric field. Figure 2.6(b) shows a logarithmic plot of the dependence of stabilization time on the electric field. An exponential dependence is found for $(t_{stab,j})_{start}$ as a function of electric field for most of the field range except for fields very close to the threshold coercive field in forward poling geometry. Dropping the subscript *start*, we can write this dependence as

$$t_{stab,j} = t_{stab,jo} exp(\frac{\delta_{stab,j}}{E - E_{c,j}}) \tag{2.2}$$

where j=f or r, the activation values are $\delta_{stab,f}$ = 1.72 ± 0.32kV/cm and $\delta_{stab,r}$ = 11.6 ± 1.67kV/cm. The pre-exponent values are $\ln[t_{stab,fo}(ms)]$ = 5.6±0.05 and $\ln[t_{stab,ro}(ms)]$ = 2.08 ± 0.53. Referring back to the discussion of Fig. 2.4, we now briefly discuss the negative threshold coercive fields when the cycling time $t_{g,j}$ is below the pulse stabilization time $t_{stab,j'}$, where (j,j')=(f,r) or (r,f). As an example, let a square electric field pulse with $E > E_{c,f}$ and a pulse width of approximately equal to, but slightly smaller than, $(t_{stab,f})_{start}$ be applied to the crystal in forward poling. Domain reversal (forward poling) takes place during the pulse duration, and domain backswitching (reverse poling) takes place immediately after the pulse has ended and the electric field E is zero. In this situation, the external electric field required for reverse poling is zero, i.e., $E_{c,r} \approx 0$ and $t_{g,r} \approx (t_{stab,f})_{start}$. This defines the zero crossing of the threshold coercive field curve in Fig. 2.4(b). When the pulse width of the external pulse is much less than $(t_{stab,f})_{start}$, $E_{c,r} < 0$ in Fig. 2.4(b), implying that a short electric field pulse of magnitude $\geq E_{c,r}$ in the forward poling direction would be needed to prevent domain reversal in the reverse poling direction from taking place during backswitching. A similar case can also be made for negative $E_{c,f}$ in Fig. 2.4(a) by interchanging the phrase *forward poling* (and subscripts f) and the phrase *reverse poling* (and subscripts r) in the above arguments.

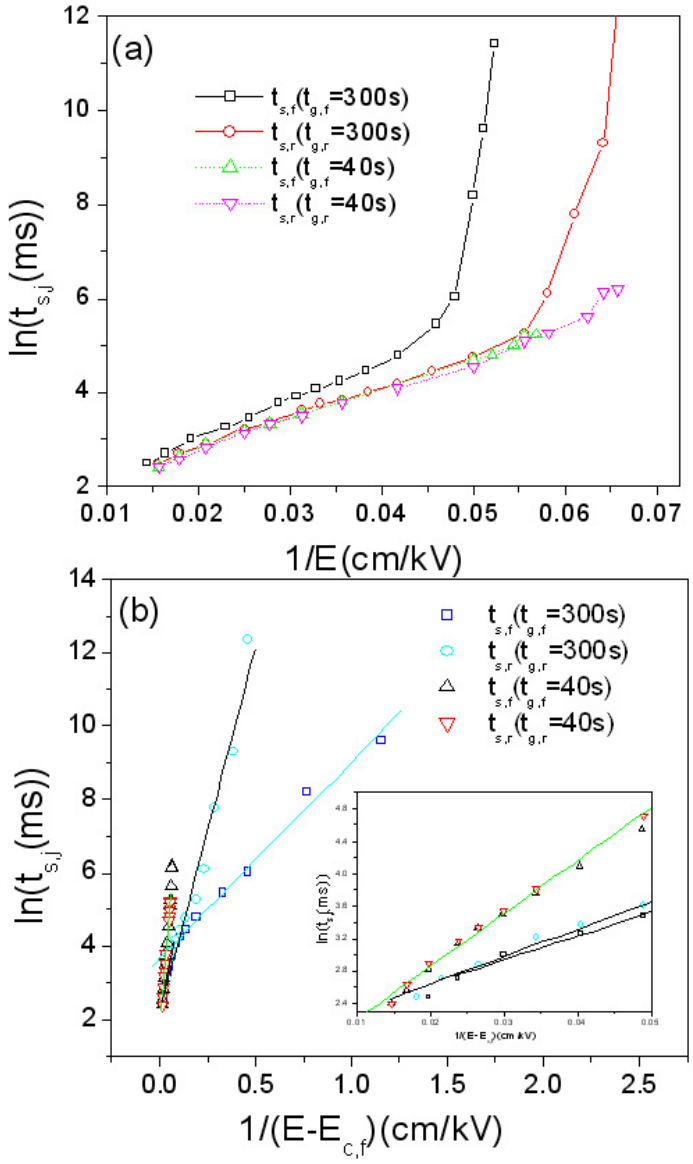

Fig. 2.7. (a) The domain switching time for z-cut near-stoichiometric $LiTaO_3$ crystals in forward (f) and reverse (r) poling for various time gaps, $t_{g,j}$, j=(f,r). The electrode area was 20 mm^2. (b) A log plot of the same information as in (a) the solid lines are fits according to Eq. 2.3. The coercive fields $E_{c,f}$=18.7 kV/cm and $E_{c,r}$=14.4 kV/cm for $t_{g,j}$=300s and $E_{c,f}$=1.36 kV/cm and $E_{c,r}$=1.23 kV/cm for $t_{g,j}$=40s. The activation field and preexponents from the fit are listed in Table 2.2.

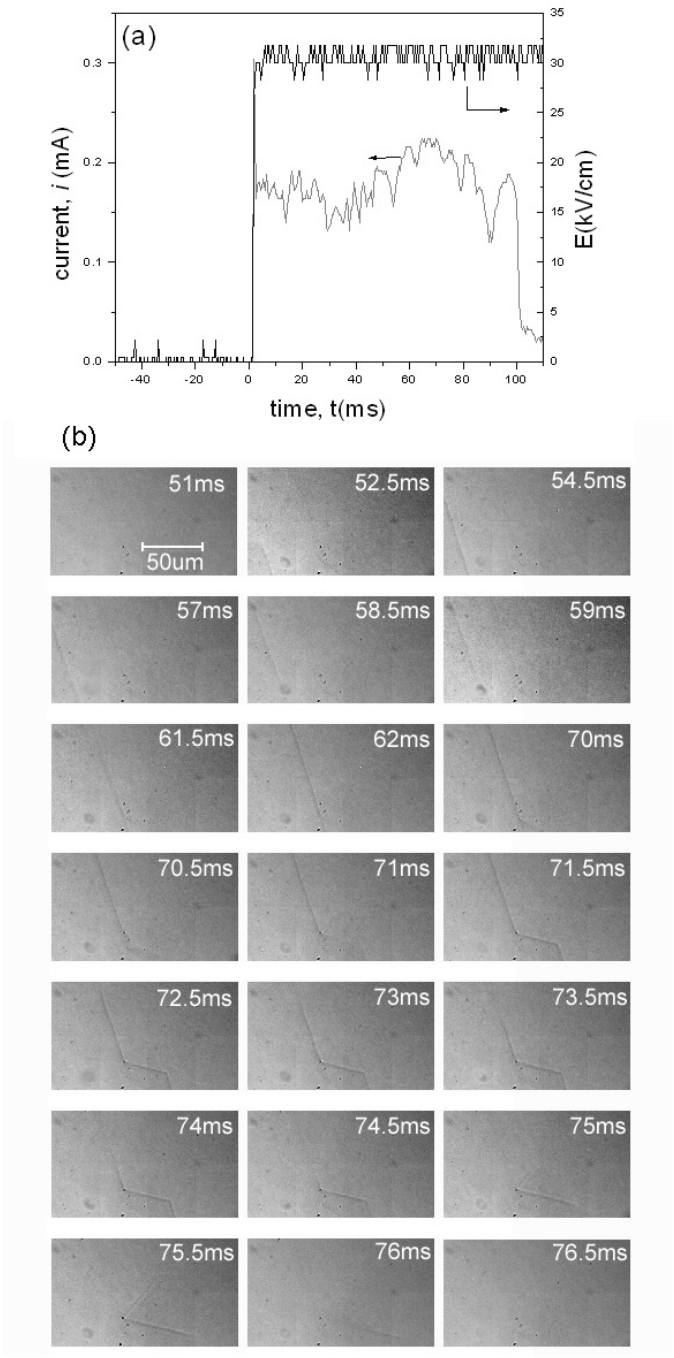

Fig. 2.8. High speed, real-time tracking of domain motion in z-cut near-stoichiometric $LiTaO_3$ under a forward poling external field of 30 kV/cm. The transient current (a) and the corresponding optical images (b) using a high speed camera (Kodak Ektapro) capable of real-time 2000 frames/s. The time instant, t elapsed after the application of field at t=0, is also marked in each frame.

Crystal: (coercive field)	Poling direction $t_{g,f}$	Field Regimes	$\delta_j(kV/cm)$ j=(f,r)	ln[$t_{s,jo}$(ms)] j=(f,r)
near-stoichiometric	forward(f)	$E - E_{c,f}$ >13.9kV/cm	26.48±2.1	2.1±0.1
$LiTaO_3$	$t_{g,f}$=300s	$E - E_{c,f}$ <13.9kV/cm	5.34±0.2	3.18±0.1
($E_{c,f}$=18.7kV/cm	reverse(r)	$E - E_{c,r}$ >16.1kV/cm	33.4±2.1	1.98±0.08
$E_{c,r}$=14.4kV/cm)	$t_{g,r}$=300s	$E - E_{c,r}$ <16.1kV/cm	19.85±1.4	2.2±0.34
	forward(f) $t_{g,f}$=40s	$E > E_{c,f}$	64.73±1.3	1.57±0.05
	reverse(r) $t_{g,r}$=40s	$E > E_{c,r}$	70.05±2.3	1.39±0.10
Congruent	forward(f)	$E - E_{c,f}$ >3.8kV/cm	51.4±5.9	-0.4±1.04
$LiTaO_3$	$t_{g,f}$=300s	$E - E_{c,f}$ <3.8kV/cm	1.49±0.5	11.35±0.35
($E_{c,f}$=211kV/cm)	reverse(r)	$E - E_{c,r}$ >2.1kV/cm	36.93±5.0	-1.8±1.03
	$t_{g,r}$=300s	$E - E_{c,r}$ <2.1kV/cm	0.95±0.5	10.44±0.76

Table 2.2. The fitting parameters for switching times $t_{s,j}$ in Eq. 2.4 obtained from transient current measurements in near-stoichiometric (Fig. 2.7) and congruent (Ref. [9]) compositions of $LiTaO_3$.

2.2.3 Switching time

Figure 2.7 shows electric field E versus switching time, $t_{s,f}$(during forward poling) and $t_{s,r}$(during reverse poling), respectively. Switching time here is interpreted as the total time required to switch the entire electrode area (20 mm^2 in this case). Two sets of data are shown, one for $t_{g,j}$=300s and $t_{g,j}$=40s. For $t_{g,j}$=300s two distinct activation fields appear to be present for each of the forward and reverse domain reversal processes that follow the exponential switching time relationships given by

$$t_{s,j} = t_{sb,jo} exp(\frac{\delta_j}{E - E_{c,j}}) \tag{2.3}$$

where j=f or r. By this definition, when the electric field E=$E_{c,f}$ or $E_{c,r}$, the switching times $t_{s,f}$ and $t_{s,r}$ tend towards infinity. For practical purposes, the extrapolated switching times at the measured threshold coercive fields are greater than 30 min in our case. A logarithmic plot of electric field E versus switching time $t_{s,f}$ in Fig. 2.7(b) shows the different activation field regimes more clearly. Table 2.2 lists the activation fields δ_f, δ_r

and the pre-exponents t_{fo} and t_{ro} . Some key observations are as follows. (1) Switching time decreases with decreasing $t_{g,j}$ following a similar trend to the threshold coercive fields in Fig. 2.4 As already shown (see Fig. 2.4), decreasing time gap $t_{g,j}$ results in a decreasing threshold coercive field $E_{c,j}$. For a fixed external electric field, a decrease in the threshold coercive field will result in a greater mobility of the domain wall and therefore a decrease in the switching time, which qualitatively explains this observation. (2) For $t_{g,j}$=300s, the switching times in the forward and reverse poling regimes show two distinct slopes (activation fields) for low and high external field regimes, the slope being considerably higher in the high field regime. (3) For $t_{g,j}$=40s, the distinction between high and low field regimes disappears, resulting in only one field regime. In this single regime, the switching times as well as the activation fields are equal for the forward and reverse poling as listed in Table 2.2. For shorter time gaps, $t_{g,j}$ approaching the stabilization time $t_{stab,j'}$, the difference between threshold coercive fields $E_{c,f}$ and $E_{c,r}$ become similar as seen from Fig. 2.4, as both of these quantities rapidly tend to zero. The switching times therefore become similar as will be seen here. The differences in forward and reverse threshold coercive fields and switching times are accentuated only for long time gaps, $t_{g,j}$.

2.2.4 Wall mobility

As seen in Fig. 2.2, the transient current shows a series of very sharp spikes on the order of milliseconds even at a constant driving field. Real-time video confirms this to correspond to discrete and sporadic jumps of domain walls. In the very-low field regime close to threshold coercive field (≈15.5-22kV/cm in the present samples), the domain motion occurs over a few milliseconds or less during the occurrence of transient current spikes. These spikes are sporadic and are often separated by seconds or minutes, in which time, no domain motion is seen on the macroscopic length scales (> 10μm). Since the regular VCRs with 30 frames/s do not have the dynamic time range of milliseconds-to-minutes, real-time measurement of domain mobility is not feasible. At higher electric fields of >22 kV/cm, which lie well within the high field regime discussed in Ch 2.2.3, the switching times are in the millisecond range, and the transient

current shows peaks which are merged into each other as shown in Fig. 2.8 (a). The fast domain wall velocities were measured with a high-speed charge coupled device camera (Kodak Ektapro) capable of 2000 frames per second in real time. Figure 2.8(b) shows a series of images from real-time domain motion with a time resolution of 0.5 ms between frames. It is noted that domain walls still show pinning and sporadic motion at these high fields. At all the studied fields, a single domain wall front was observed to sweep across the video screen in this particular sample area. Two parameters were measured from these real-time images: the maximum domain wall velocity of this wall, $v_{s,f}$ and the pinned time, $t_{p,f}$, spent by this domain wall in a pinned state, when it is not moving.

Analyzing the video frames in Fig. 2.9(b) and other similar ones at different electric fields shows that the measured maximum sideways wall velocities $v_{s,f}$ increase with electric field. The maximum pinning time $t_{p,f}$ and switching time $t_{s,f}$ decrease with electric field. These are plotted in Fig. 2.9(a). Figure 2.9(b) shows the relative time fraction $t_{p,f}/t_{s,f}$ that the domain front spends not moving, as a function of electric field. It is clear that the domain wall pinning dominates the total switching time $t_{s,f}$ at lower electric fields. Based on Miller-Weinreich analysis [10], we assume an exponential velocity dependence on electric field as

$$v_{s,j} = v_{s,jo} exp\left(-\frac{\alpha_{s,j}}{E - E_{c,j}}\right) \tag{2.4}$$

where j=f or r. The velocity data is re-plotted as a log plot in Fig. 2.9(c). Our experimental measurements of the velocity have very low scatter in the high field regime as compared to the larger scatter in the low field measurements where random regime alone (E-$E_{c,f}$ >19 kV/cm) gives ln[l/v_{fo}(s/mm)]=-6.59±0.06 and $\alpha_{s,f}$22.09±2.17 kV/cm, which does not extrapolate well into low field regime data. Therefore we conclude that the data really represents two field regimes. For E-$E_{c,f}$¡19 kV/cm, the scatter in the measured velocity data is large, and therefore a range of activation fields exists, with a mean value of $\alpha_{s,f}$ ≈6.8kV/cm. The fitting parameters are summarized in Table 2.3. We assume an exponential behavior of the pinned time $t_{p,f}$ as a function of electric field E

as

$$t_{p,f} = t_{p,fo} exp\left(\frac{\delta_{p,f}}{E - E_{c,f}}\right) \tag{2.5}$$

and overlay this plot as well in Fig. 2.9(c). In addition, for comparison we plot the switching time $t_{s,f}$ obtained from the video data on the same plot. The fitting parameters for switching time [Eq. 2.3], sideways wall velocity [Eq. 2.4], and pinning time [Eq. 2.5] are presented together in Table 2.3. All three physical properties show a discontinuity around the field range of E-$E_{c,f}$=18-20kV/cm. In the higher electric field regime (E-$E_{c,f}$ >19 kV/cm) the activation fields $\alpha_{s,f}$(≈22kV/cm) for the sideways domain wall velocity and the activation field δ_f(≈21kV/cm) for the total switching time are similar, while that for pinning time $\delta_{p,f}$(≈70.5 kV/cm) is significantly higher, indicating that sideways domain wall motion dominates the switching time $t_{s,f}$ in this field regime. In the low electric field regime (E-$E_{c,f}$ <19 kV/cm), the activation fields $delta_{p,f}$, $\alpha_{s,f}$, and δ_f are all similar. However, the magnitude of switching time is dominated by the pinning time in this regime as seen in Fig. 2.9(b).

Crystal: (coercive field)	$t_{s,f}, v_{s,f}$ $t_{p,f}$	Electric Field regimes	$Activation field \delta_{s,f}$ or $\alpha_{s,f}$(kV/cm)	Pre-exponential factors $ln(t_{s,fo)}, ln(1/v_{s,fo}), ln(t_{p,fo})$
near-stoichiometric	$t_{s,f}$	$E - E_{c,f}$ >20kV/cm	$\delta_{s,f} = 20.86 \pm 0.75$	$ln[t_{s,fo}(ms)] = 3.15 \pm 0.22$
$LiTaO_3$		$E - E_{c,f}$ <20kV/cm	$\delta_{s,f} = 6.8 \pm 0.54$	$ln[t_{s,fo}(ms)] = 3.9 \pm 0.6$
($E_{c,f}$=18.7kV/cm	$v_{s,f}$	$E - E_{c,f}$ >19kV/cm	$\alpha_{s,f} = 22.09 \pm 2.17$	$ln[1/v_{s,fo}(s/mm)] = -6.59 \pm 0.06$
$E_{c,r}$=14.4kV/cm)		$E - E_{c,f}$ <19kV/cm	$\alpha_{s,f} = 6.8 \pm 2.39$	$ln[1/v_{s,fo}(s/mm)] = 2.20 \pm 0.34$
	$t_{p,f}$	$E - E_{c,f}$ >18kV/cm	$\delta_{p,f} = 70.5 \pm 1.78$	$ln[t_{p,fo}(ms)] = -0.58 \pm 0.32$
		$E - E_{c,f}$ <18kV/cm	$\delta_{p,f} = 4.8 \pm 0.91$	$ln[t_{p,fo}(ms)] = 2.70 \pm 0.10$
Congruent	$t_{s,f}$	$E - E_{c,f}$ >3.8kV/cm	$\delta_{s,f} = 51.4 \pm 5.88$	$ln[t_{s,fo}(ms)] = -0.40 \pm 1.04$
$LiTaO_3$		$E - E_{c,f}$ <3.8kV/cm	$\delta_{s,f} = 1.49 \pm 0.52$	$ln[t_{s,fo}(ms)] = 11.35 \pm 0.35$
($E_{c,f}$=211kV/cm)	$v_{s,f}$	$E - E_{c,f}$ >4kV/cm	$\alpha_{s,f} = 42.56$	$ln[1/v_{s,fo}(s/mm)] = -2.95$
		$E - E_{c,f}$ <2kV/cm	$\alpha_{s,f} = 0.46$	$ln[1/v_{s,fo}(s/mm)] = 10.09$

Table 2.3. The fitting parameters for switching time $t_{s,f}$, pinning time $t_{p,f}$, and sideways wall velocity $v_{s,f}$ measured from the real-time video data in Fig. 2.8(b) during forward poling in near-stoichiometric $LiTaO_3$. The results for congruent crystals (Refs. [8] and [9]) are also given for comparison.

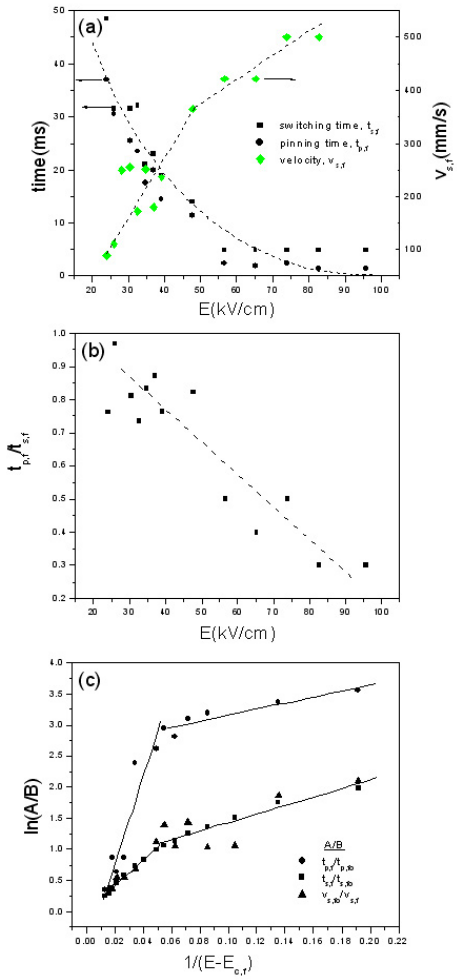

Fig. 2.9. (a) Analysis of the switching time $t_{s,f}$, the maximum pinning time $t_{p,f}$, and the sideways wall velocity $v_{s,f}$, analyzed from the video frames showing domain motion in Fig. 2.8(b). (b) The ratio of the pinning time to the switching time, $t_{p,f}/t_{s,f}$, indicating that at lower electric fields the pinning time dominates the switching time. (c) The log plots of $t_{s,f}$, $v_{s,f}$, and $t_{p,f}$ plotted according to Eqs. 2.32.5, respectively. The coercive fields $E_{c,f}$=18.7 kV/cm. The fitting parameters to the linear solid line fits are given in Table 2.3.

2.3 Comparison of near-stoichiometric and congruent composition crystal

Many of the polarization reversal properties depend strongly on the lithium non-stoichiometry in $LiTaO_3$ and $LiNbO_3$. This section compares and contrasts the congruent [Li/(Li+Ta)≈0.485] and near-stoichiometric [Li/(Li +Ta)≈0.4977-0.4992] compositions of $LiTaO_3$. The most dramatic difference is that the threshold coercive field required for domain reversal in congruent $LiTaO_3$ is ≈210-220 kV/cm for forward poling and 110-120 kV/cm for reverse poling direction at room temperature. The internal field is therefore E_{int} ≈45-50 kV/cm. This contrasts with threshold coercive fields of 17 kV/cm for forward and 15 kV/cm for reverse poling directions, and therefore an internal field E_{int} ≈1 kV/cm in the near-stoichiometric crystals studied here. In lithium niobate similar large changes are observed, and the variation of threshold coercive fields with lithium concentration, C=Li/(Li+Nb), is found to be approximately linear in this composition range [4]. This linearity, though not strictly confirmed in isostructural $LiTaO_3$, is also expected [5]. Another clear difference is the domain wall contrast under optical microscope at room temperature. In congruent crystals, domain walls are easily observed under an optical microscope without any external field. The region adjacent to these walls has been shown to possess optical birefringence [11] of 10^5 to 10^4, lattice strains [12], and local electric fields [6]. There features are explored in greater detail in the subsequent chapters. On the other hand, in near-stoichiometric crystals, optical birefringence is significantly lower (estimated well below 10^{-6}), and strains can hardly be observed even with x-ray synchrotron imaging. Therefore there is a close relationship between lithium non-stoichiometry and domain wall structure. The local relaxation of point defect dipoles arising from nonstoichiometry in the region of the domain wall leads to the observed strains, fields, and optical birefringence.

The variation of threshold coercive fields with repeated polarization cycling shows similarities and differences in congruent and near-stoichiometric composition crystals. Figure 2.10 shows the threshold coercive field $E_{c,j}$ versus time gap $t_{g,j}$ for congruent $LiTaO_3$. Like near-stoichiometric crystals, congruent crystals also show large negative threshold coercive field when the time gap is shorter than its stabilization

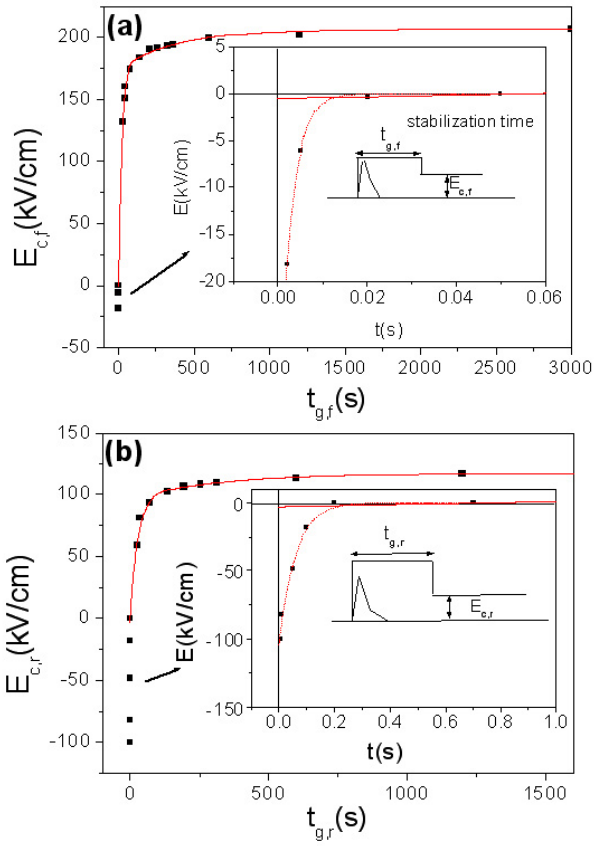

Fig. 2.10. The dependence of coercive field $E_{c,j}$ as a function of the cycling time gap $t_{g,j}$ for forward and reverse poling for z-cut congruent $LiTaO_3$, where (a) j=f and (b) j=r. The time axis crossings at $E_{c,j}$=0 is equal to the measured stabilization time of $t_{stab,j'}$, where (a) (j,j')=(f,r) and (b) (j,j')=(r,f). This crossing and the negative coercive fields are shown more clearly in the insets. The solid line is a double exponential fit for $t_{g,j} > t_{stab,j'}$ and a single exponential fit for $t_{g,j} < t_{stab,j'}$ as described by Eq. 2.1. The fitting parameters are given in Table 2.1. The inset schematic describes the meaning of negative coercive field as a minimum baseline voltage following the main pulse needed to prevent domain backswitching after the end of the pulse.

times. Again, the data point for the zero crossing of the field axis was obtained from the stabilization time $t_{stab,j'}$ where (j,j')=(f,r) or (r,f). Similar to the measurements on near-stoichiometric crystals shown in Fig. 2.4(a), this measurement on congruent crystals can be fit to multiple exponential curves given by Eq. 2.1. However, one clearly notes that the fit for the negative threshold coercive fields is different from that for positive threshold coercive field, with a discontinuity of the derivative at the zero field crossing corresponding to the stabilization time. In Table 2.1 the parameters for this fit are shown, with the caveat that the zero time gap intercept for the fit to negative coercive fields has large uncertainty due to the very small time gaps involved. Both stoichiometric and congruent crystals show an abrupt decrease in threshold coercive field at $t_{g,f}$=5 min. For time gaps longer than stabilization time, near-stoichiometric compositions exhibit time constants of $\tau_{1,f}$=26s and $\tau_{2,f}$=177s, while congruent compositions exhibit $\tau_{1,f}$=29s and $\tau_{2,f}$=523s. The time constants $\tau_{i,f}$ are very similar for both compositions even though the magnitudes of threshold coercive fields show an order of magnitude difference. This implies that even though the defect densities in the two compositions are very different, the relaxation mechanism occurs by the same underlying physical phenomenon. In Ch.2.4 I propose such a mechanism based on slow reorientation of defect dipoles following polarization reversal.

The switching times for congruent and stoichiometric compositions exhibit similarities and differences as well. The switching time $t_{s,j}$ as a function of external electric field E-$E_{c,j}$ for congruent crystals is shown in Fig. 2.11. Shown overlapped are the switching times for stoichiometric crystals as well. Note that these measurements for congruent crystals were reported before in literature, but were plotted as a function of E-E_{int} [9], [13]. However, based on the exponential relationship between switching time and electric field [see Eq. 2.3], at E=$E_{c,j}$ the switching time goes to infinity. This is physically more realistic than assuming the same thing at E=E_{int} as was done in Refs [9], [13]. Both congruent and stoichiometric crystals exhibit two distinct electric field regimes of E-$E_{c,j}$, where the activation fields δ_j are different. These activation fields are listed in Table 2.2. Note that in the high field regime, the activation fields for both congruent and near-stoichiometric $LiTaO_3$ are similar indicating again a similar

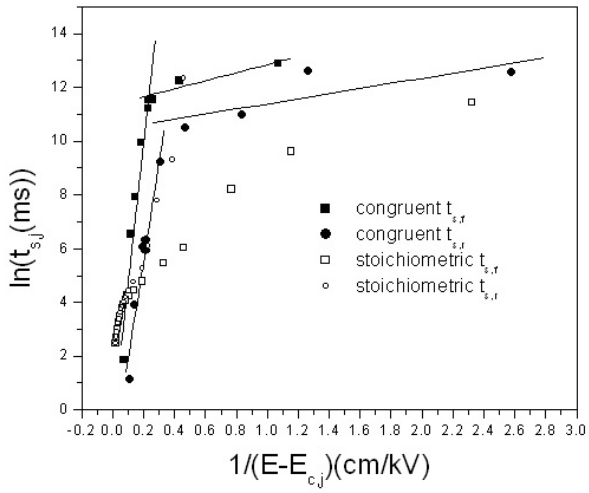

Fig. 2.11. The domain switching times for z-cut congruent $LiTaO_3$ crystals in forward for time gaps $t_{g,f}$=300 s. The linear solid line fits are according to Eq. 2.4. The coercive fields $E_{c,f}$=211 kV/cm for congruent $LiTaO_3$. The activation field and preexponents from the fit are listed in Table 2.2. Also overlapped for comparison are the switching times for z-cut nearstoichiometric $LiTaO_3$ crystals from Fig. 2.7(b). The electrode area was 20 mm^2 for both cases.

mechanism for domain wall motion. In the low electric field regime, the domain wall pinning dominates the switching time as shown earlier in Fig. 2.9(b). This is true for both near-stoichiometric and congruent compositions. However, since the nonstoichiometric defect density is lower in the near-stoichiometric crystals, the pinning process and hence the switching time is quite random and varies drastically from one area of the same sample to another. With higher defect density in congruent $LiTaO_3$ this variance from area to area decreases. The difference in the switching time behavior with field in the low field regime between the near-stoichiometric and congruent compositions is a direct result of this process. Note that implicit in this argument, we are proposing that the pinning sites are also correlated with nonstoichiometric defects or defect aggregates. This proposition is supported by the fact that the threshold coercive field in congruent crystal appears to be a pinning-depinning transition. Small reversible pinning and

bending of a domain wall locally on micrometer length scales has been observed [11] in congruent crystals at fields of E<20 kV/cm which is an order of magnitude lower than the threshold coercive field of ≈210 kV/cm. Since the threshold coercive field also changes drastically with point defect concentration, the process of pinning and the actual pinning sites themselves must be correlated with point defects. We propose below that the point defect complexes have an electrical dipole, which prefer to orient parallel to the lattice polarization. Simple electrostatic calculations then show that there is an energy barrier associated with a domain wall having to cross a defect dipole in its path, which is the precise role of a pinning site.

The concept of stabilization time also is closely related to the presence of point defect dipoles in the crystal. At room temperature, the stabilization times for forward and reverse poling in congruent $LiTaO_3$ are $t_{stab,f}$=1.4-2s and $t_{stab,r}$=0.1-0.3s, respectively. On the other hand, the near-stoichiometric composition exhibits stabilization times of $t_{stab,f}$=0.25-0.9s and $t_{stab,r}$=0.015-0.1s. Both compositions show an order of magnitude difference between $t_{stab,f}$ and $t_{stab,r}$. In addition, the stabilization times for congruent compositions are an order of magnitude larger than that for stoichiometric crystals in both forward and reverse poling directions. In the following section we present a model where the origin of domain stabilization time is proposed to be directly related to the time taken for the slow reorientation of the electrical dipole moment associated with the movement of Ta_{Li} defect ions through close packed oxygen planes. Longer stabilization times in congruent crystals suggest that this movement of the defect ion is slower in congruent crystals as compared to near-stoichiometric crystals. The difference in forward versus reverse stabilization time in each composition arises from the fact that the lithium vacancies V_{Li} surrounding a Ta_{Li} defect ion do not rearrange around the new Ta_{Li} position after domain reversal at room temperature, thus creating a frustrated defect dipole. These are explained in greater detail in the following section.

Figure 2.12 shows the sideways wall velocity $v_{s,f}$ as a function of electric field $E\text{-}E_{c,f}$ for congruent $LiTaO_3$ [10]. The wall velocity of independently growing domains is an order of magnitude lower than merged, serrated domain fronts as reported earlier due to preferential nucleations at the serrations at the domain walls [10], [13]. We

note that the behavior of switching time $t_{s,f}$ and sideways wall velocity $1/v_{s,f}$, as a function of electric field $E\text{-}E_{c,f}$, show similarities in both congruent and stoichiometric compositions. Both switching times $t_{s,f}$ and inverse sideways wall velocity $1/v_{s,f}$show two electric field regimes where the activation fields δ_f and $\alpha_{s,f}$ change from one regime to another. These electric field regimes are similar, as are the activation fields δ_f and $\alpha_{s,f}$ for the switching times and the sideways wall velocities, respectively. In congruent composition, the high electric field regime is $E\text{-}E_{c,f}$ >3.8 kV/cm for switching time and $E\text{-}E_{c,f}$ >4 kV/cm for sideways wall velocity. The activation fields are δ_f ≈51 kV/cm and $\alpha_{s,f}$ ≈43 kV/cm in the high field regimes and δ_f ≈1.5 kV/cm and $\alpha_{s,f}$ ≈0.5 kV/cm in the low field regime. In the near-stoichiometric composition, the high electric field regime is $E\text{-}E_{c,f}$ >14 kV/cm for switching time and $E\text{-}E_{c,f}$ >17 kV/cm for sideways wall velocity. The activation field values are δ_f ≈26 kV/cm and $\alpha_{s,f}$ ≈22 kV/cm in the high field regime and δ_f ≈5.4-6.8 kV/cm and $\alpha_{s,f}$ ≈6.8 kV/cm in the low field regime. [The $\alpha_{s,f}$ in the low field regime is very approximate due to a large scatter in the velocity data in Fig. 2.9(c)]. These comparisons show that while the actual magnitudes of the threshold coercive fields and wall velocities are very different in the congruent and stoichiometric compositions, there are strong similarities. Above the threshold coercive field, the electric field shows at least two distinct ranges in both cases, which we denote as low and high electric field ranges. The domain wall pinning is dominant in the low field regime, and wall velocity is dominant in the high field regime in both compositions.

2.4 Defect dipoles and domain reversal

In this chapter, I present a defect model based on nonstoichiometric dipolar defects in $LiTaO_3$. This model is based on the basic concept of bulk dipolar defect complexes giving rise to domain stabilization and internal fields in ferroelectrics as has been detailed in the works of Arlt [14], Lambeck [15], and Warren [16]. The model provides a qualitative explanation of the domain reversal processes such as the dependence of threshold coercive field on defect density and on repeated cycling at different frequencies, the phenomena of domain stabilization time, and that of domain *backswitching* in lithium niobate and tantalate.

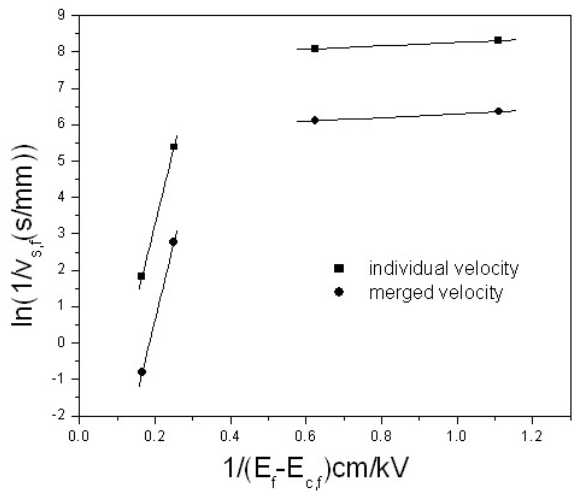

Fig. 2.12. Sideways wall velocity $v_{s,f}$ as a function of electric field for z-cut congruent $LiTaO_3$. The measured coercive field $E_{c,f}$=213kV/cm. Solid line fits are according to Eq. 2.5. The fitting parameters are listed in Table 2.3.

2.4.1 Nonstoichiometric dipolar defect

A comparison of stoichiometric and congruent crystals makes it clear that non-stoichiometry in $LiTaO_3$ is intricately related to the domain wall structure and kinetics [6]. The above discussion raises the question as to what the exact nature of non-stoichiometric point defects or defect complexes is. Below, we will discuss defect models in iso-structural congruent $LiNbO_3$ which has been more extensively studied. We will then draw a parallel between defect models in $LiNbO_3$ and $LiTaO_3$ based on the fact that they have the same lattice structure, threshold coercive fields, switching times, internal fields, domain wall contrast, and phenomena of domain wall pinning and stabilization, differing only in the magnitudes of these effects [6]. In congruent composition of $LiNbO_3$, Prokhorov and Kuzminov [17] concluded that lithium vacancies $(V_{Li})^+$ and oxygen vacancies $(V_O)^{2+}$ dominate at room temperature, corresponding to a congruent defect structure of $[Li_{0.944}V_{0.056}]Nb[O_{2.972}V_{0.028}]$ which we

refer to as *model I*. However, the density of $LiNbO_3$ increases with increasing lithium deficiency which is incompatible with the oxygen vacancy model [18]. Schirmer et al. concluded that niobium antisites $(Nb_{Li})^{4+}$ and niobium vacancies $(V_{Nb})^{5-}$ are the dominant point defects and that oxygen vacancy is present at most in negligible concentrations, except when brute force treatments such as high energy electron irradiation are applied [19]. The chemical formula for this defect model suggested by Abrahams and Marsh is $[Li_{0.947}Nb_{0.053}] \times [Nb_{0.9528}V_{0.047}]O_3$, to be referred to as *model II*. However, Donnerberg et al [20] showed that the formation of a niobium vacancy was found to be energetically unfavorable as compared to the formation of a lithium vacancy. The third proposed defect model (*model III*) is the presence of niobium antisites $(Nb_{Li})^{4+}$ and lithium vacancies $(V_{Li})^{-}$ [21]. The neutron diffraction studies by Iyi et al [22] and Zotov et al [23] support this defect model with a chemical formula of $[Li_{0.95}V_{0.04}Nb_{0.01}]NbO_3$. Schirmer et al. [19] point out that the niobium vacancy model and the lithium vacancy model can be reconciled if it is assumed that there are ilmenite type stacking faults in the regular $LiNbO_3$ crystal structure. However, a different suggestion has come from Ivanova and Yatsenko et al. [24], [25] who have recently interpreted the nuclear magnetic resonance (NMR) spectra in congruent $LiNbO_3$. They conclude that at room temperature, a combination of *models I* and *III* in a ratio of 1.1:1.0 would provide a "rather good qualitative and quantitative agreement with the NMR ^{7}Li spectra." However, the authors assert that only the *model III* (with allowance for mobility of Li^+ ions in LiO_6 octahedra) can explain the temperature dependence of the experimental NMR ^{7}Li and ^{93}Nb spectra from 77 to 4.2 K. Accordingly, the authors propose the structure of a defect complex as comprising of a niobium antisite surrounded by three Li^+ vacancies in the nearest neighborhood, plus one independent Li^+ vacancy along the polar z direction. Yatsenko [26] has also reported that the preliminary analysis of the structural distortions caused by a Nb_{Li} antisite defect reveals a contraction of the nearest three oxygen atoms, and a displacement from the c axis of the nearest three ^{93}Nb nuclei. This defect complex comprising of one Nb_{Li} with four V_{Li} certainly possesses an electrical dipole moment, arising primarily along the z axis from antisite Nb_{Li} itself as well as from the relative arrangement of V_{Li} around the antisite. This defect model is also supported

by x-ray and neutron diffuse scattering of congruent $LiNbO_3$ reported by Zhdanov et al., [27] Ivanov et al., [28] and most recently by Zotov et al. [29] These studies conclude that the diffuse lines in scattering arise from a one-dimensional (1D) displacive and substitutional disorder in the three pseduo-cubic directions along the Li-O-Li-... chains. These directions correspond to pseudo-cubic directions [24.1], [$2\bar{2}$.1], and [$\overline{42}$.1] (in orthohexagonal notation) which are related to each other by the threefold symmetry axis (polarization *c* axis) and are inclined at 52° to the c axis. Diffuse maxima around the Bragg positions reflect some three-dimensional (3D) short-range order of the defect elements and the homogeneous part of the diffuse planes indicate random distribution of the defect clusters. Since each niobium antisite requires four lithium vacancies in the neighborhood for overall charge neutrality, Zotov et al. [29] suggest chains such as Li-Nb$_{Li}$-V-Li, Li-V-Nb$_{Li}$-V, Li-V-V-Nb$_{Li}$, etc. as possible combinations.

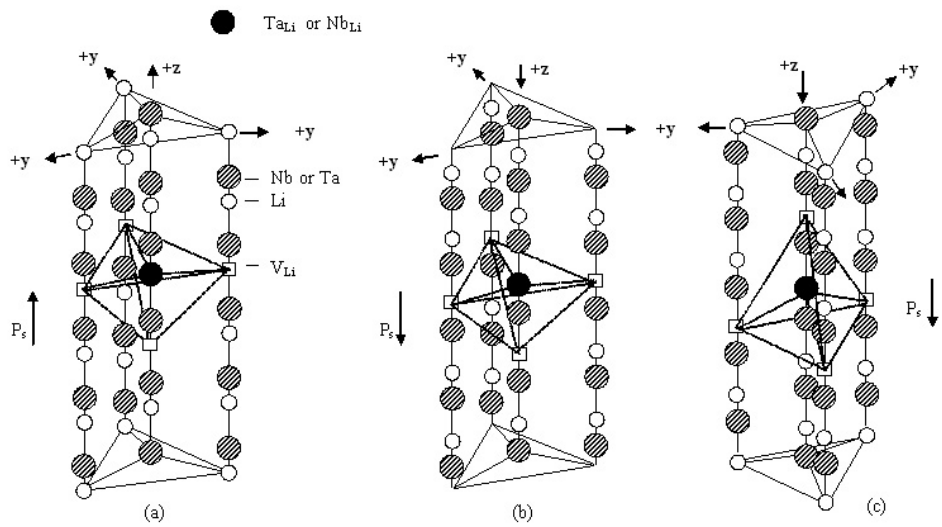

Fig. 2.13. Schematic of defect dipoles in nonstoichiometric lithium tantalate at room temperature, composed of $4[Ta_{Li}^{4+}] = [V_{Li}^{-}]$. Schematics (a) and (c) show stable low energy defect configurations in +P$_S$ and -P$_S$ domain states, respectively. Schematic (b) shows a frustrated defect state after domain reversal of state (a) by an external electric field at room temperature. State (b) will relax to state (c) after (b) is annealed at >200°C and cooled back to room temperature.

Figure 2.13 shows a possible schematic of the equilibrium states of a defect complex for an up and a down domain. Upon domain reversal, the niobium antisite defect moves to the neighboring octahedron by movement of Nb_{Li} through the close-packed oxygen plane. The lithium vacancies around the original defect in Fig. 2.13(a) need to rearrange around the new antisite position to reach the stable defect equilibrium state of Fig. 2.13(c). At room temperature, a lack of lithium mobility can result in the frustrated state of defect complex as shown in Fig. 2.13(b), which can be relieved into state (c) after a high temperature anneal. However, as pointed out by Nassau and Lines [30], the presence of two niobium ions in adjacent oxygen octahedra can be energetically unfavorable due to dense positive charge around the cluster. They propose extended stacking fault defects in the structure. Zotov et al. [29], however, restrict the size of such clusters to ≈ 11.4Å (about four cation sites) in order to match the correlation length L_c≈13Å along the chains calculated from the full width at half maximum of the diffuse streaks in x-ray.The average spacing between defect clusters along the chains is estimated to be ≈76 Å. The temperature dependence of diffuse x-ray streaks [29] suggest that at low temperatures, the lateral correlations between defect clusters become quite substantial. With increasing temperature, these correlations decrease, resulting in more random 1D disorder. The changes in the threshold coercive and internal fields with temperature as reported by Battle et al. [31] also point to the breaking up of eating followed by reformation of the defect dipole in an energetically favorable orientation upon cooling down to room temperature.

2.4.2 Backswitching and internal fields

Following the approach and interpretation of Arlt and Neumann in Ref [14]. we propose a qualitative defect model for explaining internal fields and stabilization times in $LiTaO_3$ and $LiNbO_3$. Drawing an analogy between $LiNbO_3$ and $LiTaO_3$ we will assume a simple defect model primarily based on a tantalum antisite defect and lithium vacancies in lithium tantalate as depicted in Fig. 2.13. With this physical basis we will now proceed to build a model for domain reversal in $LiTaO_3$ .The process of domain reversal in $LiTaO_3$ involves movement of lithium atoms, Li_{Li}, through the adjacent

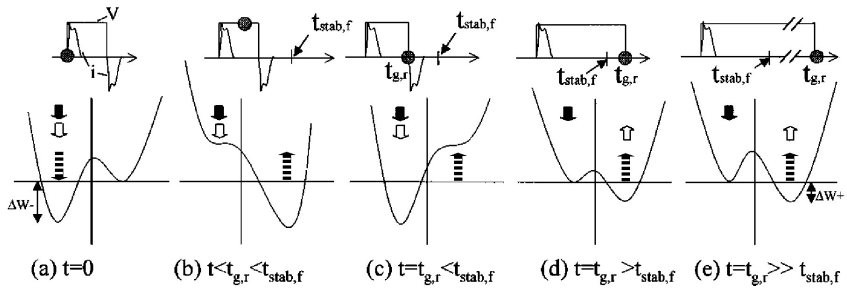

Fig. 2.14. A schematic describing the process of forward domain reversal and domain backswitching in the presence of dipolar defects shown in Fig. 2.13. Each of the five schematics (a)-(e) shows the voltage pulse V and the transient current i (top), followed by the corresponding potential energy well (below) for the lattice polarization in the presence of defects at the time instant t denoted by a gray circle in the voltage pulse schematic. The notations are lattice polarization Ps (denoted by dotted up or down arrow), defect dipole associated with Ta_{Li} antisite defect (denoted by ↑ or ↓), defect dipole associated with the arrangement of V_{Li} (denoted by ⇑ or ⇓), the time gap $t_{g,r}$ that domain spends in the $-P_s$ state before being forward poled to the $+P_s$ state, and stabilization time $t_{stab,r}$.

close-packed oxygen planes into the neighboring vacant oxygen octahedra. This is accompanied by a simultaneous motion of the tantalum atom, Ta_{Ta}, from its acentric location within its normal oxygen octahedral site to a centrosymmetrically opposite site within its octahedra. At room temperature, the lithium ion has to force its way through the opening in the oxygen triangle formed by three adjacent oxygen ions. This process is postulated to be anelastic, in the sense that this motion requires strain in the close-packed oxygen planes of the lattice, creation and relaxation of which is expected to be time dependent. At a constant external driving field, say E, the motion of the lithium ion is a function of time, corresponding to time-dependent changes in the free energy potential, G. Let us now consider the Ta_{Li} antisite defect. Upon domain reversal under an electric field we now postulate that this tantalum atom also has to pass through the adjacent close-packed oxygen layer and into the adjoining vacant oxygen octahedron. We start with the premise that this anelastic process is driven by the domain reversal caused by electric field, and that this is a key step that needs to occur for the newly created

domain to be stable. Referring back to Figs. 2.13(a) and 2.13(b), while the Ta_{Li} atoms move upon domain reversal, the lithium vacancies surrounding the antisite defects do not move at room temperature. This is suggested by the fact that ionic conduction at room temperature is negligible and becomes substantial only at temperatures above 150 °C, primarily due to lithium-site ionic motion [31]. Therefore, at room temperature, the lithium vacancies around a tantalum antisite are in a frustrated state [Fig. 2.131(b)] after the tantalum antisite atom Ta_{Li} has moved into the adjoining octahedron under electric field induced domain reversal. This configuration has higher energy, which can be only lowered by rearrangement of lithium vacancies in a new configuration, achieved by heating and cooling, for example, which yields the final stable configuration of Fig. 2.13(c). The defect complex in Fig. 2.13 is assumed to comprise of a dipole moment, which has two contributions. These are (a) the contribution to the electrical dipole arising only from the Ta_{Li} antisite defect, and (b) the contribution to the electrical dipole arising from the relative arrangement of the lithium vacancies V_{Li} around a tantalum antisite defect Ta_{Li}. Upon domain reversal at room temperature, the electric field can move the Ta_{Li} antisite defect through the neighboring oxygen triangle and therefore reverse the component (a) of the electrical dipole moment associated with only Ta_{Li}. However, the component (b) of the electrical dipole moment associated with the arrangement lithium vacancies is not reversed by the electric field. This results in the frustrated domain state shown in Fig. 2.13(b). This requires thermal activation at > 150°C for a few minutes followed by cooling to rearrange lithium vacancies to achieve the low energy domain state shown in Fig. 2.13(c). Figures 2.14(a)-2.14(e) show a schematic of the potential energy diagram at room temperature for the forward switching process at various instants of time t on application of a voltage pulse of width $t_{g,r}$. The energy diagram represents the electrostatic energy of the lattice polarization, modified by the interaction energy resulting from the interaction between defect polarization and bulk lattice polarization, and due to external field contributions to the total lattice energy. For a first order ferroelectric phase transition, the difference between the free energy G per unit volume in a ferroelectric state and that in the paraelectric state G_o can written as [3]

$$G - G_o|_{\pm P_S} = -\frac{A}{2}P^2 + \frac{B}{4}P^4 - E_D(t)P - EP \tag{2.6}$$

where P is the lattice polarization, A and B are positive physical constants, E_D(t) is the effective time dependent defect field, and E is the external field applied. Note that the above equation is applicable near the $\pm P_s$ states only. Here P_s indicates spontaneous lattice polarization at the minimum energy state. Before any external field is applied [E=0 at t=0; see Fig. 2.14(a)], the -P_s lattice polarization state is stabilized by the defect polarization by an amount of Δw^- per defect dipole, with respect to the +P_s state. If all the defect dipoles are aligned parallel to the -P_s direction in Fig. 2.14(a), then the magnitude of the defect field E_D at time t=0 is given by [14]

$$E_D(0) = \frac{N\Delta w^-}{2P_s} \tag{2.7}$$

where N is total number of defect dipoles per unit volume. As Arlt and Neumann point out [14], this effective defect field is not an existing electric field in the material. Rather, it is a formal equivalent to the energetic difference between the two poling states. The defect that stabilizes the -P_s polarization is thought of as being comprised of two components: one arising from Ta_{Li} (indicated by ⇓) and the other arising from the relative arrangement of lithium vacancies around the antisite defect (indicated by ↓). The application of an external electric field, +E, decreases the energy of the +P_s state by E·P and increases the energy of the -P_s state by a corresponding amount. This results in the reversal of the lattice domain state from -P_s to +Ps state as shown in Fig. 2.14(b). However, at a time instant $t < t_{stab,f}$, the defect polarizations ⇓ and ↓ have not reversed from their original state in Fig. 2.14(a). We now consider three cases. (i) When the applied voltage pulse width $t_{g,r}$ is less than the stabilization time $t_{stab,f}$. At the end of the pulse (time instant t=$t_{g,r} < t_{stab,f}$), domain backswitching occurs as shown in Fig. 2.14(c). This is directly due to the fact that the external field related energy contribution E·P →0 on removal of the voltage pulse, and the system returns to the -P_s state, stabilized by defect polarization. (ii) When the applied voltage pulse width, $t_{g,r}$ is just equal to or greater than $t_{stab,f}$ [Fig. 2.14(d)], no backswitching occurs. In

this case the defect polarization component ⇓ reverses to the ⇑ state, corresponding to a movement of Ta_{Li} through close-packed oxygen planes. Referring to Table 2.1, the time constant for the realignment of defect polarization relating to Ta_{Li} movement is proposed to be of the order of $\tau_{1,f} \approx 20.3s$ for congruent and 26.4 s for near-stoichiometric $LiTaO_3$ during forward poling. The stabilization time $t_{stab,r}$ in this interpretation would approximately correspond to the time taken for the Ta_{Li} atoms to cross the close-packed oxygen plane. The new defect polarization component stabilizes the polarization state $+P_s$, thus preventing the backswitching. Note, however, that the defect polarization component ↓ still does not reverse due to the lack of rearrangement of V_{Li} around the new Ta_{Li} position at room temperature. (iii) When the applied voltage pulse width $t_{g,r} >> t_{stab,f}$ [Fig. 2.14(e)], no backswitching occurs as in case (ii). In addition, a slow time-dependent relaxation of the lattice polarization takes place in the presence of a frustrated defect dipole (a combination of ⇑ and ↓ in Fig. 2.14), in reaching a final equilibrium state as shown in Fig. 2.14(e). Referring to Table 2.1, the time constant for this slow relaxation is attributed to $\tau_{2,f} \approx 399.6s$ (congruent) and 177.5s (near-stoichiometric) time constants observed from Eq. 2.1. The final effective defect field E_D in Fig. 2.14(e) is given by

$$E_D(t >> t_{stab,r}) = \frac{N\Delta w^+}{2P_s} \tag{2.8}$$

Note that the effective defect fields E_D in Eqs. 2.7 and 2.8 are not equal, a direct consequence of the frustrated defect dipole component ↓ related to lithium vacancies in Fig.2.14(e). The threshold coercive field E_c can be written as $E_c(t)=E_D(t) + E_{intrinsic}(t)$, where $E_{intrinsic}$ is the intrinsic threshold coercive field of exactly stoichiometric $LiTaO_3$ with no defects present. This immediately suggests many qualitative features of domain reversal. First, changes in the threshold coercive field with time (see, for example, Figs. 2.4 and 2.10) are directly related, in part, to the time dependent changes in the effective defect field E_D arising from the reorientation of the defect dipole denoted by ⇑ in Fig. 2.14. Second, since the magnitude of the effective defect field E_D is directly proportional to the density of defects N [Eqs. 2.7 and 2.8], the threshold coercive field E_c is directly proportional to defect density N. This has indeed been confirmed in $LiNbO_3$ where

the threshold coercive field varies linearly with the ratio Li/(Li+Nb) between congruent and stoichiometric compositions [6]. Third, the internal field, E_{int}, given by the offset in the hysteresis loop along the field axis arises directly from the difference in the defect fields E_D between times t=0 [Eq. 2.7] and t$\gg t_{stab,j}$ [Eq. 8]. Assuming that magnitude of the intrinsic threshold coercive field, $E_{intrinsic}$, does not change between domain state in Figs. 2.14(a) and 2.14(e), we can write the internal field [4], [5], [6] $E_{int} \approx [E_D(t=0) - E_D(t..t_{stab,j'})]/2$ for slow polarization cycling ($t_{g,j} \gg t_{stab,j'}$) as

$$E_{int} \approx \frac{N(\Delta w^- - \Delta w^+)}{4P_s} \tag{2.9}$$

Again, the internal field clearly depends linearly on the density of defect dipoles as is also experimentally observed [6].As mentioned before, it must be emphasized that the defect and internal electric fields discussed above are not to be thought of actual electric fields, but as energy equivalents to the differences in the energy levels between different states. These energy differences can include not only electrostatic energy differences but elastic energy differences as well due to lattice distortions. The electrical dipoles associated with defect complexes can therefore also have elastic dipole components [14].

2.4.3 Domain wall pinning and backswitching at a dipolar defect

Based on the defect dipole model presented above, backswitching and stabilzation time can be sucessfuly explained. To demonstrate this model, we present a simple 1-D Time Dependent Ginzburg Landau analysis. To intuitively understand the backswitching effect, we consider only the 1-D case, and ignored the strain energy terms.

Equations 2.10 to 2.13 shows all energy terms that were used in our 1-D modeling.

$$F_p = -\frac{\Psi_1 P_z^2}{2} + \frac{\Psi_2 P_z^4}{4} \tag{2.10}$$

$$F_g = g \cdot P_{z,1}^2 \tag{2.11}$$

$$F_{ext} = -E_{ext} \cdot P_z \tag{2.12}$$

$$F_{def} = -E_{def} \cdot P_z \tag{2.13}$$

$$\tag{2.14}$$

where F_g is polarization energy, F_g is gradient energy, F_{ext} is external field induced energy, and F_{def} is defect dipole induced energy. $\Psi_1 = 1/2\epsilon_{33}$ and $\Psi_2 = \Psi_1/P_s^2$. we used $\epsilon_{33} = 30$, spontaneous polarization value for normal case is $\pm 1C/m^2$, and g=$6\times10^{-3}C^{-2} \cdot N \cdot m^{-4}$. E_{ext} is an externally biased electric field, and E_{def} is an electric field induced by defect dipole. This equivalent defect dipole(P_D)(=$2C/m^2$) induced field can be calculated by using defect dipole moment inside a crystal as can be seen in Eqn. 2.15.

$$E_{def} = \vec{r}\ \frac{Q \cdot L \cdot cos(\theta)}{2 \cdot \pi\epsilon_{33} r^3} + \vec{\theta}\ \frac{Q \cdot L \cdot sin(\theta)}{4 \cdot \pi\epsilon_{33} r^3} \tag{2.15}$$

Here, $\vec{r}$ is a unit vector between defect dipole and lattice dipole, and $\vec{\theta}$ is a unit vector for the angle between defect dipole and lattice dipole as can be seen in Fig. 2.15 (b). Figure 2.15 show the schematic diagram of 1-D TDGL simulation. A one-dimensional TDGL equation is given in Eq. 2.17

$$F_{Total} = F_p + F_g + F_{ext} + F_{def} \tag{2.16}$$

$$\frac{\partial}{\partial t} P_\beta(\mathbf{r}, t) = -\mu \frac{\delta F_{Total}}{\delta P_\beta(\mathbf{r}, t)} + noise(\mathbf{r}, t) \tag{2.17}$$

The numerical code for the solving the above equation is given in Appendix A. As an initial condition, a single sharp domain wall already exists. The left side domain has a normalized P_s value of -1 and the right side has a value of +1. When t>0, the

electric field $E_{ext} = 10^8 V/m$ points towards the down direction , which is favorable to the left side domain, as can be seen in Fig. 2.15. As explained in previous section, a defect dipole takes more time to be poled by external field than normal dipole. In simulation, we fixed defect dipole moment value 1C·m which does not change during the simulation, even though the domain wall pass across the defect dipole area. This would e the case if the entire simualtion is done within the stabilization time according to the above described defect dipole model. We also incorporate a bulk crystal relaxation effect. As soon as dipole is revered to other dipole, the double potential well height decreases to 10 percent of the original value (Ψ_1 and Ψ_2 decrease to 10 percent of the original value). This decreased potential well helps domain back-switching with the defect dipole. Without this relaxation, the back switching becomes very difficult as can be seen in Fig. 2.16. After we incorporate the relaxation term, domain backswitching can be easily achieved by simulation. Figure 2.17 shows how a combination of defrect dipole and relaxation effect results in domain backswitching.

2.4.4 The dependence of Coercive fields on domain walls and defects

In this chapter, we have seen an order of magnitude change in coercive fields with the presence of a small amount of nonstoichiometric defects in lithium niobate and tantalate crystals. It turns out that even these coercive fields (of 2-21 kV/mm) are one or two orders of magnitude smaller than intrinsic coercive fields predicted from Landau theory of ferroelectrics.

Why are the experimentally measured coercive fields for domain reversal in ferroelectrics many orders of magnitude smaller than theoretical estimates? The question mirrors a similar one asked with regard to mechanical strength of materials, namely, why is, for example, the measured critical resolved shear stress in materials (e.g., $\approx 10^{10} N/m^2$ in metals) many orders of magnitude lower than experimentally observed deformation shear stresses (e.g., $\approx 10^6 N/m^2$ in metals) [32]. This discrepancy in mechanical strength is explained by the presence of dislocations in materials. The discrepancy in ferroelectrics has primarily been discussed through the recognition that while the simple estimate of intrinsic coercive fields from the Landau-Ginzburg (LG) theory does not

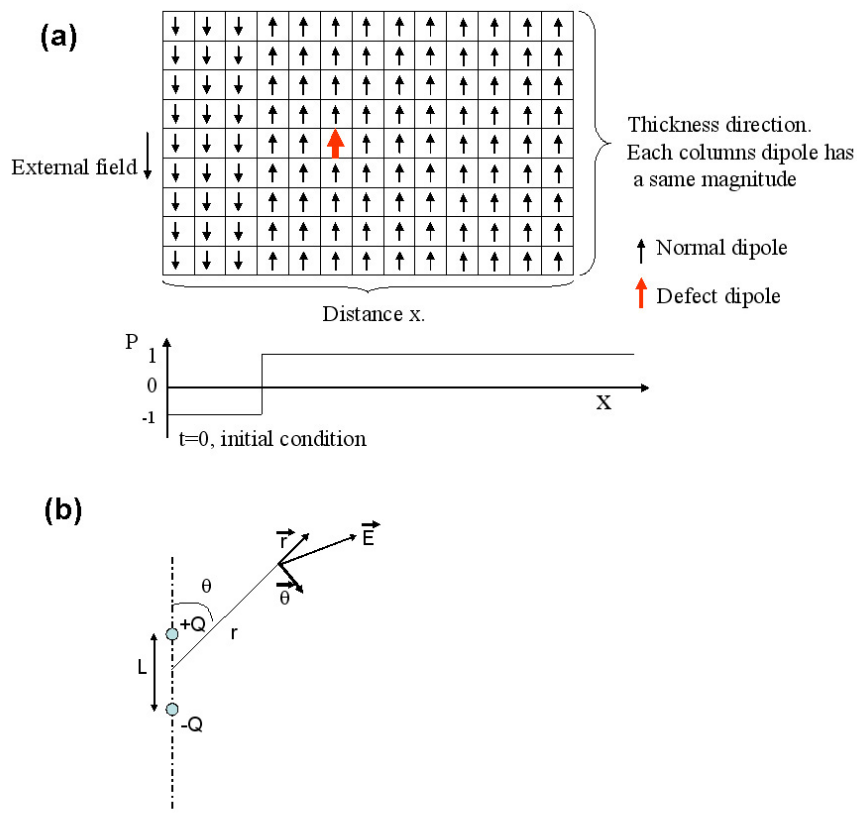

Fig. 2.15. (a) 1D TDGL modeling diagram when time equal 0(no bias). Down arrow represent -1 dipole value and up arrow represent -1 dipole value. Lower figures shows initial condition that contains a sharp domain wall. (b)Defect induced field at a distance r and angle θ from defect dipole(QL).

account for the presence of domain walls or other defects, real single domain crystals nonetheless possess defect sites where it is easier to nucleate domains [33] [34]. Once a domain nuclei exists, the Miller and Weinreich theory [35] explains the effective lateral motion of pre-existing, atomically sharp domain walls, in terms of the probability of overcoming an energy barrier, U, to preferentially nucleate small wedge-shaped domains adjoining the wall. Though not uniquely defined, one can consider the maximum electric field, E=dU/dP required to completely overcome the steepest climb out of the

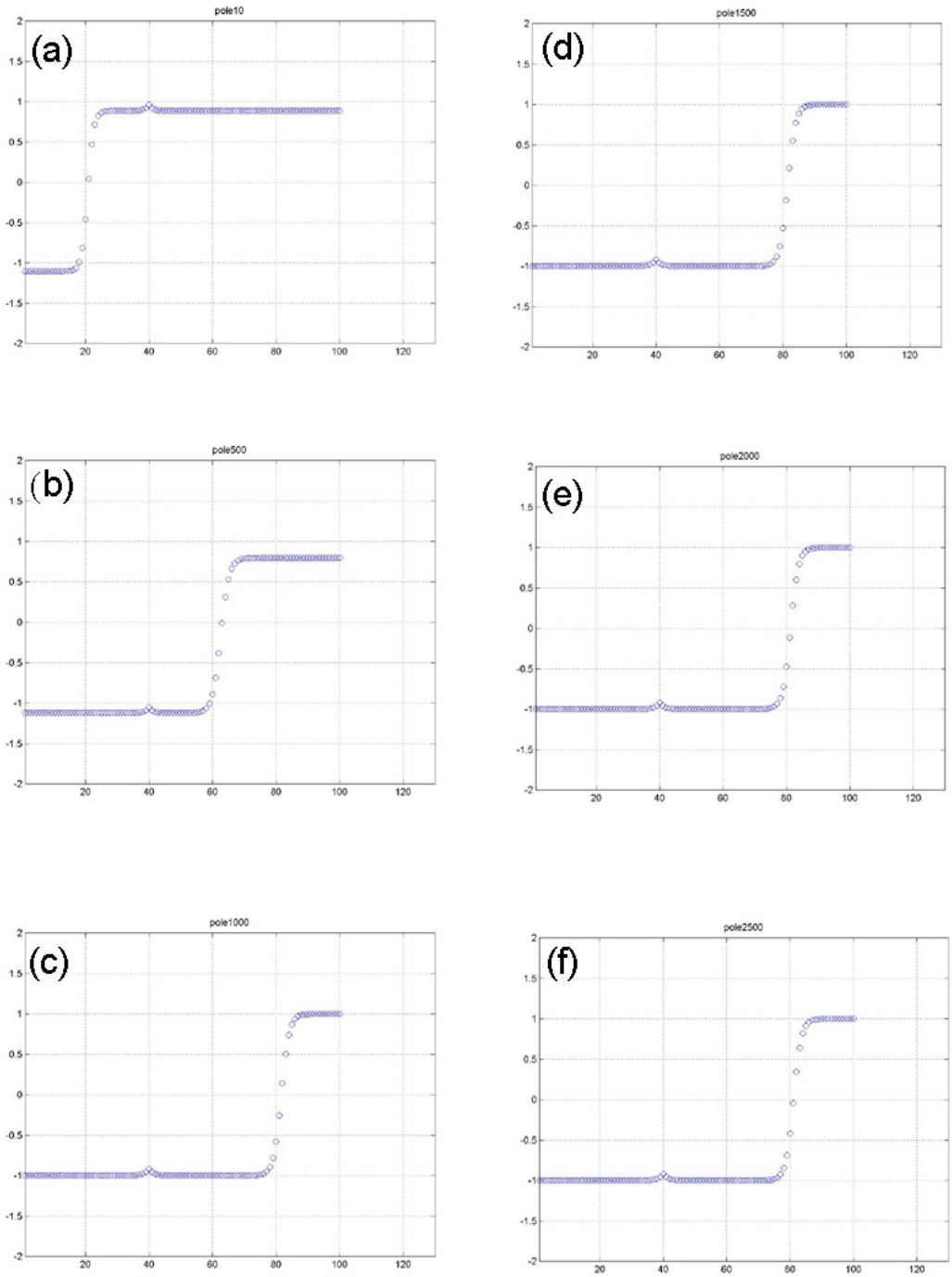

Fig. 2.16. Domain switching without potential well relaxation. Backswitching is not happening. Time is 10, 500, 1000, 1500, 2000, 2500 from (a) to (f). -10^5kV/m external field is on t=1 and off at t>700.

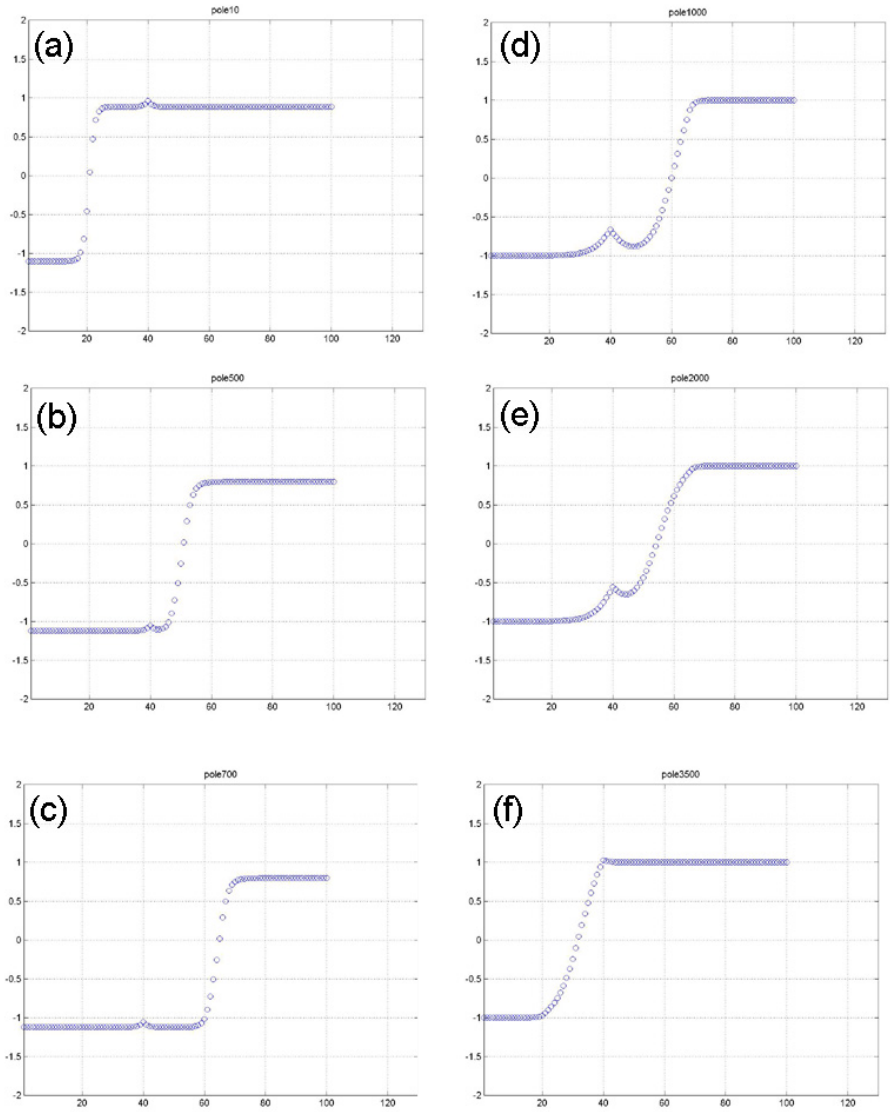

Fig. 2.17. Domain switching with potential well relaxation (90 percent decreasing). Backswitching is really happening. Time is 10, 500, 700, 1000, 2000, 3500 from (a) to (f). -10^5kV/m external field is on t=1 and off at t>700.

energy well, U versus P (polarization), as an estimate of the intrinsic coercive field. Domain wall pinning at physical defects can also contribute to the experimental coercive fields, which manifests as the threshold field for wall depinning [36]. I explore the theoretical estimate of coercive field from the Landau-Ginzburg (LG) theory in the presence of preexisting 180 domain walls with finite wall widths. Specifically, I wish to show that a finite polarization gradient at the domain wall can lower the local intrinsic coercive fields adjacent to the wall, thereby facilitating local wall motion. The problem is treated generally for any ferroelectric with a second-order phase transition, and two possible antiparallel domain states. Let us first calculate the theoretical coercive field for 180 domain reversal in these materials. The Ginzburg-Landau-Devonshire free energy per unit volume, G, of a ferroelectric with a second order phase transition is given by [33]

$$G = -\frac{\alpha_1}{2}P^2 + \frac{\alpha_2}{4}P^4 \tag{2.18}$$

where the order parameter is the polarization, P. One can calculate the effective α_1 and α_2 coefficients from the dielectric constant ϵ_{33} and the homogeneous spontaneous polarization, P_s as α_1=1/(2ϵ_{33}) and $\alpha_2 \approx \alpha_1/P_s^2$. These values at room temperature are ϵ_{33}=43.5ϵ_o and P_s=0.55 C/m^2 for $LiTaO_3$, ϵ_{33}=30ϵ_o, P_s=0.55 C/m^2, for $LiNbO_3$. The equation of state, E=dG/dP defines the theoretical P versus E hysteresis loop. The coercive field E=E_c is defined as the turning point $(dE/dP)_{E=E_c}$=0, which determines the polarization P_c at the coercive field as $P_c = \pm\sqrt{\alpha_1/(3\alpha_2)}$. Substituting this value back in the equation of state yields the coercive field E_c as

$$E_c = \pm\frac{2}{3\sqrt{3}}\sqrt{\frac{\alpha_1^3}{\alpha_2}} \approx 0.385\alpha_1 P_s \tag{2.19}$$

Substituting for the values of α_1 and α_2 in Eq. 2.19, the intrinsic coercive fields are Ec≈2750kV/cm ($LiTaO_3$) and Ec≈5420kV/cm ($LiNbO_3$). In contrast, the coercive fields for near-stoichiometric $LiTaO_3$ is ≈17 kV/cm [37], for near-stoichiometric $LiNbO_3$ is $\approx 40kV/cm$ [38], and for congruent compositions of both materials is ≈210kV/cm [37] [38]. In the following analysis, we now consider the presence of pre-existing 180° domain

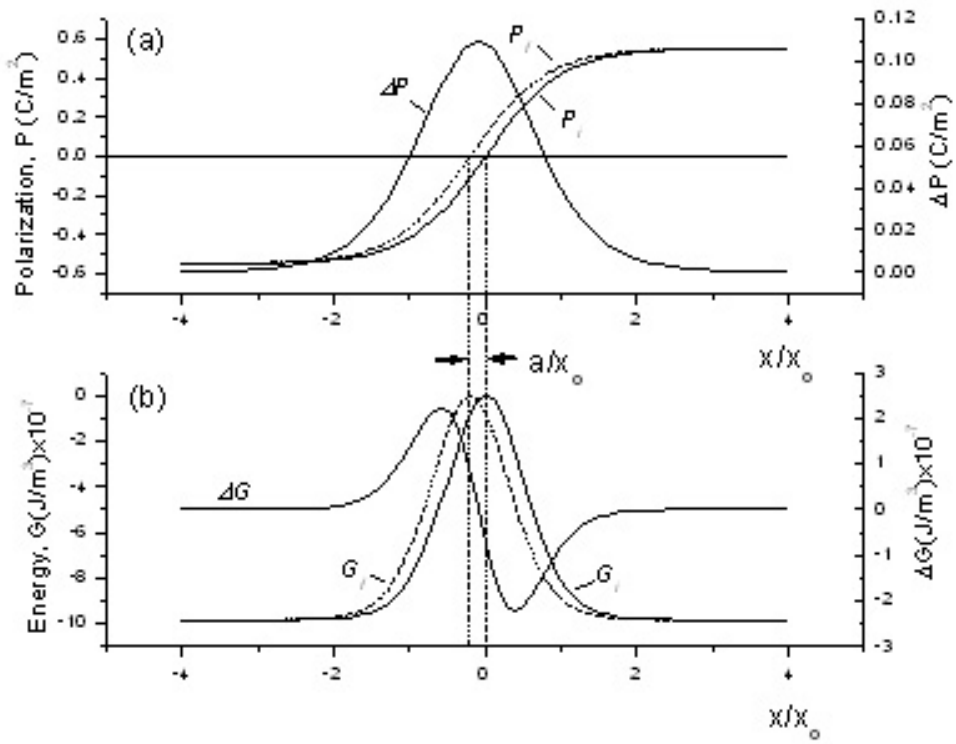

Fig. 2.18. (a) A plot of the polarization gradients (Eq. 2.20), P_i (initial), P_f (final), and $\Delta P = P_f - P_i$, of a 180 domain wall in $LiTaO_3$ after movement of the wall by an amount a under the influence of an external field E in the +x direction. (b) The corresponding polarization energies (Eq. 2.18), G_i, and G_f, and $\Delta G = G_f - G_i$ are also shown. The normalization term x_o is the domain half width according to Eq. 2.20.

walls with a finite wall width of polarization gradient, P(x) defined as [33]

$$P = P_s tanh(x/x_o) \tag{2.20}$$

where P_s is the spontaneous polarization, x is coordinate normal to the wall and $2x_o$ is the characteristic wall width. This polarization, P and the associated free energy, G (from Eq. 2.18 is plotted in Fig. 2.18(a) for $LiTaO_3$. Now we ask the following question: What is the free energy change ΔG when such a domain wall moves by one lattice

parameter, Δx=a, resulting in a change of polarization and energy at every location x by amounts ΔP=P$_f$-P$_i$ and ΔG=G$_f$ $-$ G_i(Subscripts i and f stand for initial and final states, respectively, as shown in Fig. 2.18). One can numerically calculate these quantities. On the other hand, if one assumed that a/x$_o$ is small, then, one can analytically evaluate ΔP=(dP/dx)Δx from Eq. 2.20. The corresponding free energy change is calculated as ΔG=$(\partial G/\partial P)\Delta P$, using Eq.2.18 and ΔP. For example, from Fig.2.18, it is clear that for the wall to move in the -x direction, there is a positive energy barrier, ΔG that the external field, +E has to overcome, which is less than the original energy barrier, G for a graded wall. The minimum external field required to overcome this barrier is therefore, the steepest slope of the energy well DG versus P, i.e., $E_c^{'} = (-d(\Delta G)/dP)_{max}$. This occurs at the wall center (x=0). The negative sign reflects the negative slope of ΔG versus P at the wall center under a positive field +E (see Fig. 2.18). The coercive field for domain motion can therefore be simplified at the wall center as

$$E_c^{'} = P_s\alpha_1 a/x_o \tag{2.21}$$

where K=$P_s\alpha_1$ was determined as 0.368 V for $LiTaO_3$ and 0.726 volts for $LiNbO_3$. Clearly, the coercive field contribution for this type of domain wall motion is inversely proportional to the wall width, 2x$_o$. Out of curiosity, if we presently ignore other mechanisms, and calculate the values of the equivalent domain wall widths, x$_o$ required to account for experimentally measured coercive fields in near-stoichiometric lithium niobate and lithium tantalate [37], we arrive at the upper limits of domain wall widths of x$_o$ $\approx$216 nm for near-stoichiometric $LiTaO_3$ and x$_o$ $\approx$181 nm for near-stoichiometric $LiNbO_3$. For congruent compositions, these widths would be 17.5 nm ($LiTaO_3$) and 34.5 nm ($LiNbO_3$).

Are these polarization widths at all reasonable? On the one hand, first-principle calculations on 180 domain walls suggest that they may be just a unit cell ($\approx$0.4 nm) wide [39]. On the other hand, recent work on domain walls in $LiNbO_3$ and $LiTaO_3$ show unexpectedly wide regions of strain [40] and optical birefringence (extending over micrometers) around individual domain walls, which are strongly correlated with the

presence of nonstoichiometry in the crystal [36]. In situ x-ray synchrotron experiments of individual domain wall strains under external fields in lithium niobate single crystals show that extended domain wall strains develop over 10-50 mm around the wall at fields an order of magnitude below experimental coercive fields as shown in Ch. 4.2.1. One naturally enquires if the corresponding polarization gradient at the domain walls might be broadened as well in these materials due to nonstoichiometry or in the presence of an external field. A piezoelectric scanning probe microscopy image of domain walls in congruent $LiTaO_3$ is shown in Fig. 2.19. The principle of domain imaging in the piezoresponse mode is described in detail elsewhere [41]. Figure 2.19 also shows a cross section profile of the piezoresponse signal across the domain wall (i.e., along the black line in the image). Due to possible artifacts related to sample leveling, we refer not just to the distance between maximum and minimum values of the piezoresponse signal (which is ≈400 nm wide) but also to the actual image of the wall, which was found to be about 120 nm. The best resolution that could be expected can be as small as the radius of the tip-sample contact area, i.e., of the order of several nanometers. However, the observed widths should be treated as upper limits until a detailed modeling of the image is performed.

In addition to wall broadening, other factors can contribute to coercive fields. Taking some these into account, we can therefore write the net experimentally observed coercive fields as,

$$E_c = E_c^{'} - E_{sc} + E_{defect} \tag{2.22}$$

where E_{sc} is the space-charge field, and E_{defect} is the bulk dipolar defect field. Surface polarization relaxation [42] can give rise to a polarization gradient and hence a space-charge layer near the crystal surface as recently observed in $LiNbO_3$ [43] [44]. Even if the space-charge density (charge/area) in this layer is $\sigma \approx 10^{-2} - 10^{-3} P_s$, the space-charge field, $E_{sc} = \sigma/\epsilon$ would be of the same order of magnitude as the experimental coercive fields in lithium niobate and tantalate, and will aid in domain wall motion. The dipolar defects, which stabilize domains, such as defect complexes of Ta or Nb antisites and lithium vacancies proposed here [37], will give rise to equivalent defect fields, E_{defect} [45], which tend to increase the coercive fields. As noted in Refs. [37]

and [45], the defect field E_{defect} is not an existing electric field in the material. Rather, it is a formal equivalent to the energetic difference between the two domain states $+P_s$ and $-P_s$, one stabilized by the dipolar defects by an amount of energy $-E_{defect} \cdot P_s$ and another raised in energy by the same amount.

Therefore, a very likely scenario for near-stoichiometric crystals, ($E_{defects} \approx 0$) is that the experimentally measured coercive field, E_c, may be equal to the net sum of the first two terms in Eq. 2.22 (and perhaps further contributions arising from other types of defects). Since the stoichiometric composition of $LiTaO_3$ has a coercive field of ≤17 kV/cm, the defect field in the congruent composition would be ≥210-17=193 kV/cm, which clearly dominates the experimentally observed coercive fields (210 kV/cm) in congruent compositions.

The important conclusion of this discussion is that, compared with theoretical estimates, the local coercive field in the presence of a polarization gradient at a 180° domain wall is reduced by a factor of $\approx 0.385\ x_o/a$, where a is the lattice parameter and $2x_o$ is the wall width. More generally, one could expect that any significant polarization fluctuation in a ferroelectric crystal, not just limited to a domain wall, would potentially reduce the coercive field for domain reversal in that region. The precise experimental determination of polarization wall width (particularly in the presence of small amounts of nonstoichiometry and under external fields) is central to resolving the issue of theoretical coercive fields in ferroelectric crystals.

2.5 Conclusion

As conclusion, we showed that that the presence of nonstoichiometry in ferroelectric $LiTaO_3$ gives rise to large changes in the polarization reversal properties of this material. In particular we have presented real-time studies of domain motion in near-stoichiometric composition [C =Li/(Li+Ta)≈0.4977- 0.4992] crystals. We have directly imaged and tracked the domain backswitching process in lithium tantalate. We have systematically investigated the polarization hysteresis loops, threshold coercive fields, stabilization times, switching times, and wall velocities of these crystals at

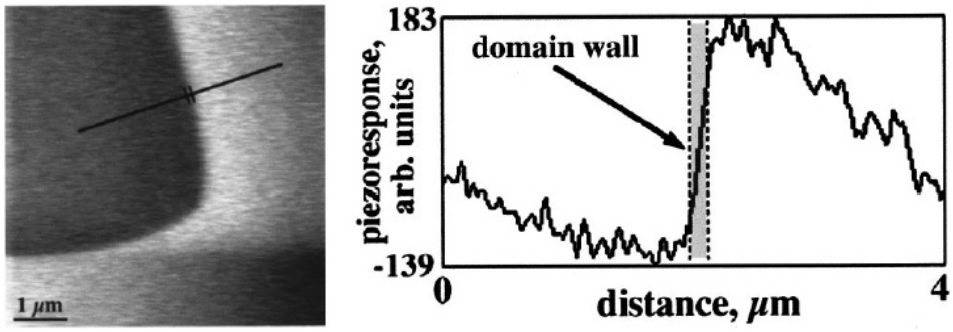

Fig. 2.19. First harmonic piezoresponse signal image (left-hand side) of one vertex of a triangular 180° domain in a congruent $LiTaO_3$ crystal using a scanning probe microscope. Polarization is normal to the image plane. The cross section profile of the piezoresponse signal across the domain wall (i.e., along the black line in the image) is shown on the right-hand side. The imaging voltage of 5 V, 10 kHz was applied using a standard Au-coated Si_3N_4 cantilever with a spring constant of 0.1 N/m and a resonant frequency of 34 kHz. The probing tip with an apex curvature radius of about 20 nm was in mechanical contact with the sample surface during the measurements (repulsive force regime). The image scan rate was 0.5 Hz.

room temperature. These results are then compared and contrasted with those for congruent compositions (C=0.485). The threshold coercive field for domain reversal and domain stabilization time increases by an order of magnitude with increasing lithium deficiency from near-stoichiometric to congruent compositions. The presence of lithium nonstoichiometry also introduces internal fields, which increase with increasing lithium deficiency. The sideways domain wall velocities are two orders of magnitude higher in nearstoichiometric crystals as compared to congruent crystals. There are similarities between the dependence of switching times and wall velocities with electric field in both nearstoichiometric and congruent compositions. In both compositions the domain wall motion is dominated by wall pinning at electric fields close to threshold coercive fields, and by wall velocity in the high field regime. We propose a physical defect dipole composed of lithium vacancies and tantalum antisites. Based on the concept of domain stabilization by bulk dipolar defects, this model qualitatively predicts many of the observed features of domain reversal such as the dependence of threshold coercive field on

defect density and on time spent in a domain state after its creation, the phenomenon of domain stabilization time, domain backswitching, and internal fields. The experiments and modeling results in this chapter can be applied to lithium niobate ($LiNbO_3$) as well, which shows very similar domain reversal properties.

We also showed that the local coercive field in the presence of a polarization gradient at a 180 domain wall is reduced by a factor of $\approx 0.385\ x_0/a$, where a is the lattice parameter and $2x_0$ is the wall width, compared with theoretical estimates.

The experiments and modeling results in this chapter can be applied to lithium niobate ($LiNbO_3$) as well, which shows very similar domain reversal properties.

References

[1] M. Fejer R. L. Byer R. G. Batchko, V. Y. Shur. *Appl. Phys. Lett.*, 75:1673, 1999.

[2] J. M. Robinson Q. X. Jia T. E. Mitchell M. J. Kawas T. E. Schlesinger D. D. Stancil K. T. Gahagan, V. Gopalan. *Appl. Opt.*, 38:1186, 1999.

[3] G. W. Burr D. Psaltis. *Computer*, 31:52, 1998.

[4] Y. Furukawa K. Kitamura V. Gopalan, T. E. Michell. *Appl. Phys. Lett.*, 72:1981, 1998.

[5] K. Niwa V. Gopalan T. E. Michell K. Kitamura, Y. Furukawa. *Appl. Phys. Lett.*, 73:3073, 1998.

[6] J. A. Aust K. Kitamura Furukawa V. Gopalan, N. A. Sanford. *Handbook of Advanced Electronic and Photonic Materials and Devices, vol. 4 Ferroelectric and Dielectrics*. Academic New York, 2000.

[7] E. Suzuki K. Niwa Y. Furukawa, K.Kitamura. *J. Cryst. Growth*, 197:889, 1999.

[8] V. Gopalan and T. E. Michel. *J. Appl. Phys.*, 85:2304, 1999.

[9] V. Gopalan and T. E. Michell. *J. Appl. Phys.*, 83:941, 1998.

[10] R. C. Miller and G. Weinreich. *Phys. Rev.*, 117:477, 1997.

[11] V. Gopalan P. J. Swart T. J. Yang, U. Mohideen. *Phys. Rev. Lett.*, 82:4106, 1999.

[12] B. Steiner S. Kim, V. Gopalan. *Appl. Phys. Lett.*, 77:2051, 2000.

[13] A. Itagi V. Gopalan Q. X. Jia T. E. Michell T. E. Schlesinger D. D. Stancil V. Gopalan, S. S. A. Gerstl. *J. Appl. Phys.*, 86:1683, 1999.

[14] G. Arlt and H. Neumann. *Ferroelectrics*, 87:109, 1988.

[15] P. V. Lambeck and G. H. Jonker. *Ferroelectrics*, 22:729, 1978.

[16] D. Dimos B. A. Tuttle J. Robertson W. L. Warren, G. E. Pike. *J. Appl. Phys.*, 79:9250, 1996.

[17] A. M. Prokhorov and Y. S. Kuziminov. *Physics and Chemistryof Crystalline Lithium Niobate*. Hilger, Bristol, 1990.

[18] D. M. Smith. *Ferroelectrics*, 50:93, 1983.

[19] M. Wohlecke O. F. Schirmer, O. Thiemann. *J. phys. Chem. Solids.*, 52:185, 1991.

[20] C. R. A. Catlow H. J. Donnerberg, S. M. Tomlinson. *J. Phys. Chem. Solids.*, 52:201, 1991.

[21] J. P. Dumas P. Lerner, C. Legras. *J. Crys. Growth*, 3/4:231, 1968.

[22] F. Izumi K. Yamamoto T. Hayashi H. Asano S. Kimura N. Iyi, K. Kitamura. *J. Solid. State. Chem.*, 101:340, 1992.

[23] F. Frey T. Metzger E. Born N. S. Zotov, H. Boysen. *J. Phys. Chem. Solids.*, 55:145, 1994.

[24] A. V. Yatsenko E. M. Ivanova, N. A. Sergeev. *Kristallografiya*, 43:337, 1998.

[25] N. A. Sergeev A. V. Yatsenko, E. N. Ivanova. *Physica B*, 240:254, 1997.

[26] A. V. Yatsenko. *Phys. Solid. State.*, 40:109, 1998.

[27] E. V. Kolonysova A. E. Korneev G. S. Zhdanov, S. A. Ivanov. *Ferroelectrics*, 21:463, 1978.

[28] E. V. Kolontsova N. Yu. Venentsev S. A. Ivanov, A. E. Korneev. *Kristallografiya*, 23:1071, 1978.

[29] H. Boysen H. Lehnert A. Hornsteiner B. Straus R. Sonntag H. M. Mayer F. Guthoff D. Hohlwein N. Zotov, F. Frey. *Acta Crystallogr. Sec. B: Struc. Sci.*, B51:961, 1995.

[30] M. E. Lines N. Nassau. *J. Appl. Phys.*, 41:533, 1970.

[31] V. Gopalan C. Battle, S. Kim. *Appl. Phys. Lett.*, 76:2436, 2000.

[32] R. E. Reed-Hill. *Physical Metallurgy Principles*. PWSKent,Boston, MA, 1991.

[33] M. E. Lines and A. M. Glass. *Principles and Applications of Ferroelectrics and Related Materials*. Clarendon, Oxford, 1977.

[34] A. V. Bune S. P. Palto L. M. Blinov N. N. Petukhova S. G. Yudin S. Ducharme, V. M. Fridkin. *Phys. Rev. Lett.*, 84:175, 2000.

[35] G. Weinreich R. C. Miller. *Phys. Rev.*, 117:1460, 1960.

[36] V. Gopalan P. Swart T. J. Yang, U. Mohideen. *Phys. Rev. Lett.*, 82:4106, 1999.

[37] V. Gopalan S. Kim. *J. Appl. Phys.*, 90:2949, 2001.

[38] Y. Furukawa K. Kitamura V. Gopalan, T. E. Mitchell. *Appl. Phys. Lett.*, 72:1981, 1998.

[39] D. Vanderbilt J. Padilla, W. Zhong. *Phys. Rev. B*, 53:R5969, 1996.

[40] V. Gopalan S. Kim, B. Steiner. *Appl. Phys. Lett.*, 77:2021, 2000.

[41] H. Tokumoto A. Gruverman, O. Auciello. *Annu. Rev. Mater. Sci.*, 28:101, 1998.

[42] D. Vanderbilt J. Padilla. *Phys. Rev. B*, 56:1625, 1997.

[43] R. Williams. *J. Phys. Chem. Solids.*, 26:399, 1965.

[44] H. Ito Y. Cho, S. Kazuta. *Appl. Phys. Lett.*, 79:2955, 2001.

[45] H. Neumann G. Arlt. *Ferroelectrics*, 87:109, 1998.

Chapter 3

Time Dependent Ginzburg Landau Ferroelectric Domain Simulation

Ferroelectrics comprise of several domain states, such as 180° domain walls usually observed in trigonal, tetragonal and hexagonal crystal systems, and 90° walls in tetragonal systems. More complex domain walls exist in other crystal systems [1]. Most of the ferroelectric domain structures evolve while these crystals are cooled down from a high temperature, higher symmetry paraelectric phase and undergo a paraelectric to ferroelectric phase transition. A single domain region has a homogeneous spontaneous polarization and a specific crystallographic orientation. Because of the spontaneous polarization, it also has spontaneous strain that accompanies the creation of the polarization. When polarization value varies spatially (i.e. gradient of polarization), as in the case near a domain wall, it creates electrical charge and therefore anisotropic energy (or domain wall energy). A sum of all these energies (polarization, strain, and gradient) will finally determine the domain structure. A useful technique to study such a complex domain pattern formation and phase transitions is the Time Dependent Ginzburg Landau (TDGL) theory. In the context of the ferroelectric phase transition, this approach has been successfully used to study pattern formation and growth of domains ([2], [3], [4], [5]). The 3-D free energy including strain and electrostrictive coupling is already well studied [6]. The uniqueness of my approach here is that it also includes higher order anisotropic gradient energy terms. By using these higher order anisotropic energy terms, various domain shapes, such as hexagonal or triangular domains in $LiNbO_3$ and $LiTaO_3$ can be predicted.

3.1 3D tdgl modeling

3.1.1 Free energy expressions for a Ferroelectric system

The high temperature prophase (paraelectric phase) of $LiNbO_3$ and $LiTaO_3$ have a $\bar{3}m$ (R$\bar{3}$c:space group) point group symmetry. At room temperature, both crystals have the lower symmetry 3m (R3c:space group). $LiNbO_3$ becomes ferroelectric below 1210°C, and $LiTaO_3$ below 665°C. Because of inversion symmetry along the crystallographic z-direction, only $\pm P_z$ spontaneous polarization is allowed. But it is possible that adjacent to a domain wall, polarizations $\pm P_x$, and $\pm P_y$ (in-plane) can exist. In the mutidomain state of a ferroelectric, there are two kinds of long-range interactions: strain and electrostatic. Usually in a 180° domain system where polarization is along $\pm P_z$, there is no expected crystallographic restrictions on specific domain shapes within the $x - y$ plane. These preferences, if they exist, arise either electrostatic energy or anisotropy energy, and are responsible for the unique domain shapes in $LiNbO_3$ and $LiTaO_3$ crystals. Even though the primary order parameter is P_z in a 180° domain wall system, we include P_x and P_y components here as well in order to account for the possible charged domain walls.

The total free energy per unit volume of a ferroelectric system is given by,

$$f_{Total} = f_l + f_s + f_c + f_g + f_{d-d} \tag{3.1}$$

Here, the f_l is the ferroelectric polarization energy (also called landau free energy), f_s is the elastic energy, f_c is the electrostrictive energy that couples polarization and strain, f_g is the gradient energy, related to polarization gradients in the material, and f_{d-d} is the dipole-dipole interaction energy related to electrostatic charges at domain walls. Each of these terms is now discussed in detail.

The Landau free energy is given by

$$f_l = -\frac{\psi_1 P_z^2}{2} + \frac{\psi_2 P_z^4}{4} + \frac{\psi_3 (P_x^2 + P_y^2)}{2} \tag{3.2}$$

The energy terms $f_l(r)$ and polarization $P_z(r)$ are functions of location r(x,y,z). For brevity, this dependence is not explicitly stated in the equations above and those that follow. The coefficients Ψ are related to the physical constants of the material (dielectric constant and spontaneous polarization). These relations are explicitly given as

$$\Psi_1 = 1/(2 \cdot \epsilon_{33}) \tag{3.3}$$

$$\Psi_2 \approx \Psi_1/P_s^2 \tag{3.4}$$

Relative *clamped* dielectric constants of 30 and 43.5 are used for $LiNbO_3$ and $LiTaO_3$, respectively. The spontaneous polarization for $LiNbO_3$ ia a 0.75[C/m^2] and for $LiTaO_3$ is 0.55[C/m^2]. The energy term $f_l(r)$ and polarization P(r) are also a function of location r(x,y,z), which is not explicitly shown for simplifying the notation. The Elastic energy, f_s is given by,

$$f_s = \frac{1}{2} C_{ijkl} \epsilon_{ij} \epsilon_{kl} \tag{3.5}$$

where, C_{ijkl} is the elasticity tensor, and ϵ_{ij} the strain tensor. The terms f_s and ϵ are also functions of location, r, but not explicitly stated for brevity. The coupling energy can be represented as

$$f_c = Q_{ijkl} \epsilon_{ij} P_k P_l \tag{3.6}$$

where Q_{ijkl} is the electrostrictive tensor.

The gradient free energy density is given by,

$$f_g = g_1 \left[\left(\frac{\partial P_z}{\partial x} \right)^2 + \left(\frac{\partial P_z}{\partial y} \right)^2 \right] + g_2 \left(\frac{\partial P_z}{\partial z} \right)^2 \tag{3.7}$$

Here, g_1 is an in-plane gradient energy coefficient for homogeneous case. The term g_2 is a coefficient for the polarization variation in the z direction. Higher order gradient energy will be derived in the later part of this chapter. The dipole-dipole interaction free energy is given by,

$$f_{d-d} = -\mathbf{P} \cdot \mathbf{E} \tag{3.8}$$

Here **E** is a electric field which is generated by inhomogeneous polarization distribution. Now stress σ_{ij} can be defined by

$$\sigma_{ij} = \frac{1}{2}C_{ijkl}\epsilon_{kl} + Q_{ijkl}P_kP_l \tag{3.9}$$

Because of the mechanical equilibrium condition of no net forces,

$$\begin{aligned}
\frac{\partial \sigma_{ij}}{\partial x_j} = 0 &= \frac{\partial}{\partial x_j}\left[\frac{1}{2}C_{ijkl}\left(\frac{\partial u_k}{\partial x_l} + \frac{\partial u_l}{\partial x_k}\right) + Q_{ijkl}P_kP_l\right] \\
&= \frac{\partial}{\partial x_j}\left[C_{ijkl}\frac{\partial}{\partial x_l}\int \widetilde{u_k}e^{i\vec{\mathbf{k}}\cdot\vec{\mathbf{r}}}\,d\mathbf{k}^3 + Q_{ijkl}\int \widetilde{P_kP_l}e^{i\vec{\mathbf{k}}\cdot\vec{\mathbf{r}}}\,d\mathbf{k}^3\right] \\
&= \int \left(C_{ijkl}(ik_jik_l)\widetilde{u_k} + Q_{ijkl}(ik_j)\widetilde{P_kP_l}\right)e^{i\vec{\mathbf{k}}\cdot\vec{\mathbf{r}}}\,d\mathbf{k}^3 = 0
\end{aligned} \tag{3.10}$$

To satisfy the above equation,

$$C_{ijkl}k_jk_l\widetilde{u_k} = iQ_{ijkl}\widetilde{P_kP_l}k_j \tag{3.11}$$

I can set

$$\begin{aligned}
G_{ik}^{-1} &= C_{ijkl}k_jk_l = |k|^2\,C_{ijkl}n_jn_l = |k|^2\,\Omega_{ik}^{-1} \\
\widetilde{T_{ij}} &= Q_{ijkl}\widetilde{P_kP_l}
\end{aligned} \tag{3.12}$$

it makes simple equation,

$$G_{ik}^{-1}\widetilde{u_k} = i\widetilde{T_{ij}}k_j \tag{3.13}$$

So displacement field in Fourier space can be,

$$\widetilde{u(\mathbf{k})} = iG_{ki}\widetilde{T_{ij}}k_j = \frac{i}{|k|}\Omega_{ki}^{-1}\widetilde{T_{ij}}n_j \tag{3.14}$$

The real space displacement can be written as,

$$u_k(\vec{\mathbf{r}}) = i \int \frac{dk^3}{(2\pi)^3} \frac{1}{|k|} \Omega_{ki} \widetilde{T_{ij}} n_j e^{i\vec{\mathbf{k}}\vec{\mathbf{r}}} \tag{3.15}$$

Based on displacement field, I can get integrated eleastic(F_{el}) and coupling(F_{cp}) energy in the system

$$\begin{aligned}
F_{el} + F_{cp} &= \int d\mathbf{r}^3 (f_s + f_c) \\
&= \int d\mathbf{r}^3 \left(\frac{1}{2} C_{ijkl} \epsilon_{ij} \epsilon_{kl} + Q_{ijkl} \epsilon_{ij} P_k P_l \right) \\
&= \int d\mathbf{r}^3 \frac{1}{2} C_{ijkl} \int (d\mathbf{k}'^3) \widetilde{\epsilon_{ij}} e^{i\mathbf{k}'\mathbf{r}} \int (d\mathbf{k}''^3) \widetilde{\epsilon_{kl}} e^{i\mathbf{k}''\mathbf{r}} \\
&\quad + Q_{ijkl} \int (d\mathbf{k}'^3) \widetilde{\epsilon_{ij}} e^{i\mathbf{k}'\mathbf{r}} \int (d\mathbf{k}''^3) \widetilde{P_k P_l} e^{i\mathbf{k}''\mathbf{r}} \\
&= -\int (d\mathbf{k}^3) \left(\frac{1}{2} C_{ijkl} \widetilde{\epsilon_{ij}} \widetilde{\epsilon_{kl}}^* + Q_{ijkl} \widetilde{\epsilon_{ij}} \widetilde{P_k P_l}^* \right) \\
&= -\int (d\mathbf{k}^3) \left(-\frac{1}{2} C_{ijkl} k_j k_l \widetilde{u_i} \widetilde{u_k}^* + i Q_{ijkl} k_j \widetilde{u_i} \widetilde{P_k P_l}^* \right) \\
&= \int (d\mathbf{k}^3) \left(\frac{1}{2} G_{ik}^{-1} \widetilde{u_i} \widetilde{u_k}^* - i \widetilde{T_{ij}^*} k_j \widetilde{u_i} \right) \\
&= \int (d\mathbf{k}^3) \left(\frac{1}{2} i \widetilde{T_{ij}^*} k_j \widetilde{u_i} - i \widetilde{T_{ij}^*} k_j \widetilde{u_i} \right) \\
&= \int (d\mathbf{k}^3) \left(\frac{1}{2} i \widetilde{T_{ij}^*} k_j i G_{ij} \widetilde{T_{jl}} k_l - i \widetilde{T_{ij}^*} k_j i G_{ij} \widetilde{T_{jl}} k_l \right) \\
&= \int (d\mathbf{k}^3) \left(\frac{1}{2} \widetilde{T_{ij}^*} k_j G_{ij} \widetilde{T_{jl}} k_l \right)
\end{aligned} \tag{3.16}$$

The integrated Landau free energy can be easily represented by,

$$F_{landau} = \int (d\mathbf{x})^3 \left(-\frac{\psi_1 P_z^2}{2} + \frac{\psi_2 P_z^4}{4} + \frac{\psi_3 (P_x^2 + P_y^2)}{2} \right) \tag{3.17}$$

The integrated gradient and dipole-dipole interaction energies are similarly calculated as

$$F_g = \int (d\mathbf{x})^3 \left(g_1 \left[\left(\frac{\partial P_z}{\partial x} \right)^2 + \left(\frac{\partial P_z}{\partial y} \right)^2 \right] + g_2 \left(\frac{\partial P_z}{\partial z} \right)^2 \right) \tag{3.18}$$

$$F_{d-d} = -\int (d\mathbf{x})^3 \left(\mathbf{P} \cdot \mathbf{E} \right) \tag{3.19}$$

3.1.2 Symmetry invariant terms in the energy

Because of the nature of the 180° domain walls, the gradient energy is dominant in determining the domain wall orientation in the $x-y$ plane. By using crystal symmetry, we can deduce the invariant terms in the gradient energy. The gradient energy arises from the gradient of the primary order parameter, P_z. All the energy terms, including the gradient term, have to satisfy the point group symmetries of the prototype phase, namely, 3-fold rotation axis about the polarization direction, mirror plane in the $y-z$ plane (a c-glide plane to be more precise), and finally the inversion symmetry. In other words, the energy terms *cannot change* when the coordinates are transformed using an allowed symmetry. To examine the tensor properties in the trigonal or hexagonal systems, it is often convenient to transform the real axes x and y into complex axes η and ξ as follows.

$$\begin{bmatrix} \xi \\ \eta \\ z \end{bmatrix} = \begin{bmatrix} i & -1 & 0 \\ i & 1 & 0 \\ 0 & 0 & 1 \end{bmatrix} \begin{bmatrix} x \\ y \\ z \end{bmatrix} \tag{3.20}$$

A three-fold rotation symmetry operation in the [x,y,z] coordinate is

$$R = \begin{bmatrix} cos(2\pi/3) & sin(2\pi/3) & 0 \\ -sin(2\pi/3) & cos(2\pi/3) & 0 \\ 0 & 0 & 1 \end{bmatrix}$$

and the mirror operation about the $y - z$ plane is given by

$$M = \begin{bmatrix} -1 & 0 & 0 \\ 0 & 1 & 0 \\ 0 & 0 & 1 \end{bmatrix}$$

The inversion operation in the [x,y,z] coordinate system is

$$I = \begin{bmatrix} -1 & 0 & 0 \\ 0 & -1 & 0 \\ 0 & 0 & -1 \end{bmatrix}$$

By using similarity transformation, these above symmetry operations can be transformed in the $[\xi, \eta, z]$ coordinate system as follows. A three-fold symmetry operator in $[\xi, \eta, z]$ coordinate is

$$R' = \begin{bmatrix} e^{-(2\pi i/3)} & 0 & 0 \\ 0 & e^{(2\pi i/3)} & 0 \\ 0 & 0 & 1 \end{bmatrix}$$

The mirror operation in $[\xi, \eta, z]$ coordinate is

$$M' = \begin{bmatrix} 0 & -1 & 0 \\ -1 & 0 & 0 \\ 0 & 0 & 1 \end{bmatrix}$$

and inversion operation is in $[\xi, \eta, z]$ coordinate is

$$I' = \begin{bmatrix} -1 & 0 & 0 \\ 0 & -1 & 0 \\ 0 & 0 & -1 \end{bmatrix}$$

Similarity matrix transformation makes R′ as a diagonal matrix, which is why complex transformation is used. But the gradient energy element $P_{z,\xi}$ ($or\ \frac{\partial P_z}{\partial \xi}$) should be treated a bit carefully. Unlike a normal contravariant tensor, $P_{z,\xi}$ becomes a mixed tensor. Because the coordinate z coordinate and the in-plane axes ξ and η are independent, therefore, P_z can be treated as a contravariant, and the derivative part can be treated as a covariant tensor. For covariant transformation of the partial derivative term, the inversion matrix of R′, M′, and I′ is used. Table 3.1 shows the results of such symmetry transformation. By using Table 3.1, many invariant terms can be generated. As an

	3fold Rotaion	Inversion	Mirror
$P'_{z,\xi}$	$e^{i2\pi/3}P_{z,\xi}$	$P_{z,\xi}$	$-P_{z,\eta}$
$P'_{z,\eta}$	$e^{-i2\pi/3}P_{z,\eta}$	$P_{z,\xi}$	$-P_{z,\xi}$

Table 3.1. symmetrical operation for the gradient energy term

example, $P'_{z,\xi}P'_{z,\eta} = P_{z,\xi}P_{z,\eta}$ is one of the invariant gradient terms. Due to the isotropy in the $x-y$ plane, the $P'^2_{z,\xi} + P'^2_{z,\eta}$ invariant energy term exists. Similarly, $P'^3_{z,\xi} - P'^3_{z,\eta}$ (which contains a 3-fold symmetry), and $P'^6_{z,\xi} + P'^6_{z,\eta}$ energy term (which contains 6-fold symmetry) are allowed. For stoichiometric $LiNbO_3$ and $LiTaO_3$ crystals, and congruent $LiNbO_3$ crystals, one observes hexagonal shaped domains. It will be shown below that this is explained by the presence of a 6-fold symmetry gradient energy term. In stoichiometric $LiTaO_3$ crystals, triangular domains are observed, which can be explained

by including a 3 fold symmetry gradient energy term.

$$f_{g:isotropic} = g_{iso:xy}(P^2_{z,\xi} + P^2_{z,\eta}) + g_{iso:z}P^2_{z,z} \tag{3.21}$$

$$f_{g:3fold} = g_{3fold:xy}(P^3_{z,\xi} - P^3_{z,\eta}) + g_{iso:z}P^2_{z,z} \tag{3.22}$$

$$f_{g:6fold} = g_{6fold:xy}(P^6_{z,\xi} + P^6_{z,\eta}) + g_{iso:z}P^2_{z,z} \tag{3.23}$$

Here $g_{j:xy}$ (j can be iso, 3-fold, or 6-fold) are in-plane gradient energy coefficients, and $g_{iso:z}$ is a z-direction gradient energy coefficient. By using the transformation matrix, these gradient energy terms can be written in terms of x and y coordinates as follows:

$$f_{g:isotropic} = g_{iso:xy}(P^2_{z,x} + P^2_{z,y}) + g_{iso:z}P^2_{z,z} \tag{3.24}$$

$$f_{g:3fold} = g_{3fold:xy}(6P^2_{z,x}P_{z,y} - 2P^3_{z,y}) + g_{iso:z}P^2_{z,z} \tag{3.25}$$

$$f_{g:6fold} = g_{6fold:xy}(2P^6_{z,y} - 2P^6_{z,x} + 30P^4_{z,x}P^2_{z,y} - 30P^2_{z,x}P^4_{z,y}) + g_{iso:z}P^2_{z,z} \tag{3.26}$$

Integrated gradient energy is

$$F_{gradient} = \int (dx)^3 f_{g:j} \tag{3.27}$$

Here, j can be isotropic, 3-fold, or 6-fold depending on the system. Now, the total energy of the system can be calculated. Initially, this system is not in an equilibrium state. But by using Time Dependent Ginzburg Landau equation, this system can be moved towards the equilibrium state. This equation can be defined as

$$\frac{\partial}{\partial t}P_\beta(\mathbf{r},t) = -\mu\frac{\delta F_{Total}}{\delta P_\beta(\mathbf{r},t)} + noise(\mathbf{r},t) \tag{3.28}$$

Here, μ is a mobility, and noise($\mathbf{r}$,t) is a Gaussian random noise to agitate the system so that it does not rest in a local minimum, but rather tries to find the global minimum. In our simulations, this noise term was not found to be necessary. F is the integrated total

energy, given by,

$$F_{Total} = F_{landau} + F_{el} + F_{cp} + F_{gradient} + F_{d-d} \tag{3.29}$$

The governing TDGL Eqn. 3.28 can be solved in either real space or reciprocal space. First, the functional derivative of Landau free energy can be easily solved in real space

$$\frac{\delta F_{landau}}{\delta P_\beta} = \int (d\mathbf{x})^3 \left(-\frac{\partial}{\partial P_\beta}\left(\frac{\psi_1 P_z^2}{2}\right) + \frac{\partial}{\partial P_\beta}\left(\frac{\psi_2 P_z^4}{4}\right) + \frac{\partial}{\partial P_\beta}\left(\frac{\psi_3 (P_x^2 + P_y^2)}{2}\right)\right) \tag{3.30}$$

In P_β, β can be x, y, and z. Next, we need to solve the functional derivative of the elastic and coupling energy terms.

$$\begin{aligned} \frac{\delta(F_{el} + F_{cp})}{\delta P_\beta(\mathbf{r})} &= \frac{\delta}{\delta P_\beta(\mathbf{r})} \int (d\mathbf{k})^3 \left(\widetilde{T^*_{ij}} k_j \widetilde{G_{il}} \widetilde{T_{lm}} k_m \right) \\ &= \int (d\mathbf{k})^3 \left(\frac{\delta}{\delta P_\beta(\mathbf{r})} (\widetilde{T^*_{ij}}) k_j \widetilde{G_{ij}} \widetilde{T_{lm}} k_m \right) \\ &\quad + \int (d\mathbf{k})^3 \left(\widetilde{T^*_{ij}} k_j \widetilde{G_{ij}} \frac{\delta}{\delta P_\beta(\mathbf{r})} (\widetilde{T_{lm}}) k_m \right) \end{aligned} \tag{3.31}$$

Let's first solve first term of Eqn 3.31. To simplify this equation, let us introduce a new variable Π.

$$\Pi_{ij}(\mathbf{r}) = \int (d\mathbf{k})^3 \left(k_j \widetilde{G_{il}} \widetilde{T_{lm}} k_m e^{i\vec{\mathbf{k}}\vec{\mathbf{r}}} \right) \tag{3.32}$$

Then the first term in Eqn. 3.31 can be written as

$$\int (d\mathbf{k})^3 \frac{\delta}{\delta P_\beta(\mathbf{r})} \left(\int (d\mathbf{r}')^3 T^*_{ij}(\mathbf{r}') e^{i\vec{\mathbf{k}}\vec{\mathbf{r}}'} \right) \int (d\mathbf{r}'')^3 \Pi_{ij}(\mathbf{r}'') e^{-i\vec{\mathbf{k}}\vec{\mathbf{r}}''} \tag{3.33}$$

$$\Leftrightarrow \int (d\mathbf{k})^3 \int (d\mathbf{r}'')^3 \frac{\delta T^*_{ij}(\mathbf{r})}{\delta P_\beta(\mathbf{r})} \Pi_{ij}(\mathbf{r}'') e^{i\vec{\mathbf{k}}(\vec{\mathbf{r}} - \vec{\mathbf{r}}'')} \tag{3.34}$$

$$\Leftrightarrow \frac{\delta T^*_{ij}(\mathbf{r})}{\delta P_\beta(\mathbf{r})} \Pi_{ij}(\mathbf{r}) \tag{3.35}$$

From Eqn. 3.34 to 3.35 $\int (d\mathbf{k})^3 e^{i\vec{\mathbf{k}}(\vec{\mathbf{r}}-\vec{\mathbf{r}}'')} = \delta(\vec{\mathbf{r}} - \vec{\mathbf{r}}'')$ is used. By applying same process, second part of the Eqn 3.31 also can be written as

$$\Pi^*_{lm}(\mathbf{r})\frac{\delta T^*_{lm}(\mathbf{r})}{\delta P_\beta(\mathbf{r})} \tag{3.36}$$

For the gradient energy functional derivative case, both the reciprocal space and the real space can be used. But for higher order terms, real space functional derivative is more flexible.

$$\begin{aligned}\frac{\delta F_{gradient}}{\delta P_z(\mathbf{r})} &= \frac{\delta}{\delta P_z(\mathbf{r})}\int (d\mathbf{r})^3 f_g\left(P(\mathbf{r}'), \frac{\partial P_\beta(\mathbf{r}')}{\partial \mathbf{r}'}\right) \\ &= \frac{\partial f_g\left(P(\mathbf{r}), \frac{\partial P_\beta(\mathbf{r})}{\partial \mathbf{r}}\right)}{\partial P_z} - \partial_{\mathbf{r}}\left(\frac{\partial f_g\left(P(\mathbf{r}), \frac{\partial P_\beta(\mathbf{r})}{\partial \mathbf{r}}\right)}{\partial\left(\frac{\partial P_\beta(\mathbf{r})}{\partial(\mathbf{r})}\right)}\right)\end{aligned} \tag{3.37}$$

Dipole-dipole interaction terms can be represented as a function of electric field, which is generated by the polarization gradient. The Poisson's equation relating the potential ϕ generated by the gradient of polarization, is given by

$$\frac{\partial^2\phi}{\partial x^2} + \frac{\partial^2\phi}{\partial y^2} + \frac{\partial^2\phi}{\partial z^2} = \frac{1}{\epsilon_0}\left(\frac{\partial P_x}{\partial x} + \frac{\partial P_y}{\partial y} + \frac{\partial P_z}{\partial z}\right) \tag{3.38}$$

By using Fourier transformation,

$$\widetilde{\phi} = \frac{i}{\epsilon_0}\frac{k_x\widetilde{P_x} + k_y\widetilde{P_y} + k_z\widetilde{P_z}}{k_x^2 + k_y^2 + k_z^2} \tag{3.39}$$

In real space, the electric field is related to this potential as, E=-∇Φ. In reciprocal space, electric field can be calculated. Foe example,

$$\widetilde{E_x} = \frac{1}{\epsilon_0}\frac{k_x^2\widetilde{P_x} + k_xk_y\widetilde{P_y} + k_xk_z\widetilde{P_z}}{k_x^2 + k_y^2 + k_z^2} \tag{3.40}$$

By using inverse Fourier transformation, the electric field E_x in real-space can easily be calculated. Similarly, E_y, and E_z can be calculated by the same process.

3.1.3 Simulation Details

Till now, I have derived all the individual energy terms and calculated the functional derivative of these energy terms in order to solve the TDGL time evolution equation (Eq. 3.28). Both $LiNbO_3$ and $LiTaO_3$ have the same crystal symmetry $\bar{3}$m. Because of the crystal symmetry, all the matrix or tensor components also satisfy the symmetry operations. Many of the coefficients disappear as a result. Elasticity coefficients C_{ij} and electrostrictive coefficients Q'_{ij} are represented by

$$C_{ij} = \begin{bmatrix} C_{11} & C_{12} & C_{13} & C_{14} & \bullet & \bullet \\ C_{12} & C_{12} & C_{13} & -C_{14} & \bullet & \bullet \\ C_{13} & C_{13} & C_{33} & \bullet & \bullet & \bullet \\ C_{14} & -C_{14} & \bullet & C_{44} & \bullet & \bullet \\ \bullet & \bullet & \bullet & \bullet & C_{44} & C_{14} \\ \bullet & \bullet & \bullet & \bullet & C_{14} & 1/2(C_{11} - C_{12}) \end{bmatrix}$$

$$Q'_{ij} = \begin{bmatrix} \bullet & \bullet & Q'_{31} & Q'_{41} & \bullet & \bullet \\ \bullet & \bullet & Q'_{31} & Q'_{42} & \bullet & \bullet \\ Q'_{31} & Q'_{31} & Q'_{33} & \bullet & \bullet & \bullet \\ Q'_{41} & Q'_{42} & \bullet & Q'_{44} & \bullet & \bullet \\ \bullet & \bullet & \bullet & \bullet & \bullet & -2Q'_{42} \\ \bullet & \bullet & \bullet & \bullet & -Q'_{42} & \bullet \end{bmatrix}$$

The prime notation on the Q' coefficient is added to distinguish between two different definitions of electrostrictive coefficients.

$$\epsilon_{ij} = Q'_{ijkl} P_k P_l \tag{3.41}$$

and its dimension is $[C^2/m^4]$. But the Q-coefficient, which is used in TDGL equation is given by,

$$Q_{ijmn} = C_{ijkl}Q'_{klmn} \tag{3.42}$$

And its dimensions are $[NC^2/m^6]$. The elastic coefficient of $LiNbO_3$, and $LiTaO_3$ crystal are listed in the Table 3.2. The electrostrictive coefficients used for of $LiNbO_3$, and

	C_{11}	C_{12}	C_{13}	C_{33}	C_{44}	C_{14}
$LiNbO_3$	2.03	0.53	0.75	2.45	0.60	0.09
$LiTaO_3$	2.33	0.47	0.80	2.75	0.94	-0.11

Table 3.2. Elastic coefficient value $[N/m^2]\times10^{11}$ (from Landolt Bornstein II)

$LiTaO_3$ crystals are listed in Table 3.3 below.

	Q'_{31}	Q'_{33}	Q'_{42}	Q'_{44}
$LiNbO_3$	-0.003	0.016	0.02	0.065
$LiTaO_3$	-0.0047	0.011	0.016	0.052

Table 3.3. Electrostrictive coefficient value $[C^2/m^4]$(from Landolt Bornstein II)

The final TDGL equation 3.28 is solved based on the derived energy terms. For isotropic gradient energy coefficient, I used $g_{iso:xy}$=1.25×$10^{-3}[C^{-2}\cdot N\cdot m^4]$. In $LiNbO_3$, I used 6-fold symmetry gradient energy coefficient which is $g_{6fold:xy}$=1.25×$10^-27[C^{-6}\cdot$

$N \cdot m^{16}$]. For $LiTaO_3$, 3-fold symmetry gradient energy coefficient was used which was $g_{3fold:xy}$=3.15×10^{-9}[$C^{-6} \cdot N \cdot m^{16}$]. The isotropic energy term is very stable. I can use any isotropic gradient energy coefficient value which is smaller than 1.25×10^{-2}[$C^{-2} \cdot N \cdot m^4$]. But the stable range of higher order energy coefficients is very narrow. It is only stable within less than ± 5 % percent of the above simulation values. This 3-D TDGL equation is simulated by Matlab based code(see Appendix C).

First from Fig. 3.1 to 3.8 shows each strain component and the main P_z polarization for Lithium Niobate. Only after including higher order gradient energy term, one can observe hexagonal domain patterns. This simulation is started from tiny nucleation sites, and biased to be favorable to the inside domain. Even though the initial nuclei is circular in shape, it transformed to hexagonal domain while it is growing. After it grows into a regular hexagonal shape, the bias field was turned off to see the strain distribution under no external field. Fig. 3.1 shows the P_z polarization distribution, and Fig. 3.2 shows the z-direction displacement. This displacement value shows a 3-fold symmetry consistent with the trigonal symmetry of the lattice. From Fig. 3.3 to Fig. 3.7 are shown various strain components ϵ_{xx}, ϵ_{yy}, ϵ_{xy}, ϵ_{xz}, and ϵ_{yz} for lithium niobate.

The first interesting observation is that the z-direction displacement field (see Fig. 3.2) or ϵ_{zz} has a very nice 3- fold symmetry. Because of the z- direction displacement, ϵ_{xz}(Fig. 3.6) and ϵ_{yz}(Fig. 3.7) are induced. These results are experimentally observed in X-Ray synchrotron experiments in Ch. 4.1.2.3. The strain component normal to the domain walls is observed uniformly through the all domain wall orientations equally. Figure 3.8 shows equal amounts of normal component of the displacement along the domain wall, and has a maximum value at the domain wall.

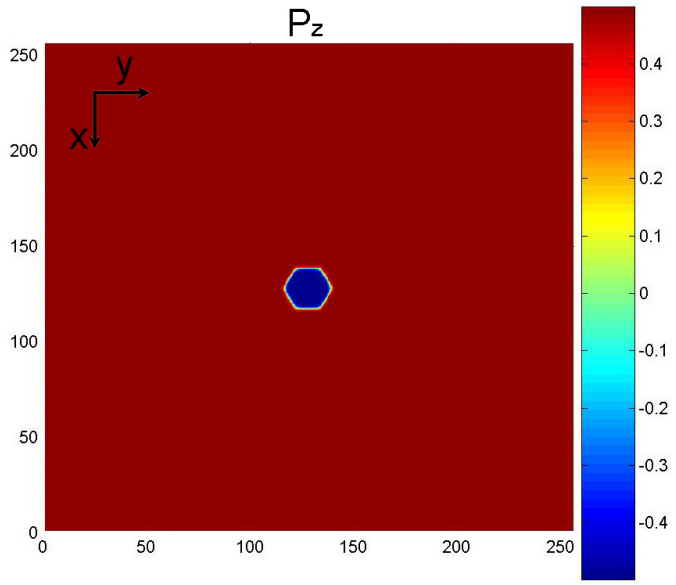

Fig. 3.1. Main polarization component Pz

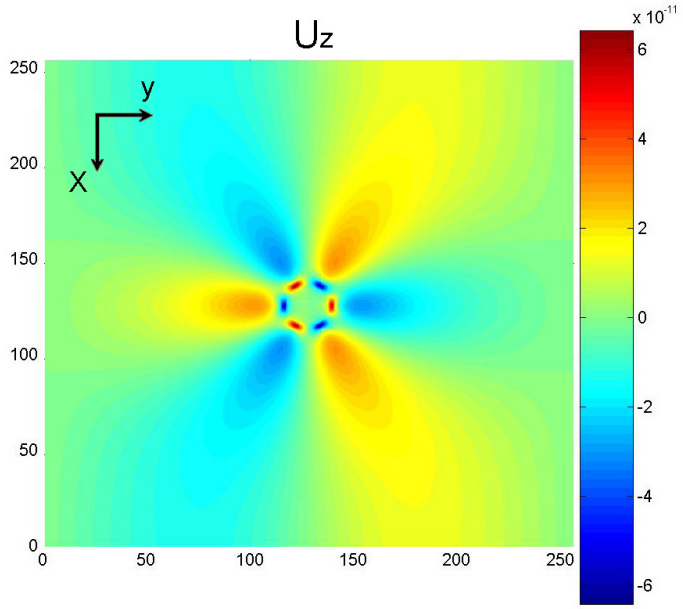

Fig. 3.2. $LiNbO_3$: z direction displacement

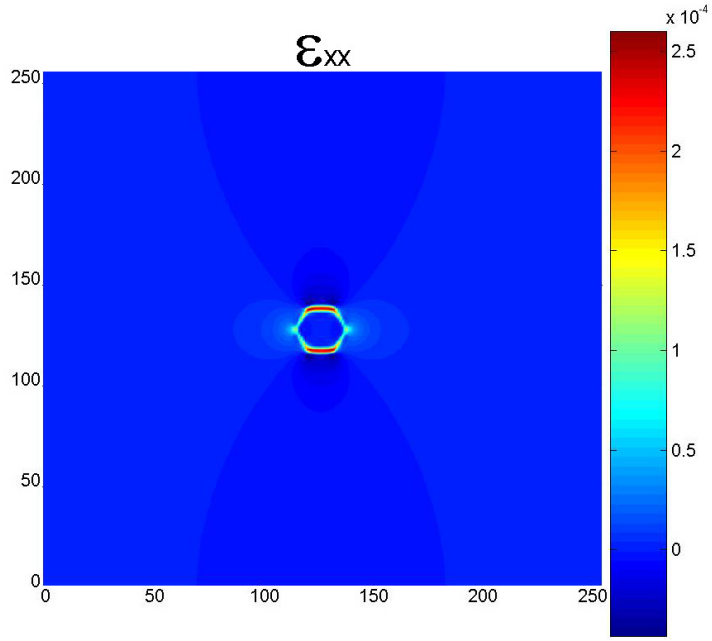

Fig. 3.3. $LiNbO_3$: ϵ_{xx}

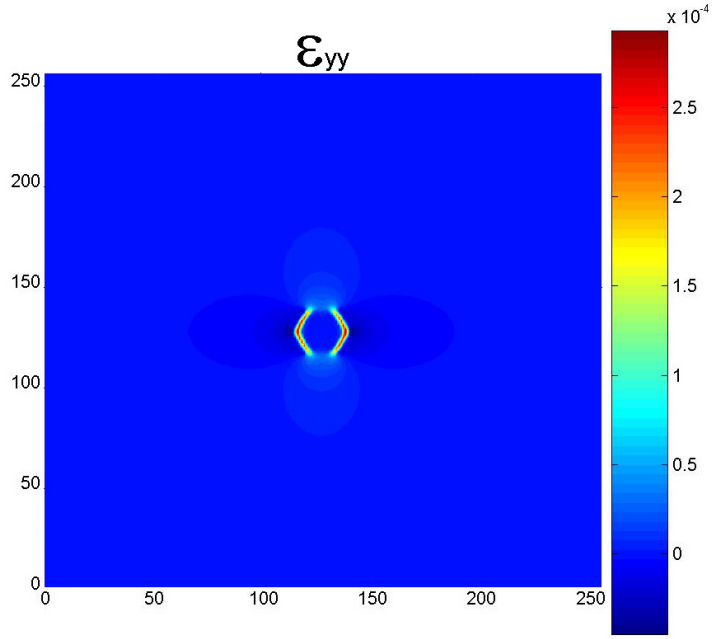

Fig. 3.4. $LiNbO_3$: ϵ_{yy}

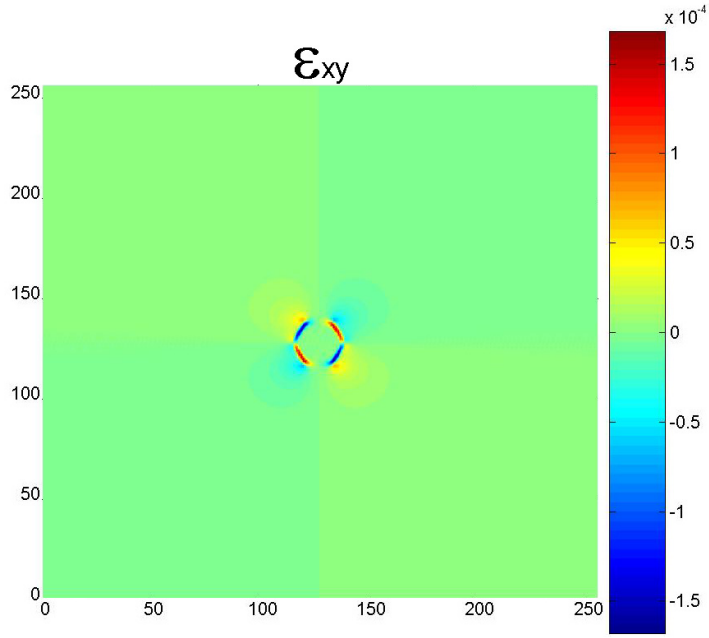

Fig. 3.5. $LiNbO_3$: ϵ_{xy}

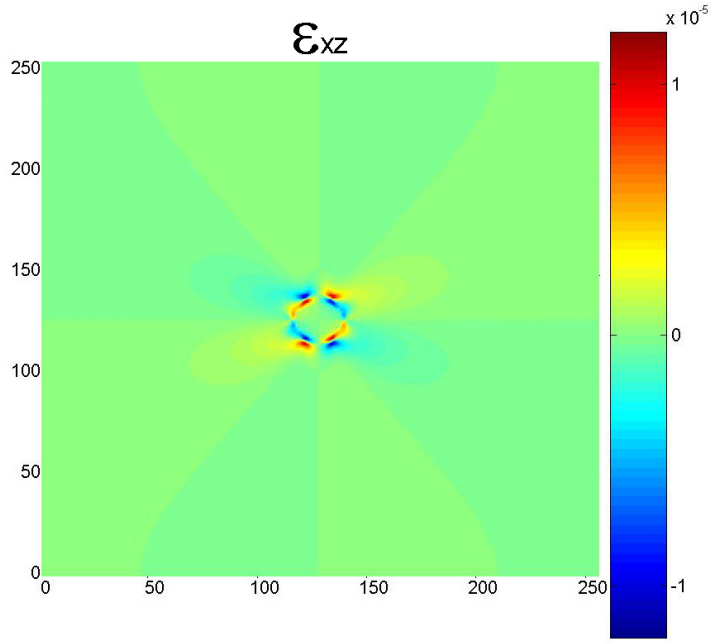

Fig. 3.6. $LiNbO_3$: ϵ_{xz}

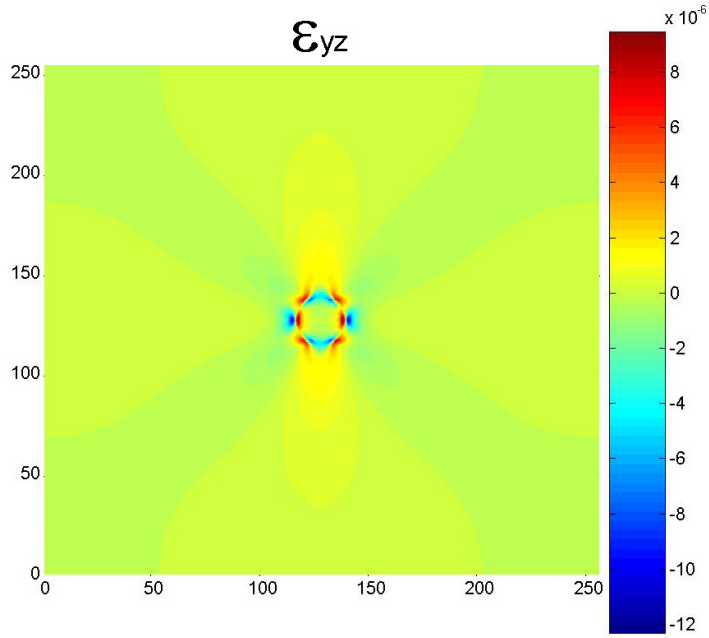

Fig. 3.7. $LiNbO_3$: ϵ_{yz}

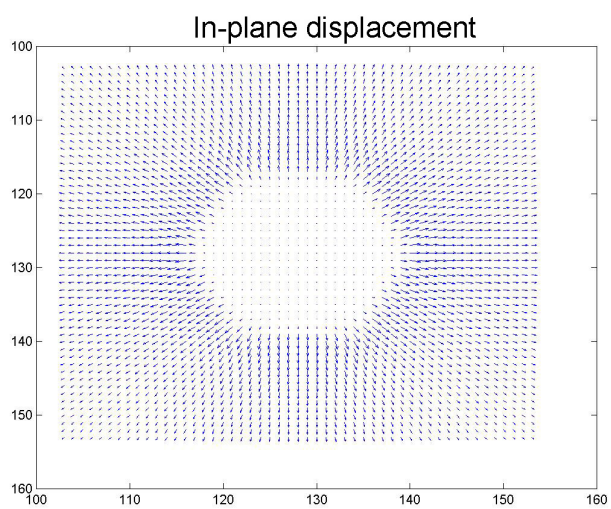

Fig. 3.8. $LiNbO_3$: In plane displacement

By simply changing elastic coefficient, electro strictive coefficient, and different gradient energy polynominal(3-fold symmetry) in addition to isotropic symmetry term , triangular domain structures can also be generated, as can be seen from Fig. 3.9 to 3.16. . Again, the z-direction displacement shows a 3-fold symmetry. The main difference between $LiNbO_3$ and $LiTaO_3$ is the in-plane strain distribution. We observed uniform in- plane displacement in $LiNbO_3$ along the domain boundary (see Fig. 3.8), but in $LiTaO_3$, three triangular corners show a strong displacement field (see Fig. 3.16) or in-plane strain (see Fig. 3.11 and 3.12).

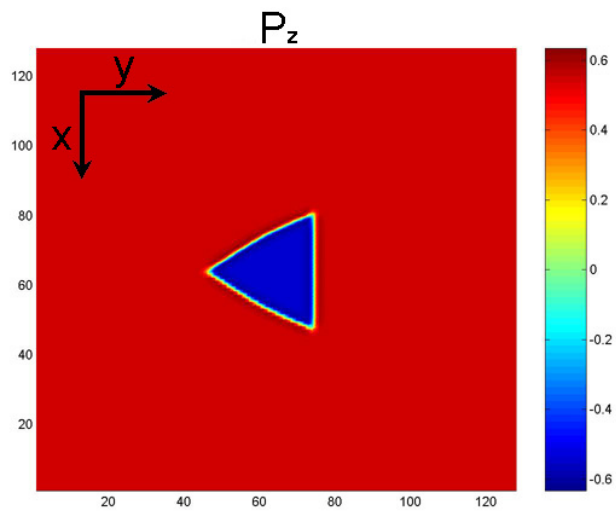

Fig. 3.9. $LiTaO_3$: Main polarization component Pz

As a summary of the above results, both $LiNbO_3$ and $LiTaO_3$ domain patterns were started from one small circular nucleation site at the center of the calculation space. By applying a voltage that is larger than the coercive field, this domain nuclei can be grown into hexagonal or triangular shapes depending on the gradient energy polynominal. After the domain has fully grown into its desired shape, the external

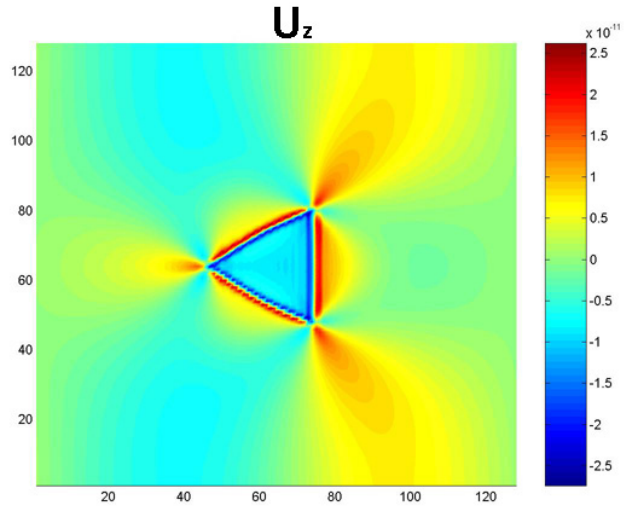

Fig. 3.10. $LiTaO_3$: z direction displacement

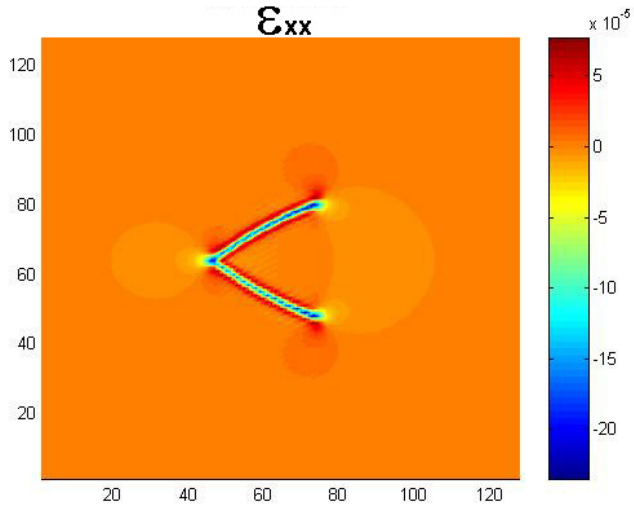

Fig. 3.11. $LiTaO_3$: ϵ_{xx}

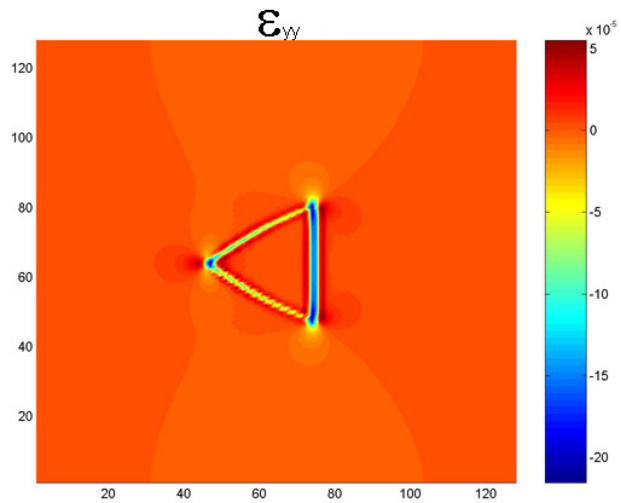

Fig. 3.12. $LiTaO_3$: ϵ_{yy}

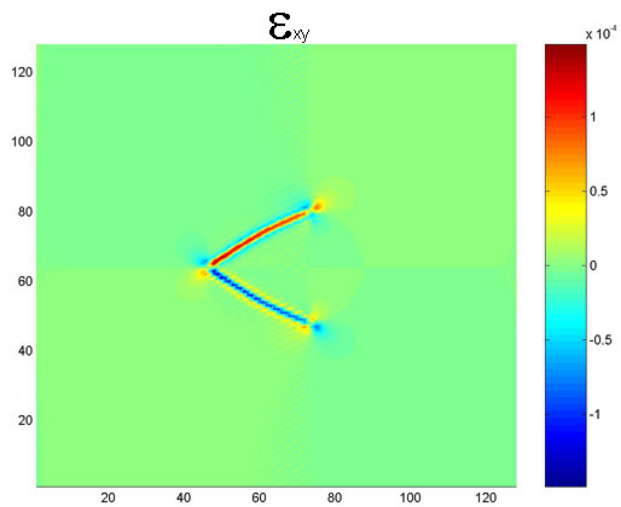

Fig. 3.13. $LiTaO_3$: ϵ_{xy}

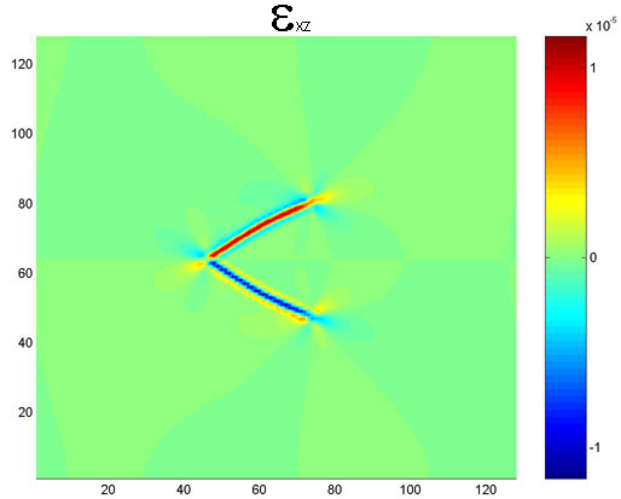

Fig. 3.14. $LiTaO_3$: ϵ_{xz}

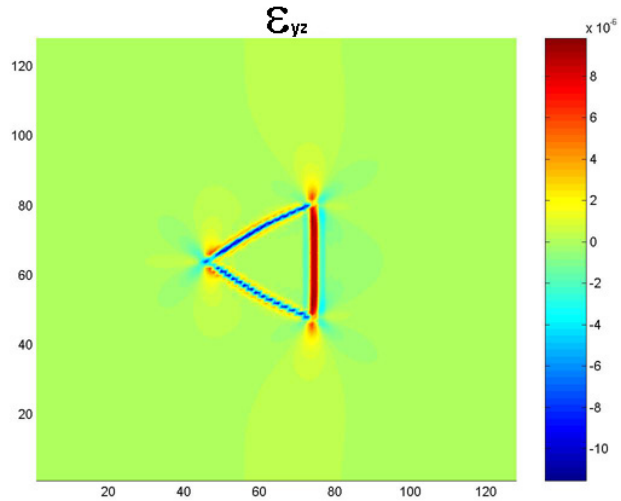

Fig. 3.15. $LiTaO_3$: ϵ_{yz}

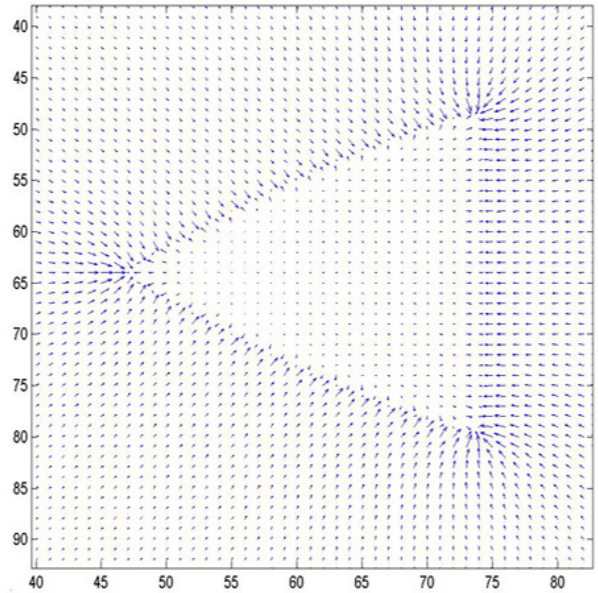

Fig. 3.16. $LiTaO_3$: In plane displacement

field was turned off to stop the domain growth. The strain and the displacement information is then saved. If only the isotropic gradient energy term is used, only circular domain pattern is observed, since the minimum free energy can be achieved through an isotropic circular domain pattern. Only after including higher order anisotropic gradient energy terms, one can regenerate triangular and hexagonal domain patterns. It implies that in 180° domain system, gradient energy is dominant in determining domain wall orientations.

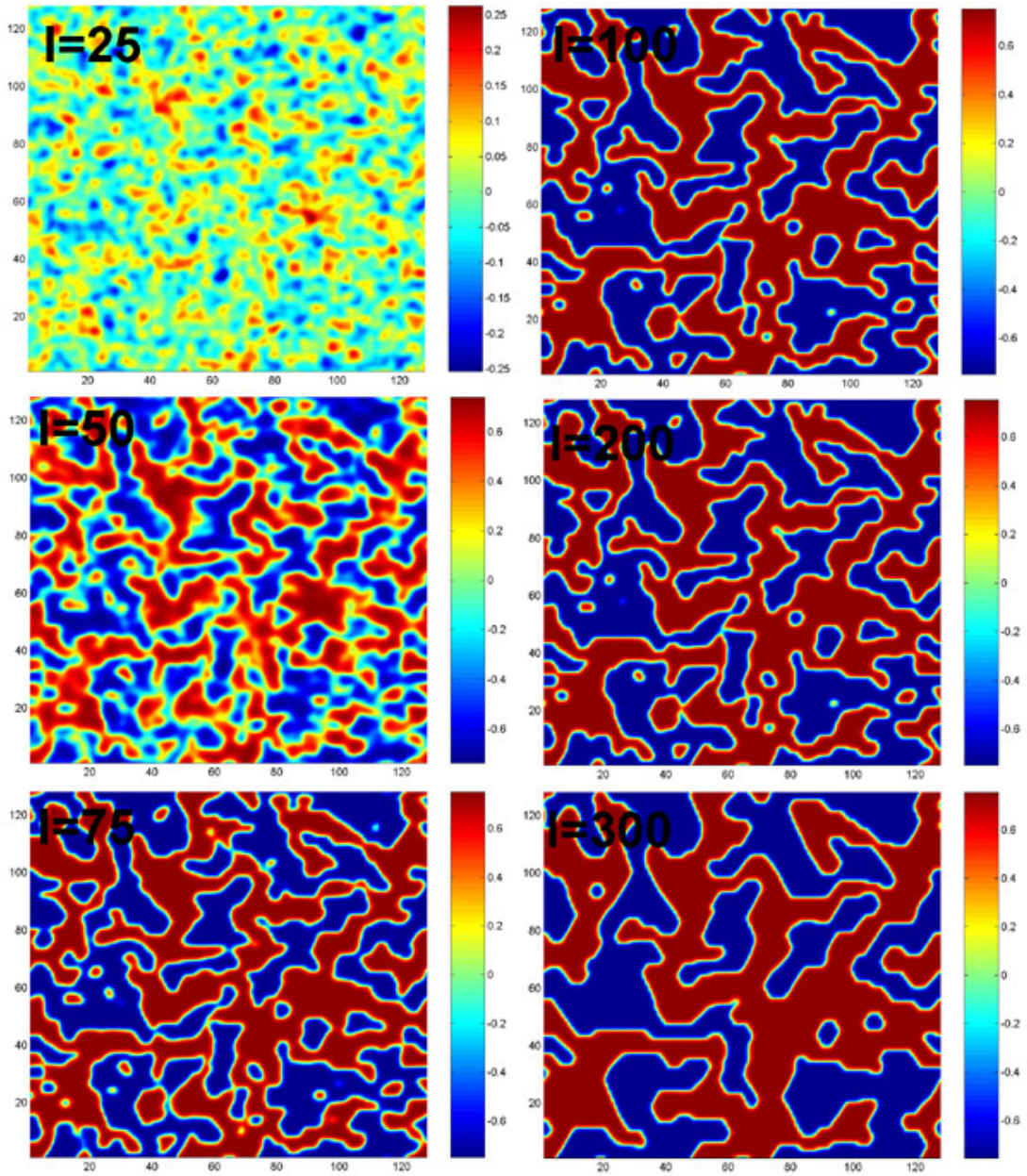

Fig. 3.17. $LiNbO_3$ pattern formation from random nucleation. The number labeled I is the iteration number. From left top to right bottom I=25, 50, 75, 100, 200, 300

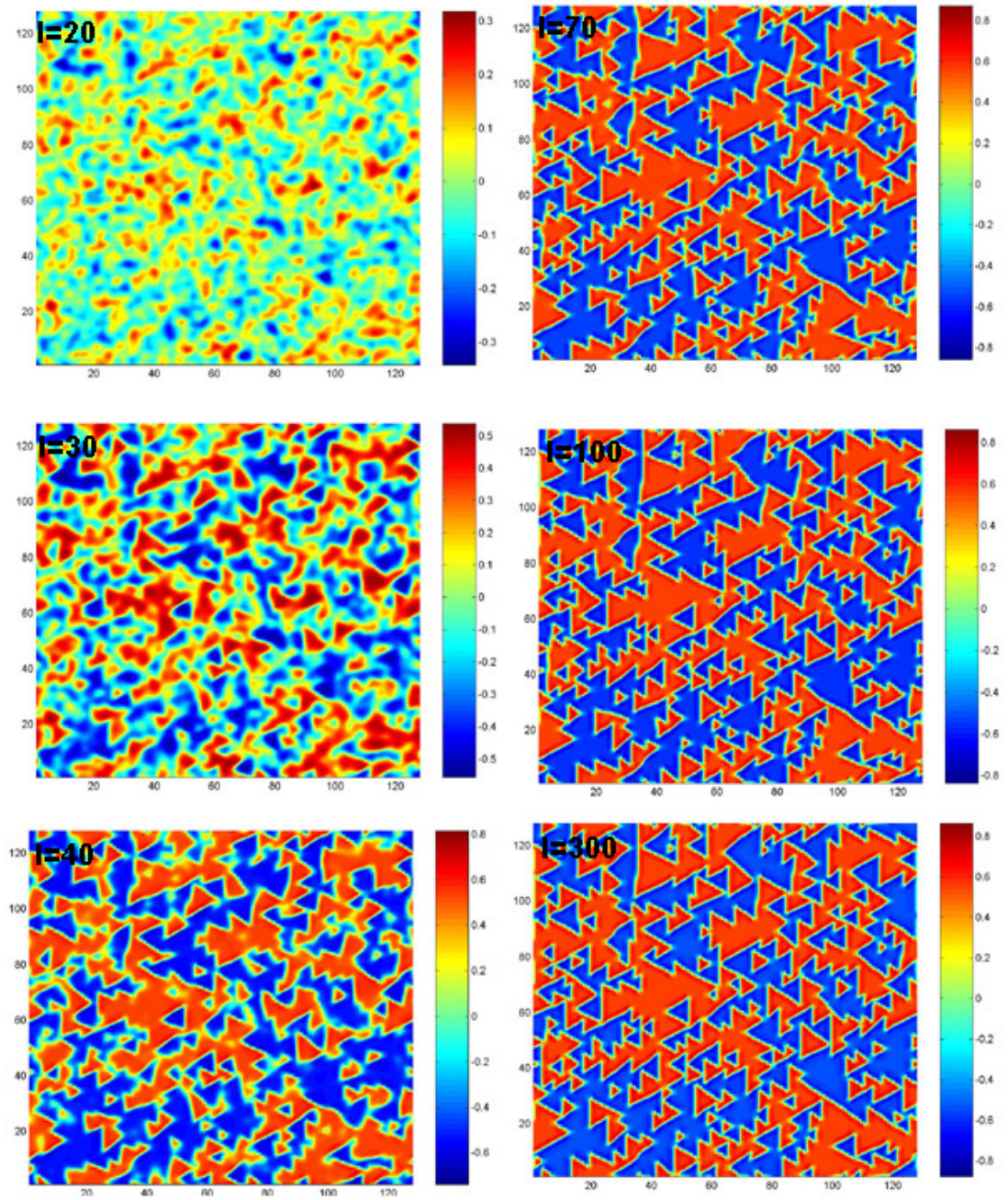

Fig. 3.18. $LiTaO_3$ pattern formation from random nucleation I is iteration number. From left top to right bottom I=20, 30, 40, 70, 100, 300

Figure 3.17 and 3.18 shows how domain pattern is formed from random nucleations *without* any external field in $LiNbO_3$ and $LiTaO_3$ crystal, respectively. This therefore reflects a steady-state configuration without external bias. In $LiNbO_3$, arbitrary growing domain pattern, both positive and negative domain has a same preferred domain wall direction. But in $LiTaO_3$ crystal case, the domain pattern appears inverted between positive and negative domains (see the direction of the triangular vertex). The coordinate axes shown in both Fig. 3.1and 3.9 are for the positive domain area. If this area is inverted to a negative domain, then the coordinate system should be rotated 180° holding the x-axis constant. Therefore, even though the triangular domain patterns for the two domain states in $LiTaO_3$ looks different, they are actually the same crystallographic orientation.

Figure 3.19 shows the dynamics of how an external field can switch from one domain state to the other domain state. At the beginning, a random domain microstructure is generated before T=300 under zero bias. After T=300, an external electric field of $+5 * 10^7 V/m$ is applied which is preferable to positive domain. Interestingly, while domain switches from one state to the other, the preferred domain wall orientation does not change. It always prefers the triangular shape. Another thing that can be easily noticed is that the wall velocity is not uniform for all domain walls even at a constant external electric field. As an example, a relatively small-sized domain, the walls move faster. For example, the domain labeled **A** in Figure 3.19 is a small island domain. It disappears very quickly as soon as the bias field is applied. This is probably because the displacement fields of the vertices of the triangular domains interact strongly with each other in small domains. For larger domains, the wall velocities may still vary depending on their geometry. Domain wall B has a relatively flat wall shape, and domain wall C has a saw-tooth type shape, formed out of multiple small vertices of domains merged together. It is clear that the type C domain wall moves much faster than the type B wall. This phenomenon has been experimentally observed in lithium tantalate as reported in Ref. [7]. The difference in wall velocities again arises because the triangular ledges formed by intersecting domains for a preferential low energy site for the nucleation of

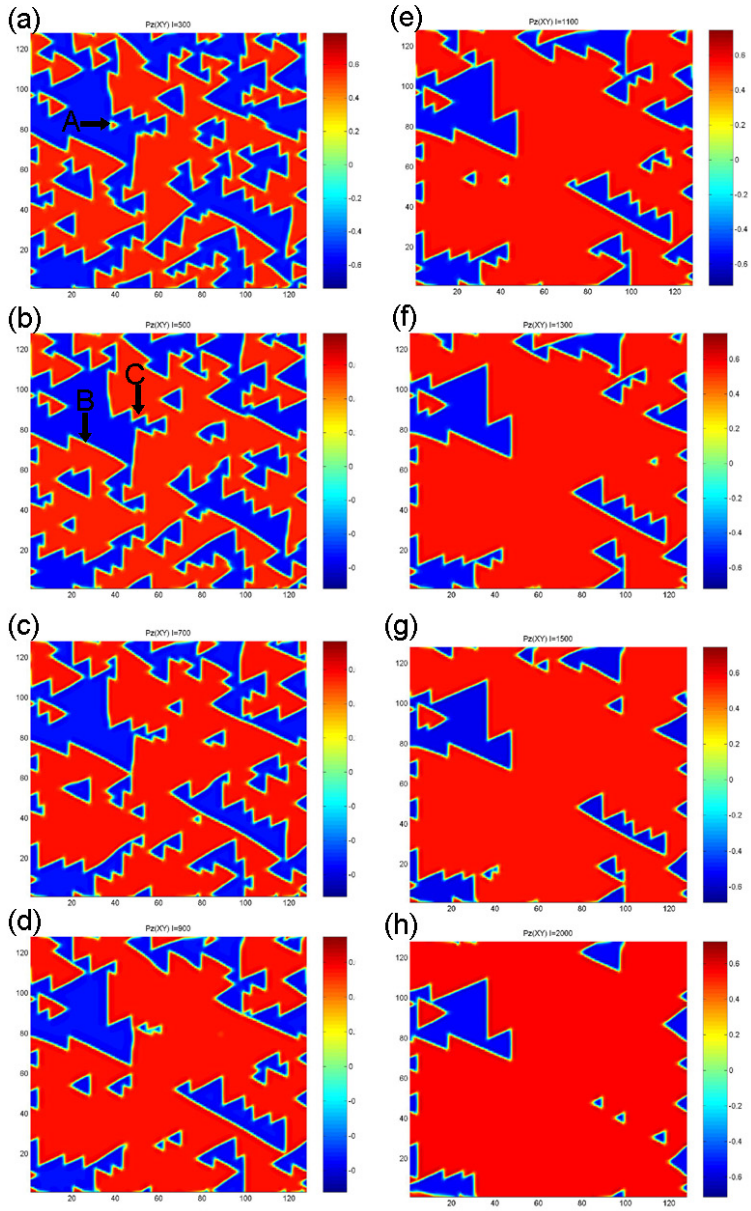

Fig. 3.19. $LiTaO_3$ domain growing by applied exteranl field. From (a) to (h), T=300, 500, 700, 900, 1100, 1300, 1500, 2000, respectively. Before T=300, it transfroms from a random domain state to a stable equilibrium condition. For T>300 the external field turned on to grow domain.

further domains, as compared to a flat domain surface. Larger the number of ledges, larger the degree of serration, and faster the overall wall front moves forward.

In conclusion, we have developed a 3D TDGL code and successfully regenerated hexagonal $LiNbO_3$ and triangle $LiTaO_3$ domain shapes by using higher order non-isotropic gradient energy terms. By simulating the growth of a single domain, we get the detailed strain distribution around the domain wall and the corners of a domain. In addition, external fields are applied and the wall dynamics observed and compared qualitatively with experiments.

References

[1] M. E. Lines and A. M. Glass. *Principles and Applications of Ferroelectrics and Related Materials*. Clarendon, Oxford, 1977.

[2] S. Nambu and D. A. Sagala. *Phys. Rev. B*, 50:5838, 1994.

[3] H. L. Hu and L. Q. Chen. *Materials. Science. Engineering*, A238:182, 1997.

[4] S. Xie W. Cao, S. Tavener. *J. Appl. Phys*, 86:5793, 1999.

[5] R. Ahluwalia and W. Cao. *Phys. Rev. B*, 63:012103, 2001.

[6] W. Cao and L. E. Cross. *Phys. Rev. B*, 44:5, 1991.

[7] V. Gopalan and T. E. Mitchell. *J. Appl. Phys.*, 85:2304, 1999.

Chapter 4

Local Strains at a Domain Wall

4.1 Static image

This chapter discusses the imaging and simulation of local strains at individual 180° domain walls in lithium niobate. The technique of x-ray topography, using a synchrotron source is used. Xray topography is simply x-ray pictures. It can be in transmission (Laue) or reflection (Bragg) imaging geometries, depending on which diffracted beams are studied. Usually, x-ray penetration depth is very small,(order of 10 μm) [1] since it has a strong absorption in most materials; therefore transmission mode is not usual in normal x-ray experiments which are instead performed in Bragg geometry. However, under specific conditions, called *Borrmann effect*, x-ray can be transmitted through millimeter distances through the material. X-ray diffraction occurs only when Bragg condition for wavevector matching is satisfied. Therefore, defects or strain inside the crystal, or distortions of the lattice planes on the surface of the crystal are easily imaged by x-ray topography as the changes in the diffracted beam intensity. The sensitivity of this technique depends on the parallelism of the x-ray beam as well as the camera resolutions. Traditionally x-ray topography used laboratory x-ray sources, but the best images are now obtained using synchrotron source. Synchrotron source has a very high brightness, and can be made to have very low beam divergence (1 arc second), both of which are important for topography. The small divergence provides a lattice strain sensitivity of 10^{-4}. X-ray topography was performed on 500μm thick $LiTaO_3$ and $LiNbO_3$ crystals in two places: Beam Line X-21 at Brook Haven National Laboratory and 1-ID and 4-ID beamlines of the SRI-CAT at the Advanced Photon Source, Argonne National Laboratory. Images were taken in both transmission (Laue) and reflection (Bragg) geometries. In both geometries, a strong contrast was observed around the domain walls, as well as detailed crystal imperfections such as

dislocations and grain boundaries were imaged. Detailed experimental preparation and results will be described in Section 4.1.1 and Section 4.1.2. These images have been analyzed here by beam tracing methods based on x-ray dynamical theory [2] and Eikonal theory [3].

4.1.1 Reflection geometry

The starting crystal is in a single domain virgin state. It is then is partially polarized (forward poled) by using uniform water electrodes at room temperature. X-ray reflection image shows unusually strong and broad domain image. Figure 4.1 shows symmetrical (0,0,.,12) plane and asymmetrical (1,0,.,10)Bragg geometry image of the 1cm×1cm $LiNbO_3$ crystal image, taken in Brookhaven National Laboratory. The beam size was 1cm by 1 cm and the beam divergence was less than 1 arc second. The image was collected using a high resolution silver halide film, with a lateral resolution of 1μm. One observes low angle grain boundaries A and B in Fig 4.1 as shown by arrows. Using the rocking curves, the grain misorientation with respect to the (0,0,.,12) planes is estimated to be only few 10^{-3} degrees. This is seen by the series of images shown in Fig 4.2, taken with a difference in incident angles of 3×10^{-3} degrees as can be seen in Fig 4.2. However, one notices that domains and domain walls cut across such a low angle boundary. The role of grain boundary is related to nucleation and pinning of domain walls.

To analyze the detailed strain information around a domain wall, z-cut crystal with a thickness of 0.5 mm were used to study reflection from stable domains with zero applied field. A series of (0,0,.,12) Bragg reflection images are shown in Fig. 4.3 for three slightly different angles of incidence. The ferroelectric polarization direction, P_s inside the hexagonal domains is in the +z direction (outward normal to image plane in Fig. 4.3) and in the -z direction in the matrix domain(outside the hexagonal domains).

There are three mechanisms which contribute to the visibility of ferroelectric domains in congruent $LiNbO_3$: a) the difference in the structure factor between the antiparallel domains and the surrounding completely polarized single crystal matrix, b) any difference in the lattice spacing in the volume of diffraction, and c) distortions

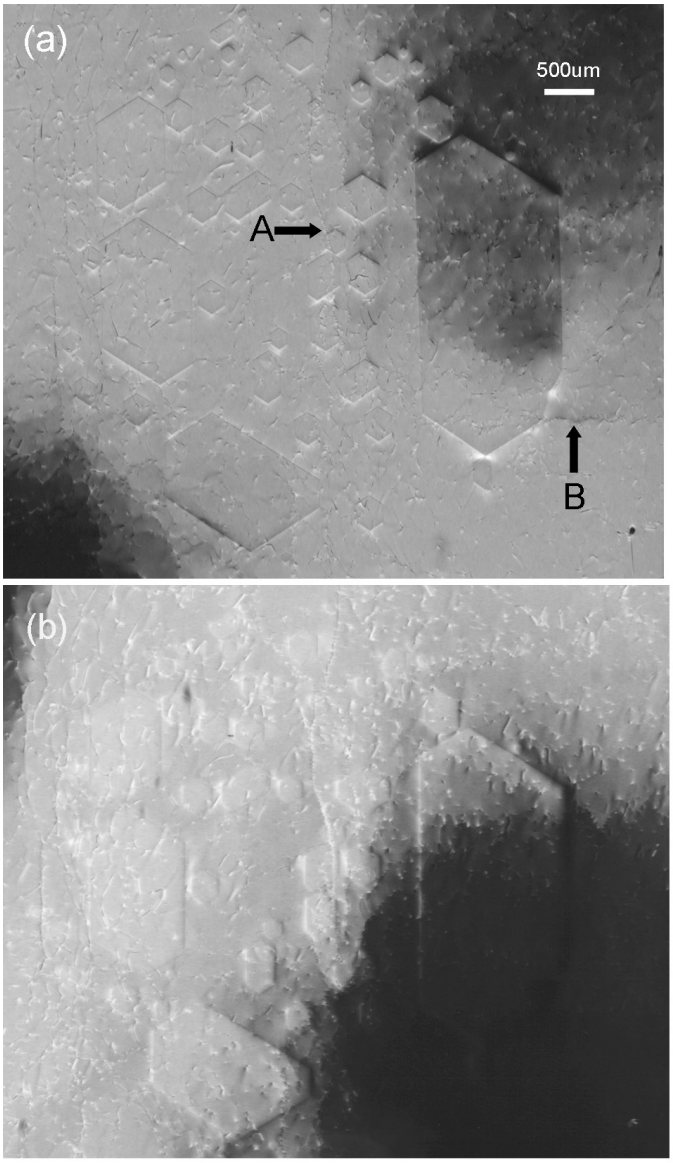

Fig. 4.1. Bragg Geometry (a) is (1,0,.,10) asymmetric reflection plane, and (b) is (0,0,.,12) symmetrical reflection plane.

of the bulk resulting in a displacement of the surface normal from the ordinary crystallographic axis. The presence of lithium vacancies and niobium antisite defects in the congruent material give rise to a remnant internal field such that the antiparallel domain is not simply a symmetry inversion of the polarized matrix [4]. One can estimate the

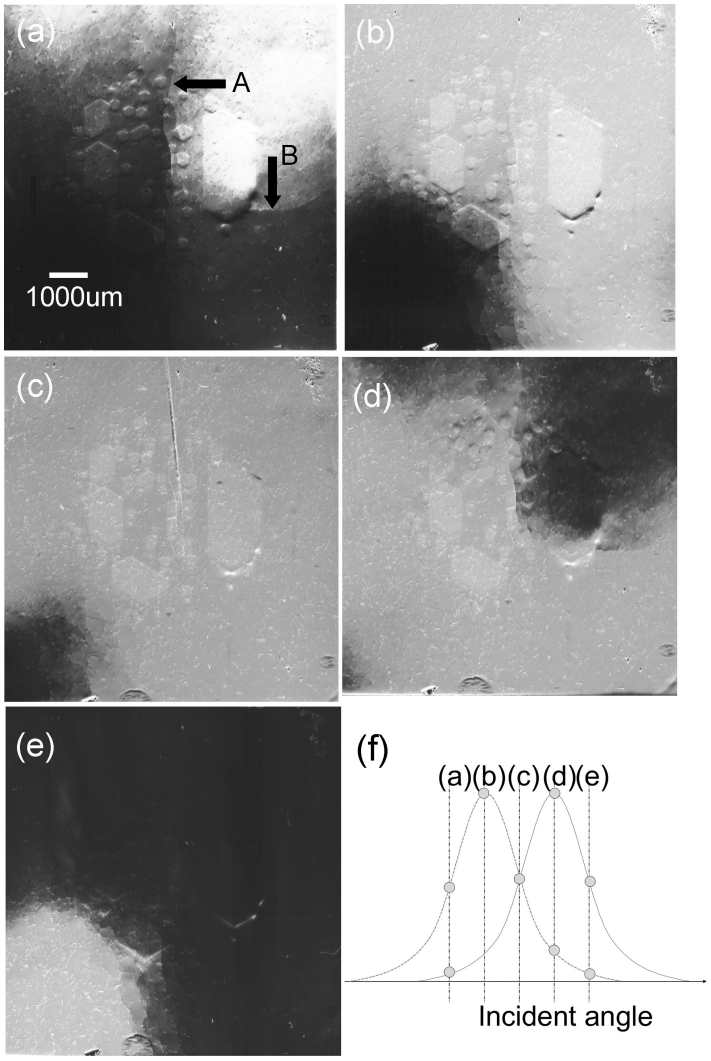

Fig. 4.2. (0,0,.,12) plane rocking image of $LiNbO_3$ crystal in Bragg geometry is shown from (a) to (e). Frame (f) shows a schematic of the rocking curves. Left rocking curve corresponds to top right area which is enclosed by low ngle boundaries A and B. The right rocking curve corresponds to the rest of the area. $\Delta\theta$ between successive rocking curve images is 0.003°. Incident angle positions from (a) to (e) frames are marked in (f).

contribution to Bragg intensity contrast due to the different structure factors between reversed domains in congruent $LiNbO_3$.

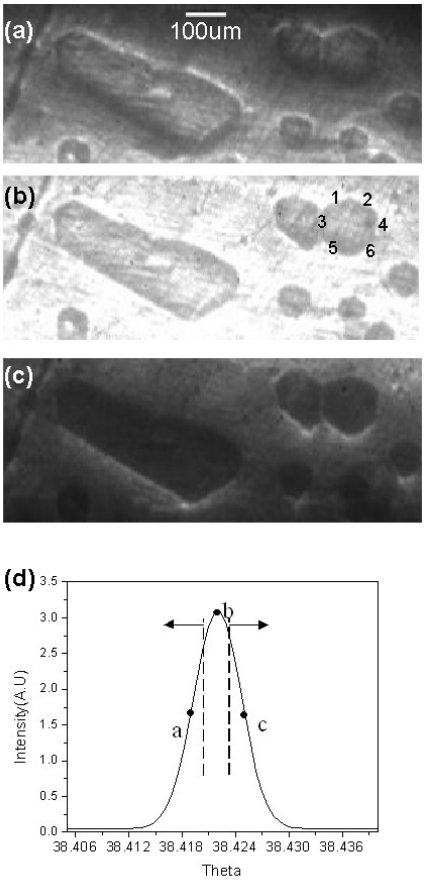

Fig. 4.3. (a) Bragg topograph of $LiNbO_3$ crystal at position 'a' (θ_B-0.003) on the (0,0,.,12) rocking curve; (b) Bragg topograph of $LiNbO_3$ crystal at position 'b'(θ_B) on the (0,0,.,12) rocking curve; (c) Bragg topograph of $LiNbO_3$ crystal at position 'c' (θ_B + 0.003) on the (0,0,.,12) rocking curve; (d) (0,0,.,12) Bragg rocking curve for $LiNbO_3$ sample crystal, arbitrary intensity as a function of nominal goniometer Bragg angle (calculated θ_B=39.0). The region to the left of the left dashed line corresponds to the observation of bright borders at walls 1 and 2; the region to the right of the right dashed line corresponds to bright borders at walls 5 and 6. These pictures were taken at on Argonne Photon Source

For the (0,0,.,12) and (0,0,.,$\overline{12}$) reflections at 8.5 keV, this difference is 9 percent. The remaining contrast between domains and their surrounding matrix is evidently the result of surface distortions and changes in the lattice spacing. Figure 4.3(b) corresponds to the reflection at the Bragg peak. The rocking curve of the reflection is shown as a

function of the nominal value of the Bragg angle from the goniometer in Fig. 4.3(d) (the calculated Bragg angle at this energy was θ_B= 39.0°). Figs. 4.3(a,c) show the topograph in the crystal region (area 1 mm×2 mm) when the crystal is rocked about the diffraction peak. The measured full width at half-maximum (FWHM) of the rocking curve, which included the distortion effect of domains, was $\Delta\theta_B$=0.0063° =110μrad. The incidence plane in the image is vertical, being parallel to the crystallographic y-axis. From Fig. 4.3(a) to (c), we rotated the sample through 0.006° in steps of $\Delta\theta_B$=0.0005° towards increasing incidence angles. The wall types 1,2,5, and 6 (labeled in Fig. 4.3(b)) in every hexagonal domain are not parallel to the incidence plane, and show an enhanced contrast over a wide region (10 μm wide) of associated strain. The wall types 3 and 4, on the other hand, are parallel to the incidence plane and show the least contrast. This contrast phenomenon reveals itself more clearly on moving away from the Bragg peak, and suggests a curvature of lattice planes in the wall region in going from one domain to the other that can be described by the strain component dz/dn, where n is the coordinate normal to a wall and z is the coordinate along the direction of ferroelectric polarization (normal to the image plane in Fig. 4.3). Such a wall curvature would be expected to cause a deviation of the incidence angle, θ from θ_B and influences the Bragg diffraction condition most strongly when the wall is perpendicular to the incidence plane, and least when the wall is parallel to the incidence plane. This is consistent with the experimental observations in Fig. 4.3.

A closer inspection reveals that the contrast of the set of walls (1,2) is opposite to the contrast of the set of walls (5, 6). That is, if one set of walls (1,2), is bright, the other set (5,6) is dark (seen in Fig. 4.3(a) and conversely, Fig. 4.3(c)). The projections of the incident and diffracted X-ray wavevectors onto the image plane of Fig. 4.3 point in the -y direction with respect to the domain. In Fig. 4.3(a), the local region near domain walls (1,2) would appear to be closer to the Bragg diffraction peak, thus making them bright, as compared to domain walls (5,6), which are farther from the Bragg peak, giving them a darker contrast. This situation is reversed in Fig. 4.3(c). This provides additional evidence for the domain wall curvature, which we now proceed to estimate. The maximum in the Bragg peak of an average region (predominantly strain-free regions

away from the walls) corresponds to Fig. 4.3(b). However, the Bragg peak for the local region near walls (1,2) corresponds approximately to Fig 4.3(a) and that for walls (5, 6) corresponds approximately to Fig. 4.3(c). Knowing the difference between the Bragg angles between these frames, we therefore estimate that the $\Delta\theta_B$(1,2)=θ_B(1,2)-θ_B(center)=-0.0030° ± 0.0015° and similarly, θ_B(5,6)=+0.0030° ± 0.0015°. Converting these angles to radians, and neglecting the angle the domain walls make with the incidence angle, we therefore very roughly estimate the shear strain at these domain walls as $\epsilon_{zn} \approx \Delta\theta_B$, where z is positive along the outward normal to the image plane in Fig. 4.3, and n is the outward normal (pointing into the matrix domain) to the domain wall in the image plane.

In $LiNbO_3$, the domain walls are parallel to the crystallographic y-axis ([$1\bar{1}00$] direction), and therefore, the observed shear strain is ϵ_{zx}. Therefore, ϵ_{zx}(1 and 2)≈ -5.2×$10^{-5} \pm 2.6\times10^{-5}$ and ϵ_{zx}(5 and 6)≈ $+5.2\times10^{-5} \pm 2.6\times10^{-5}$. Given that Δx 10$\mu$m is the approximate strain width in the image plane observed in Fig. 4.3, the displacement observed is given by Δz=$\epsilon_{zx}\delta x$ ≈0.5 nm. This implies that when viewing the +z face of the matrix domain, the region inside the hexagonal domains (with polarization along -z) is raised by 0.5 nm in height with respect to the oppositely polarized surrounding matrix region. This is also consistent with a similar surface step across a domain wall observed using near-field optical microscopy (NSOM) in the isostructural $LiTaO_3$ crystals [5]. X-ray imaging of the -z face of the matrix domain was not performed. However, from NSOM studies, the other face (corresponding to the -z of the matrix domain and +z of the hexagonal domain) in the isostructural $LiTaO_3$ appears to show a depression of ≈0.5 nm inside the hexagonal domain area. In a cross-section of the crystal, therefore, the inverted hexagonal domain region would appear to have shifted through the entire thickness giving rise to a 0.5 nm step projection on the +z face of the matrix domain and a depression on the -z face of the matrix domain.We finally note that the large observed x-ray strains in congruent composition lithium niobate under no external fields are a result of the interaction of point defect complexes with the domain wall.

4.1.2 Transmission (Laue) geometry

In this section, the well-developed theory of dynamical x-ray transmission will be first reviewed. The goal will be to develop expressions for the intensity of diffracted beams inside the crystal within a two-beam approximation. Next, transmission of xray through a strained lattice will be presented, and necessary theoretical development for tracking xrays propagating through domain walls in transmission geometry will be derived. The following section will then describe the experimental results and the simulation of these results based on the developed theory.

4.1.2.1 Dynamical theory of x-ray diffraction in perfect lattice in Laue geometry

X-ray transmission topography images are more complex and contain more information than reflection topography, because x-ray penetrates the whole thickness direction of the crystal through the anomalous effect described below. To understand this transmission image, dynamical x-ray theory becomes an essential tool. If the crystal thickness is thin enough to consider just the first scattering event, then *kinematical theory* can explain most of the phenomena. Unlike the simple x-ray diffraction case, x-ray beam inside the crystal shows dynamical interaction with the material in an exact Laue condition. If the crystal is thick (compared with the absorption depth), x-ray beams experience multiple scattering with transfer of energy from one scattered beam to the other. Figure 4.1 shows a schematic of this dynamical two beam interaction inside perfect crystal. If we just think of two beams, let's say Ψ_o and Ψ_h inside crystal, the intensity wavefield will be

$$|\Psi|^2 = |\Psi_o|^2 + \left|\Psi_h\right|^2 + 2\left|\Psi_o\Psi_h\right| cos2\pi(\mathbf{h}\cdot\mathbf{r} + \phi) \tag{4.1}$$

where, Ψ_o is the refracted wave with wavevector K_o, and Ψ_h is the reflected wave with wavevector K_h. The term ϕ is the phase of E_h/E_o. The term $cos2\pi(\mathbf{h}\cdot\mathbf{r} + \phi)$ shows that the node is on planes parallel to the lattice and their periodicity is equal to the distance $1/h = d_{hkl}/n$, which is the periodicity of the (hkl) family of lattice planes. The nodes of standing wave can lie on the atomic plane or between atomic plane. When node is

located on atomic plane, this standing wave can have very low loss. This is how the two beams of X-rays can propagate with a very low loss through the crystal, which is called the *Borrmann effect*. This can be seen schematically on Fig 4.4.

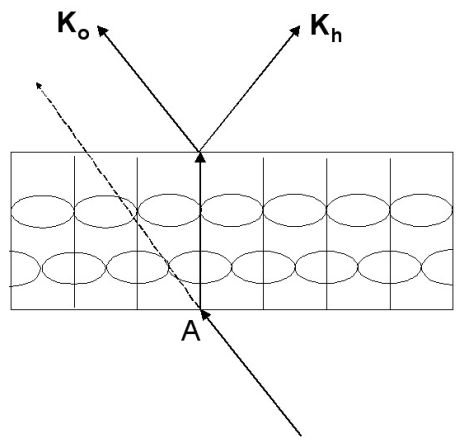

Fig. 4.4. Borrmann effect: The standing wave nodes lie on the atomic planes or antinode located on atomic planes. Former has a very low absorption.

This dynamical x-ray process has a well-established theoretical basis, with several good books, and review papers [6], [7], [2], [8]. In this section, we first describe the theory of how x-ray beam interacts inside a perfectly periodical crystal, and how this process is affected by small amount of the strain using Eikonal theory. More detailed discussion will be found in references [6], [7], [2], [8]. The staring point is Maxwell's equations, since x-ray is an electromagnetic wave. This derivation is very similar to the band theory in solid-state physics. By solving the Maxwell's equation inside periodic atomic structures, a dispersion relation ship between the energy and momentum for the x-ray beam can be derived. In a neutral crystal, the local *free* electric charge and current density are equal to zero. Then the Maxwell's equation inside a crystal becomes

$$\nabla \times \mathbf{H} = \frac{\partial \mathbf{D}}{\partial t} \tag{4.2}$$

$$\nabla \times \mathbf{E} = -\frac{\partial \mathbf{B}}{\partial t} \tag{4.3}$$

$$\nabla \bullet \mathbf{D} = 0 \tag{4.4}$$

$$\nabla \bullet \mathbf{B} = 0 \tag{4.5}$$

Terms E and H are electric field and magnetic fields, respectively. Terms D and B are displacement field and magnetic flux, respectively. If an electromagnetic wave, E(r)exp(-$2\pi i\nu$t), is propagating in a material, (ν is the frequency), the medium is polarized under the influence of the electric field creating a dielectric displacement, D in the material where E=D/ϵ, and ϵ=ϵ_0(1+χ) varies with spatial coordinates, r. (χ is the dielectric susceptibility). By eliminating D, H, and B in Maxwell's equations 4.2,4.3,4.4,4.5, the wave equation is obtained.

$$\nabla \times \nabla \times \mathbf{E} - 4\pi^2 k^2 (1 + \chi)\mathbf{E} = 0 \tag{4.6}$$

Since the index of refraction for x-rays in a material is very close to 1, (typical index values of 1-10^{-5}), it is reasonable to assume that there is a continuity of both the normal and the tangential components of **D** across any interface through which x-ray traverses. Since index $n^2 = \epsilon_0/\epsilon$, the susceptibility, χ is very small and lightly negative -10^{-5} for x-rays, and the electric field can be written, to a first approximation, as

$$\mathbf{E} = \frac{\mathbf{D}}{\epsilon_0(1+\chi)} = \frac{\mathbf{D}}{\epsilon_0}(1-\chi) \tag{4.7}$$

By using this approximation and eliminating H, one can get the propagation equation,

$$\Delta \mathbf{D} + \nabla \times \nabla \times \chi \mathbf{D} + 4\pi^2 k^2 \mathbf{D} = 0 \tag{4.8}$$

where $\Delta = \nabla^2$. As an analogy, for electrons and neutrons in periodic solids, the propagation equation of particle waves is the Schrodinger's equation, which can be written as

$$\Delta\Psi + 4\pi^2 k^2 [1 + \chi(\mathbf{r})]\psi = 0 \tag{4.9}$$

It can be easily shown that Eq. 4.8 can be reduced to Eq. 4.9 as a scalar approximation. This scalar approximation is posiible, because there is no interaction between different field component. Because this equation is a linear, homogeneous, partial differential equation, Ψ can be represented as

$$\Psi = \sum_j A_j D_j \tag{4.10}$$

The choice of the solution and the values of the coefficient A_j can be determined by boundary conditions for the problem. Even though it is based on a scalar approximation, the results hold separately for each direction of polarization of incident X-ray wave in a *two-beam case*. Polarization is taken into account by multiplying the Fourier coefficients χ_h and $\chi_{\bar{h}}$ of the polarizability (notation described further below) by a factor C, which equals to 1 for σ-polarization(X-ray is perpendicular to incident plane) and cos2θ for π-polarization(X-ray is parallel to incident plane). The wavefunction, Ψ can be written as

$$\Psi(r) = \sum_h \Psi_h exp(-2\pi i \mathbf{K}_h \cdot \mathbf{r}) \tag{4.11}$$

with

$$\mathbf{K}_h = \mathbf{K}_o - \mathbf{h} \tag{4.12}$$

Equation 4.11 shows that the wave field is a sum of plane waves whose wavevectors can be deduced from one another by a translation in the reciprocal space. In the two beam case, there are two waves in the wavefield, Ψ_o and Ψ_h. Wavevector K_o and K_h, as well as lattice reciprocal lattice, h are defined in Fig. 4.5 Far from the interaction of the two sphere, there is only one wave propagating in the crystal. When it lies on the connecting surface, there are two waves and their wave numbers are slightely different from nk(length of L_oO;n is refraction index and k is vaccume wavelength). This surface is called dispersion surface. L_a is called Laue point, and L_o is called Lorentz point. Laue point is for the pure air case, while the Lorentz point is for the case theof a negative refraction coefficient as seen by Xrays. The P point has been called the tie point by Ewald to stress that the two waves are closely linked together to form wavefield. Because the

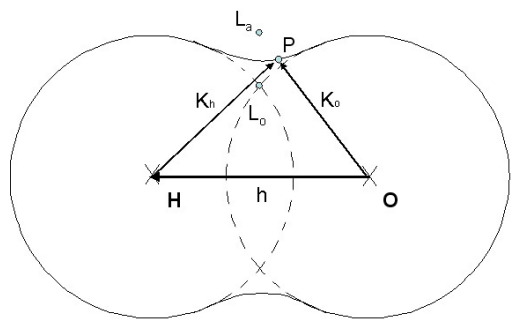

Fig. 4.5. Interaction of the refracted(OP) and incident (HP) waves. Solid curve:dispersion surface; P:tie point

crystal is a periodic medium, we can express χ as a Fourier series,

$$\chi = \sum_h \chi_h exp(2\pi i \mathbf{h} \cdot \mathbf{r}) \tag{4.13}$$

$$\chi r = \sum_h \chi_{rh} exp(2\pi i \mathbf{h} \cdot \mathbf{r}) \tag{4.14}$$

$$\chi_i = \sum_h \chi_{ih} exp(2\pi i \mathbf{h} \cdot \mathbf{r}) \tag{4.15}$$

Here the subscripts r and i represent real and imaginary parts. The solution of the propagation equation is obtained by substituting Eq.4.13 and Eq.4.11 into Eq.4.9.This gives

$$\Delta\Psi = -4\pi^2 \sum_{\mathbf{h}} K_h^2 \Psi_h exp(-2\pi i(\mathbf{K_h} \cdot \mathbf{r})) \tag{4.16}$$

The product $\chi(r)\Psi(r)$ can be written as

$$\chi(r)\Psi(r) = \left[\sum_{\mathbf{g}} \sum_{\mathbf{h'}} \chi_g \Psi_{h'} exp(2\pi i(\mathbf{g} + \mathbf{h'}) \cdot \mathbf{r})\right] exp(-2\pi i(\mathbf{K}_o \cdot \mathbf{r})) \tag{4.17}$$

The vector $\mathbf{g}$ and $\mathbf{h}'$ are reciprocal lattice vectors and their sum $\mathbf{g} + \mathbf{h}' = \mathbf{h}$ is also a reciprocal lattice vector. Therefore, we can simplify the above as,

$$\chi(\mathbf{r})\Psi(\mathbf{r}) = \sum_{\mathbf{h}} exp(-2\pi i(\mathbf{K_h} \cdot \mathbf{r})) \sum_{\mathbf{h}'} \chi_{h-h'}\Psi_{h'} \tag{4.18}$$

By combining Eq.4.16 and 4.18 into 4.9, the final propagation equation is obtained.

$$\sum_{\mathbf{h}} \left[-4\pi^2 K_h^2 \Psi_h + 4\pi^2 \Psi_h + 4\pi^2 k^2 \sum_{\mathbf{h}'} \chi_{h-h'}\Psi_{h'} \right] \times exp(-2\pi i(\mathbf{K}_h \cdot \mathbf{r})) = 0 \tag{4.19}$$

If both sides are multiplied by $exp(2\pi i(\mathbf{K}_h \cdot \mathbf{r}))$ and integrated over the space coordinates from $-\infty to + \infty$, then all the terms in the sum but one vanish, and the final *fundamental equation of dynamical theory* is obtained.

$$\Psi_h = \frac{k^2}{K_h^2 - k^2} \sum_{\mathbf{h}'} \chi_{h-h'}\Psi_{h'} \tag{4.20}$$

It is easy to see that the resonance factor in Eq. 4.20 goes to infinity when k=K_h. This is called the *Ewald condition*. Let us carefully check this solution. Under experimental conditions, if only one resonance term is very large, Eq. 4.20 reduces to

$$\Psi_h = \frac{k^2}{K_h^2 - k^2} \chi_o \Psi_h \tag{4.21}$$

To get nontrivial solution $K_h^2 = k^2(1+\chi_o)$ should be satisfied. Since χ_o <<1, one can write $K_h = k(1 + \frac{\chi_o}{2})$. If two resonance terms are very large and two nodes lie simultaneously on the Ewald sphere, Eq.4.20 becomes,

$$\Psi_o = \frac{k^2}{K_o^2 - k^2} \left[\chi_o \Psi_o + \chi_{\bar{h}} \Psi_h \right] \tag{4.22}$$

$$\Psi_h = \frac{k^2}{K_h^2 - k^2} \left[\chi_h \Psi_o + \chi_o \Psi_h \right] \tag{4.23}$$

where $\chi_{\overline{h}}$ is the Fourier coefficient of the polarizability corresponding to $\overline{h}, \overline{k}, \overline{l}$ reflection. For non-trivial solutions of these linear, homogeneous, equations to exist, the determinant should be zero. Thus the secular equation gives a relation between the lengths K_o and K_h of the field and hence gives the loci of the tie points P and the equation of the dispersion surface, as shown below.

$$\left[\frac{K_o^2-k^2}{2k} - \frac{k\chi_o}{2}\right]\Psi_o - \frac{k\chi_{\overline{h}}}{2}\Psi_h = 0$$

$$-\frac{k\chi_{\overline{h}}}{2}\Psi_o + \left[\frac{K_h^2-k^2}{2k} - \frac{k\chi_o}{2}\right]\Psi_h = 0 \tag{4.24}$$

and let's set

$$X_o = \frac{K_o^2 - k^2}{2k} - \frac{k\chi_o}{2} \tag{4.25}$$

$$X_h = \frac{K_h^2 - k^2}{2k} - \frac{k\chi_o}{2} \tag{4.26}$$

Since $K_h \approx k$, $K_o \approx k$, and $K_h^2 - k^2/2k \approx (K_h - k)$, X_o and X_h can be rewritten as,

$$X_o \approx K_o - \frac{k\chi_o}{2} \tag{4.27}$$

$$X_h \approx K_h - \frac{k\chi_o}{2} \tag{4.28}$$

These X_o and X_h represent the distance of the tie point from original sphere as shown in Fig. 4.5. Substituting Eq.4.27 and Eq. 4.28 into Eq. 4.24 gives Eq. 4.29 and Eq. 4.30.

$$X_o\Psi_o - \frac{k\chi_{\overline{h}}}{2}\Psi_h = 0 \tag{4.29}$$

$$-\frac{k\chi_h}{2}\Psi_o + X_h\Psi_h = 0 \tag{4.30}$$

The determinant of this equation is $X_o X_h - k^2 \chi_{\bar{h}} \chi h/4$, and by equating it to zero, one obtains the secular equation, which is the equation of the dispersion surface, given by

$$X_o X_h = k^2 \chi_{\bar{h}} \chi_h / 4 \tag{4.31}$$

Equation 4.31 is the equation of a hyperbola whose asymptotes are the two lines, T_o and T_h as shown in Fig 4.6.

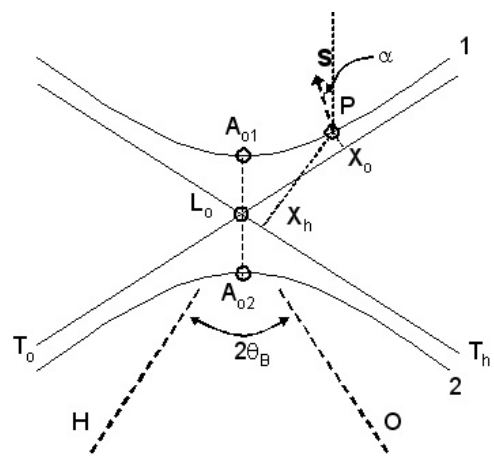

Fig. 4.6. A plot of the dispersion surfaces given by Equation 4.31. Any point P on this surface which is excited by the incoming xray is called the *tie point* of the wavefield. **S** is the Poynting vector that determines the direction of energy flow of the wavefield. X_o and X_h are the coordinates of the excited tie point. A_{o1} and A_{o2} are the vertices of the dispersion surface.

The angle between the asymptotes is $2\theta_B$. The branch of the hyperbola which lies on the same side of the asymptotes as the Laue points O and H, is called branch 1, and the other is called branch 2.

If the *tie point* is on branch 1, the signs of X_o and X_h will be defined as positive and on branch 2 they will be negative. Equation 4.29 and 4.30 can be written in the

following way in order to obtain an expression for the ratio ξ of the amplitude of the two waves (primary and refracted) in the wavefield.

$$\xi = \frac{\Psi_h}{\Psi_o} = \frac{2X_o}{k\chi_{\overline{h}}} = \frac{k\chi_h}{2X_h} \tag{4.32}$$

$$\xi^2 = \frac{\chi_h X_o}{\chi_{\overline{h}} X_h} \tag{4.33}$$

This relation shows that the ratio ξ is determined by the position of the tie point on the dispersion surface, given by X_o and X_h. The expression for the total Poynting vector, **S** which determines the direction of energy flow, will be,

$$\mathbf{S} \propto \mathbf{s_o} \left|\Psi_o\right|^2 + \mathbf{s_h} \left|\Psi_h\right|^2 = \Psi_o^2 \left[\mathbf{s_o} + |\xi|^2 \mathbf{s_h}\right] \tag{4.34}$$

and it's angle , α, with direction with reflecting plane is given by

$$tan\alpha = \frac{1 - \left|\xi^2\right|}{1 + \left|\xi^2\right|} tan\theta_B \tag{4.35}$$

Now based on this important relation, many other interesting relations can be deduced. If the incident angle of the X-ray departs from the exact Bragg condition, the tie point of the incident beam deviates from the center of the hyperbola. Figure 4.7 shows $\Delta\theta$ deviation of the incident beam from the exact Bragg condition. The wave number of incident wave in vacuum is $1/\lambda$ and OM=$K_O^{(a)}$ is the wave vector. The superscript (a) on K_o denotes air. Bragg's condition is exactly satisfied according to the geometrical theory of diffraction when M lies at L_a. The departure $\Delta\theta$ from Bragg's incidence wave is measured by the angle between the corresponding wavevectors **OM** and $\mathbf{OL_a}$. Since $\Delta\theta$ is very small as compared to the Bragg angle in most cases, it is possible to represent $\Delta\theta$ as,

$$\Delta\theta = \frac{\overline{L_a M}}{k} \tag{4.36}$$

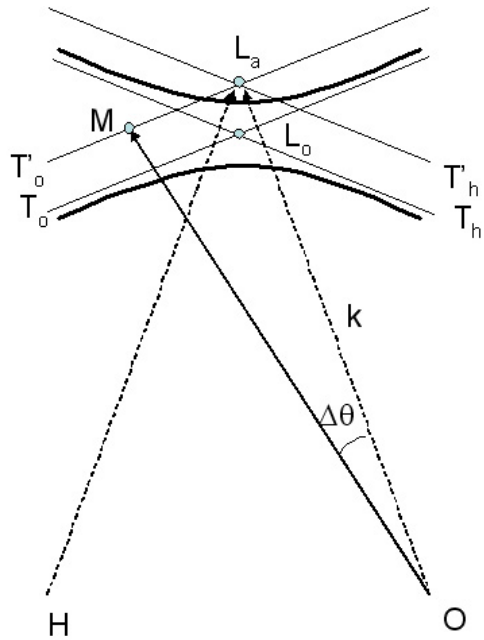

Fig. 4.7. Departure form Bragg's angle of an incident wave: $\Delta\theta = \overline{L_a M}/k$. L_a is the Laue point from exact Bragg matching. $T_o^{'}$,$T_h^{'}$ are the tangents to the spheres with centers O and H and radius k. The primes in the superscript denote the tie lines for vaccum.

To better explain the dynamical theory, the concept of a deviation parameter η is introduced.

$$\eta = \frac{\Delta\theta - \Delta\theta_{OS}}{\delta_{OS}} \tag{4.37}$$

where

$$\Delta\theta_{OS} = \frac{\overline{L_a I}}{k} = -\frac{\chi_o(1-\gamma)}{2sin2\theta_B}$$

$$\delta_{OS} = \frac{C\sqrt{|\gamma|\chi_h\chi_{\bar{h}}}}{sin2\theta_B} = \frac{\lambda}{\Lambda_o}\frac{|\gamma_h|}{sin2\theta_B}$$

$$\Lambda_o = \frac{\lambda\sqrt{\gamma_o|\gamma_h|}}{C\sqrt{\chi_h\chi_{\bar{h}}}} \tag{4.38}$$

Here $\gamma_o = \cos\Psi_o$ and $\gamma_h = \cos\Psi_h$ are the cosines of the angles between the normal to the crystal surface and the incident and reflected directions, respectively, as shown in Figure 4.9. Their ratio, γ, called the asymmetric ratio is given by

$$\gamma = \frac{\gamma_h}{\gamma_o} = \frac{\cos(\Psi_n - \theta_B)}{\cos(\Psi_n + \theta_B)} \tag{4.39}$$

The Ψ_n is explained in Fig 4.8 The factor C=1 (σ-polarization) or C=cos2θ_B (π-polarization).

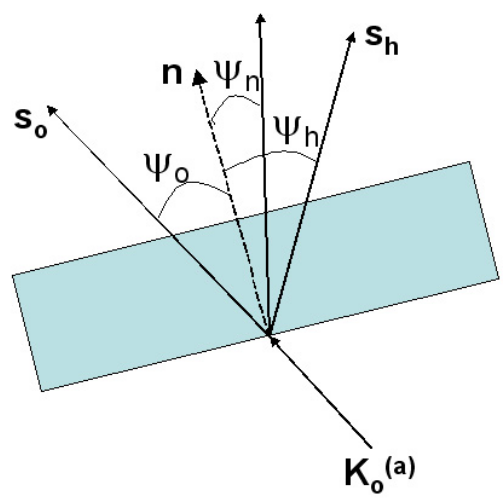

Fig. 4.8. Definition of angle Ψ_n. n is surface normal vector

Point I is at the intersection of the normal to the crystal surface (drawn from the Lorentz point, L_o,) with the asymptote T_o'. Now, as a next stage, tie point should be determined by the incident beam condition. Figure 4.7 shows the excitation point M. By using crystal surface normal vector **n** and initial excitation point M, the excitation points P_1, and P_2 on dispersion curve are determined as can be seen in Fig 4.9.

$$X_{oj} = k\frac{S(\gamma_h)}{2\sqrt{|\gamma|}}\left[\gamma_h\gamma_{\bar{h}}\right]\left[\eta \pm \sqrt{\eta^2 + S(\gamma_h)}\right] \tag{4.40}$$

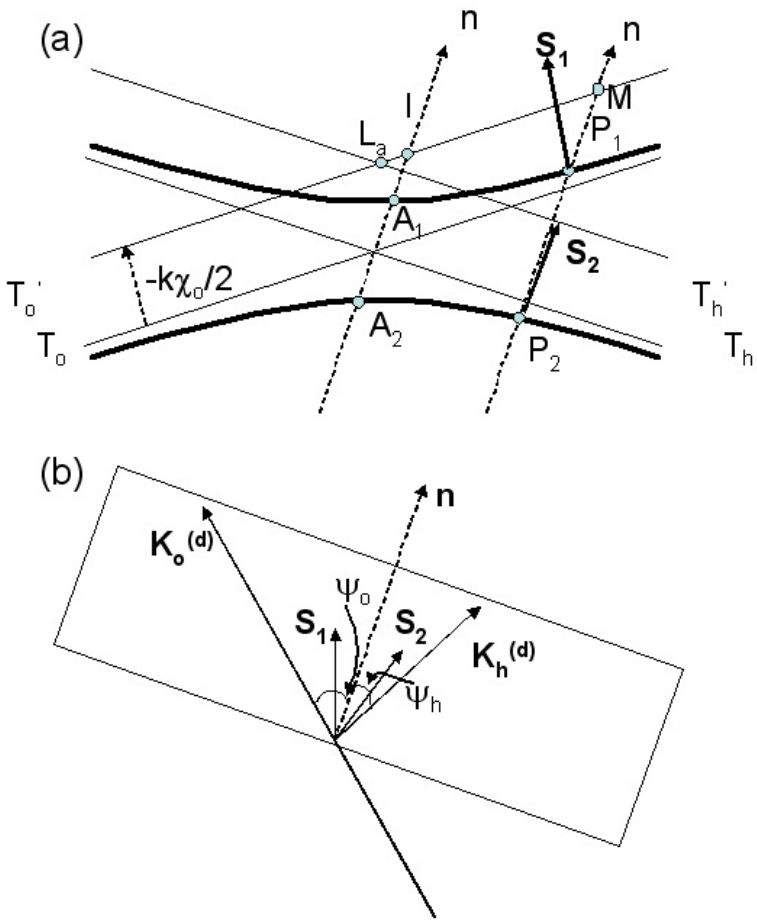

Fig. 4.9. Wavefield created inside crystal by the incident wave. M is excitation point, **n** is normal crystal surface, P_1 and P_2 is tie point, and S_1 and S_2 is Poynting vector. (a) is reciprocal space, and (b) is real space.

Where the plus sign corresponds to a tiepoint on branch 1(j=1) and the minus sign to a tie point on branch 2(j=2). S(γ_h) means sign of γ_h (+1 for transmission and -1 for reflection). The ratio ξ_j of the amplitude of the waves of the corresponding wavefields

is related to their coordinates by Eq4.32 and is

$$\begin{aligned}\xi &= \frac{\Psi_{hj}}{\Psi_{oj}} \\ &= \frac{S(\gamma_h)}{\sqrt{|\gamma|}} \frac{\sqrt{\chi_h \chi_{\bar{h}}}}{\chi_{\bar{h}}} \left[\eta \pm \sqrt{\eta^2 + S(\gamma_h)}\right]\end{aligned} \tag{4.41}$$

If this crystal is absorbing, absorption is taken into account by introducing an imaginary part to the form factor [2] and to the polarizability. So the wave vector also needs to be a complex number, given by, $K_h = K_h^r + iK_h^i$, where superscripts r and i stand for real and imaginary part. There is no absorption in vacuum and the oincident wavevector is real, so $K_o^i = K_h^i$. Because of the boundary conditions at the surface (phase velocity of the wave should be the same along the crystal-vacuum interface), the imaginary part of the $\mathbf{K_o}$ should be normal to the surface. So

$$\mathbf{K_o^i} = IM(\overline{MP_j})\mathbf{n} \tag{4.42}$$

where $IM(\ )$ means imaginary part. The subscript j is branch index. So the attenuation factor can be written as

$$exp(4\pi \mathbf{K_o^i} \cdot \mathbf{r}) = exp(-\frac{\mu_e z}{\gamma_o}) \tag{4.43}$$

where z is depth of the observation point along the normal $\mathbf{n}$ to the crystal surface, and the effective absorption coefficient μ_e is

$$\mu_e = -4\pi\gamma_o K_o^i$$

Figure 4.9 shows that

$$\gamma_o \overline{MP_1} = 1/2k\chi_o + X_o$$

It follows that

$$\mu_e = -4\pi\gamma_o K_o^i = \mu_o - 4\pi X_o^i \tag{4.44}$$

Now based on the previous equations, it is possible to derive the diffracted wave propagation inside the crystal in transmission geometry. First, incident plane wave

condition is needed. The normal to the crystal surface intersects both branches of the dispersion curve, at P_1, and P_2, and two wavefields are excited in the crystal (Fig 4.7). It creates double diffraction inside the crystal. The amplitude of these refracted and reflected waves are Ψ_{o1}, Ψ_{h1}, respectively, for wavefield 1 and Ψ_{o2}, Ψ_{h2} for wavefield 2. The boundary condition for the amplitudes at the surface are

$$\begin{aligned} \psi_o^{(a)} &= \Psi_{o1} + \Psi_{o2} \\ 0 &= \Psi_{h1} + \Psi_{h2} \end{aligned}$$

where $\Psi_o^{(a)}$ is the amplitude of the incident wave. The amplitude Ψ_{hj} and Ψ_{oj} at the entrance surface can be expressed by means of their ratio ξ_j

$$\Psi_{h1} = \frac{\xi 1 \xi 2}{\xi 2 - \xi 1}\Psi_o^{(a)};\ \Psi_{h2} = -\frac{\xi 1 \xi 2}{\xi 2 - \xi 1}\Psi_o^{(a)};$$
$$\Psi_{o1} = \frac{\xi 2}{\xi 2 - \xi 1}\Psi_o^{(a)};\ \Psi_{o2} = -\frac{\xi 1}{\xi 2 - \xi 1}\Psi_o^{(a)};$$

By substituting from Eq 4.41, it follows that

$$\Psi_{hj} = \pm\frac{\sqrt{\chi_h \chi_{\overline{h}}}}{2\sqrt{\gamma}\chi_{\overline{h}}}\frac{\Psi_o^{(a)}}{\sqrt{1+\eta^2}};$$
$$\Psi_{oj} = \mp\frac{\eta \mp \sqrt{1+\eta^2}}{2\sqrt{1+\eta^2}}\Psi_o^{(a)} \tag{4.45}$$

Using Eq 4.41, 4.44, and 4.45, it can be shown that the intensities of the four waves are

$$\left|\Psi_{oj}\right|^2 = \left|\Psi_o^{(a)}\right|^2 exp\left(\frac{-\mu_{ej}z}{\gamma_o}\right)\frac{\left[\sqrt{1+\eta_r^2} \mp \eta_r\right]^2}{4(1+\eta_r^2)}$$
$$\left|\Psi_{hj}\right|^2 = \left|\Psi_o^{(a)}\right|^2 exp\left(\frac{-\mu_{ej}z}{\gamma_o}\right)\left|\frac{F_h}{F_{\overline{h}}}\right|\frac{\gamma^{-1}}{4(1+\eta_r^2)} \tag{4.46}$$

with

$$\mu_{ej} = \mu_o \left[\frac{1}{2}(1+\gamma^{-1}) \mp \frac{\frac{1}{2}\eta_r(1-\gamma^{-1}) + \sqrt{\gamma^{-1}}\left|C\chi_{ih}/\chi_{io}\right| cos\varphi}{\sqrt{1+\eta_r^2}} \right] \tag{4.47}$$

where φ is the phase difference between χ_{rh} and χ_{ih}, which is real and imaginary part of the χ, η_r is the real part of the deviation parameter η, the upper sign is for branch 1 and lower is for branch 2. Fig 4.10 shows the variation of the Poynting vector of the two wavefields across the reflection domain.

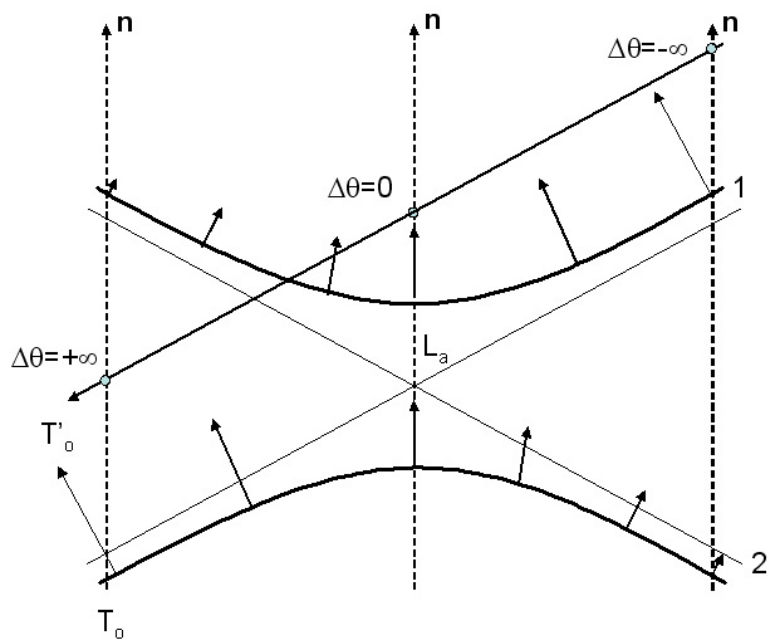

Fig. 4.10. Variation across the reflection domain of the Poynting vectors of the two wavefields excited by an incident plane wave. Symmetric transmission geometry, no absorption

4.1.2.2 Dynamical X-ray transmission through a strained lattice

In this section, the theory of Xray transmission through a weakly deformed lattice is presented. Using this theory, a scheme for tracing X-ray trajectory in a deformed crystal is developed and implemented.

If a perfect crystal is deformed, Poynting vector changes with propagation. While it propagates through the crystal, it moves along the dispersion surface. If the crystal strain is very small, then the X-ray propagation is very similar to optical wave packet propagation inside the inhomogeneous refraction index medium. In this case, wave vector $\delta k \approx \vec{\nabla}\ (n)$. It means that wave propagation direction is defined by the direction of maximum index variation. Penning and Polder [9] and Kato [10] have applied this principle to X-ray propagation under the condition of Bragg diffraction. If the crystal is deformed, any point of position vector **r** is transformed into a point P′ of position vector **r′** as shown in Fig. 4.11.

The equation can also be written as

$$\mathbf{r} = \mathbf{r'} - \mathbf{u(r)}$$

With small angle approximation, valid if the coefficient of the strain tensor, $\partial u_i/\partial x_j$, are small then,

$$\mathbf{r} \cong \mathbf{r'} - \mathbf{u(r')} \tag{4.48}$$

let us set **h′** as the reciprocal vector after deformation and **h** as the reciprocal lattice before deformation. Then the reciprocal lattice vector, **h′**, is given by

$$\mathbf{h'} = \vec{\nabla}\ H' = \mathbf{h} - \vec{\nabla}\ (\mathbf{h} \cdot \mathbf{u}) \tag{4.49}$$

The local change $\delta\mathbf{h}$ of the reciprocal lattice is therefore,

$$\delta\mathbf{h} = \mathbf{h'} - \mathbf{h} = -\ \vec{\nabla}\ (\mathbf{h} \cdot \mathbf{u}) \tag{4.50}$$

The $\delta\mathbf{h}$ is itself a function of the direct space coordinates in the deformed region and its variations are given by

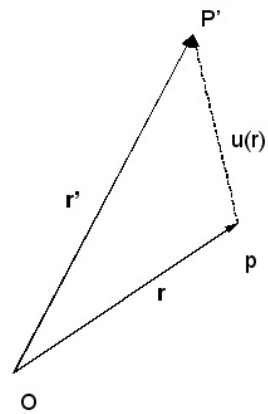

Fig. 4.11. Deformation of material. **u(r)** is deformation vector, **r**′ is new position vector after deformation.

$$(\delta \mathbf{h}_j) = (\vec{\nabla} \otimes \delta \mathbf{h}) \cdot d\mathbf{r} = -\vec{\nabla} \otimes \vec{\nabla} (\mathbf{h} \cdot \mathbf{u}) \cdot d\mathbf{r}$$

where $\otimes$ denotes a tensor product. Its components are

$$d(\delta \mathbf{h}_j) = -\frac{\partial^2 (\mathbf{h} \cdot \mathbf{u})}{\partial x_i \partial x_j} dx_i$$

Now, based on Penning and Polder [9] paper, the following section will derive the ray trajectory inside the deformed crystal. It is shown that the result of deformation is a shift $\overline{L_a L_a^{'}} = k\delta\theta$ of the Laue point along the tangent $T_o^{'}$ to the sphere of the center O and radius k as can be seen in Fig. 4.12. The Lorentz point is shifted by the same amount, $\overline{L_a L_a^{'}} = \overline{L_o L_o^{'}}$. First consider the wave which is passing through point p in Fig 4.11. Its tie point is P on the dispersion surface before deformation as can be seen in Fig. 4.12. Because of the deformation, point P will be transformed into P′, and the same wavefield, now passing through P′, will have tie point at P_d. The wavevector, $\mathbf{K_o}$, of the refracted wave has changed to $\mathbf{K_o^{'}}$ by an amount $\delta \mathbf{K}_o$

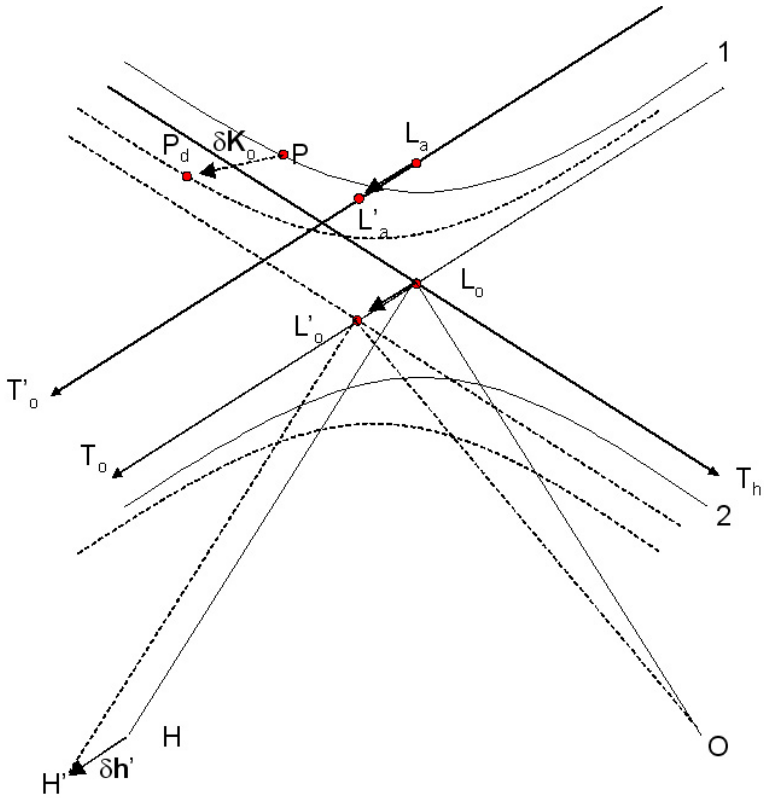

Fig. 4.12. Ray Theory. The dispersion surface after a deformation is represented by dashed line. P is tie point before deformation, P_d is tie point after deformation, L'_o is Lorentz point after deformation, and $\delta\mathbf{h}$ is variation of the reciprocal lattice vector.

$$\delta\mathbf{K_o} = \mathbf{K'_o} - \mathbf{K_o} = \mathbf{OP_d} - \mathbf{OP} = \mathbf{PP_d}$$

If one defines the *effective misorientation* as the difference between the deviation from the Bragg angle in a deformed crystal and the deviation in an undeformed crystal, then one can show that the effective misorientation is proportional to the quantity, $\delta\mathbf{h} \cdot \mathbf{s_h}$ [2]. Clearly, the effective misorientation is zero if this quantity is zero, or in other words, when the local variation in the reciprocal lattice vector is normal to the reflected direction. The invariant dispersion surface in that case is given by

$$\mathbf{h} \cdot \mathbf{K_h} = constant$$

These surfaces can therefore be interpreted as the equation of constant index of refraction and, by analogy with optical Eikonal theory, the variation of local wavevector is given by

$$\delta \mathbf{K_o} \propto \vec{\nabla}\,(\mathbf{h} \cdot \mathbf{K_h}) \tag{4.51}$$

The reflected wavevector, $\mathbf{K_h}$, changes accordingly,

$$\begin{aligned} \delta \mathbf{K_h} &= \mathbf{K_h^{'}} - \mathbf{K_h} = \mathbf{H^{'}P_d} - \mathbf{HP} = \mathbf{H^{'}H} + \mathbf{HP} + \mathbf{PP_d} - \mathbf{HP} \\ &= \delta \mathbf{K_o} - \delta \mathbf{h} \end{aligned} \tag{4.52}$$

Instead of considering that the dispersion surface glides along T_o, one can equivalently consider the tie point to be gliding as seen in Fig 4.13.The position P′ of the tie point after deformation is obtained as follows: let Q be a point deduced from the tie point P before deformation.

$$\begin{aligned} \mathbf{PQ} &= -\mathbf{L_o L_o^{'}} \\ \mathbf{QP^{'}} &= \mathbf{PP_d} = \delta \mathbf{K_o} \end{aligned} \tag{4.53}$$

so that

$$\mathbf{PP'} = \delta \mathbf{K_o} - \mathbf{L_o L_o^{'}} \tag{4.54}$$

Let $P_o, P_o^{'}, P_h, P_h^{'}$ be the projection of P and P′ on T_o and T_h, respectively. The coordinate P and P′ are

$$\begin{aligned} P &: X_o = \overline{P_o P}, X_h = \overline{P_h P} \\ P^{'} &: X_o^{'} = \overline{P_o^{'} P^{'}}, X_h^{'} = \overline{P_h^{'} P^{'}} \end{aligned} \tag{4.55}$$

after projecting $\mathbf{PP^{'}}$ on $\mathbf{s_o}$ (unit vector normal to tie-line T_o), and $\mathbf{s_h}$ (unit vector normal to tie-line T_h), it is possible to get dX_o and dX_h

$$dX_o = X_o^{'} - X_o = \mathbf{PP}^{'} \cdot \mathbf{s_o} = \delta\mathbf{K_o} \cdot \mathbf{s_o} \tag{4.56}$$

$$dX_h = X_h^{'} - X_h = \mathbf{PP}^{'} \cdot \mathbf{s_h} = \delta\mathbf{K_o} \cdot \mathbf{s_h} - \delta\mathbf{h} \cdot \mathbf{s_h} \tag{4.57}$$

dX_o and dX_h are related by differentiation of Eq. 4.31 of the dispersion surface:

$$X_o dX_h + X_h dX_o = 0 \tag{4.58}$$

Substituting dX_o and dX_h from Eq. 4.57, then

$$\delta\mathbf{h} \cdot \mathbf{s_h} = \delta\mathbf{K_o} \cdot \left(\frac{X_h}{X_o}\mathbf{s_o} + \mathbf{s_h}\right) \tag{4.59}$$

Let's set

$$\mathbf{S}^{'} = \frac{X_h}{X_o}\mathbf{s_o} + \mathbf{s_h} \tag{4.60}$$

By using $X_h/X_o = \xi^{-2} = (D_o/D_h)^2$, (Eqn 4.33), and neglecting anomalous dispersion (i.e. assuming $\chi_h = \chi_{\bar{h}}$), $S^{'}$ can be written as,

$$\mathbf{S}^{'} = \xi^{-2}\mathbf{s_o} + \mathbf{s_h} \tag{4.61}$$

It is clear that $\mathbf{S}^{'}$ is proportinal to the Poynting vector(Eqn. 4.34), so it is parallel to the local trajectory of wavefield. By using $\delta\mathbf{h} = (d\mathbf{r}\cdot \vec{\nabla})\mathbf{h}$ Eqn. 4.59 can be written as

$$\delta\mathbf{K_o} \cdot \left(\frac{X_h}{X_o}\mathbf{s_o} + \mathbf{s_h}\right) = \vec{\nabla}\ (\mathbf{h} \cdot \mathbf{s_h}) \cdot d\mathbf{r} \tag{4.62}$$

$$\delta\mathbf{K_o} \cdot \left(\xi^{-2}\mathbf{s_o} + \mathbf{s_h}\right) = \vec{\nabla}\ (\mathbf{h} \cdot \mathbf{s_h}) \cdot d\mathbf{r} \tag{4.63}$$

Note that in the above, $d\mathbf{r}$, represents an incremental distance *along the direction of the local trajectory of the Poynting vector*.

The ray trajectory will be represented with respect to the axes Aζ and Aυ, respectively parallel and perpendicular to the lattice planes as can be seen in Fig 4.14. Let **s** be

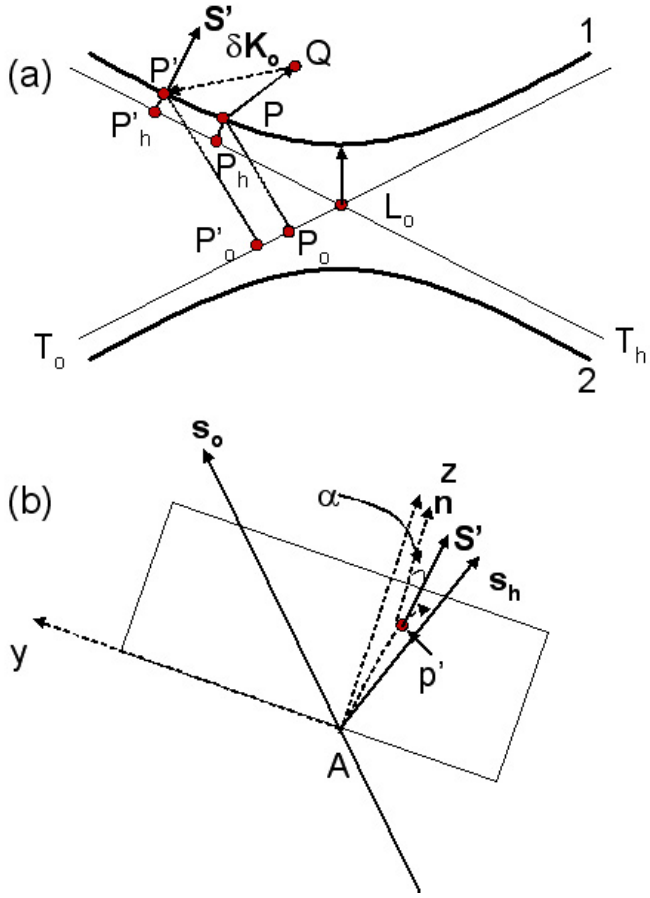

Fig. 4.13. Ray Theory. An alternative way to explain the deformation process of a crystal. (a) is reciprocal space: The dispersion surface is considered to be fixed but the tie point is gliding. P is tie point before deformation and P′ is after deformation. $PQ = -L_0L_0^{'}$ where $L_0^{'}$ is represented in Fig. 4.12. s is a unit vector parallel to lattice planes. (b) is direct space. The ray trajectory S' at p′ is represented as solid line.

a unit vector parallel to Aζ. The projection of **S′** on the lattice planes is

$$\begin{aligned} \mathbf{S'} \cdot \mathbf{s} &= S' cos\alpha \\ \mathbf{S'} \cdot \mathbf{s} &= (\xi^{-2} + 1) cos(\theta_B) \end{aligned} \tag{4.64}$$

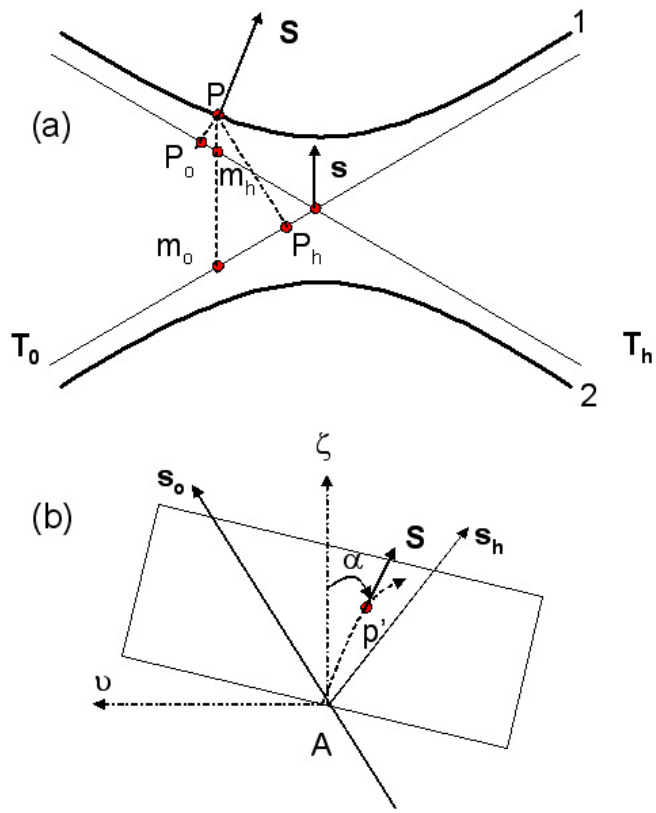

Fig. 4.14. Representation of the ray trajectory with respect to axes related to the lattice planes. (a) Reciprocal space, (b) Real space. The ray trajectory is represented by a thick dashed line. **S** is a poynting vector of wavefield at p′, Aζ, and Aυ is axes prallel and perpendicular to the lattice planes, respectively.

It follows that

$$\mathbf{S}' = (\xi^{-2} + 1)\frac{cos\theta_B}{cos\alpha}\frac{d\mathbf{r}}{dr} \tag{4.65}$$

where d**r** is an element prallel to the trajectory of the wavefield. Equation 4.63 becomes

$$(\xi^{-2} + 1)\frac{cos\theta_B}{cos\alpha}\frac{\delta\mathbf{K_o}}{dr} \cdot d\mathbf{r} = \vec{\nabla}\ (\mathbf{h} \cdot \mathbf{s_h}) \cdot d\mathbf{r} \tag{4.66}$$

By using Eqn. 4.51, $\delta\mathbf{K_o}$ can be represented by

$$\delta\mathbf{K_o} = (\xi^{-2}+1)^{-1}\frac{cos\alpha}{cos\theta_B}\vec{\nabla}(\mathbf{h}\cdot\mathbf{s_h})dr \tag{4.67}$$

since local reciprocal lattice vector h is given in terms of undeformed reciprocal lattice vector, h_o by Eqn4.49,

$$\delta K_o \cdot s_o = -(\xi^{-2}+1)^{-1}\frac{cos\alpha}{cos\theta_B}\frac{\partial^2(h\cdot u)}{\partial x_o \partial x_h}dr \tag{4.68}$$

The variation $\delta\mathbf{K_o}$ of the position of the tie point corresponds to a variation $d\xi$ of the amplitude ratio. By differentiating the first of the fundamental equation of the dispersion surface, Eqn. 4.24,

$$K_o^2 = k^2(1+\chi_o) + k^2 C\chi_{\bar{h}}\xi \tag{4.69}$$

It follows, afetr differentiation and division by $K_o \cong k$,

$$\delta\mathbf{K_o}\cdot\mathbf{s_o} = \frac{kC\chi_{\bar{h}}}{2}d\xi \tag{4.70}$$

and, after substitution in Eq 4.68,

$$\begin{aligned}(\xi^{-2}+1)d\xi = \left(\xi - \frac{1}{\xi}\right) &= -\frac{2}{kC\chi_{\bar{h}}cos\theta_B}\frac{\partial^2(\mathbf{h}\cdot\mathbf{u})}{\partial x_o \partial x_h}d\zeta \\ &= -2\beta d\zeta \end{aligned} \tag{4.71}$$

where $d\zeta = drcos\alpha$. The strain gradient

$$\beta = \frac{1}{kC\chi_{\bar{h}}cos\theta_B}\frac{\partial^2(\mathbf{h}\cdot\mathbf{u})}{\partial x_o \partial x_h} \tag{4.72}$$

The Equations 4.71 and 4.72 are the key equation we shall use. Together, they allow us to track the trajectory of the Xray inside the deformed crystal. The parameter β can be easily calculated from the z-invariant displacement, which is reasonable assumed

to be true in the case of $LiNbO_3$ domain wall structures, i.e. it is assumed that there is no gradient in lattice strain in the crystallographic c-axis direction of the crystal. In a thick c-cut single crystal, this is a reasonable assumption through the entire crystal thickness, except perhaps close to the surfaces where surface relaxation may occur. Figure 4.15 shows the geometry of the crystal, the crystal and the global coordinate system, the domain wall, the crystallographic planes studied, and the incident and diffracted beams below. From the geometry, the displacement of key interest are $u(y)$, and the reciprocal lattice vector **h** that is parallel to this displacement. One that therefore simplify the expression for β in Eqn. 4.72 as

$$\begin{aligned} |h| \frac{\partial}{\partial y_o} \frac{\partial}{\partial y_h} (u(y)) &= \frac{\partial}{\partial y_o} \left[\frac{\partial y}{\partial y_h} \frac{\partial u(y)}{\partial y} \right] |h| \\ &= \frac{\partial y}{\partial y_o} \frac{\partial}{\partial y} \left[\frac{\partial y}{\partial y_h} \frac{\partial u(y)}{\partial y} \right] |h| \\ &= \frac{\partial y}{\partial_o} \frac{\partial y}{\partial y_h} \frac{\partial^2 u(y)}{\partial y^2} |h| \\ &= sin^2\theta_B \frac{\partial^2 u(y)}{\partial y^2} |h| \end{aligned} \tag{4.73}$$

So β can be

$$\beta = \frac{|h| \, sin^2\theta_B}{kC\chi_{\overline{h}} cos\theta_B} \frac{\partial^2 u(y)}{\partial y^2} \tag{4.74}$$

4.1.2.3 Simulation and analysis of transmission images of domain walls

By using this ray tracing method, now I can now explain some key features of transmission X-ray topography images of domain walls in lithium niobate. Fig 4.16 shows (3,0,.,0) symmetrical transmission topography image. The diffraction planes in this image are in the $x-z$ planes whose projection would appear as vertical lines along x-axis in the above image. The accompanying schematic explains the geometry of probing. The projection of the incident wavevector $\mathbf{K}_o$ on the x-y plane of the image points in the $-y$ direction. This image shows dislocations and low angle grain boundaries (Fig 4.16(a)

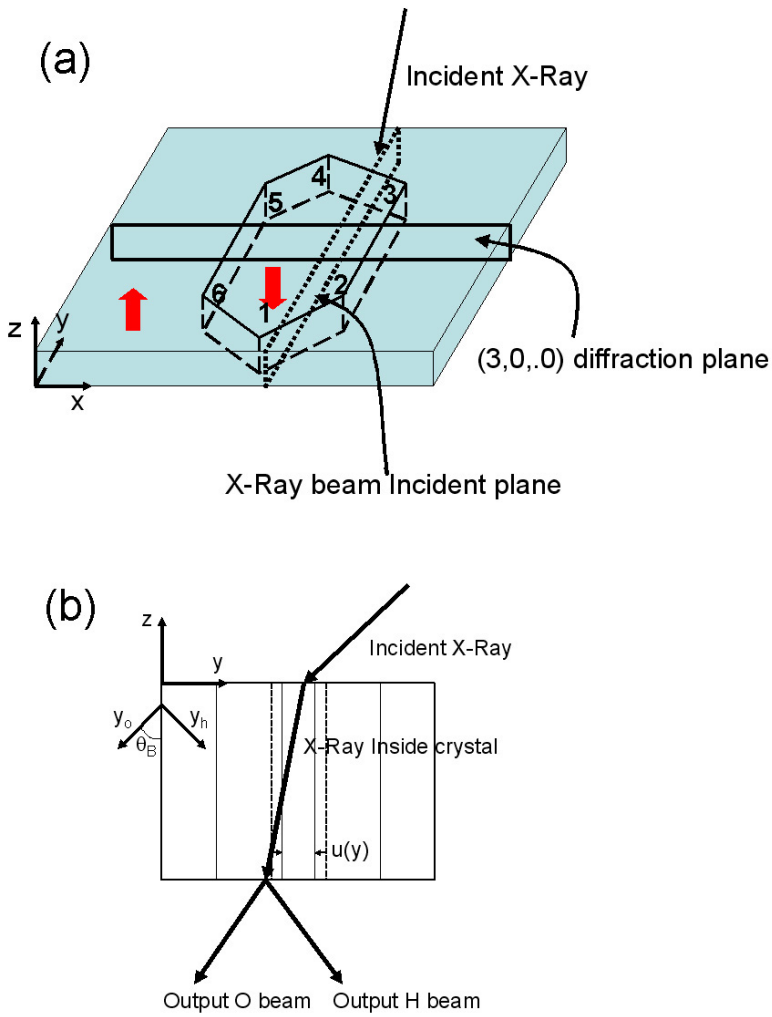

Fig. 4.15. Schematic (3,0,.,0) transmission diffraction diagram. (a) shows the X-ray incident plane and the diffraction plane. (b) is a detailed X-ray incident plane of (a). It shows original diffraction plane as vertical dotted line, and distorted diffraction plane with amount of displacement u(y). It shows new coordinate y_o and y_h axis.

and (b)) more clearly than the reflection geometry images. As also seen in reflection images, the low angle grain boundary is pinning ferroelectric domains as can be seen in Fig 4.16(a) and (b). Along the low angle grain boundaries (a), one of the biggest domain wall is pinned. Also many other small domain is aligned along the low angle grain boundaries (b). However, the dislocations appear to cut across domain walls. Also, the contrast around a domain wall is stronger than in the reflection geometry. Especially the corner vertices of hexagonal domains show a very strong and broad strain, which was not observed in the reflection geometry. The most-straight forward and simple explanation of this image is that the dark contrast in the image means that the Bragg condition is not satisfied. That's the main reason why dislocations are easily detected as a dark thin line. But to understand this complex contrast more accurately in transmission geometry, *dynamical theory* is necessary. By using basic dynamical theory and Eikonal theory, complex topography images can be reasonably explained.

Though there are many interesting contrasts in Fig 4.16, we pick two of the most interesting contrast distribution features and try to explain them semi-quantitatively. These are (1) Small domains such as (c) in Fig 4.17, which have alternate bright and dark vertices of the hexagon. We show below that this can be explained by the different z-displacement strains at the adjacent vertices, which due to their proximity in a small domain, interact with each other and provide alternating Xray contrast. (2) Larger domain (d) in Fig 4.22 which clearly show asymmetric contrast between domain walls to the left and to the right of the hexagon. We show below that such asymmetry can arise simply from the incident wave vector geometry, and the asymmetric dispersion points that are excited by this beam inside the bulk of the crystal for the two sets of domain walls. This results is in different trajectories of the Xray beam for the two sets of domain walls inside the crystal.

Case 1: Contrast at domain vertices: Let's first carefully see domain (c) in Fig 4.16. This domain image is expanded in Fig 4.17(a). As a reminder, the projection of the incident wavevector $\mathbf{K}_o$ on the x-y plane of the image points in the $-y$ direction, or in other words, the incident beam is incident from the left side of the image. To get an accurate contrast, this image was converted as a digitized matrix by using the MATLAB

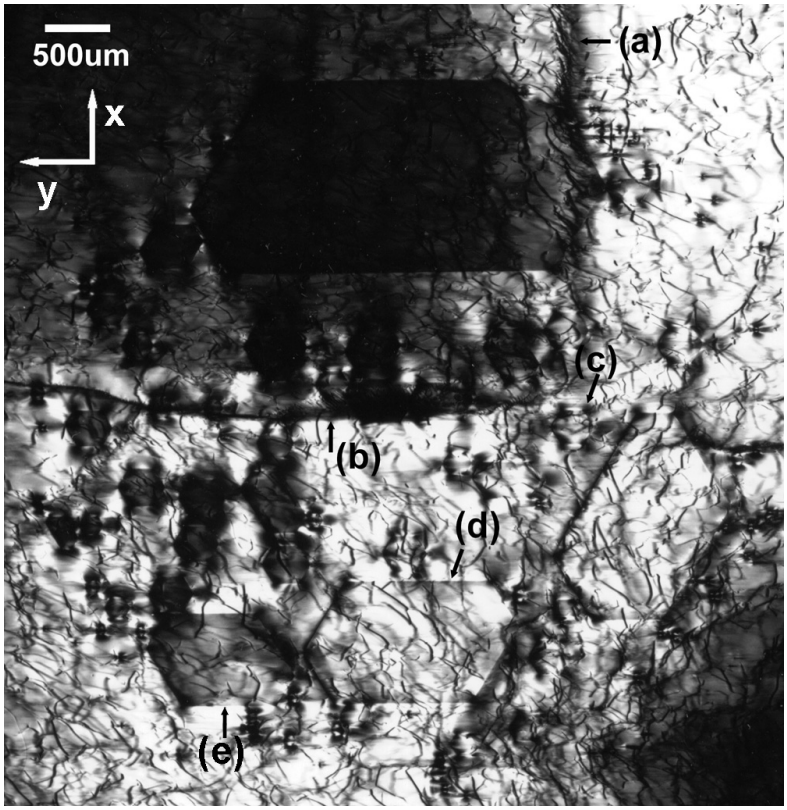

Fig. 4.16. (3 0.0)symmetrical transmission topography image. (a) and (b) is low angle grain boundary, domain (c) and domain(d)is magnified in Fig 4.17 and 4.22 respectively. The background consists of a large number of thin complex lines that are dislocations inside the crystal. The coordinate represented in Figure is for the matrix domain. This topography image is for the O beam.

command *imread*. Fig 4.17(b) shows scanning line profile of the line in Fig 4.17(a). The vertical dashed lines indicate the approximate domain vertex positions in the hexagonal domain. One notices that within the domain region, the region adjacent to the left vertex is dark and the right vertex is bright. These features are now explained below. Figure 4.18 shows the flow chart or the simulation scheme for implementing the X-ray Eikonal theory. First it requires the initial conditions both for the incident beams and for the surface curvature. By using both these conditions, the initial tie point in dispersion curve is determined. After getting this initial tie point, the ray will be propagate through the

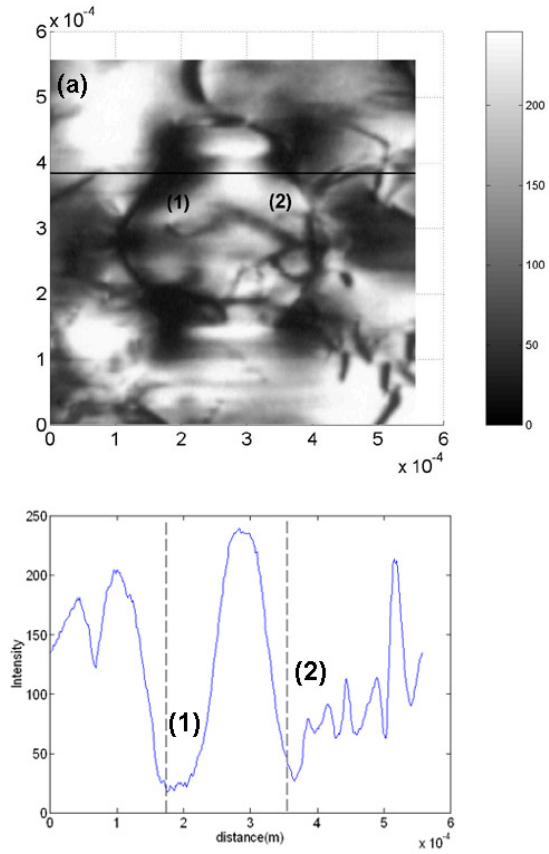

Fig. 4.17. (a) is magnified domain image of Fig 4.16(c). (b) is line scan of line in (a). It is clear that contrast of corner(1) is opposite with corner(2)

crystal according to ray projection equation 4.76 until it reaches the exit surface. A new variable a_M is introduced to solve Eqn 4.71. It is defined as,

$$a_M = \xi - \frac{1}{\xi} \tag{4.75}$$

This definition gives the a_M update equation as,

$$a_M^{new} = a_M^{old} - 2\beta\Delta z \tag{4.76}$$

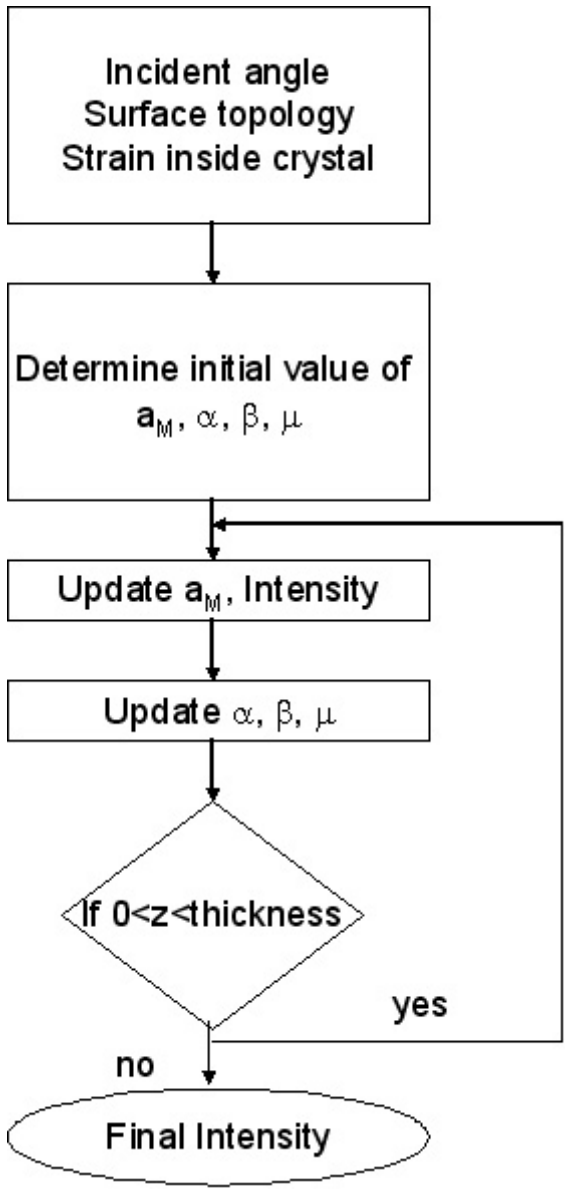

Fig. 4.18. Flow chart of ray trajectory code.

After updating a_M, α is updated by using Eqn. 4.35, and μ is updated by using Eqn. 4.47. The term μ describes how fast X-ray intensity will be decaying. The term α describes the direction compared to surface normal direction. The term β describes the second derivative of the displacement in new coordinates. Table 4.1 lists all the parameters used for our simulation with 8.5391 KeV photon energy. Thus, the ray direction and the intensity can be calculated at every point inside the crystal. The MATLAB code used for simulating this process is given in Appendix D

$LiNbO_3$ parameter	
lattice contant a($10^{-10}m$)	5.1483
lattice contant c($10^{-10}m$)	13.863
lattice spacing d($10^{-10}m$)	1.4862
n=1+A+B*i Complex refraction index	A=1.2049×10^{-5} B=4.2144×10^{-7}
Bragg angle	29.2671°
$\lvert\chi_{rh}\rvert$, $\lvert\chi_{ih}\rvert$ (Sigma polarization)	0.12023×10^{-4}, 0.79176×10^{-6}
Relative intensity(χ_h/χ_o)	0.49967

Table 4.1. Data

In Fig. 4.17, the X-ray beam is incident from the left side of the image. The difraction planes (3 0.0) are perpendicular to the y-axis. Therefore, the strain distribution along the y-direction is the most important variable to analyze in this image. The tie-point on the dispersion surface excited by the incident beam is strongly affected by the surface curvature. If there is any surface curvature and surface relaxation is very fast, then incident bragg angle deviation is directly related with surface curvature. This surface curvature can be modeled by Time dependent Ginzburg Landau (TDGL) simulations as described in detail in Ch. 3. Figure 4.19(a) shows the z-displacement on

the top surface ($x - y$ plane), and (b) shows the z-displacement *along* the y-domain wall. The TDGL simulations indicate that the z-displacements, δz defined as the deviation from a flat-surface alternates in sign between negative and positive values as one goes around the six vertices of the hexagonal domain in lithium niobate. The vertices are labeled from 1-6 in Figure 4.15 with vertices 1,3,5 having -z displacement, and 2,4,6 having +z displacement. Because the projection of the incident wavevector on the $x - y$ plane is in the -y direction, dz/dy(or $\Delta\theta$) determines the initial tie point. This surface curvature, dz/dy, gives rise to a deviation from the flat-surface incident angle. Fig. 4.20 shows the incident angle deviation compared to a flat surface incident angle, and the final exit surface X-ray O beam intensity. Vertical dashed lines indicate the hexagonal domain vertex locations. Qualitatively speaking, the simulated exit beam's intensity is very similar to the experimental results in Fig.4.17 (b), exhibiting the characteristic darker contrast near the left vertex, and a brighter contrast near the right vertex.

In order to understand the role of the strain interaction between the two vertices due to their proximity, (100 μm in this case), we perform a second simulation with a much large separation between the vertices. Figure 4.21 shows the deviation angle and exit beam intensity for domain walls separated by 500μm. Even though the precise position of the left vertex has a dark contrast and right vertex has a bright contrast, overall the dark and the bright contrast is reduced by increasing the distance between vertices. This effect is therefore expected to have the best contrast for smaller domains, as is experimentally seen as well.

Case 2: Asymmetry in contrast between different sets of domain walls.: We now focus on a somewhat larger domain (d) in Fig. 4.16. An interesting feature is that the Bragg-peaks and the rocking curves for inside and outside hexagonal domains are different. This is schematically shown in Fig 4.22 of the rocking image of domains (d), and (e) in Fig. 4.16. In Fig. 4.22 (a), inside domain has a darker contrast, but in (d), inside domain has brighter contrast. It means that in Fig. 4.23, curve 2 corresponds to the outside (matrix)domain, and curve 1 to the inside (reversed) domain. We can roughly guess that inside domain's Bragg angle is smaller than the outside domain by an amount of 0.001°. By using the simple relation, $\frac{\Delta}{d} = -\frac{cos\theta}{sin\theta}d\theta$, the stain difference between the two

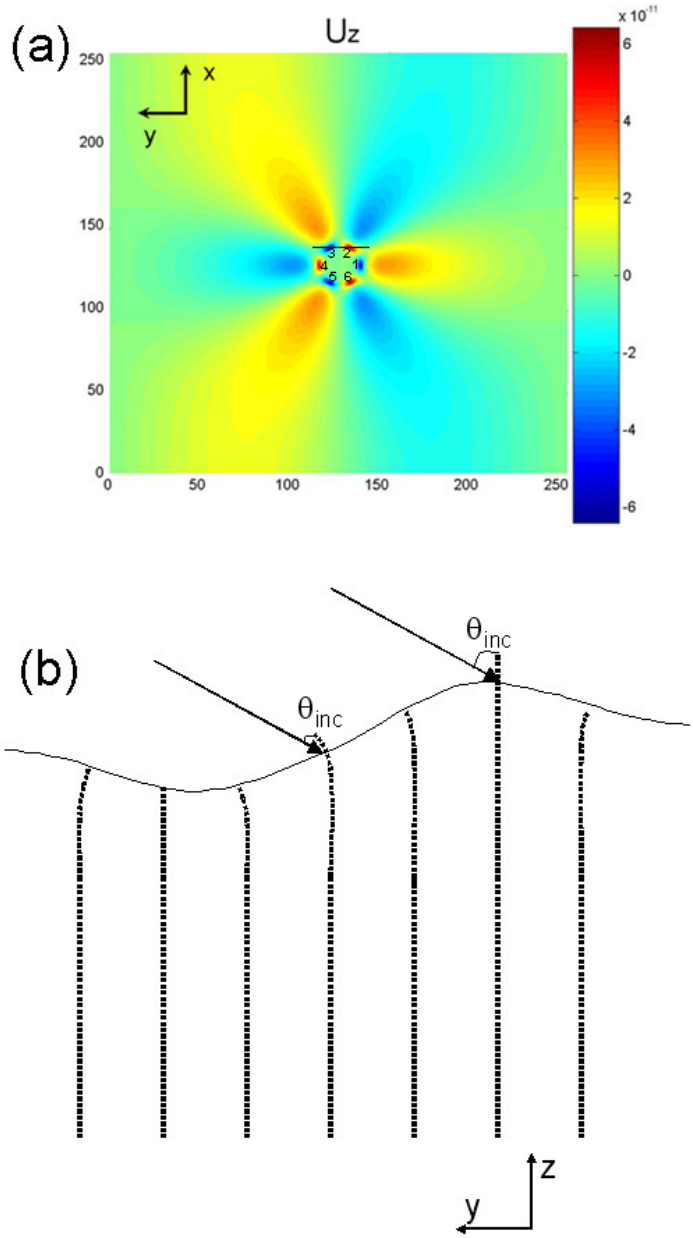

Fig. 4.19. (a)A 2-dimensional plot of the time-dependent Ginzburg Landau simulation of the z-displacement in a $LiNbO_3$ domain wall. (b) A line scan of the z-scan profile along a line in (a) parallel to the y-axis.

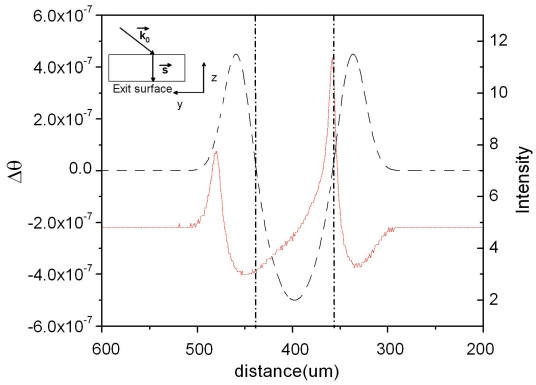

Fig. 4.20. For hexagonal domain vertex positions 2 and 3 in Fig 4.19, indicated by vertical dotted lines, the dotted line is the deviation angle compared to a flat surface incident angle, and the solid line is the exit O-beam intensity after traversing a $LiNbO_3$ crystal of 0.5 mm thickness

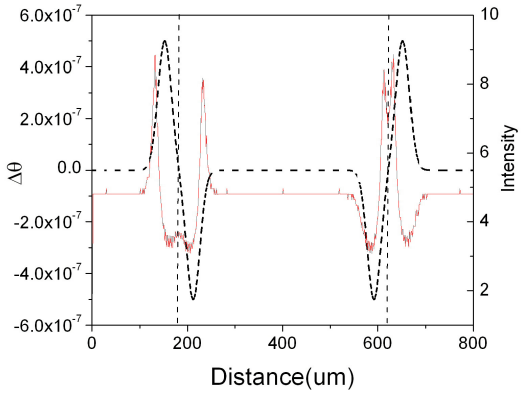

Fig. 4.21. For hexagonal domain vertex positions indicated by vertical dotted lines, the dotted line is the deviation angle compared to a flat surface incident angle, and the solid line is the exit beam intensity after traversing a $LiNbO_3$ crystal of 0.5 mm thickness

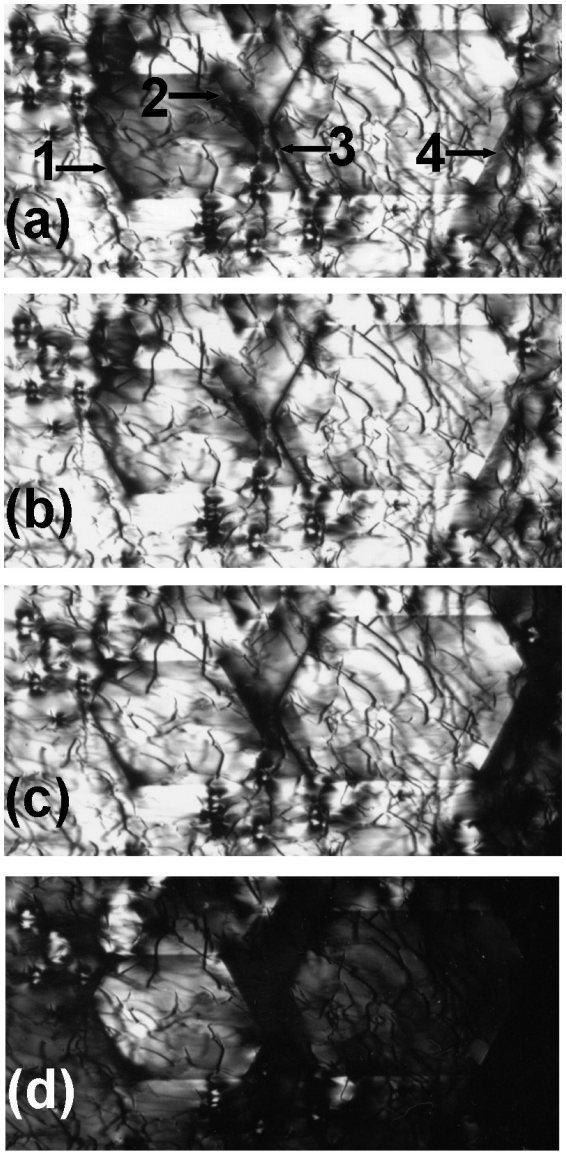

Fig. 4.22. Rocking image of domain (d), and (e) of Fig. 4.16. Incident angle from (a) to (d) is 22.151°, 22.149°, 22.147°, and 22.145 °, respectively, for (3,0,0) symmetrica transmission.

domain is roughly estimated to be $\epsilon_{yy} \ -4 * 10^{-5}$. Because of the negative sign, the inside domain has a higher lattice spacing $d_{(3,0,.,0)}$ than the outside matrix domain.

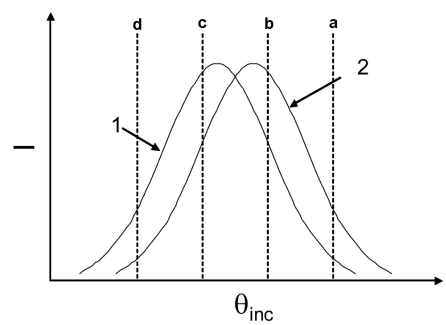

Fig. 4.23. Schematic Rocking curve for the inside domain(1) and outside domain(2).

In addition to the constant strain or lattice constant difference between inside and outside domains, the wall contrast also differs depending on the symmetrical position. The domain walls 1 and 3 looks much sharper than domain walls 2 and in Fig. 4.16 for all rocking curves around the Bragg peak. This asymmetrical contrast can only be explained by the dynamical theory, because the left and right sides of the dispersion curve are not symmetrical. Figure 4.24(a) shows the strain(ϵ_{yy}) distribution for different orientation domains, and the simulated contrast at the exit surface. This simulated image also shows an asymmetrical contrast for different domain walls, namely, Wall type 1 and 3 with smaller contrast width and walls 2 and 4 with broader contrast widths.

An additional source of asymmetric contrast can arise from the small shear strain $\epsilon_{zx} \approx 5 \times 10^{-5}$ that was observed at the domain walls in the Bragg geometry (Section 4.1.1). This results in the entire hexagonal domain being slightly shifted in the z-direction with respect to the matrix. If it is assumed that this strain exists throughout the entire crystal depth in the z-direction, then for an incident wavevector from the left side of Fig. 4.22, the domain sets 1,3, verses 2,4 can result in different contrasts. Such a difference is also seen in Bragg geometry in Fig. 4.3. It is important to note that such a shear

strain, ϵ_{zx}, observed in the Bragg geometry, is not predicted by the simple TDGL model (Chapter 3) which does not include the effect of crystal non-stoichiometry or internal fields. This shear strain, however is not inconsistent with the z-displacements predicted by the TDGL model at the vertices of the hexagon as shown in Fig.4.19. In other words, the two can co-exist.

But in the transmission geometry simulation, this effect is not modeled here for the following reason. Because of the tightly localized shear strain(within tens of μm), the spatial derivative of the shear strain is large. If this value is too high, namely very high value of β, then the ray theory can't be applied. This shear strain will effect the transmission topological image, but this effect may be localized in a small area compared to the other strains mentioned in case 1 and case 2 models.

As a conclusion, by using dynamical X-ray tracing program, we have explained the asymmetrical contrast at the vertices of hexagonal domains in lithium niobate. We also show that the overall lattice strain ϵ_{yy} seen inside the domains can explaint the asymmetric contrast widths of different sets of domain walls in the same hexagonal domain. Even though it is difficult to predict the exact strain values, the simulation provides a qualitatively good agreement with the experimental data.

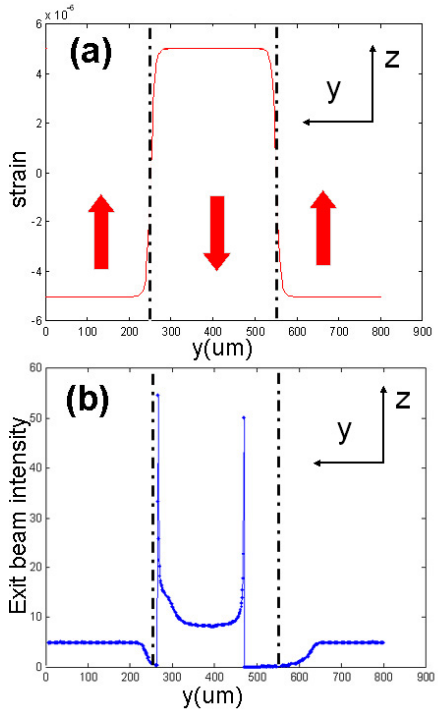

Fig. 4.24. (a) ϵ_{yy} profile. Red arrow is spontaneous polarization direction.(b) is exit beam's intensity calculated by ray tracing method according to strain distribution in (a)

4.2 In situ experiment

By using static reflection and transmission x-ray topography, detailed local static structure of domain walls was detected and described in previous sections. This section probes the detailed dynamical strain evolution by applying an electric field under the presence of X-rays. Both transmission and reflection geometry give very interesting dynamical behavior of strain evolution as a function of external fields. In reflection geometry, long-range piezoelectric strains evolve and interact with neighboring domains even well below the coercive field. By using ANSYS simulation and x-ray tracing simulation, accurate dynamical strain values at the domain wall can be deduced as a function of external field. In transmission in-situ experiments, a very complex strain evolution is observed inside the crystal, which was not amenable to clear interpretations and

simulation. This section therefore focuses only on the *in-situ* simulations in the Bragg reflection geometry.

4.2.1 reflection geometry

The synchrotron beamline produce an x-ray beam with a vertical divergence of less than 36 μrad. More importantly, the local divergence angle on a microscopic area of the crystal due to the source size and distance from the undulator is 1.4 μrad. This is far smaller than the width of the symmetric double crystal Si(111) monochromator Bragg reflection (44.5 μrad) or the intrinsic rocking curve width of $LiNbO_3$ (16.3 μrad). It is thus possible to do excellent topography using the symmetric crystal monochromator. For diffraction with an applied electric field, conductive electrodes consisting of a 100 nm film of amorphous carbon were deposited on both sides of a z-cut crystal over an approximately 1 cm x 1 cm area in the center of the crystal. The crystals were mounted on an insulated stage in a 6-circle goniometer. Regions of the order of 1 mm^2 -2 mm^2 illuminated by the incident beam were imaged in the (0,0,.,12) Bragg reflection using a magnifying x-ray camera. The camera consisted of a Gd oxysulfide sputtered fluorescent film deposited on a magnifying optical taper which is coupled to a cooled CCD detector with 12 bit readout accuracy. The fluorescent film was relatively insensitive to 3rd harmonic radiation from the monochromator. The lateral resolution of the combination was 6 m over a 3mm $\times$ 3mm field. The camera was mounted 0.47 m from the sample crystal. The images were recorded with integration times of 50 ms-1s, depending on the degree of attenuation employed downstream in the diffracted beam.

The evolution of these domain wall strains under a uniform external field is now described. These experiments were conducted on a congruent z-cut crystal of thickness 0.5 mm after the amorphous carbon electrodes were deposited as described above. The measured rocking curve width of the (0,0,.,12) Bragg reflection with electrodes in the region of the image was θ_B=110 μrad as observed previously, although at places on this sample, rocking curves showed structure resolvable into individual Bragg peaks with widths of 27.2 μrad. Fig. 4.25 shows topographs with applied voltages of (a) 0 V, (b) +4500 V, and (c) -4400 volts. The incidence plane is the $y-z$ plane, whose projection with

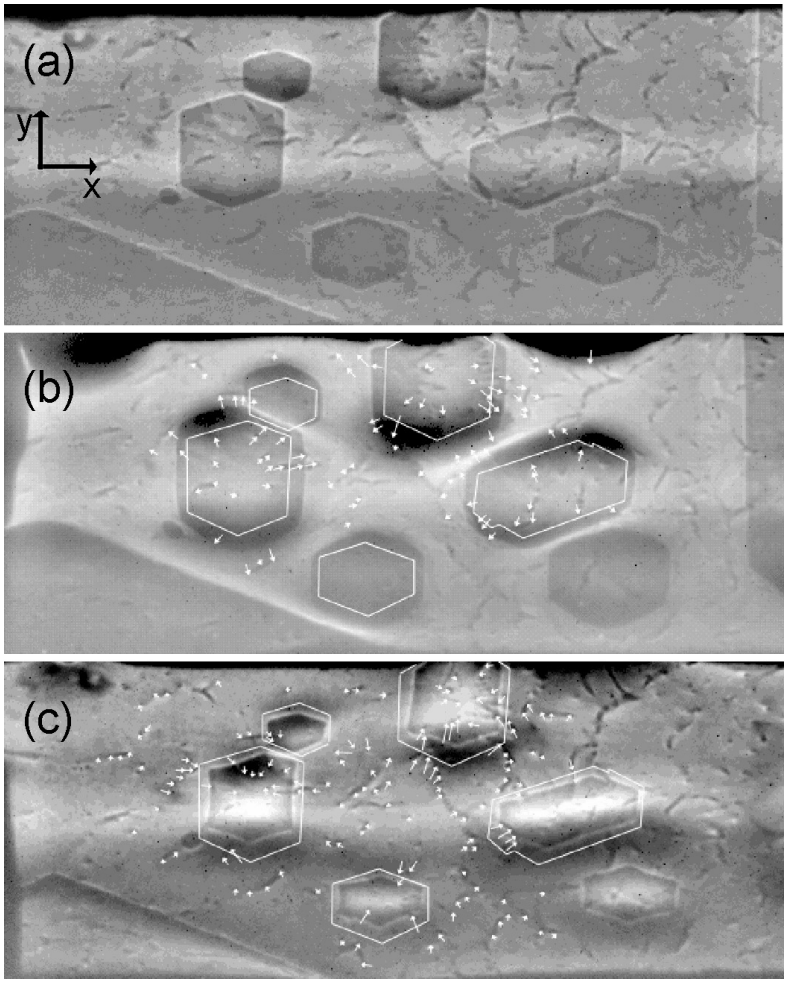

Fig. 4.25. (0 0 . 12) Bragg topograph of $LiNbO_3$ crystal (a) at applied voltage V=0; (b) at applied voltage V=+4500 V (forward bias: electric field parallel to polarization inside the hexagonal domains); (c) at applied voltage V=-4400 V (reverse bias: electric field antiparallel to polarization inside the hexagonal domains). The domain outlines as seen for V=0 are shown in (b) and (c). The arrows show the apparent motion of defect features from the position at V=0

the image plane is a vertical line along the y-axis. The xray is incident from bottom's up in the image plane. Fig. 4.25 (a) clearly shows several hexagonal ferroelectric domains in addition to numerous dislocations and defects within an extinction depth of the surface of the $LiNbO_3$ crystal. Fig. 4.25 (b) shows an apparent growth in the domain

size as well as a decrease in the spacing between the domains. The apparent growth is a consequence of the application of a forward bias (positive voltage: applied electric field E parallel to the polarization P_s inside the hexagonal domains). The domains as observed with no applied field in Fig. 4.25 (a) are shown in outline. Fig. 4.25 (c) shows an apparent shrinkage of the domains as well as an increase in the spacing between the domains. The apparent shrinkage is the consequence of the application of a reverse bias state (negative voltage; applied electric field E opposite to the polarization P_s inside the hexagonal domains).

The coercive field for domain reversal in congruent $LiNbO_3$ single crystals is 240kV/cm in the forward bias state and 150kV/cm in the reverse bias state. The difference arises from the presence of internal fields as reported before [11]. Since our application of ±90 kV/cm is considerably lower than the coercive fields for $LiNbO_3$, no domain wall motion is expected, consistent with prior in-situ optical experiments. [5]To check this, we verified using optical microscopy after the experiment that the ferroelectric domain walls had not moved at all by the application of the field. To clarify the effect in the topographs, we tracked the changes in the apparent positions of dislocation features as a result of the application of the external field. These deviations between the initial state of no applied voltage and the final state of high applied voltage are shown as small arrows in Figs. 4.25 (b) and (c). Under close inspection we see no major evidence of domain walls moving relative to neighboring dislocations as a result of voltages applied here. Furthermore, in Fig. 4.25 (b) we see apparent expansion of the distance between dislocations in domains with the application of forward bias, and the contraction of the distance between dislocations in the intervening matrix. In Fig. 4.25 (c) we see the opposite effect, the apparent contraction of the distance between dislocations within a domain under the action of a reverse bias, and the expansion of the distance between dislocations in the intervening matrix.

It is significant that dislocation features far away from domain walls show the least apparent motion under the application of the field, independent of whether inside or outside a domain. Fig. 4.26 shows a larger area view of the same domain region under the application of a forward bias of (a) 0 V, (b) +1500 V, (c) +3000 V, and (d) +4500

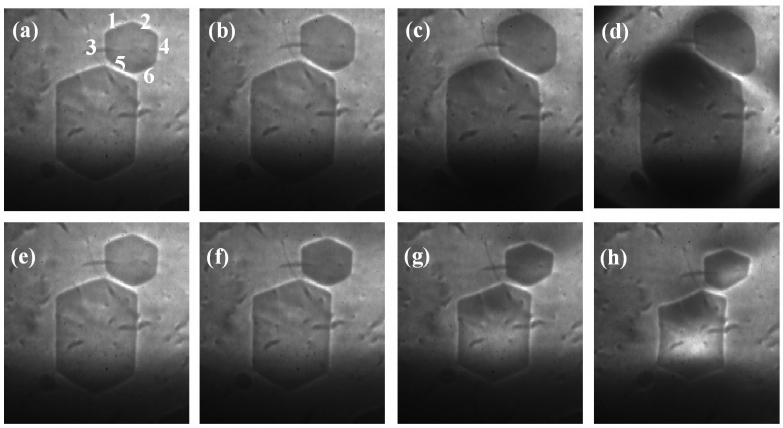

Fig. 4.26. Detail of the (00.12) Bragg topograph for positive applied voltage (forward bias) of (a) 0 V, (b) +1500 V, (c) +3000 V, and (d) +4500 V; for negative applied voltage (reverse bias) of (e) 0 V; (f) -1500 V, (g) -3000 V, and (h) -4400 V.

V. The bias was then returned to (e) 0 V, and we applied a reverse bias of (f) -1500 V, (g) 3000 V, and (h) 4400 V. The x-ray images of the hexagonal domains appear to be growing continuously from Fig. 4.26(a) to (d), and appear to be shrinking continuously from Figs. 4.26 (e) to (h).

In summary of the observed effects, large relative changes are observed in the apparent domain size as well as distance between domains as a result of applied electric fields less than the coercive field. The apparent growth or shrinkage of domain walls are never observed to cross dislocations or other defects, and the change in the apparent position of any random feature (such as a dislocation) in the images of Fig. 4.25 is directly dependent on its proximity to a domain wall.

To understand these dynamic image changes, Finite Element Method based ANSYS simulations were performed, combined with X-ray tracing simulations. The symmetry of $LiNbO_3$ is trigonal (3m). For a z-cut crystal with large surfaces normal to the z-axis, the only nonzero piezoelectric coefficient is d_{333} along the z-axis [12]. In the tensor notation, the piezoelectric strain is given by $\epsilon_{jk} = d_{ijk}E_i$, where E_i is the applied electric field, and d_{ijk} is the relevant piezoelectric tensor coefficient. For a uniform

applied field E_3, (where 3 refers to the z-axis of $LiNbO_3$, the piezoelectric strain ϵ_{33} is given by $\epsilon_{33} = d_{333}E_3$, which therefore depends on the sign of E_3 and d_{333}. The field E_3 is positive when it is parallel to the polarization direction **Ps** (+z axis) of a domain region, and E_3 is negative when it is antiparallel to $\mathbf{P_s}$. Since d_{333} is positive for $LiNbO_3$, in the forward bias field (E_3 parallel to $\mathbf{P_s}$ inside the hexagonal domains and antiparallel outside), the matrix shrinks in the z direction (negative ϵ_{33}) and the regions inside of the hexagonal domains expand along z direction (positive ϵ_{33}).

Before proceeding further with discussing piezoelectric strains, we note the distinction between piezoelectric and electrostrictive strains. Electrostrictive strain, ϵ_{el} (also called spontaneous strain) in the context of this paper, occurs due to atomic movements that give rise to a spontaneous polarization, $\mathbf{P_s}$ in the crystal and requires no external field. In calculating the strain tensor, we observe that $\epsilon_{el} \propto \mathbf{P_s^2}$. The piezoelectric strain, ϵ_p arises from the interaction between an external electric field, E and the polarization P_s,$\epsilon_p \propto \mathbf{E} \cdot \mathbf{P_s}$. Far away on either side of a 180 ° domain wall, ϵ_{el} has the same magnitude and sign; it varies only in the wall region itself, in response to the variation of the polarization magnitude. On the other hand, the piezoelectric strain, under a uniform external field, +E, though possessing symmetric magnitude about the wall center, reverses sign across the domain wall. Solving for these strains under elastic compatibility conditions, one finds that the ϵ_{el} (under no external field) is confined in width to the same length scale over which the polarization varies, while ϵ_p (under a uniform external field E) results in a broad piezoelectric shear strain, ϵ_{zn} adjacent to domain walls. The lateral width and magnitude of the piezoelectric shear strain ϵ_{zn} increases proportional to the external electric field and deforms the surface (0001) lattice planes across a domain wall. In the present case, for forward bias field, the hexagonal domain regions in lithium niobate bulge and behave like convex mirrors for x rays in Bragg geometry. This is schematically shown in Fig. 4.27. Under a reverse bias field they adopt a concave curvature and focus the diffracted x-ray beams. This is also consistent with the observation that the interior of the large hexagonal domain becomes dark under forward bias (in Fig. 4.26(d)), and bright under reverse bias (Fig. 4.26(h)).

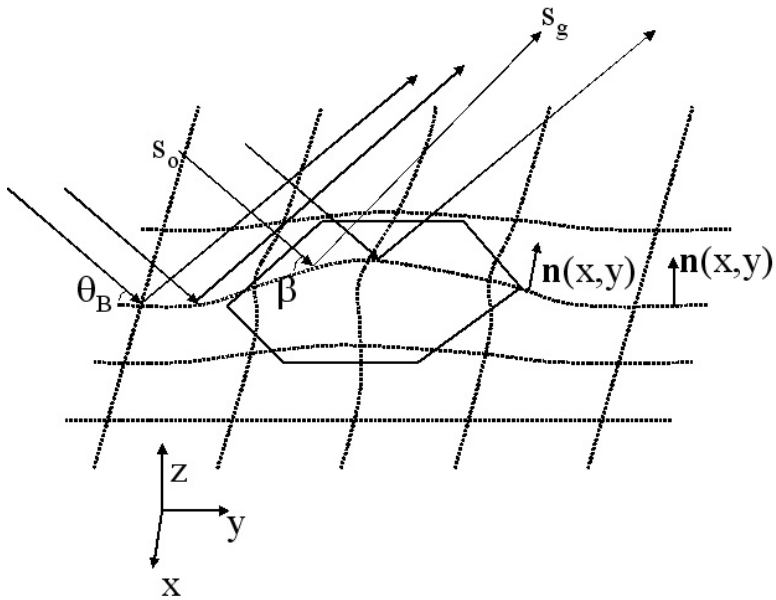

Fig. 4.27. Surface of 180 ° domain showing surface normal and the effect on kinematical diffraction of an incident x-ray beam.

To understand quantitatively the influence of piezoelectric strain at domain walls on the distortion of x-ray images in Fig. 4.26, we have performed strain calculations using commercial finite element analysis (FEA) software. As inputs to the calculation, we use reported single crystal values for piezoelectric and elastic stiffness tensor coefficients for $LiNbO_3$ [13]. We define a sharp domain wall by inverting the crystallographic z- and the y- axes across a wall. A finite sample has stress-free boundary conditions. After exact calculations of the lattice displacements at the domain walls using FEA, we calculate the lattice normal vector for (0,0,1) planes at all the walls with an external electric field. The calculated local surface lattice normal was then used as the input to a ray- tracing program, assuming kinematical diffraction to simulate the actual x-ray image of the distorted sample surface. The ray tracing is similar to a previously reported method [14] for screw dislocation analysis, assuming that the lattice distortions at the crystal surface are primarily contributing to the reflected image. We use a parallel input

beam and track the diffracted intensity based on deviation from the Bragg condition. If $\vec{K}_o$ is the incident x-ray wavevector, and $\vec{K}_G$, the diffracted x-ray wavevector, then from simple geometrical considerations,

$$\vec{K}_G = \vec{K}_G - 2\,\vec{K}_G \cdot \hat{n} \tag{4.77}$$

where $\hat{n}$ is the local unit surface normal vector for (0001) lattice planes. From the surface displacement data obtained from FEA, we calculate the surface normal vector $\hat{n}$ of the distorted surface lattice of a crystal, and trace the reflected x-ray wavevector, $\vec{K}_G$. At the detector, we simply count the arriving flux of the diffracted beam.

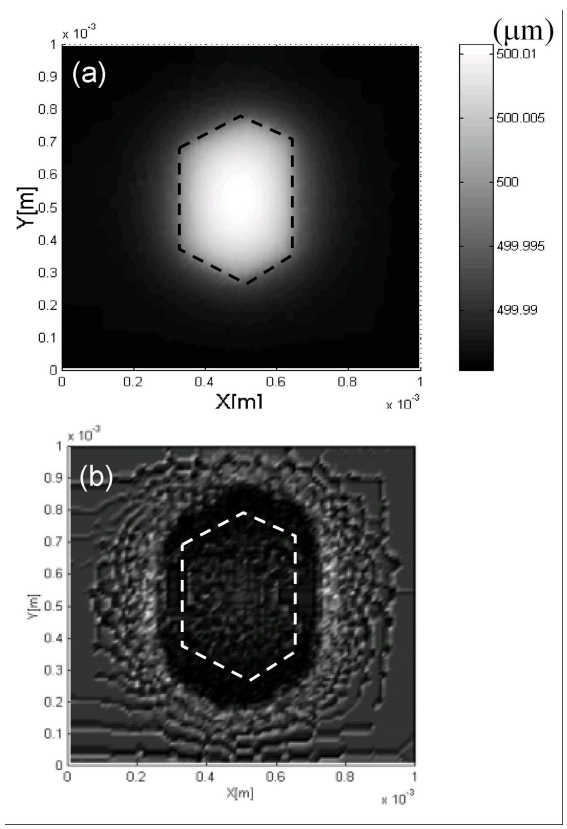

Fig. 4.28. (a) Calculated surface displacement and (b) calculated (0 0.12) diffracted ray projection from domain for V=+4400 V (forward bias).

Fig. 4.28 shows (a) the calculated strain and (b) the simulated x-ray topograph under a forward bias field of 90kV/cm. In this case, the magnitude of the normal strain ϵ_{33} is +5×10^{-5} (domain), -5×10^{-5} (matrix) and the shear strain ϵ_{zx} is $\pm 2 \times 10^{-4}$, where the piezoelectric coefficient $d_{333} = 0.6 \times 10^{-11}$ C/N. The width of the shear strain region is about 100 μm, and the step between walls is about 25 nm. The domain wall itself is located in the region of maximum shear strain, and does not actually move. The calculated strain and x-ray images demonstrate respectively, a bulge normal to the crystal surface, and the domain with apparently convex walls as was recorded with increasing field in Fig. 4.26 (b-d). The increased contrast arises primarily from the field induced piezoelectric strain at the walls. Only a shear strain component can change the shapes of x-ray domain images. As observed, this strain destroys the Bragg condition most effectively at domain wall types 1,2,5, and 6 in Fig 4.26 that are at an angle to the incidence plane. It is weak at walls 3 and 4, which are parallel to the incidence plane.

The other contrast mechanism under an external field at all wall types arises from the change in the lattice parameter c with strain ϵ_{33}. In the forward bias, c increases inside the hexagonal domains, while it decreases in the matrix domain. With a reverse field bias, the opposite is true. This lattice constant variation only changes the contrast rather than changing the image shape. A compression or expansion of the lattice parameter is the equivalent of an effective change in the Bragg angle [$\Delta\theta_B = -(\Delta c/c)tan\theta_B = \epsilon_{33}tan\theta_B$] which enhances the domain contrast. For the values of ϵ_{33} calculated above, we would expect the application of +4500 V to shift the Bragg angle by $\Delta\theta_B = \pm 40\mu rad$ for a domain and surrounding matrix, respectively. This is significant compared to the observed rocking curve width.

Simulated x-ray topographic images for the rocking curve angles $\theta_B = \pm 0.005°$ are shown in Figs. 4.29 (a) and (b). The simulated topographs accurately demonstrate the bright and dark contrast of different sets of domain walls arising from domain edge curvature effects similar to what is seen in Figs. 4.3 (a) and (c) without any external field. However, we note specifically that the domain wall curvature effects in Fig. 4.3 are under zero external electric field and are intrinsic to the material (with its point defects).

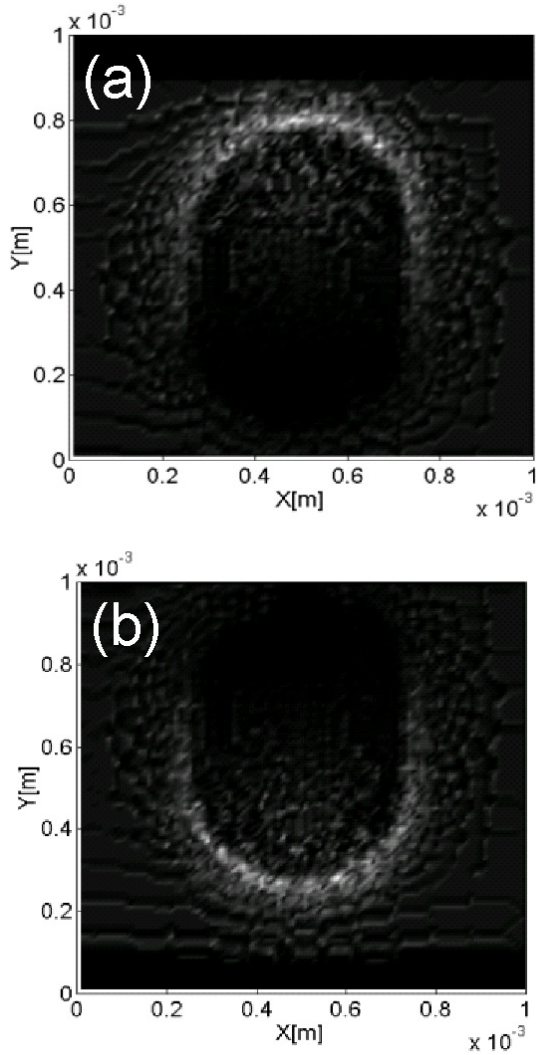

Fig. 4.29. Calculated ray projection of (0 0.12) diffraction from the vicinity of the 180° domain in Fig.4.26 for (a)$\theta = \theta_B - 0.005°$, (b)$\theta = \theta_B + 0.005°$.

The curvature effects in Fig 4.29, on the other hand, are extrinsic in that they arise from the piezoelectric effect due to the application of a uniform external electric field.

The calculated strain and simulated x-ray images under a reverse bias of 90 kV/cm are shown in Figs. 4.30 (a) and (b) respectively. In addition to a dimpling of the surface

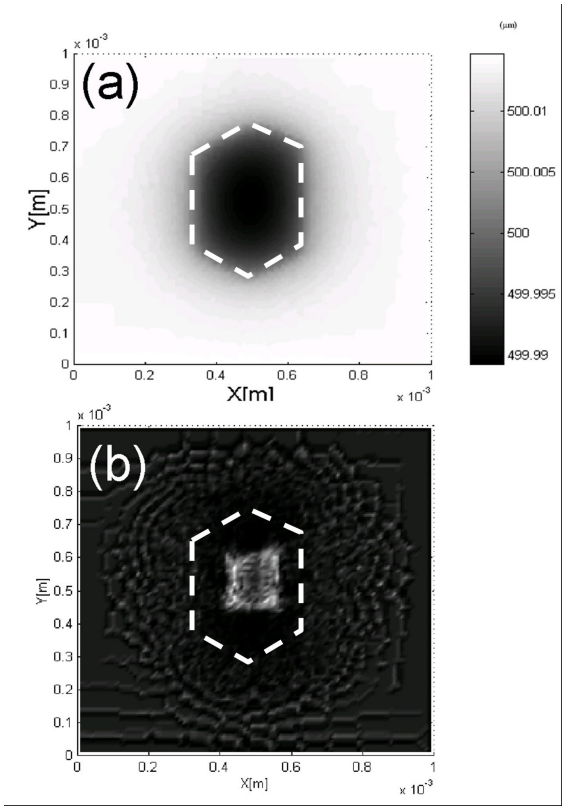

Fig. 4.30. (a) Calculated surface displacement and (b) calculated (0 0.12) diffracted ray projection from domain for V=-4400 V (reverse bias).

rather than a bulge, the calculations indicate that domain walls would appear concave as was recorded with increasing reversed field in Fig. 4.26 (f-h).

A careful quantitative analysis of the data, however, reveals that the extent of expansion or contraction in the simulated image exceeds that seen in experiments, suggesting that the actual experimental surface displacements and shear strains at the domain walls may be smaller than the values calculated from the FEA simulation. The surface displacements and strains were obtained from the measurements of the experimental images. Starting with Fig. 4.26(a) that corresponds to zero field-induced strain as the reference, and comparing with the strained images 4.26(d) and 4.26(h), we measured the displacement at every point on a horizontal line scan across the large

hexagonal domain, tracking the movement of dislocations and defects. This is shown in Figs. 4.31(a) (forward bias) and 4.32(a) (reverse bias) for image strains extracted from Figs. 4.26(d) and 4.26(h), respectively, along with smooth spline fits. The domain wall piezoelectric strain width as determined by this transition appear to be of the order of 100 μm thick.

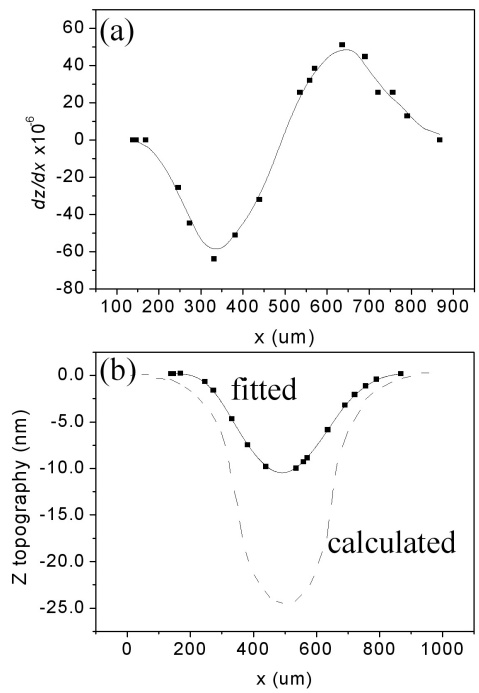

Fig. 4.31. (a) Surface strain with forward bias measured by a displacement of details between Fig. 4.26(d) and Fig. 4.26(a) by a line scan across a 180° domain in $LiNbO_3$. The line is a spline fit to the measured points. (b) Positive surface displacement (solid line) derived by integrating the curve 4.31(a). The dashed line is the predicted effect using bulk coefficients and a finite element calculation at room temperature.

Applying our ray-tracing in reverse from the image plane to the sample surface, we calculated the surface normal vector $\mathbf{n}=-f_x\mathbf{i}-f_y\mathbf{j}+\mathbf{k}$, using Eq. 4.77, where $f_x = \partial z/\partial x$,

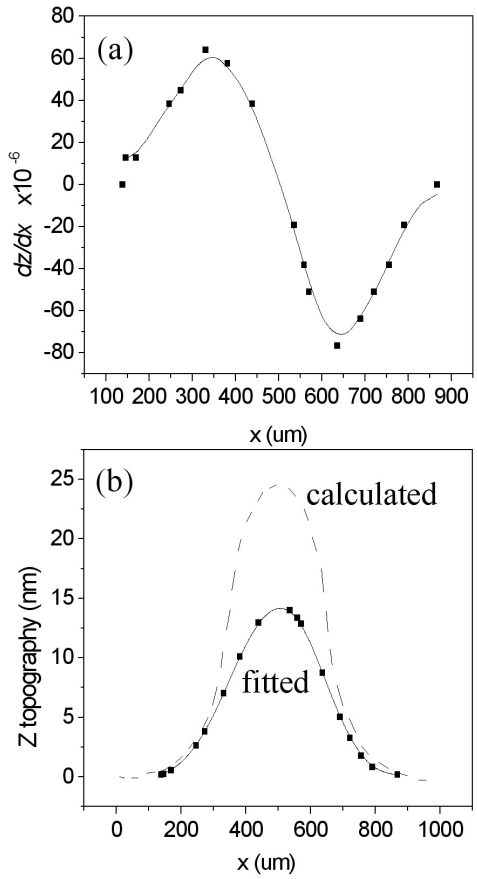

Fig. 4.32. (a) Surface strain with reverse bias measured by a displacement of details between Fig. 4.26(h) and Fig. 4.26(a) by a line scan across a 180° domain in $LiNbO_3$. The line is a spline fit to the measured points. (b) Negative surface displacement (solid line) derived by integrating the curve 4.32(a). The dashed line is the predicted effect using bulk coefficients and a finite element calculation at room temperature.

$f_y = \partial z/\partial y$, and (**i**,**j**,**k**) are unit vectors along the crystallographic directions **x**, **y**, and **z** of the matrix domain. For $LiNbO_3$, the domain walls are y-walls , and therefore f_y=0. The surface normal is therefore determined only by the shear strain f_x, given by

$$f_x = \frac{-sin\theta_B \cdot l_0 \pm \sqrt{sin^2\theta_B \cdot l_0^2 - \Delta^2 \cdot cos^2\theta_b \cdot (cos^2\theta_B - sin^2\theta_B)}}{cos^2\theta_B - sin^2\theta_B} \tag{4.78}$$

where l_0 is the distance between sample and detector, Δ is a topography image change between applied voltage and without external field along x direction. The derivation of the above expression is given in Appendix B.

This vector gives the shear strain components, ϵ_{zx}, and the integration of the components gives the profile of the bulge or depression of the domain under the influence of the applied field. Fig. 4.31(b) (solid line) shows the surface domain expansion deduced by integrating the profile in Fig. 4.31(a). For comparison, the surface expansion calculated from the FEA program for forward field bias is shown as well (dashed line). Fig. 4.32(b) shows the measured surface displacement (solid line) for the reverse bias obtained by integrating the curve in Fig. 4.32(a) compared with the value from the FEA calculation (dashed line). Even for a 400 μm wide domain, the maximum displacements observed experimentally, +14nm and -11 nm, for the forward and reverse bias fields, are only 0.56 and 0.44 respectively, of the calculated values using bulk piezoelectric and elastic constants. The shear strains, ϵ_{zx} observed experimentally are also suppressed compared to the bulk predictions. The overall experimental piezoelectric response appears then to be significantly lower in magnitude than the calculated response for a single crystal with a uniform d_{333} coefficient throughout and 400 μm wide inverted domain region.

There are several reasons to consider for this discrepancy. One possibility is that localized charge states near the surface of the crystal screen the bulk applied field in the region between the electrodes by more than a factor of two. A second possibility is that absorbed x-rays from the intense x-ray beam during the application of the electric field could also locally screen the electric field by creating electron-hole pairs in the material. Though we did observe some photoconductive current with x-rays [15], we were able to rule out a large effect due to this type of screening by measurements with similar graphite electrodes on thinner crystals. In those instances, the measured coercive field for permanent domain reversal under x-ray illumination was close to the actual reported

value with water-based electrodes without x-rays. A third possibility is that the size of the domain may play a role in the mechanical clamping of the displacement, thus suppressing it. This mechanical compatibility condition is accounted for by FEA, unless the input material parameters are different from the bulk.

It is worth considering the possibility that perhaps the piezoelectric coefficients d_{333} are lower (by about 2), and/or the stiffness coefficients, C_{3333} are higher, in the vicinity of a domain wall. The presence of local strain and wall structure even in the absence of external field (Fig. 4.3) arising from point defects in these crystals suggests that the variation of defect fields across a wall may play some role in the observed suppression of lattice displacement near the walls. Finally, there is also the possibility of field-induced broadening of the polarization gradient at a domain wall, as has been recently proposed [16]. Since the piezoelectric coefficient, d_{333} is linearly proportional to the spontaneous polarization, $\mathbf{P_s}$, a broadened polarization gradient across a domain wall that goes through zero at the center of the wall can locally induce a gradient of d_{333} coefficient across the wall as well, thus suppressing the overall piezoelectric response in that region. Pernot-Rejmnkov, Laprus, and Baruchel have previously described an overall curvature of congruent $LiNbO_3$ resulting in x-ray focusing which did not include the effect of visible stable domains [12]. That effect was observed in fields applied across x- and y-cut crystals but not z-cut crystals and their explanation requires the assumption of an inhomogeneous crystal. The behavior observed here in a z-cut crystal was consistent with the assumption of a single piezoelectric coefficient.

References

[1] B. D. Cullity. *Element of X-ray diffraction*. Addison-Wesley, 1978.

[2] DAndre Authier. *Dynamical Theory of X-Ray Diffraction*. OXFORD SCIENCE PUBLICATIONS, 2001.

[3] A. Gerrard and J. M. Burch. *Introduction to Matrix Methods in Optics*. Dover Publications, 1994.

[4] K. Kitamura Y. Furukawa Sungwon. kim, V. Gopalan. Domain reversal and non-stoichiometry in lithium tantalate. *J. Appl. Phys*, 90:2949, 2001.

[5] T. J. Yang and U. Mohideen. *Physics Letters A*, 250:205, 1998.

[6] B. K. Tanner. *X-Ray Diffraction Topography*. PERGAMON, 1976.

[7] D.Keith Bowen and Brian K. Tanner. *High Resolution X-Ray Diffractometry and Topography*. TAYLOR and FRANCIS, 1998.

[8] D. Keith Bowen and Brian K. Tanner. *"High Resolution X-Ray Diffractometry and Topography". Electronics and Communications in Japan Part2*, 81(5):9–15, 1998.

[9] Penning. P and Polder. D. *Philips. Res. Repts*, 16:419–440, 1961.

[10] Kato. N. *J. Phys. Soc. Jap*, 18:1785–1791, 1963.

[11] Y. Furukawa K. Kitamura V. Gopalan, T. E. Michell. *Appl. Phys. Lett*, 72:1981, 1998.

[12] J. Baruchel P. Pernot-Rejmankova, W. Laprus. *Eur. Phys. AP*, 8:225, 1999.

[13] K. H. Hellwege. *Landolt-Bornstein. Numerical Data and functional relationships in science and technology*. Springer-Verlag Berlin, 1961.

[14] W. M. Vetter W. Huang W. Si C. H. Carter,Jr X. R. Huang, M. Dudley. *J. Appl. Cryst*, 32:516, 1999.

[15] S. Durbin V. Gopalan D. Bright T. Jach, S. Kim. *Fundamental Physics of Ferroelectrics*, 626:269, 2002.

[16] A. Gruverman S. Kim, V. Gopalan. *Appl. Phys. Lett.*, 80:2740, 2002.

Chapter 5

Local Optical Properties of a Domain Wall

5.1 Overview of Near-field Scanning Optical Microscopy

This chapter describes the qualitative and quantitative probing of the local optical properties of a single 180 degree domain wall in single crystals of lithium niobate and lithium tantalate. The primary experimental tool used in this study is Near-field Scanning Optical Microscopy (NSOM).

After the first demonstration of NSOM in bell labs in 1982 [1], extensive experimental and numerical research has been carried out in this area. NSOM can perform most of the traditional optical microscopy functions, but with enhanced resolution upto 40nm length scales. From the simplest linear optical reflection and transmission microscopy, to nonlinear optical [2], femto second pulse, [3] [4] and heterodyne experiments [5], many conventional optical measurement methods have been adapted to the NSOM system. Figure 5.1 shows the overall schematic of an NSOM system. [Ref] The essential component of NSOM is a tapered fiber tip with a sub-wavelength aperture of ≈40nm at its end. Light is either forced through the fiber tip or collected through it. The tip is scanned within ≈20nm over the surface of a sample, and either reflected or transmitted light is used to image the optical properties of the sample. Simultaneously, an electrical feedback circuit allows the fiber tip to follow the surface contours, [6] and therefore provides the surface topography image as well. Based on its modes of operation, NSOM is categorized as *collection mode*, or *illumination mode*. In the illumination mode, the input laser signal is forced through the fiber tip aperture. If the desired optical signal is collected through NSOM tip aperture instead, it is called the collection mode. The spatial resolution in both illumination and collection modes is determined by size of the fiber tip aperture. Current technology can easily make aperture size as tens of nanometers [7]. There are various methods to make nano aperture by using optical

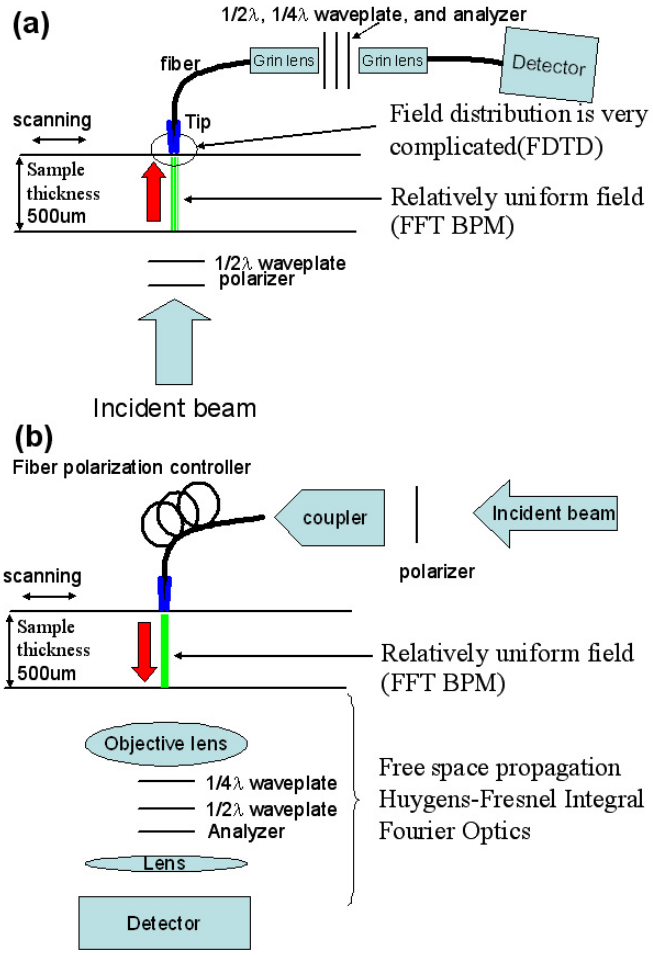

Fig. 5.1. Schematic of an NSOM system for (a) collection and (b) illumination mode with the adopted simulation method

fibers. The most common method is to heat an optical fiber locally using a CO_2 laser, while it is simultaneously stretched till the point of necking and ultimate breakage, resulting in an ≈40nm aperture at the end of the tapered tip [8]. Another frequently used method is chemical etching [9] [10]. A drawback of these optical fiber tips is the leakage of light around the fiber taper before it exits the tip. To confine light inside the tapered aperture, the taper wall of the fiber is coated with a thin metal film of ≈100nm. However, this additional coating degrades the topological resolution to 100nm scale,

as well as effects the optical resolution of the images. To overcome this disadvantage, apertureless NSOM imaging methods is currently being explored [11] [12] [13]. In this dissertation, NSOM has been used with a tapered fiber tip coated with 100nm film of aluminium.

Even though extensive research has been carried out using NSOM, there is still no standard method to analyze the NSOM images. The inverse problem in simulation is to start from the image and extract the optical characteristics of the sample studied (index and absorption profiles, for example) by tracking the light in reverse through the entire NSOM imaging process. A key element in solving this is the *transfer function* of the tip, which determines how the amplitude and phase of light is affected by passing from outside into the sub-wavelength fiber tip, or vice versa. There has been a significant research effort to calculate the transfer function to calculate the inverse problem and estimate the spatial resolution. If we can successfully estimate the transfer function, we can calculate the actual field distribution underneath the aperture by using the measured electric field amplitude and phase during imaging. This transfer function itself gives the NSOM spatial resolution, because the inverse Fourier transform of this transfer function is the point-spread function(PSF). This point spread function is delta source response, whose full width half maximum (FWHM) gives the spatial resolution. However, to calculate the transfer function is not a trivial process, especially if the sample surface has large topological variations. Transfer function concepts are based on the *linearity* properties of the tip. It means that for different tip locations over the sample, the tip and the sample interaction changes, resulting in a different transfer function, and therefore, a different proportion in which the amplitude and phase of light enters or exits the fiber tip near the sample. If the sample surface has strong topological variations, the tip and the sample surface interaction is not linear. Even though theoretically, a general transfer function cannot exist, within some restrictions, certain averaged transfer functions can be defined [14] [15] [16]. Other research groups have already shown that in the case of weak topological variations, one can introduce pseudo-transfer function concepts. To numerically calculate these transfer functions, many numerical methods and assumptions have been tried [17] [18] [19] [20] [21] [22] [23].

Among the numerous numerical techniques, Finite Difference Time Domain [24] [25] method (FDTD) is the most versatile and accurate of tools. It can account for the metal coating around the tip, the complex geometries near the tip-sample region, the exact phase information, short laser pulse experiments, nonlinear optical responses from the sample, etc [18] [19] [20] [21]. The primary drawback is the calculation domain size, which is practically limited to regions of the order of 100x100 wavelengths of light. To calculate larger areas of optical wave propagation, other methods should be linked with FDTD. In this dissertation, I have introduced a hybrid method that seamlessly tailors together FDTD and Beam Propagation Method (BPM) [26] for calculating accurately, large area responses of sample to optical signals.

By using fiber-aperture NSOM, ferroelectric domains have been imaged in this work in both collection (Ch. 5.4) and illumination geometries(Ch. 5.5). Also by applying electric fields to the sample while performing NSOM imaging, we study the domain wall response to electric fields(Ch. 5.6). By combining these above experiments, with simulations using FDTD(Ch. 5.2) and BPM numerical methods(Ch. 5.3), we quantitatively map the refractive index profiles at individual ferroelectric domain walls in $LiNbO_3$ and $LiTaO_3$ single crystals. We begin, however, by first calculating the transfer function for our experimental geometry in Ch. 5.2.

5.2 NSOM transfer function calculation using FDTD method

To understand the data collection process in NSOM, and estimate the resolution of the process, many numerical methods have been applied. The most common and early approach was to calculate the optical response at a step topology, as a function of sample refraction index, tip sample distance, and step height [27] [28]. This kind of approach is, however, very restrictive for general applications. Every different scanning and sample condition would require a different simulation. For a more general appoach, the optical transfer function concept is required. In many experimental cases, the optical signal is generated inside a dielectric sample, or as in our present case of domain wall probing, the incident beam is modulated in passing through a dielectric sample. In these cases, a lot of signal may not even reach the detector, because of a large component of

evanescent waves in the modulated signal. In particular, if the incident angle is larger than the critical angle for total internal reflection from the dielectric sample surface, only evanescent waves exist outside the sample surface. If the detector is close to the sample surface, some of the evanescent waves can be coupled into the fiber tip aperture, resulting in enhanced resolution. Especially in ferroelectric domain imaging experiments in the *collection* mode geometry described further on, most of the optical signal is modulated while it is propagating through the sample thickness as shown in figure 5.2(a). When sample surface is very flat and has a homogeneous dielectric

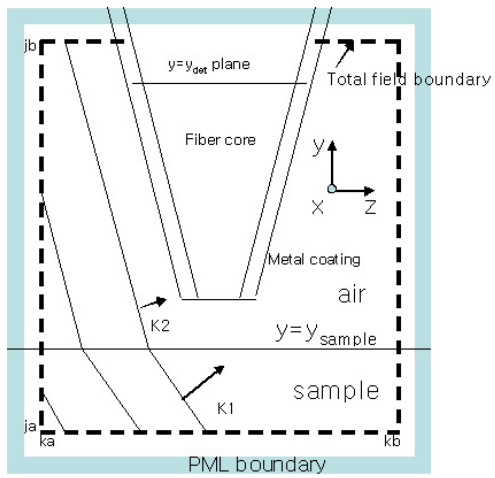

Fig. 5.2. FDTD NSOM tip simulation diagram

constant, the tip and sample interaction becomes linear. Theoretically, in such a case, a transfer function does exist. In ferroelectric domain wall imaging experiments, the sample surface has no strong topography, (1-2nm steps reported earlier [29]) and the index contrast at the domain wall is small ($\approx 10^{-4}$). Therefore, a numerical transfer function can be introduced in our case. We describe below, such a calculation for *collection mode geometry*, where light first passes through the sample and is then collects by the fiber tip.

In order to numerically calculate this transfer function, FDTD method is used in this work. FDTD method can calculate very complicated geometries with good accuracy. A 3- dimensional FDTD code was written for this purpose based on MATLABR. This code includes Perfect Matching Layer (PML) boundary conditions, and multi-incident beam method for Total/Scattering field simulation in a inhomogeneous medium. To directly calculate the transfer function in the spatial frequency domain, we activate different incident angle plane waves, with wavevector k_1 underneath the sample surface. After those plane waves hit the sample surface, FDTD code activates a second set of waves (wavevector k_2) in accordance with the analytical solutions. When the incident angle, θ, is smaller than the critical angle $sin^{-1}(1/n)$ at the sample/air interface, the wavevectors k_1 and k_2 are related through Snell's law, given by $k_1 \cdot \sin\theta = k_2 \cdot \sin\theta_t$, where $\theta(t)$is the transmitted angle from the surface normal. If the incident angle, θ, is higher than the critical angle, the transmitted k_2 wave become an evanescent wave. Equations 5.1 to 5.2 analytically describe these evanescent waves on sample surface. The electric fields, $\vec{E}(\vec{r})$ and magnetic fields, $\vec{H}(\vec{r})$, of the evanescent waves as a function of spatial coordinates, $\vec{r}$, are given as

$$\vec{E}_{TE}(\vec{r}) = E^i_{TE}\frac{2\cos\theta}{\cos\theta - i\sqrt{\sin^2\theta - n^{-2}}} \cdot exp(-y/d_p) \cdot \vec{e}_x \tag{5.1}$$

$$\vec{H}_{TE}(\vec{r}) = H^i_{TE}\frac{2\cos\theta \cdot (\sin\theta \cdot \vec{e}_y + i\sqrt{\sin^2\theta - n^{-2}} \cdot \vec{e}_z)}{\cos\theta - i\sqrt{\sin^2\theta - n^{-2}}} \cdot exp(-y/d_p) \tag{5.2}$$

$$\vec{E}_{TM}(\vec{r}) = E^i_{TM}\frac{-2\cos\theta \cdot (\sin\theta \cdot \vec{e}_y + i\sqrt{\sin^2\theta - n^{-2}} \cdot \vec{e}_z)}{n^{-2}\cos\theta - i\sqrt{\sin^2\theta - n^{-2}}} \cdot exp(-y/d_p) \tag{5.3}$$

$$\vec{H}_{TM}(\vec{r}) = H^i_{TM}\frac{n^{-2}\cos\theta}{n^{-1}\cos\theta - i\sqrt{n^2\sin^2\theta - 1}} \cdot exp(-y/d_p) \cdot \vec{e}_x \tag{5.4}$$

those field decaying exponentially with d_p decaying constant.

$$d_p = \frac{\lambda}{2\pi\sqrt{n^2 \sin^2\theta - 1}} \tag{5.5}$$

The polarizations of light can be either transverse electric, (subscript TE), or transverse magnetic, (subscript TM). The incidence plane in figure 5.2 is y-z. The TM polarization incident wave has E_y, E_z, H_x components and the TE polarization has E_x, H_y, H_z components. Monochromatic incident light has a wavelength λ=600nm in air, and the sample index n is varied between 2.286 and 2.386 for all directions. The fiber core is assumed to have an isotropic refraction index coefficient of 1.586. Tip taper slope is set to 70°. A total of 3000 time steps is used for each simulation. Because of the computational size, simulation beyond the fiber taper was not possible. Our simulation domain size was $2\times2\times2\mu m$, with an overall simulated taper length of $\approx 1.7\mu m$. In all the simulation domains used, we observed good convergence of the field behavior well within the taper, as will be shown later. Typically, in most cases, the field values reached a steady state value after 1000 time steps. However, for time-domain fourier transform, we used the time domain data only after >2500 time steps. We generated individual plane waves k_1 with incident angles from the surface normal varying between 0°-80°. The phase of each incident plane wave was phase locked at 0° at the phase reference point, r_0, that lies at the intersection of the y=y_{sample} surface and the axis of the fiber tip.

As an example, Figure 5.3 shows the simulation results for $\theta = 0°$ and 40° incident angles using a TM wave. Surprisingly, the field distribution of the main polarization, E_z parallel to the interface is similar for any incident angle case, as shown in figure 5.3(a), and (c). When this simulation data is collected at a plane closer to the fiber aperture, the field distributions become different for different incident angles. This can be easily understood by seeing the phase distribution of the electric field component E_z on the yx plane (figure 5.3(b,d)) which contains the axis of the tip. The phase distribution is quite complicated near the tip aperture, but after some propagation distance through the fiber tip, these fields are strongly guided by the metal coating. After about y=100(grid number from the bottom of simulation domain), we can see a linear phase change with distance as shown in figure 5.3 (b,d). We can assume that after y=100, no additional

phase difference will be accumulated between individual plane waves coupled within the taper. Another important result of this simulation is that most of the energy flow into the detector depends mostly on the main polarization component(component with the maximum magnitude of the field). In TE mode case, $E_x \cdot H_y$ poynting vector component is much stronger than $E_z \cdot H_x$, but $E_z \cdot H_x$ component becomes dominant in TM mode case. This ratio between the main polarization and minor polarization components is higher than 98 percent in both TE and TM modes. Based on FDTD simulations, we can

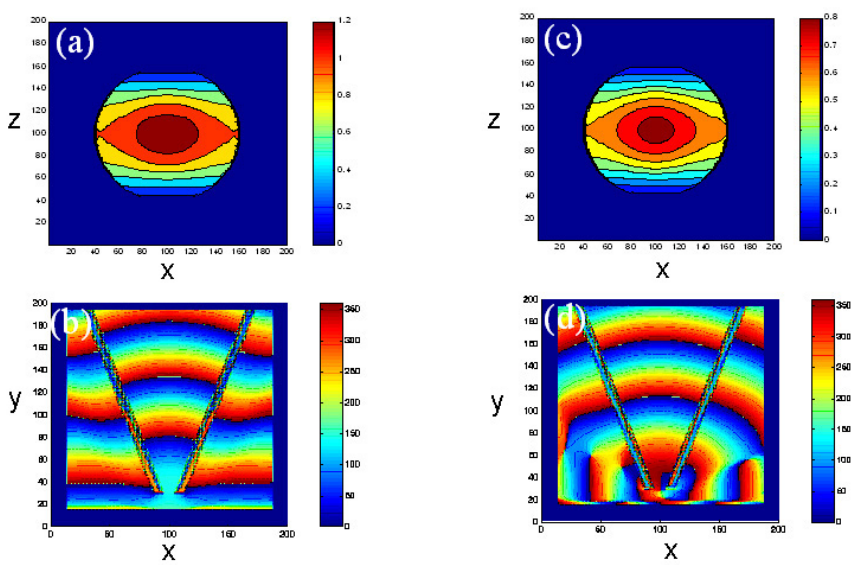

Fig. 5.3. NSOM Field distributions TM polarized light of 600nm, for $\theta = 0°$ (a,b)and $\theta = 40°$ (c,d). The steady-state electric field amplitude, E_z, inside the taper is shown in (a,c). The phase of light is shown in (b,d).

summarize that the main polarization components E_x, and H_z in TE mode, E_z, and H_x in TM mode are quite similar in their overall shape of field distribution at y=y_{det} plane for all incident angles considered. All the phase difference between individual plane waves is induced before y=100, and after that point, there is no additional phase delay

accumulation, and finally the energy flow inside the fiber is mainly dominated by the main polarization component.

Now the complex NSOM data collection process can be explained by the collected magnitude and phase information of each main polarization field component. To calculate the final detector response for individual plane waves, we need only the magnitude function $\widetilde{M(k)}$ and the phase function$\widetilde{\Phi(k)}$, both of which are measured at the center point on the y=y_{det} plane, instead of requiring the complete field distribution at that plane. Fig 5.4 (a) shows these functions, $\widetilde{M(k)}$ and $\widetilde{\Phi(k)}$, for the main polarization field for the TE and the TM modes. The X-axis represents incident angle which is equivalent to the spatial frequency k_x=$2 \cdot \pi \cdot n \cdot \sin\theta/\lambda$. The maximum value of k_x in our simulation is $2 \cdot \pi$n/λ, because only propagating incident waves can be simulated. We extrapolate $\widetilde{M(k)}$ and $\widetilde{\Phi(k)}$ data to get higher spatial frequency data than n$\cdot 2 \cdot \pi/\lambda$ assuming it is decaying exponentially. Spatial frequencies higher than n$\cdot 2 \cdot \pi/\Lambda$ do not contribute much to the actual signals because of their small magnitude. We note that for both TE and TM modes (Figure 5.4), there is finite coupling magnitude even beyond the critical angle for total internal reflection. This occurs due to the coupling of the evanescent wave into an NSOM tip. This coupling becomes weaker if the tip-sample distance increases. In this simulation, the critical angle $\theta = 25.9410^\circ$ or $\theta = 24.7785^\circ$ for n=2.286, and n=2.386, respectively. Around this critical angle, the TE mode has a very strong peak in the magnitude transfer function. This is due to the high transmitivity of the TE mode near the critical angle. After the critical angle, the magnitude of the transfer function decreases exponentially, because the incident beam becomes an evanescent wave at the dielectric/air boundary. Surprisingly, the phase function shows a very strong dispersion as the spatial frequency increase. Since the phase difference for different plane wave components can reach and exceed a phase shift of π, it implies that there will be some destructive interference processes. This phase dispersion strongly limits the NSOM spatial resolution. Now the complex NSOM data collection process can be explained by the collected magnitude and phase information of each main polarization field component. To calculate the final detector response for individual plane waves, we need only the magnitude function $\widetilde{M(k)}$and the phase function$\widetilde{\Phi(k)}$, both of which are

measured at the center point on the y=y_{det} plane, instead of requiring the complete field distribution on that plane. Fig 5.4 (a) shows these functions, $\widetilde{M(k)}$ and $\widetilde{\Phi(k)}$, for the main polarization field for the TE and the TM modes. The X-axis represents incident angle which is equivalent to the spatial frequency k_x=$2 \cdot \pi \cdot n \cdot \sin\theta/\lambda$. The maximum value of k_x in our simulation is $2 \cdot \pi$n/λ, because of only propagation incident wave can be simulated. We extrapolate $\widetilde{M(k)}$ and $\widetilde{\Phi(k)}$ data to get higher spatial frequency data than n$\cdot 2 \cdot \pi/\lambda$ assuming it is decaying exponentially. Spatial frequencies higher than n$\cdot 2 \cdot \pi/\Lambda$ do not contribute much to the actual signals because of their small magnitude. We note that for both TE and TM modes (Figure 5.4), there is finite coupling magnitude even beyond the critical angle for total internal reflection. This occurs due to the coupling of the evanescent wave into an NSOM tip. This coupling becomes weaker if the tip-sample distance increases. In this simulation, the critical angle $\theta = 25.9410°$ or $\theta = 24.7785°$ for n=2.286, and n=2.386, respectively. Around this critical angle, the TE mode has a very strong peak in the magnitude transfer function. This is due to the high transmitivity of the TE mode near the critical angle. After the critical angle, the magnitude of the transfer function decreases exponentially, because the incident beam becomes an evanescent wave at the dielectric/air boundary. Surprisingly, the phase function shows a very strong dispersion as the spatial frequency increase. Since the phase difference for different plane wave components can reach and exceed a phase shift of π, it implies that there will be some destructive interference processes. This phase dispersion strongly limits the NSOM spatial resolution.

The tip coupling ratio diagram in Fig. 5.4 can indeed be interpreted as the *transfer function* of the NSOM tip because of the assumed linear response of the tip-sample interactions. We can easily prove that this tip response function is the *true* transfer function. The spatial Fourier transform of the product of the incident field with this transfer function gives the phase and magnitude information of the individual plane wave components. First let's get all plane wave components of incident field E(r) on y=y_{sample} plane by using Fourier transform.

$$\tilde{E}(k)_{reference=r_0} = \int E(r) \cdot exp(-ikr) \cdot dr \tag{5.6}$$

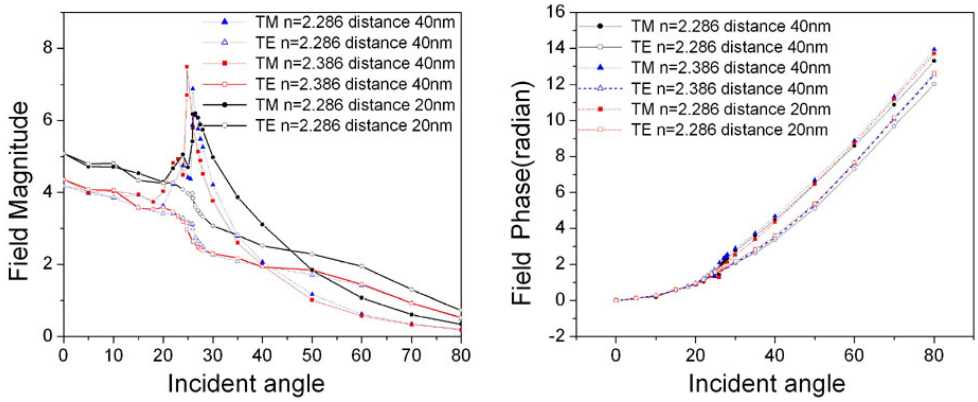

Fig. 5.4. Magnitude and Phase Transfer function

If the tip is exactly located on top of this reference point r=r_0, then total coupling field S(r=r_0) will be a summation of multiplexing of plane wave component with complex tip response function $\tilde{T}(k) = \tilde{M}(k)\exp(i\tilde{\phi}(k))$.

$$S_{r=r_0} = \int \tilde{E}(k)_{reference=r_0} \cdot \tilde{M}(k) \cdot \exp(i\tilde{\phi}(k)) \cdot dk \tag{5.7}$$

If the tip is moved to r=r_t positions for scanning, then the new tip coupling field $S_{r=r_t}$ will be

$$S_{r=r_t} = \int \tilde{E}(k)_{reference=r_t} \cdot \tilde{M}(k) \cdot \exp(i\tilde{\phi}(k)) \cdot dk \tag{5.8}$$

In the above step, we have made use of the fact that because of linearity, we can use the same tip response function $\tilde{M}(k)\exp(i\tilde{\phi}(k))$ at r=r_t. Therefore, the new plane wave component referenced at $r = r_t$ point can be written as,

$$\tilde{E}(k)_{reference=r_t} = \int E(r - r_t) \cdot exp(-ikr) \cdot dr = E(k)_{reference=r_0} \cdot exp(-ikr_t) \tag{5.9}$$

Now, we can rewrite the total coupling field

$$S_{(r=r_t)} = \int \tilde{E}(k)_{reference=r_0} \cdot \tilde{M}(k) \cdot \exp(i\tilde{\phi}(k)) \cdot exp(-ikr_t) \cdot dk \tag{5.10}$$

Because of the symmetrical tip structure $\tilde{M}$(k) and $\tilde{\phi}$(k) can be considered as symmetrical functions. Then $S_{(r=r_t)}$ can be rewritten as

$$S_{(r=r_t)} = \int \tilde{E}(k)^*_{reference=r_0} \cdot \tilde{M}(k) \cdot \exp(i\tilde{\phi}(k)) \cdot exp(ikr_t) \cdot dk = \Im^{-1}(\tilde{E}(k)^*_{reference=r_0} \cdot \tilde{T}(k)) \tag{5.11}$$

The above equation states that the total field response at any point $r = r_t$ is simply the inverse Fourier transform of the product of the reference field at $r = r_o$ and the total transfer function $\tilde{T}(k)$. We have therefore proven that complex tip response function $\tilde{T}(k) = \tilde{M}(k)\exp(i\tilde{\phi}(k))$ is indeed the true transfer function. The inverse Fourier transform of this transfer function yields the point spread function. This point-spread function is actually the tip response to a delta function source. By calculating FWHM, we can get NSOM tip spatial resolution. Figure 5.5 shows several point spread functions and their FWHM values. For any tiny light *source* such as biological cells, or quantum well lasers located inside the sample beneath the sample surface, the maximum resolution for our simulation conditions of n=2.286, and tip sample distance 20nm will be 360nm. The primary reason for lower resolution than the actual NSOM aperture size is that the components of light source incident at the sample air interface at angles greater than the the critical angle $\arcsin(1/n)$ become evanescent waves at the air-sample boundary. Even though these evanescent waves are collected to tip, they have a stronger phase dispersion and a weaker collection efficiency. In general therefore, whenever a light source or signal originates inside a high dielectric constant (high index) medium, it's resolution is limited by the critical angle.

In summary, a successful calculation of the NSOM transfer function and the point spread function has been demonstrated here, for the case of a flat sample surface and an embedded light source. Even though this model uses the most simple of sample-tip interactions, it gives a fundamental understanding of the NSOM data collection process

and the limitations of spatial resolution. This resolution is strongly limited by the phase dispersion of the light collected by the NSOM tip as well as by the critical angle for total internal reflection determined by the sample refractive index.

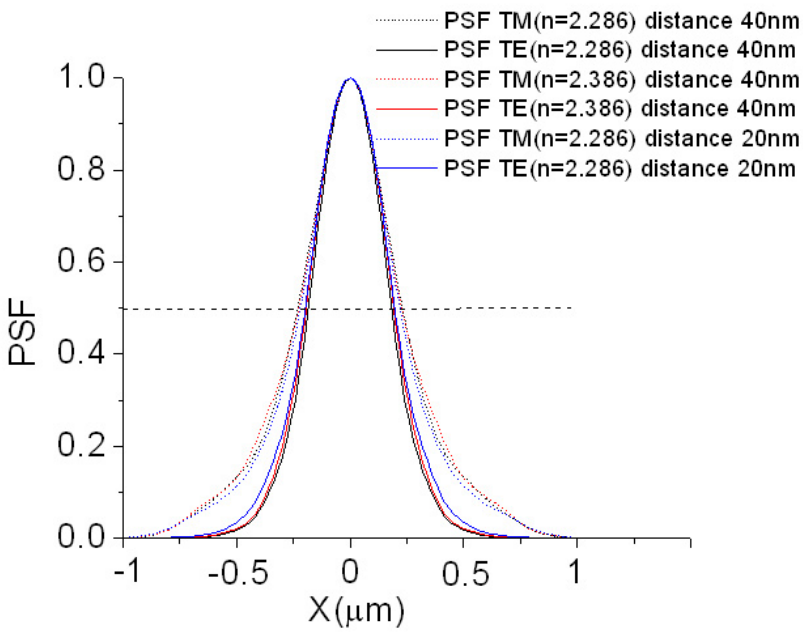

Fig. 5.5. Point Spread Function=$\left|\Im^{-1}(\tilde{T}(k))\right|$: dash line corresponds to half maximum line

5.3 BPM wave modeling

Although FDTD modeling is very accurate and accommodates complex sample topology, scattering, and non linearity, a limitation is that it can only simulate relatively small areas of the order of 10x10x10 wavelengths in order to keep the computation time reasonable. However, in domain imaging experiments described below in both

collection and illumination modes, the domain wall image is built up while the beam is traveling the crystal along the z or thickness direction. This distance is usually of the order of 300-500 μm range. However FDTD can only compute light travel within a few μm scale.

In order to handle light propagation over larger distances farther from the near-field optical tip, another numerical method called the Beam Propagation Method (BPM) is chosen in this study. Beam Propagation uses scalar Helmholtz equation which is much simpler than the vectorial Maxwell's equations. A MATLAB based Fourier Transform Beam Propagation Method (FFT-BPM) code was written for this purpose to simulate experimental NSOM images. Appendix E shows the detailed MATLAB code developed here. This FFT-BPM [26] code is based on three dimensional scalar Helmholtz equation.

$$\frac{\partial^2 E}{\partial z^2} + \nabla_t^2 E + k_0^2 n^2(x, y, z)E = 0 \tag{5.12}$$

E is the transverse scalar field component, $k_0$is free space wavevector, n is refractive index, and ∇_t^2 is defined by

$$\nabla_t^2 = \frac{\partial^2}{\partial x^2} + \frac{\partial^2}{\partial y^2} \tag{5.13}$$

if $\partial(n^2)/\partial z \cong 0$, the traveling wave solution to 5.12 has the same behavior as the solution of the first order partial differential equation

$$\frac{\partial E}{\partial z} = -j(\nabla_t^2 + k_o^2 n^2)^{1/2} E \tag{5.14}$$

The field, E can be expressed as the product of a slowly varying complex amplitude E and a fast changing term exp(-j$k_o n_o$z) with respect to the propagating z direction

$$E = E(x, y, z) exp(-jk_o n_o z) \tag{5.15}$$

by using Eq. 5.14 we can get

$$\frac{\partial E}{\partial z} = -j[(\nabla_t^2 + k_o^2 n^2)^{1/2} - k_o n_o]E \tag{5.16}$$

here n_o is averaging homogeneouse refraction index. Equation 5.16 can be rewritten as

$$\frac{\partial E}{\partial z} = -j[\frac{\nabla_t^2}{(\nabla_t^2 + k_o^2 n^2)^{1/2} + k_o n_o} + k_o(n - n_o)] \tag{5.17}$$

The propagating wave is calculated by dividing it into the homogeneous medium diffraction part and phase rotation effect as can be seen in Eq. 5.18.

$$E(x, y, \Delta z) = exp(-k_o(n - n_o)\Delta z) \int \tilde{E}(k_t) exp(\frac{jk_t^2}{(k_o^2 n^2 - k_t^2)^{1/2} + k_o n_o} \Delta z) dk_t \tag{5.18}$$

The term k_t^2 is Fourier component of the ∇_t^2, $\tilde{E}(k_t)$is the Fourier component of the E(x,y,z) field in the previous time step. BPM program is just calculating Eq. 5.18 iteratively every step until it propagates $z = z_{max}$.

In Section 5.5 and Section 5.4, experimental and simulated NSOM images of domain walls will be compared. The approach is to first make an educated guess for the refractive index profile within the domain wall, and then use a combination of FFT-BPM and FDTD methods to calculate the expected NSOM images. The simulated images are then compared with experimental images and the original index profile refined to achieve convergence between the two. Uniqueness of the index profile is determined by finding agreement between images using both collection and illumination geometries of NSOM. Therefore, overall this process is a trial and error process in determining the optimum refractive index profile.

The other approach for analyzing images is to solve the *inverse problem*. There have been some attempts at extracting the refractive index profiles from experimental images, but until now, no successful attempts have been reported in solving the inverse problem. One of the fundamental reasons is that inverse Beam Propagation is not possible since BPM tracks only the propagating wave component. The evanescent field part is filtered out automatically at every time step. So in the reverse problem, one cannot recover the lost evanescent components.

In this work, for a complete regeneration of the experimental NSOM images, we have combined the BPM approach with FDTD, Fourier optic code, and Fraunhaufer code. Figure 5.1 shows this process. In Section 5.5, the detailed simulation process will be described.

5.4 collection mode image

In the collection mode geometry, the tiny fiber aperture NSOM tip becomes the light source. In this geometry, we uses He-Ne 632nm laser to detect linear optical signal. In collection geometry, NSOM tip can collect significant evanescent wave signal because of close tip and sample distance as can be seen in Fig. 5.4. If the sample surface has a topological variation, it creates a strong evanescent wave near the surface. The surface topological variation can change the NSOM image significantly. Therefore, both topological information and optical signal should be collected simultaneously in order to extract the pure optical image. Fortunately, in $LiNbO_3$ and $LiTaO_3$ ferroelectric domain walls, topological structure is very small (less than 2nm). We can therefore assume that NSOM optical images do not include topological effects. In our experiments, the NSOM signal is build up by the incident beam propagating through a $500\mu m$ thick crystal. Figure 5.6 shows the experimental transmission-collection mode setup.

Figure 5.7 (a) and (b) shows transmission-collection mode images of 180° domain walls in $LiNbO_3$ and $LiTaO_3$. The first surprising observation to make is that any optical contrast is present at all, since 180° domains must ideally possess the same refractive index. However, the contrast indicates that a refractive index gradient exists at the domain wall, and perhaps even between these two domain states. The hexagonal (triangular) shaped ferroelectric domain states imaged here in congruent $LiNbO_3$($LiTaO_3$) were created by applying electric fields (higher than coercive field) to a single domain crystal at room temperature. The matrix domain in the images is the *virgin crystal*, and the inside of the hexagonal or triangular regions is the electrically reversed domain state at room temperature. The bright and dark fringes indicate that the light is bending while it is propagating along the domain wall. Based on the Eikonal theory, one can predict that light bends from the low-index region to the higher index region [30]. One

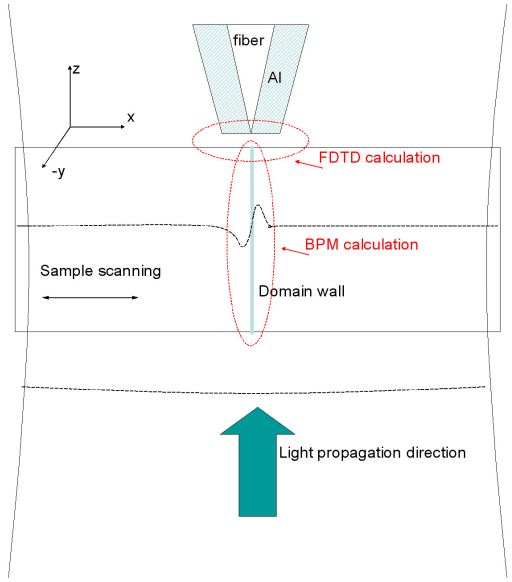

Fig. 5.6. NSOM Collection experimental and simulation diagram. Crystal thickness is $500\mu m$. Near the tip, FDTD calculation is required. BPM simulation calculates the beam profile while the beam is traveling in the z (thickness) direction

can therefore guess that bright side of the domain walls has a higher refractive index than the darker side. By using this simple basic idea, we construct several possible index distributions. These initial guesses for the index distribution are then tested and refined using a combination of BPM and FDTD simulations Figure 5.8(a) shows the refined index distribution model and the resultant BPM simulation data after light has traveled through a 500μ m crystal. Figure 5.8(b)shows three experimental line scans across the domain wall in $LiNbO_3$ with the numerically simulated fit (solid thick line). The agreement between the two is excellent. In order to get the final image collected by the fiber tip, one needs to multiply the total field of the light after the propagation through the crystal (calculated by BPM and shown in Figure 5.8), by the transfer function of the tip. An important issue in NSOM imaging is whether NSOM tip can collect this data without any additional distortion. This can be answered by the transfer function which is calculated in Section 5.4 by using FDTD method. Fourier transformed BPM simulation data from Figure 5.8 shows that all the important frequency data is inside

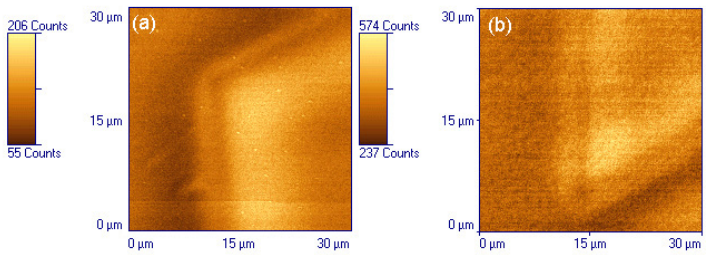

Fig. 5.7. This is experimental transmission-collection mode image of 180° domains in congruent $LiNbO_3$ in (a), and congruent $LiTaO_3$ in (b) domain. From inside to outside the domain, (R to L), the contrast successively changes as bright-dark-bright-dark. The inner dark and bright lines are narrower than the outer contrasts.

the very flat and dispersion-free range of plane-waves. This frequency domain data is shown in Fig. 5.9. Multiplying the BPM simulated field by such a constant transfer function for all its component plane waves results in no distortion of the resultant beam in this case by the tip. Therefore, all the wave information at the sample surface can be imaged by the NSOM tip without introducing any further distortions.

A closer look at the refined refractive index profile indicates that in $LiNbO_3$, there is a broader step-change in index of $\approx 10^{-3}$ across a domain wall, spread over a distance of $\approx 20\mu m$. The refractive index is higher ($n_o \approx 2.288$) in the domain-inverted region as compared to the matrix domain in the virgin state ($n_o \approx 2.287$). This essentially explains why the domain-inverted region is brighter than the matrix domain. In addition, there is a finer rib-like dark and bright lines in going across the wall. This arises from a sharp gradient of $\approx 3\times10^{-3}$ in the refractive index at the wall. Though this index profile is not a unique solution to the observed transmittance image spectrum in Fig. 5.8, it is indeed shown to be uniquely determined for $LiNbO_3$ by simulating the collection mode image as well, as shown in a later section.

The origin of this index distribution origin can be from two possible sources. The first may arise from the confined domain size effect, where a small hexagonal or triangular domain in a large matrix domain crystal may be elastically confined to

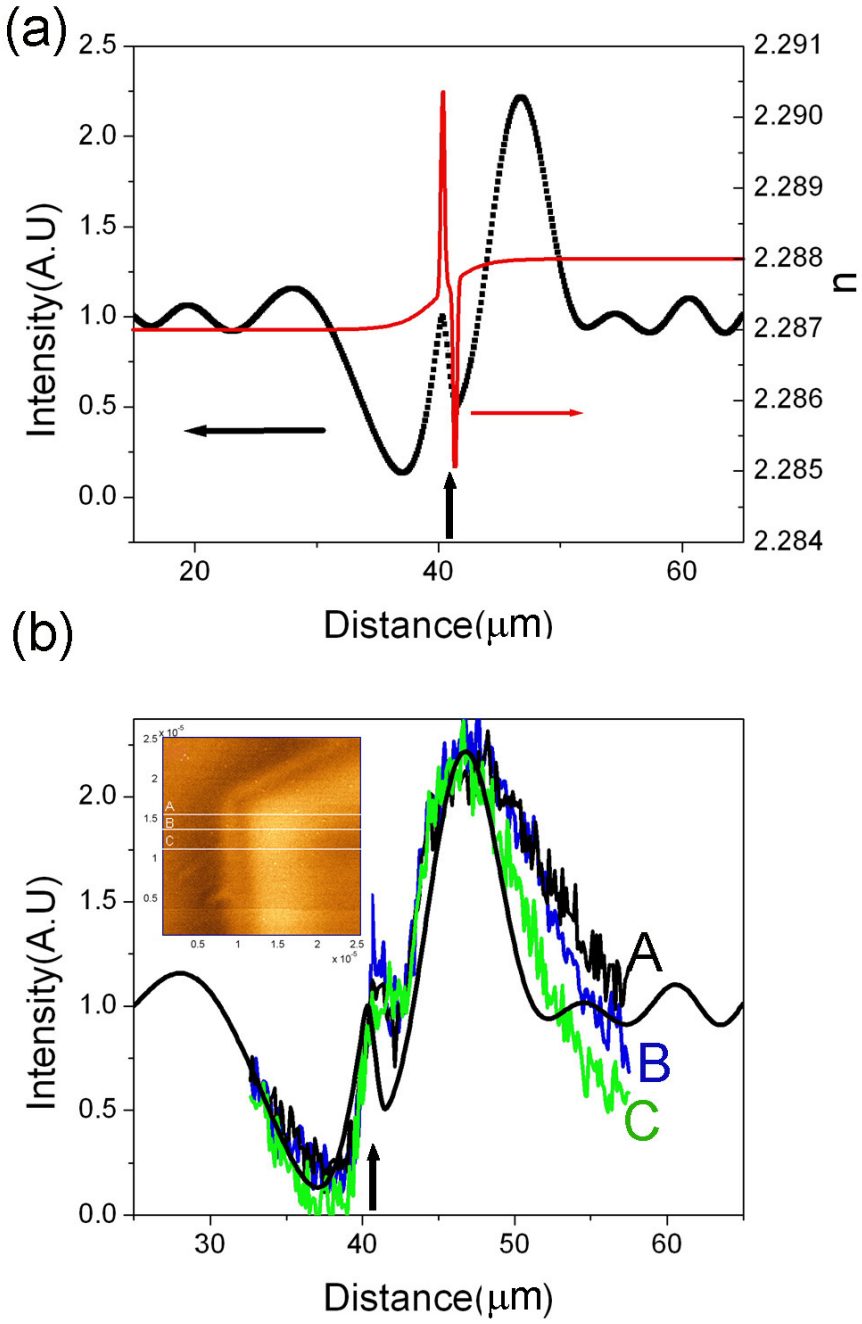

Fig. 5.8. (a) Numerically calculated NSOM collection scanning data. (b)Three experimental line scans across a $LiNbO_3$ domain wall as shown in the inset, and numerically calculated fit as thick solid line. vertical arrow in (a) and (b) indicate domain wall position

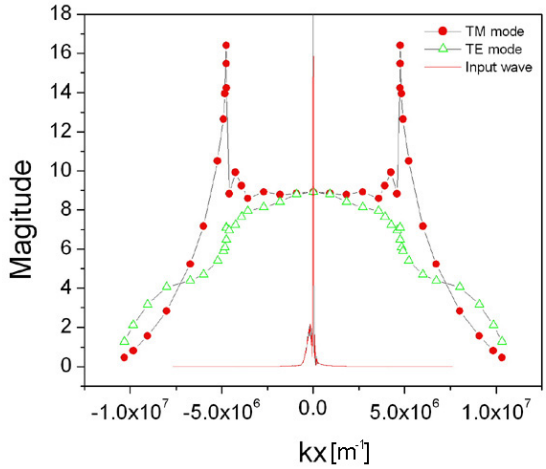

Fig. 5.9. Comparision between Magnitude Transfer Function(MTF) and Phase Transfer Function (PTF) with input beam's spatial frequency component

give rise to index changes through the elasto-optic effect. The second possibility is that the local light scattering at a domain wall may be related to the internal structure and chemical defects within the domains and the wall. The defect dipole model and internal field concepts are already explained in Ch. 2. The origin of the optical contrast was confirmed to be the latter (defect dipoles inside the crystal), and not the former (elastically constrained domains) by the following experiment.

For a virgin crystal, defect dipoles have the most stable configuration such as those shown in figure 2.13 in Ch. 2. On the other hand, domains created in this virgin crystal by an external electric field at room temperature consist of *frustrated* defect structures, which make this domain state relatively less stable than the virgin state. It can be seen from the polarization hysteresis loops(Fig. 5.10), that the electric field required to create the reversed domains from a virgin state is much higher than to re-invert this domain state back to a virgin domain state. This difference in the coercive fields gives rise to internal fields that are effectively parallel to the virgin state. Since this defect field of $\approx 2E_{int} \approx 6kV/mm$ in $LiNbO_3$ is biased antiparallel to the domain-inverted state, an electro-optic increase in index of $\Delta n = 0.5 \cdot n_o^3 \cdot r_{13} E_{int}$ can be

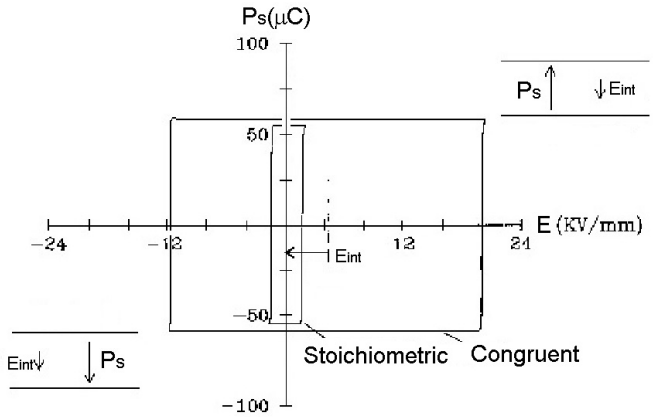

Fig. 5.10. Hysterisis loop for stoichiometric(inside small one) and congruemt(out side large one) $LiTaO_3$

expected. Assuming bulk value of r_{13} ≈9.6 pm/V, one can calculate, $\Delta n \approx 3.4 \times 10^{-4}$ which is of the correct order of magnitude of index change, even though it is little bit less, shown in Figure 5.8. Additional contributions from strain induced index changes through the elasto-optic effect are also likely. The sharp localized change in refractive index at the domain wall may arise from further index changes due to highly localized strains or distortions at the wall. To conclusively prove that the internal fields related to nonstoichiometric defect dipoles are responsible for the observed optical contrast, the following experiment is performed. First a virgin $LiNbO_3$ crystal is completely domain inverted at room-temperature, such that the starting matrix domain can now be considered in a *domain-inverted* state. Starting with this state, an applied field partially creates hexagonal domain regions that have the same orientation as the original virgin crystal, with the exception of having some domain reversal history. Now, the domain region inside these hexagons have a more stable defect configuration, as compared to the outside matrix domain. Therefore, the internal field is opposite to the outside domain matrix and the electro-optic effect would therefore be expected to increase the index in the matrix domain. This would result in a brighter matrix domain than the interior of the hexagonal domain regions. Thus, the NSOM image contrast will be expected to be

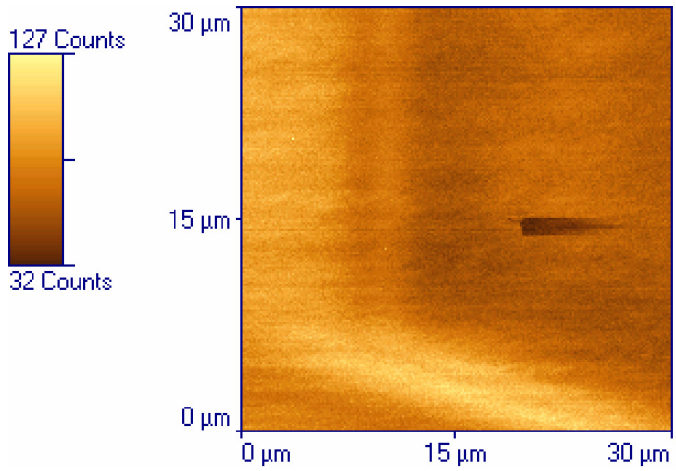

Fig. 5.11. Inverse contrast compared with Fig 5.7 (a). Inside the hexagonal domain region has the same orientation as the original virgin state except with one cycle of poling history. The matrix domain is the electric field induced domain-inverted state at room temperature

reversed in this case as compared to the Figure 5.8. Indeed this is observed, as shown in Figure 5.11.The sharp localized change in refractive index at the domain wall may arise from further index changes due to highly localized strains or distortions at the wall.

5.5 illumination mode image

One way in which the index gradient extracted from the collection mode imaging was tested for uniqueness was to check if the same gradient also explained the images in the illumination mode geometry. In the illumination mode NSOM, the small nano-size aperture fiber-tip becomes the light source. This tiny light source scans the desired sample area. If the sample surface has a strong topological or index variation, the tip-sample interaction changes dramatically while the sample is scanned. So the overall intensity that is collected in the far-field objective is strongly affected by the surface condition and hence the tip-sample surface interactions. In addition to the surface and tip interactions, in the NSOM imaging of domains in $LiNbO_3$ and $LiTaO_3$, the light modulation in propagating through the crystal thickness has an important role

in generating the NSOM image. Like the collection geometry, BPM code is used to simulate how this light emitted from a tiny source propagates through the crystal. After this beam passes through the sample, it continues to propagate until the collection objective lens. An infinity corrected microscopy objective lens with a numerical aperture of 0.5, a working distance of 7mm, and 40x magnification is used. Depending on the focal point of this objective lens, the beam propagation behavior after this objective lens will change. This beam propagates until the detection system. This detection system is composed of a focusing lens that focuses the light into a photo-multiplier tube. Figure 5.12 shows the experimental setup, which was also used for the simulation purposes.

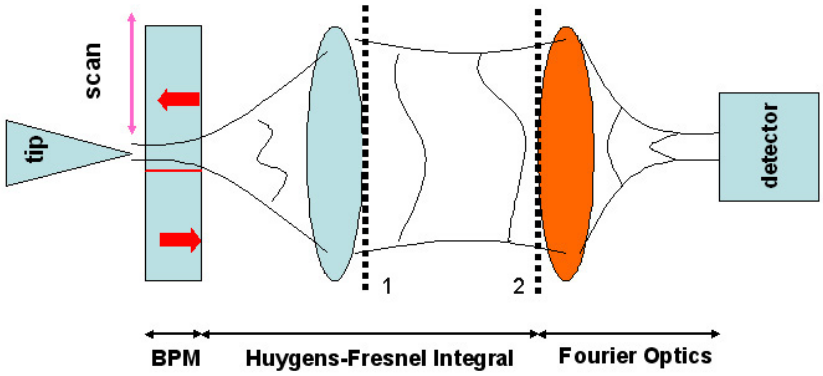

Fig. 5.12. Detailed experimental and simulation setup. FDTD is used near the tip, BPM is applied inside the inhomogeneous sample, and Hyugens-Fresnell equation is used to calculate the free space beam propagation. At the last lens, we used Fourier optics to calculate the detector response

The illumination image generation is completely different from the images collected in the collection geometry. In the collection mode, the source beam is a collimated beam and collection is through the tip which detects the signal very locally. In the illumination mode, the source beam is a point source at the tip, and highly diverges through the sample. Most of this diverging beam is again collected by high numerical aperture

objective lens. Similar to the collection geometry case, both the tip-sample interaction and the inhomogeneous index distribution inside the sample will affect the image reconstruction. Based on the topological data, it is reasonable to ignore the tip-sample surface interaction terms in the illumination mode. Because of the flat sample surface, light-coupling ratio will be mostly constant during the whole scanning process. So most of the image contrast comes from an inhomogeneous index distribution inside the sample. There will be two types of index distributions. One is the real part of the index, and the other is the imaginary part of the index. Since the absorption of the material in visible wavelengths is negligible, the imaginary part of the index can be ignored. In this case, light diffraction due to index variation will be the main mechanism for the image contrast. Again, as in the collection mode case, Beam propagation method will be the most useful numerical technique for simulating this light diffraction inside the sample.

The same index distribution as shown in Figure 5.8(a) is used in the illumination geometry to regenerate the NSOM contrast. But the BPM method can only can be used for the beam propagation inside the sample, which is 500μm thick. Between the exit surface of the sample and the first collection lens, the propagation distance is almost 8.7mm, and the medium is homogeneous air. Therefore it is unnecessary to use BPM in that region. Usually, Fraunhofer approximation [31] can be used for wave propagation in air or homogeneous medium. If propagation distance is much longer than aperture size, Fraunhofer approximation is valid($z > \frac{2D^2}{\lambda}$ where z is the propagation distance, D is input aperture, and λ is the wavelength) But in NSOM simulation, the wave front changes very quickly, because of the extent of beam divergence starting from the small size of the NSOM tip source. Therefore the Fraunhofer approximation is insufficient in our case. Even though computationally expensive, the Huygens-Fresnel Integral equation, given below is used:

$$U(P_2) = \frac{1}{j\lambda} \int \int_{\Sigma} U(P_1) \frac{exp(jkr_{12})}{r_{12}} cos\theta ds \tag{5.19}$$

where the distance r_{12} is given exactly by

$$r_{12} = \sqrt{z^2 + (x-\xi)^2 + (y-\eta)^2} \tag{5.20}$$

Detailed notation is described in Fig 5.13. where θ is the angle between the normal to

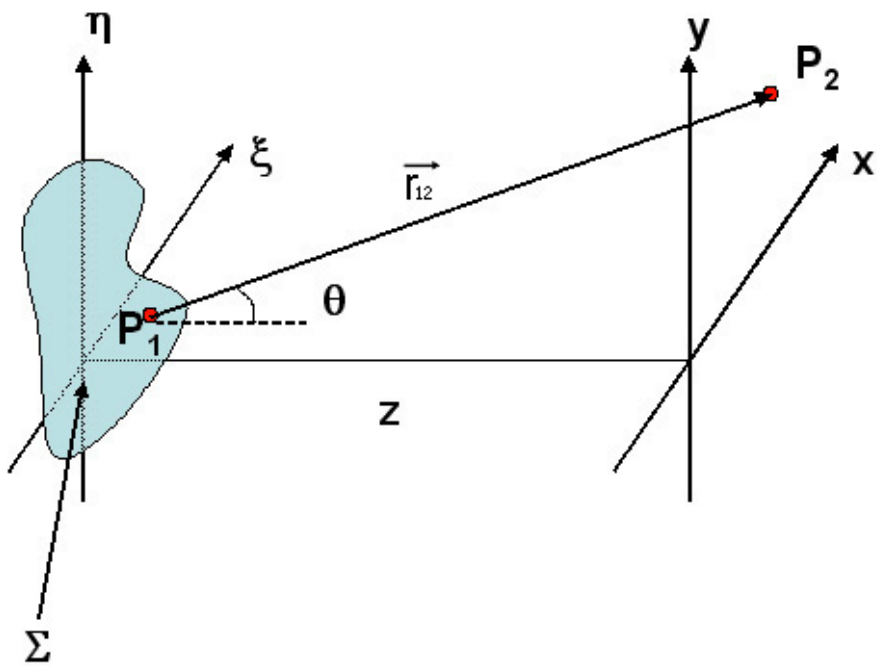

Fig. 5.13. Diffraction geometry for the Huygens-Fresnel integration

the input plane and the vector r_{12} pointing from P_1 to P_2. The quantity U is a field such as electric field. Σ is an area of interest in $\xi - \eta$ plane.

By combining BPM and Huygens-Fresnel equation, the NSOM illumination image can be simulated. Fig 5.14, and Fig 5.15, respectively show the $LiNbO_3$ and $LiTaO_3$ experimental NSOM illumination images with the fiber tip at the focus of the objective lens (the first lens in Fig 5.12). Both $LiNbO_3$ and $LiTaO_3$ images show the darkest

boundary near the domain wall. But as can be seen in the intensity scale, the image contrast is very weak. If the objective lens location is moved away form the position of

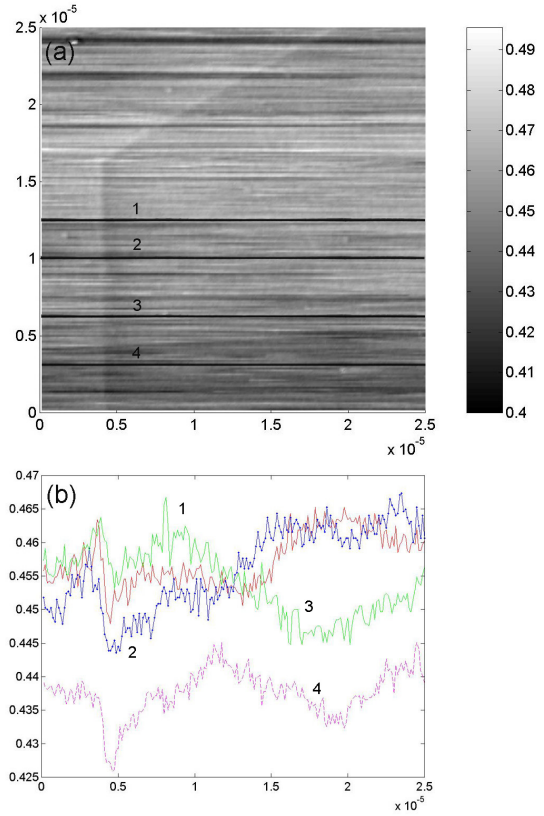

Fig. 5.14. (a) NSOM image of domain walls in $LiNbO_3$ in illumination scanning geometry. The objective lens is placed with focus at the fiber tip. (b) is line scan across the different lines indicated in (a).

focus at the fiber tip toward detector, then the domain image contrasts in both $LiNbO_3$ and $LiTaO_3$ crystals improve significantly. Figure 5.16 shows a $LiTaO_3$ domain and 5.17 $LiNbO_3$ domain image taken with moving the objective lens from the exact focal point. One notices in these images that in moving from the outside matrix domain to inside the triangular (or hexagonal) domain, the line scans show a peak (bright fringe) followed

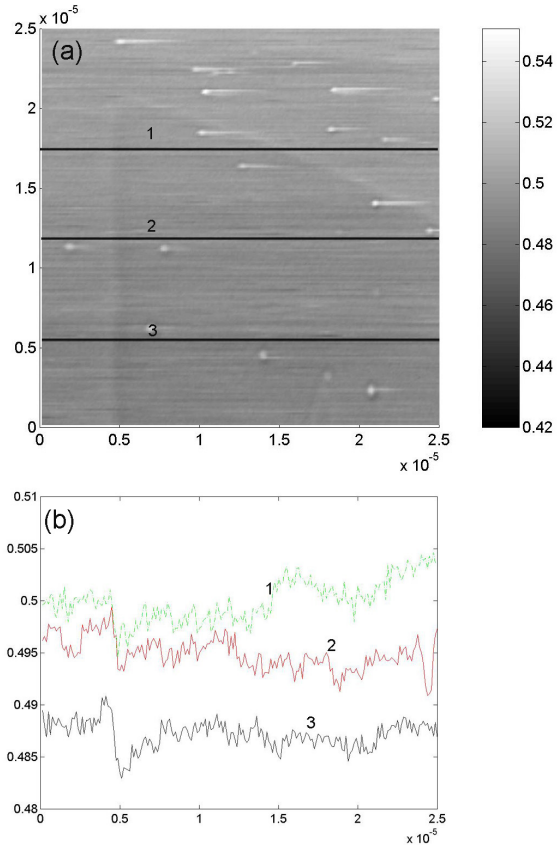

Fig. 5.15. (a) NSOM image of domain walls in $LiTaO_3$ in illumination scanning geometry. The objective lens is placed with focus at the fiber tip. (b) is line scan across the different lines indicated in (a).

by a valley (dark fringe). This contrast is similar to the two center fringes observed at the domain wall in the collection geometry images in Fig 5.7. In Figure 5.16, the matrix domain is in the virgin state, and the inside of the domain pattern is in the room temperature domain-inverted state. If this order is reversed, by creating a sample with virgin domain inside and domain-inverted matrix outside, the contrast also reverses just as in the collection mode case (see Figure 5.11). This is shown in Figure 5.17 for $LibO_3$, where the inside domain is in virgin state.

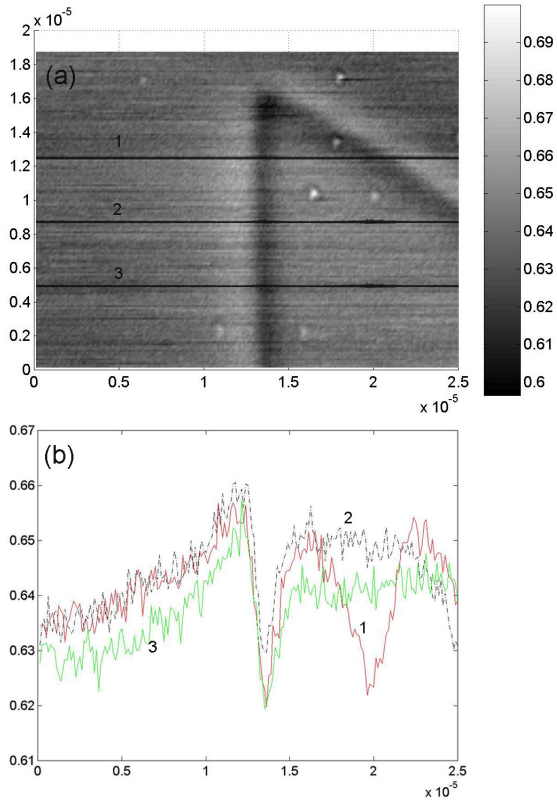

Fig. 5.16. Defocused NSOM illumination scanning image of domain walls in $LiTaO_3$ in (a). Objective lens under the sample has been moved from exact focal point toward detector. (b) is the line scan for the different lines shown in (a)

The domain walls in Figure 5.17 have a very interesting contrast. As can be seen from the line scans in Figure 5.17 (b), the central bright and dark contrast is greater than the background. The difference between Figures 5.16 and 5.17 is that the latter depicts the defocusing effect of the collection optics. Even though a strong defocus has weakened the overall signal (the background in Fig. 5.17 is much weaker than in Fig. 5.16), the contrast has been enhanced strongly.

To summarize the observations, we can pose the following questions. (1)Why does the domain wall become dark at exact focus with a very small contrast. (2)Why does the defocusing influence the magnitude of the contrast? To answer these questions,

the following simulations were done. First, an inhomogeneous index distribution at the domain walls was assumed, the same as in Figure 5.8(a) deduced from the collection mode image simulation. If it is close to the real index distribution, then both collection and illumination modes should match the experimental data. For the wave propagation inside the sample, FFT-BPM was used. For regenerating the scanned images, the tip location is fixed and the sample moved in the simulation, which is the same as in a real NSOM system.

Figure 5.18 (a), (b), and (c) shows the electric field intensity at the exit surface of the sample, and (d) shows the sample index distribution and the scanning positions. When the tip is exactly on top of the domain wall, most of the light will be guided through the high index regions. As the tip scans away from the center, some of the light is guided, but most of the light will be reflected from the high index profile region and create an interference pattern. This BPM simulation result is then the input to the Huygens-Fresnel integral equation, in order to get the intensity just before the first objective lens.

Figure 5.19 (a), (b), and (c) show the light intensity that reaches the first objective lens. If the objective lens is placed such that the fiber aperture is at the exact focal position, then the diverging light wave is collimated by the lens, and most of the signal will be collected by the detector. To get the detector response, the intensity data from Fig 5.19 is integrated separately at each different tip location over the sample. A simulated line scan is thus obtained. Figure 5.20 shows such a numerically calculated line scan image. As can be seen in Fig 5.21, at the exact focus case, the detector response is proportional to the integration of the whole aperture of the first lens. When the tip is on low index region this simulation shows weak intensity, and in high index region it shows high intensity as can be seen in Fig 5.20. In the low index region, the light coming from tip will diverge more strongly than in the high index. In a real experiment, we use a really high NA objective lens. This high numerical aperture (NA) objective lens will collect most of the diverging beam. Therefore, the collected light intensity in both low and high index regions will be similar. But in a BPM simulation, we use absorbing boundary conditions. So a highly diverging beam will be absorbed more.

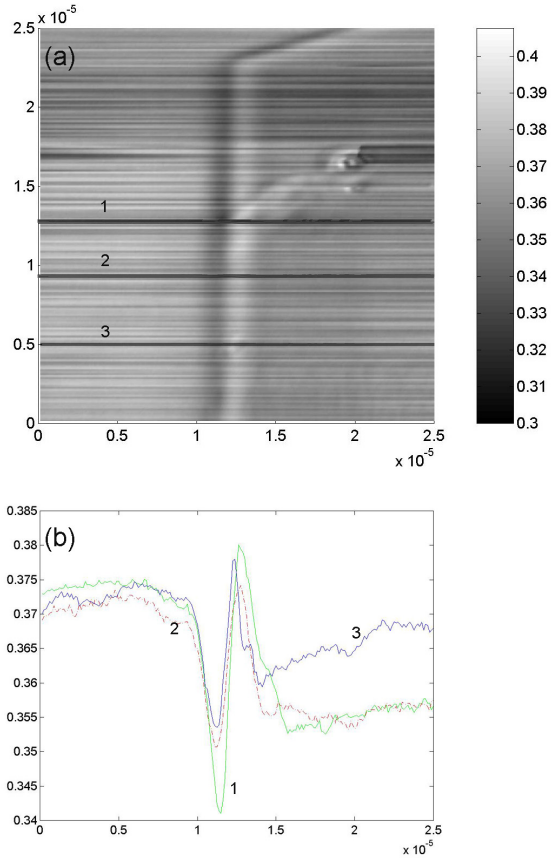

Fig. 5.17. Defocused NSOM illumination scanning image of $LiNbO_3$ in (a). (b) is line scanning for each different line in (a)

This simulation boundary absorption will reduce the simulation scanning signal in the low index region, which is not the real experimental case. In a real experiment with the tip at the focus of the collection objective, we only see a sharp boundary with one domain slightly darker than the other. We believe that this is a differential absorption effect between the two domains, which can't be simulated in the present BPM simulation. For the defocusing case, only the center part of the wave can be collected by the detector as explained in Fig 5.21. If the lens moves towards the detector, it will converge. But if defocusing towards the detector increases, this converging beam will change to a diverging beam. So either direction of defocusing will make the beam

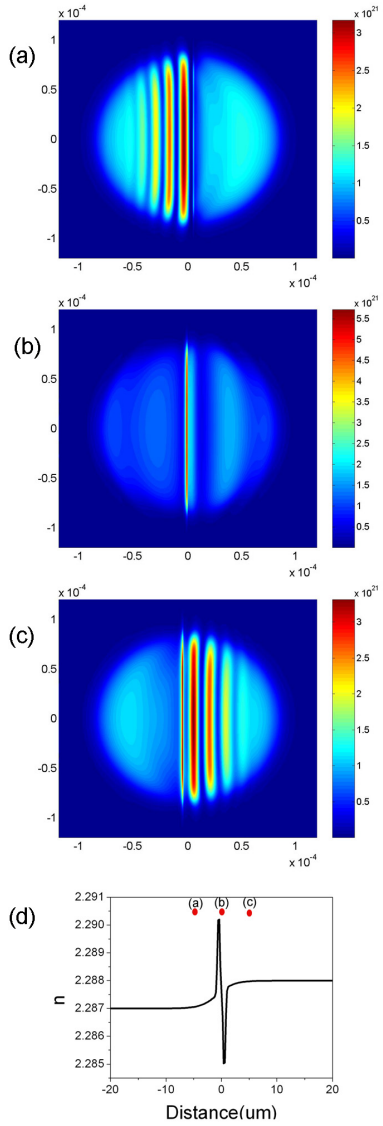

Fig. 5.18. BPM simulation results on the exit surface. (a), (b) , and (c) are the output light intensity depending on domain wall location compared to tip location. (d) shows the index profile and the three tip location is notated as a circle.

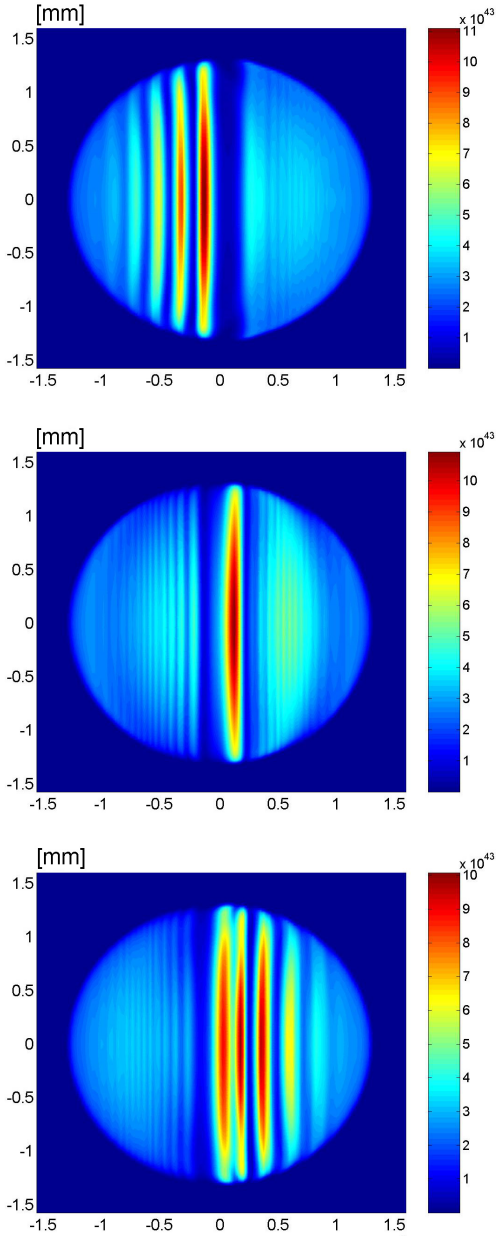

Fig. 5.19. Intensity: Calculated from Huygens-Fresnal integration of the BPM data from Fig. 5.18 (a), (b), and (c) up to first objective lens

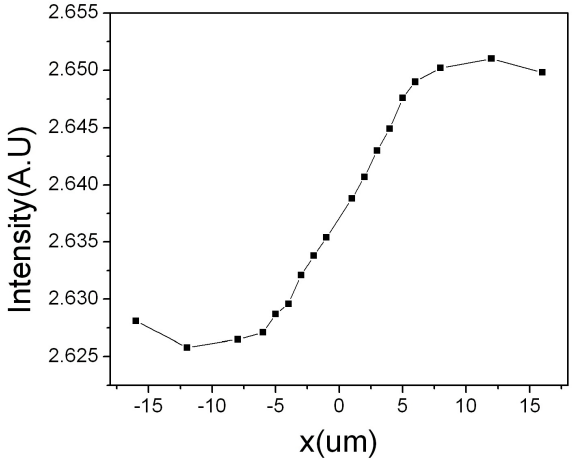

Fig. 5.20. Scanning simulation image. x axis is scanning range and y axis is integrated intensity right behind first objective lens

diverge at the detector. In other words, only the wave propagating along the domain wall can be collected in either direction of defocusing. This is because waves that are not incident close to the center of the lens will diverge after the first objective lens, because the objective lens cannot perfectly recover the diverging phase. Therefore, for the defocus-imaging case, the experimental image closely resembles the index profile at the wall. Figure 5.22 shows the simulated line scan image for the defocused case for lithium niobate using an imaginary aperture of 375μm radius around the center of the objective lens(focus case aperture size is 3mm). This simulation image closely resembles the experimental image of Fig. 5.17. In addition, this simulated scan profile also closely resembles the actual sample index profile. By using a combination of the BPM and Huygens-Fresnel integration, the illumination NSOM experimental data can be regenerated with the proper index profile model. This index profile model also gives a reasonable collection simulation which is very close to the experiments.

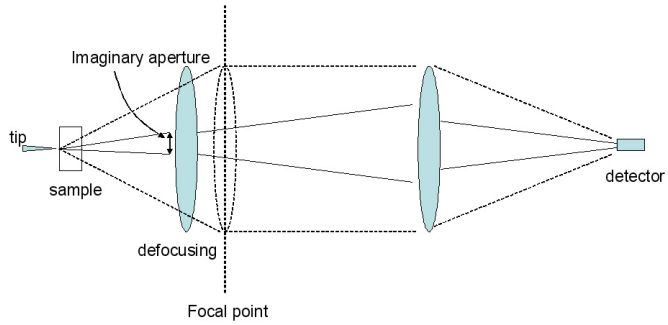

Fig. 5.21. Schematic diagram showing the effect of defocusing the objective lens on the image collection process in NSOM. Dotted line and dotted lens is the ray trajectory and objective lens location when the tip is located exactly at the focus of the first objective lens. Solid ray trajectory line and filled lens depicts the defocus case. Only light inside of the ray trajectory lines can be collected by the detector (PMT). In the defocus case, only the signal inside the imaginary aperture is the useful data.

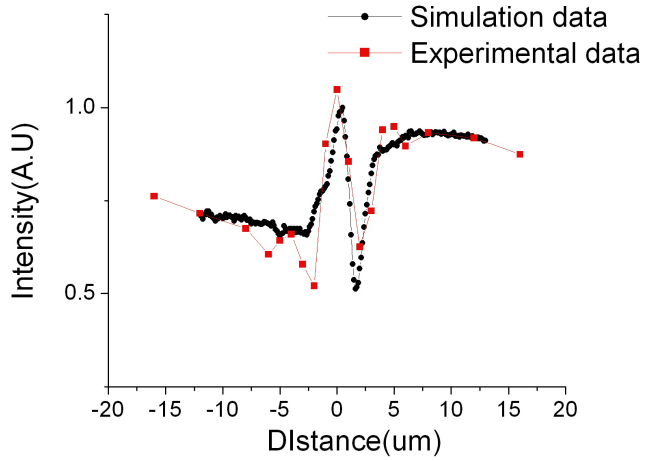

Fig. 5.22. A comparison of the experimental line scan across a domain wall in $LiNbO_3$ in Fig. 5.17 with simulation results using an aperture in front of the collection lens. Right side is virgin state.

5.6 In situ NSOM scanning

If an external electric field is applied to a partially domain reversed crystal, it creates a strain distribution at the domain walls due to the piezoelectric effect. In Ch. 4.2, x-ray imaging was used to study these strain distributions around the domain walls, especially near the crystal surface. Unlike the x-ray studies, *in-situ*NSOM experiments gives dynamical index distribution inside crystals, because the image is generated while it is propagating. Similar experiments have been reported by other groups [32] looking at local motion and pinning of domain walls. Here we look at the wall contrast changes with applied field. To apply an electric field, indium-tin-oxide thin film was deposited on the bottom surface. On the top surface that is scanned by the gold tip, a 40nm Au/Pd(80/20 atomic percent) film was deposited with a smooth surface. In the illumination mode, increased tip-sample surface distance destroys the detailed information in the optical images. Even in the collection geometry, it's difficult to image the domain structure, because of scattering losses due to the deposited metal film. However, an applied electric field induces an additional index difference between different domain orientations through the electro-optic effect, which can be imaged even with the electrodes. Figure 5.23 (a), and (c) shows NSOM transmission-collection image under different voltage bias conditions. A simulation of these images would require account-

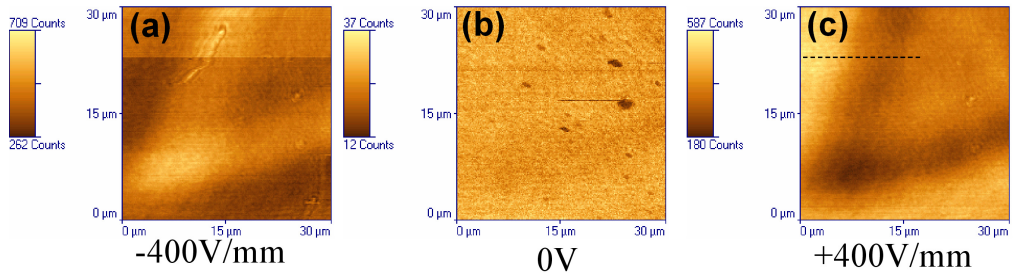

Fig. 5.23. Collection mode NSOM images under an applied bias.

ing for the top and bottom electrodes on the sample. However, even qualitatively, these simulations verify that our previous analysis is reasonable. For example, if a positive bias is applied to crystal, the field is parallel to the ferroelectric polarization inside the domain-inverted region (inside the triangular domains), and will therefore decrease the extraordinary index, n_x and n_y inside the domain. The light propagating parallel the domain wall will therefore bend from inside the domain to the outside matrix domain. This is confirmed by the experimental data is shown in Fig. 5.23 (c), and it's line profile is shown again in Fig. 5.24 (b). Similarly, for a negative bias, the index in the matrix domain will decrease and light will bend away from the matrix and towards the domain-inverted region, as seen from Fig. 5.24 (a).

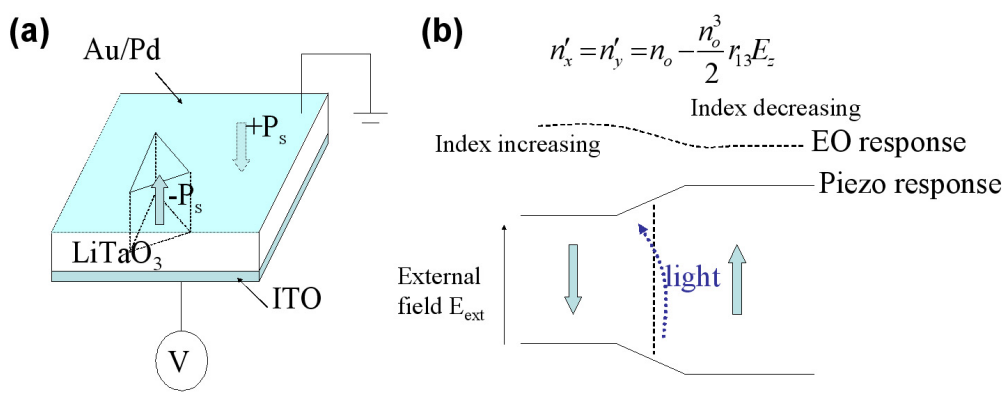

Fig. 5.24. (a)Experimental setup for collection mode under bias, and (b)Schematic explanation of the index change and light travel across a domain wall

References

[1] M. Lanz D. W. Pohl, W. Denk. *"Optical stethoscopy: Image recording with resolution"*. *Appl. Phys. Lett.*, 44:651–653, 1984.

[2] C. C. Davis S. Rudin I. I. Smolyaninov, C. H. Lee. Near-field imaging of surface-enhanced second harmonic generation. *J. Microsc.*, 194:532–536, 1995.

[3] J. M. Kikkawa D. D. Awschalom N. Samarth J. Levy, V. Nikitin. *J. Appl. Phys.*, 79:6095, 1996.

[4] M. Achermann F. Morier-Genaud A. Schertel Keller B. A. Nechay, U. Siegner. *J. Microsc.*, 194:329, 1999.

[5] C. C. Davis S. Pilevar, W. A. Atia. *Ultramicroscopy*, 61:233, 1995.

[6] Robert D. Grober Khaled Karrai.

[7] T. D. Harris J. S. Weiner R. L. Kostelak E. Betzig, J. K. Trautman. Near-field imaging of surface-enhanced second harmonic generation. *Science*, 251:1468, 1991.

[8] G. H. Morrison G. A. Valaskovic, M. Holton. *Appl. Opt.*, 34:1215, 1995.

[9] V. Deckert R. Zenobi R. Stockle, C. Fokas. *Appl. Phys. Lett.*, 75:160, 1999.

[10] M. Ohtsu S. Mononobe. *J. Lightwave Technol.*, 14:2231, 1996.

[11] H. Fuchs U. C. Fischer, J. Koglin. *J. Microsc.*, 176:231, 1994.

[12] S. Kawata Y. Inouye. *Ultramicroscopy*, 57:313, 1995.

[13] H. K. Wickramasinghe F. Zenhausern, Y. Martin. *Science*, 269:1083, 1995.

[14] F. F. Froehlich R. W. Ziolkowski J. B. Judkins J. L. Kann, T. D. Milster. *J. Opt. Soc. Am. A.*, 12:1677, 1995.

[15] R. Dandliker P. Blattner, H. P. Herzig. *Opt. Commun.*, 155:245, 1998.

[16] D. Barchiesi. *Opt. Commun.*, 154:167, 1998.

[17] D.courjon C. Girard. , *Phys. Rev. B*, 42:9340, 1990.

[18] S. Kawata H. Furukawa. *Opt. Commun.*, 196:93, 2001.

[19] D. A. Christensen. *Ultramicroscopy*, 57:189, 1995.

[20] S. T. Chu A. Chavez-Pirson. *J. Microsc.*, 194:421, 1999.

[21] A. Taflove E. Vasilyeva. *Opts. Lett.*, 23:1155, 1998.

[22] P. Regli L. Novotny, D. W. Pohl. *J. Opt. Soc. Am. A.*, 11:1768, 1994.

[23] D. V. Labeke D. Barchiesi. *Ultramicroscopy*, 57:196, 1995.

[24] Susan C. Hagness Allen Taflove. *Computational Electrodynamics: the finite-difference time-domain method*. Artech house, inc, 2000.

[25] K. S. Yee. Numerical solution of initial boundary value problems involving maxwell's equation in isotropic media. *IEEE Trams. Antennas Propagat.*, AP-14(3):302–307, 1966.

[26] Masanori Koshiba Masayuki Yamamoto, Yasuhide Tsuji. *"Reformulation of FFT-BPM for Highly Accurate Analysis"*. *Electronics and Communications in Japan Part2*, 81(5):9–15, 1998.

[27] D. Barchiesi. Characteriztion of reflection scanning near-field optical microscopy and scanning tunnelling optical microscopy/photon scanning tunnelling microscopy working in preliminary approach contrast height scanning mode. *J. Microsc.*, 194:299–306, 1999.

[28] Fred Froehlich Richard W. Ziolkowski Justin Judkins Joshua L. Kann, Tom D. Milster. Numerical analysis of a two-dimensional near-field probe. *Ultramicroscopy*, 57:251–256, 1995.

[29] U. Mohideen T. J. Yang. Nanoscale measurement of ferroelectric domain wall strain and energy by near-field scanning optical microscopy. *Physics Lett. A.*, A250:205–210, 1998.

[30] A. Gerrard and J. M. Burch. *Introduction to Matrix Methods in Optics*. Dover Publications, 1994.

[31] Joseph W. Goodman. *Introduction to Fourier Optics*. McGraw-hill international editions, 1996.

[32] P. J. Swart U. Mohidden T. J. Yang, V. Gopalan. Direct observation of pinning and bowing of a single ferroelectric domain wall. *Phys. Rev. Lett.*, 82:4106–4109, 1999.

Chapter 6

Summary and Conclusions

6.1 Summary and Cross-Correlations

This thesis has investigated $LiNbO_3$ and $LiTaO_3$ ferroelectric domains and the critical role of non-stoichiometric defects in determining the macro-to-nanoscale domain phenomena. Based on electrical switching experiments under optical microscopy, the basics of domain wall dynamics, the possible structure, defect dipoles and the mechanism by which they influence the phenomena of domain backswitching, domain stabilization, and negative coercive fields is developed. By using 3-dimensional Time Dependent Ginzburg Landau (TDGL) simulation, a detailed strain distribution along the domain wall, the effect of anisotropic gradient energy, and domain wall kinetics are investigated. This defect dipole model not only explains the macroscale electrical switching data but also forms the basis for observing and understanding the induced strain at domain walls on local scale, (confirmed by using X-ray topography) and local optical index contrast (observed using Near Field Scanning Optical Microscopy, NSOM) experiments. Detailed and accurate X-ray topography (especially for the strain) experiments in congruent lithium niobate reveals that the defect dipole model and strain distribution predicted by Time Dependent Ginzburg Landau (TDGL) are consistent. A difference in lattice constant between virgin domain state and domain reversed states at room temperature (see Ch. 4.1.2.3) was observed. The TDGL also shows that there is a 3-fold symmetrical shear strain at the corners of hexagonal domains, with alternating positive and negative shear strains at the vertices around the domain. This is reflected in the 3-fold symmetry of the contrast at domain corners in Anomalous Laue transmission geometry experiments(see Ch. 4.1.2.3). In addition, a very local structure around domain wall is detected as a topological step(see Ch. 4.1.1). These features are however not predicted by the TDGL simulation, which instead predicts that the y-walls

for lithium niobate should have zero strain ϵ_{xz}, except at the corners. This discrepancy originates from the presence of non-stoichiometry in the crystals, the influence of which is not included in the free energy functionalism of the TDGL model.. However, in stoichiometric crystals, no such shear strain or lattice step is experimentally observed, consistent with the TDGL model.

Near Field Optical Microscopy (NSOM) experiment proves that there is real bias strain(see Ch. 5.4) between two different domain states as expected by the defect-dipole model and detected by X-Ray topography. This is reflected in an index difference between the two domains. In addition to this broad strain distribution (which is order of tens of microns), a narrow index kink within a micron range is observed to be localized near the domain wall. This was deduced by simulating both illumination and transmission NSOM images consistently to yield an index contrast at the wall. We believe that this narrow kink in index is related to the strain data in the reflection X-ray images, where a local topological step at the domain wall (see Ch. 4.1.1) was concluded. This local strain data from NSOM was detected by piezo response Atomic Force Microscopy [REF], recently.

Combining TDGL, NSOM and X-Ray measurements, it is easy to note that there are two different types of strains. One is a long-range strain due to the piezo electric effect due to the external or defect dipole induced local electric fields. This type of strain propagates over hundreds of microns. The other strain type is a very localized strain, which is on the micron scale or less. This is not related to the piezoelectric effect due to bulk defect dipole state. It is related more to the actual distortion inside a domain wall. Therefore its magnitude is very high and strongly localized at the domain wall. But interestingly, this domain wall feature is also linked to defect dipoles. The clue is that in NSOM transmission experiments, internal index distribution is reversed by changing the polarization direction inside the domain and the matrix domain. This contrast inversion can only be explained by frustrated defect states explained in Ch. 2.4. Unfortunately, this strain can't be modeled in the TDGL phenomenological theory. To understand how the structures can be distorted inside a domain wall requires the use of atomic scale simulation.

6.1.1 In-plane defect dipole biased strain between two different domain regions

In chapter 2, a defect dipole model is proposed based on electrical switching dynamics. The basic concept is that a virgin state domain is more stable than a reversed domain at room temperature because of the difference in defect dipole configuration between the two regions(see Ch. 2.4). The different dipole configurations give rise to a potential difference between the energies of the two domain states and this can be measured experimentally as an internal field. This internal field, in turn, induces various strains such as ϵ_{zz}, ϵ_{xx}, and ϵ_{yy}.

When the matrix domain is in its *virgin* state and the inside domain is in *domain reversed* state at room-temperature, the internal field is effectively parallel to the matrix (or virgin state) domain polarization and antiparallel to the polarization of the domain reversed state. Because of the piezoelectric and the electro-optic effect, differences in the sign of ϵ_{xx}, ϵ_{yy}, and magnitude of index will occur between these two domain states. This is observed in Xray (see Ch. 4.1.2.3) and NSOM transmission geometry(see Fig. 5.8). These are discussed in some detail below.

In X-ray topography of hexagonal domains in congruent lithium niobate, a bias strain of $\Delta\epsilon_{yy} = -4 \times 10^{-5}$ was measured across the wall, where the negative sign indicates that the lattice parameter of the (3,0,.,0) planes is larger in the domain reversed state than in the virgin state. The internal field is parallel to the outside matrix domain (in virgin state), and antiparallel to the inside domain (domain reversed state). Piezoelectric effect predicts that if the internal field is treated as a real electric field, the inside domain should shrink in the z- direction (thickness direction) while the matrix domain should expand in the z-direction(see Fig 6.1). The opposite is true for the in-plane strain such as ϵ_{xx}, and ϵ_{yy}, i.e. the matrix domain should shrink and the inside domain should expand. These changes in lattice parameter will result in Bragg angle deviation, which is experimentally measured in Ch. 4.1.2.3 as a $\epsilon_{yy} = 4 \times 10^{-5}$. If we consider just the simple inverse- piezoelectric effect, we can calculate the expected strain by using the inverse piezo relation ($\epsilon_i = d_{ji}E_j$) with internal field ($2E_{int}$=6 kV/mm) and $d_{31} = -0.1 * 10^{-11} CN^{-1}$. It gives $\epsilon_{yy} = 6 \times 10^{-6}$. This value is smaller than the X-ray experimental measurement of $\epsilon_{yy} = 4{\times}10^{-5}$. It implies that measured internal field may

be smaller than actual local field inside the crystal. It may also suggest that additional contributions to strain exist that is independent of piezoelectric effect. These are most likely to be strain fields induced locally by the presence of defect sites themselves. In NSOM modeling, we proved that index difference between two different domain is about 10^{-3}. But as calculated in Ch. 5.4,we got 3.4×10^{-4} by using internal field biased electro-optic effect. The index change also comes from secondary effect photoelastic effect. Based on strain(ϵ_{yy}) measured from x-ray, photoelastic induced index change can be calculated by using $\Delta n = -\frac{n_o^3}{2} \cdot (p_{12} + p_{11}) \cdot \epsilon_{yy}$. This calculated value order is 10^{-5}, which is much smaller than electro optic effect. So this photoelastic effect can't again explain the deviation.

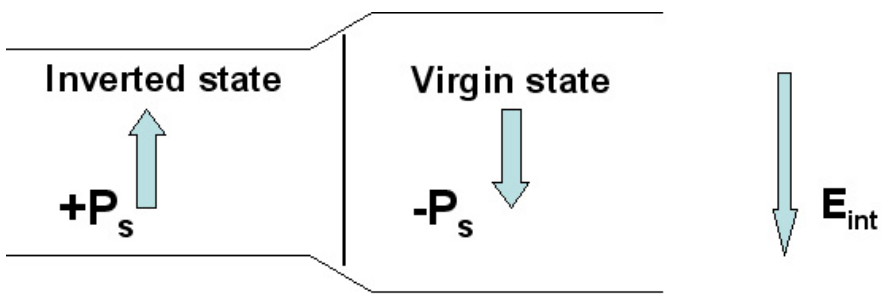

Fig. 6.1. Schematic of interal field induced piezoelectric effect

6.1.2 Strain and index distribution in the corner regions of domains

TDGL simulation shows that there is a 3- fold symmetrical z direction displacement in hexagonal $LiNbO_3$ domain corners. This symmetrical shear strain is observed by X-ray Transmission experiments (see Ch. 4.1.2.3). This strain can be detected by X-ray topography, because X-ray is very sensitive to the incident beam condition. However, neither illumination and collection NSOM images show any 3-fold symmetrical index

contrast at the corners. It is probably because NSOM is relatively insensitive to the incident boundary condition a compared to X-ray topography. In addition, in both NSOM illumination and collection modes, only index changes in the x and y (or in-plane) direction can effectively influence the incident beam, and the small z-displacements do no influence the images.

6.1.3 Stoichiometric and congruent issues on device fabrication

One of the most frequently used optical devices on domain engineered $LiNbO_3$ and $LiTaO_3$ is the quasi phase matching second harmonic generation(QPM-SHG) device. For converting infrared (e.g. 840nm wavelength) to blue light efficiently, a periodic domain grating of 3.6m is required. This SHG device is operated without any external external fields. For patterning a uniform domain grating, the small coercive field of stoichiometric crystals is very attractive, as compared with the higher coercive field congruent crystal. A related issue is the photorefractive effect or optical damage. In a strong incident beam condition, these crystals experience a a refractive index gradient in response to intensity gradients of the incident beam, resulting in beam distortion and scattering. It is a serious problem in converting the YAG:Nd laser (1.064 μ m) to the green laser (532 nm), where only low duty cycles for the pulsed laser are allowed. By doping these crystals with ¡1 mole % of MgO [1] [2], the photorefractive effect decreases considerably in stoichiometric crystals. In contrast, the congruent crystal require 5 mole % MgO doping, which decreases the crystal quality. Less photorefractive effect, small coercive fields and weak strain around domain walls make stoichiometric crystals favorable in QPM-SHG device fabrication.

In electro optic devices, high index contrast can be obtained only by applying high enough electric field (5-10 kV/mm). In domain microengineered electro-optic devices, large coercive fields which are higher than 10 kV/mm are therefore required, so that once formed, the domain micro-optical elements are not destroyed by the operating fields. So congruent composition is more useful in fabricating electro-optic devices on $LiNbO_3$ and $LiTaO_3$. One issue is the high strain around domain wall and strong asymmetric defect configuration between virgin and reversed domain state exists in

congruent crystals, as can be seen in NSOM and X-ray experimental data. Fortunately, this strain around domain wall and asymmetrical defect configuration can be reduced by annealing this crystal to temperatures of 150-200°C. Even in near-stoichiometric crystal, annealing helps to reduce any remnant strain around domain walls. The long-range step-index modulation and localized high index modulation which is observed in congruent crystals by using NSOM can't be imaged any more after annealing this crystal.

6.2 Conclusions

1. Based on electrical switching and in-situ optical microscopy experiments, we proposed a defect dipole model
2. Unique anisotropic gradient energy is adapted into phenomenological TDGL modeling to regenerate domain patterns
3. Near Field Optical Microscopy experiment provides a detailed index distribution across a domain wall, which is consistent with the proposed defect dipole model.
4. X-ray reflection topography provides surface lattice strain distribution at the wall
5. X-ray transmission topography clearly showed defect structures inside the crystal and the domain wall clearly. It also detected different lattice parameters between virgin versus domain reversed states, and a 3-fold shear strain around domain corners which is predicted by the TDGL model combined with Eikonal theory.
6. By using unique two source total and scattering FDTD modeling, NSOM Optical transfer Function is successfully calculated
7. By using FDTD, BPM, and Fourier Optic method, the entire NSOM experiment was simulated and index distribution obtained.
8. By using dynamical X-ray theory and Eikonal Ray theory, an X-ray trajectory code was developed and successfully used to analyze X-ray transmission topography images

6.3 Outstanding Issues

In terms of defect dipole modeling, TDGL is a phenomenological modeling method. Even though it gives a very good intuition for the basic ferroelectric multi-domain state interactions and phase transformations, a detailed modeling especially for the structures within a domain wall should have to involve accurate atomic scale modeling. This atomic scale modeling will provide the clue for how defect dipoles are configured inside the crystal.

As domain patterned device size shrinks to sub-microns, a more accurate and well understood control of domain kinetics required. Room temperature domain poling involves high coercive fields, strong elastic energy, and large domain wall energy. High temperature poling may provide a way to fabricate sub micron domain patterning technique by reducing the coercive field and interactions between domain wall and defect dipole. Also, the initial nucleation density also will be improved considerably by heating, making domain switching more uniform.

In measuring domain structures, we applied Near Field Optical Microscopy(NSOM), and X-ray topography methods. Theses two methods have a lot more application and potential. Non-linear NSOM is one of way to improve resolution and sensitivity of linear NSOM. Another approach to improve NSOM resolution is to use a sharp metal tip. Instead of collecting through the tip, data can be collected in far field by using the scattering field from the sharp metal tip. By using interferometric techniques, NSOM also can detect phase information around a domain. That will give a much more detailed index distribution information. All these kinds of NSOM techniques are still is not fully understood and modeling technique is not well set up. Based on our FDTD method for calculating NSOM OTF, many of these new problems can be approached.

X-ray topography experiment also has more potential to be used as an excellent nice technique to detect very accurate strain distribution. By applying external fields that are higher than coercive field, we can do in-situ strain detection during the poling process by using X-ray topography. This experiment will give very nice intuition on how defects interact with moving domain walls.

References

[1] J. M. Dziedzig F. R. Nash P. M. Bridenbaugh, J. R. Carruthers. *Appl. Phys. Lett.*, 17:104, 1970.

[2] K. Beltzler D. Xue. *Appl. Phys. B.*, 72:641, 2001.

Appendix A

1-D TDGL Matlab Code

This is 1-D TDGL code.

```
%This is function polling---This is Main TDGL program
function polling(i,n,x)
% i is a total colume number.
% x is a i*2 matrix. x(1:n,1)=defect site   x(1:n,2)=defect dipole
value
% n is a total defect number.
% p is a j colume polarization value.
%initialrize p
%polv(1:i)=rand(i);
n=1;
polv(1:20,1:11)=-1;
polv(21:i,1:11)=1;
%lx=latice constant for x, ly=latice constant for y.
%gdef=defect gradient energy constant for y direction
%g=normal gradient energy constant for x direction
global lx;
global ly;
global gdef;
global g;
global pnor;
global pdef;
global low_num;
global def_num;
global vec;
global defect_n;
global stabt

lx=10^-6;
ly=10^-6;
gdef=.1;
g=6*10^-3;
pnor=1;
pdef=1;   %only +1 or -1
low_num=i;
def_num=n;

%vec is a original defect state.---Defect contains instant information
for defect values+ or -
vec(1:low_num,1:2)=0;
for i=1:low_num
   for j=1:def_num
      if i==x(j,1)
         vec(i,1)=1;
         vec(i,2)=pdef*x(j,2);
      end
   end
end
%initial defect_v and defect_n.
defect_v=vec(:,2);
defect_n=x(:,1);
stabtime_n(1:low_num)=0;
stabtime_d(1:defect_n)=0;
mobility=2*10^-11;
t=1;
p=polv(:,1);
pre=p;
onevec(1:low_num)=1;
```

```
if(1==0)
for i=1:low_num
   p(i)=0.1*(rand(1)-0.5);
end
p=p';
end
while(t<10000)
   Eapply=-100000000;
   if t>700
      Eapply=0;
   end
   [dp,ddef_v,dtime,energy]=funev(p,defect_v,stabtime_n,Eapply);
   k1=-mobility*dp;
   [dp,ddef_v,dtime,energy]=funev(p+0.5*k1,defect_v,stabtime_n,Eapply);
   k2=-mobility*dp;
   [dp,ddef_v,dtime,energy]=funev(p+0.5*k2,defect_v,stabtime_n,Eapply);
   k3=-mobility*dp;
   [dp,ddef_v,dtime,energy]=funev(p+k3,defect_v,stabtime_n,Eapply);
   k4=-mobility*dp;
   p=p+(k1+2*k2+2*k3+k4)/6;
   for jj=1:low_num
      if (stabtime_n(jj)~=0)
         stabtime_n(jj)=stabtime_n(jj)+1;
      end
   end
   signvec=sign(p).*sign(pre);                        %1 1 1 1 -1 1 1 1
1.......   -1 change sign
   signvec_A=(signvec+1)/2;                           %1 1 1 1  0 1 1 1
1.......
   signvec_B=(signvec_A-1)*-1;                        %0 0 0 0  1 0 0 0
0.......
   pre=p;
   stabtime_n=(signvec_A.*stabtime_n'+signvec_B)';   %setting # to 1 if
sign is changed
   t=t+1;
   if(rem(t,50)==0)
   figure(1)
   plot(1:low_num,p,'*',1:low_num,defect_v,'o');grid on;axis([1 low_num
-1.5 1.5]);
   drawnow;
   figure(2)
   plot(t,Eapply,'o');
   hold on;
   drawnow;
   clear figure;
   end
   if(rem(t,10)==0)
      str=sprintf('pole%d',t);
      save(str,'p');
      %str=sprintf('field%d',t);
      %save(str,'Eapply');
      Efield(t)=Eapply;
   end
end
   save('Field','Efield');
```

```
%This is function funev---This is sub TDGL program which calculate sum
of free energy changing
function
[dpol,ddefect_v,dtime,tenergy]=funev(pol,defect_v,stabtime,Eapp)

global lx;
global ly;
global gdef;
global g;
global pnor;
global pdef;
global low_num;
global def_num;
global vec;
global defect_n;
total_energy(1:low_num)=0;
[Udipole,dUdipole,time]=dipole_energy(pol,stabtime);
[Uext,dUext]=External_energy(pol,defect_v,Eapp);
[Ugrad_col,dUgrad_col]=gradientC_energy(pol,defect_v);
[Ugrad_low,dUgrad_low]=gradientL_energy(pol);
dpol=dUdipole+dUext+dUgrad_col+dUgrad_low;
total_energy=Udipole+Uext+Ugrad_col+Ugrad_low;
tenergy=sum(total_energy);
ddefect_v=defect_n;
dtime(1:low_num)=0;
clear pol;
clear defect_V;
clear stabtime;
clear Eapp;
clear time;
clear Udipole;
clear dUdipole;
clear Uext;
clear dUext;
clear Ugrad_col;
clear dUgrad_col;
clear Ugrad_low;
clear dUgrad_low;

%This is function dipole_energy---This function calculate dipole energy
changing
function [Udipole,dUdipole,time]=dipole_energy(pol,stime)
global pnor;
global pdef;
global low_num;
global def_num;
global lx;
global ly;
global vec;
global defect_n;
limit=1;
Udipole=0;
dUdipole=0;
mul=50;
di33=30;
```

```
Psi1=1/(8.854*10^(-12)*di33);
for i=1:low_num
    if (pol(i)>-1)&(pol(i)<1)&(stime(i)<400*mul)&(stime(i)~=0)
       if ((stime(i)<1000*mul)&(stime(i)>=200*mul))
           calfactor=1;
           Udipole(i)=0.2*calfactor*Psi1*(-0.5*pol(i)^2+1/4*pol(i)^4);
           dUdipole(i)=0.2*calfactor*Psi1*(-pol(i)+pol(i)^3);
        end
        if ((stime(i)<200*mul)&(stime(i)>=100*mul))
           calfactor=1;
           Udipole(i)=0.2*calfactor*Psi1*(-0.5*pol(i)^2+1/4*pol(i)^4);
           dUdipole(i)=0.2*calfactor*Psi1*(-pol(i)+pol(i)^3);
        end
        if (stime(i)<100*mul)
           calfactor=1;
           Udipole(i)=0.10*calfactor*Psi1*(-0.5*pol(i)^2+1/4*pol(i)^4);
           dUdipole(i)=0.10*calfactor*Psi1*(-pol(i)+pol(i)^3);
        end
     else
        calfactor=1;
       Udipole(i)=calfactor*Psi1*(-0.5*pol(i)^2+1/4*pol(i)^4);
       dUdipole(i)=calfactor*Psi1*(-pol(i)+pol(i)^3);
    end
 end
Udipole=Udipole';
dUdipole=dUdipole';
time=stime;
clear stime;
clear pol;

%This is function External_energy—This function calculate defect dipole
induced energy changing
function [U,dU]=External_energy(pol,defv,Ea)
global pnor;
global pdef;
global low_num;
global def_num;
global lx;
global ly;
global vec;
global defect_n;
U=0;
dU=0;
temp=0;
E_def(1:low_num,1:1:11)=0;
total=0;
di33=30;
shield=1/(4*pi*8.854*10^(-12)*di33);
%calcurate electric field created by defect------------E_def
for l=1:low_num
   for m=1:def_num
      for k=1:11
         if (l-defect_n(m))~=0
            temp=shield*defv(defect_n(m))*pdef*(((lx*(l-
defect_n(m)))^2+(ly*k-6)^2)^(-3/2))*(3*abs(k-6)*ly/((lx*(l-
defect_n(m)))^2+(ly*(k-6))^2)^(1/2)-1);
            E_def(l,k)=E_def(l,k)+temp;
```

```
         else
            if k~=6
            temp=shield*defv(defect_n(m))*pdef*(((lx*(l-
defect_n(m)))^2+(ly*k-6)^2)^(-3/2))*(3*abs(k-6)*ly/((lx*(l-
defect_n(m)))^2+(ly*(k-6))^2)^(1/2)-1);
            E_def(l,k)=E_def(l,k)+temp;
            end
         end
      end
   end
end
%calcurate energy
l=1:low_num;k=1:11;
temp_E(l,k)=E_def;
temp_vec(l,k)=1;
temp_vec(:,6)=temp_vec(:,6).*(vec(:,1)-1)*-1;
for iter=1:11
    pol2d(l,iter)=pol;
end
U2=temp_vec.*E_def.*pol2d;
dU2=temp_vec.*(E_def+Ea);
U=(sum(U2'))';
dU=-(sum(dU2'))';
clear temp_E;
clear temp_vec;
clear E_def;
clear U2;
clear dU2;
clear pol2d;
clear pol;
clear defv;
clear Ea;

%This is function gradientC _energy—This is calculating gradient energy
for each column.
function [Ugrad,dUgrad]=gradientC_energy(pol,defv)
global gdef;
global pnor;
global pdef;
global low_num;
global def_num;
global lx;
global ly;
global vec;
global defect_n;
Ugrad(1:low_num)=0;
dUgrad(1:low_num)=0;
mag=1;
dev(1:low_num)=0;
for i=1:low_num
   dev(i)=defv(i)-pol(i);
   if defv(i)>0
      if dev(i)>0
         Ugrad(i)=-mag*dev(i)^2;
         dUgrad(i)=-2*mag*dev(i);
      end
```

```
   end
   if defv(i)<0
      if dev(i)<0
         Ugrad(i)=-mag*dev(i)^2;
         dUgrad(i)=-2*mag*dev(i);
      end
   end
end
Ugrad=Ugrad';
dUgrad=dUgrad';
clear pol;
clear defv;
clear dev;

%This is function gradientL _energy-- This is calculating gradient
energy for each low.
function [Ugrad,dUgrad]=gradientL_energy(pol)
global g;
global pnor;
global pdef;
global low_num;
global def_num;
global lx;
global ly;
global vec;
global defect;
dpol=diff(pol)/lx;
dpol(low_num)=0;
ddpol=diff(dpol)/lx;
ddpol(low_num)=0;
ddpole(1:low_num)=0;
for i=1:(low_num-1)
   ddpole(i+1)=ddpol(i);
end
ddpole(1)=ddpole(2);
dUgrad=-2*g*ddpole';
Ugrad=g*dpol.^2;
```

Appendix B

Rflection Ray Tracing

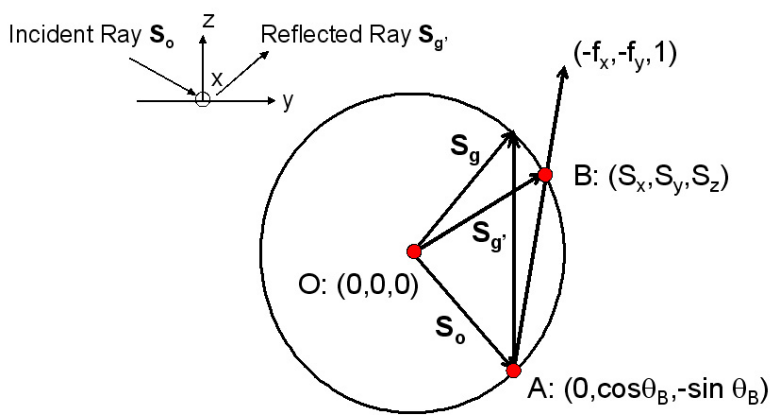

Fig. B.1. Ewald sphere and modified reflected Ray vector $S_{g'}$.

This is based on kinematical X-ray theory. Figure B.1 shows Ewald sphere with unit radius. $\mathbf{S_o}$ is the incident ray unit vector, and $\mathbf{S_g}$ is a reflected ray unit vector when the rystal is perfect. If crystal surface has a non uniform topology, reflected beam direction will be modified to $\mathbf{S_{g'}}$ which is the intersection between line $\overline{AB}$ and unit sphere. Slope of the line $\overline{AB}$ will be the surface normal vector $(-f_x, -f_y, 1)$. Function f(x,y) is a z-direction topology, and f_x, and f_y are, respectively, the x, and y direction derivatives of function f(x,y). The line $\overline{AB}$ equation will be

$$\frac{S_x}{-f_x} = \frac{S_y - cos\theta_B}{-f_y} = S_z + sin\theta_B \tag{B.1}$$

S_x, S_y, S_z will be

$$S_x = -f_x \cdot \frac{2 \cdot f_y cos\theta_B + 2sin\theta_B}{f_x^2 + f_y^2 + 1} \tag{B.2}$$

$$S_y = -f_y \cdot \frac{2 \cdot f_y cos\theta_B + 2sin\theta_B}{f_x^2 + f_y^2 + 1} + cos\theta_B \tag{B.3}$$

$$S_z = \frac{2 \cdot f_y cos\theta_B + 2sin\theta_B}{f_x^2 + f_y^2 + 1} - sin\theta_B \tag{B.4}$$

$$\tag{B.5}$$

In real space, the beam location on detector can be calculated based on $\mathbf{S_{g'}}$ vector as can be seen in Fig. B.2. The distance between reference point in sample and detector is l_0.

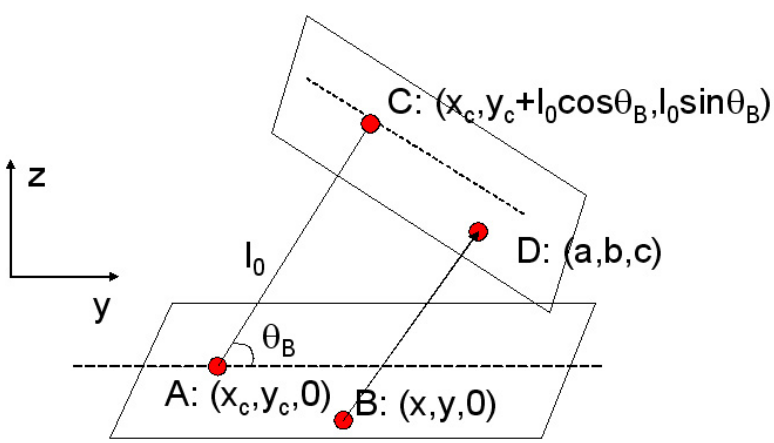

Fig. B.2. Real space Ray path. Plane contain point A, and B is sample surface, plane include point C, D is detector. By using reflected Ray vector $\mathbf{S_{g'}}$, we can Reflected ray's final destination D point.

By using plane equation of detector and Ray vector we can calculate point D: (a,b,c).

$$a = \frac{S_x}{S_y}(b-y)+x \tag{B.6}$$

$$c = \frac{S_x}{S_y}(b-y) \tag{B.7}$$

$$b = \frac{\frac{S_y}{S_z}\cdot\frac{l_o+cos\theta_B\cdot y_c}{sin\theta_B}+y}{1+\frac{S_y}{S_z}\cdot\frac{cos\theta_B}{sin\theta_B}} \tag{B.8}$$

$$\tag{B.9}$$

Now, new variable Δ is introduced.

$$a - x = \Delta \tag{B.10}$$

For convinience, we can set y=0, then Δ can be represented by,

$$\Delta cos\theta_B\cdot(cos^2\theta_B - sin^2\theta_B)\cdot f_x^2 + 2sin\theta_B cos\theta_B l_0 f_x + cos\theta_B\cdot\Delta = 0 \tag{B.11}$$

By solveing this equation, f_x can be obtained

$$f_x = \frac{-sin\theta_B\cdot l_0 \pm \sqrt{sin^2\theta_B\cdot l_0^2 - \Delta^2\cdot cos^2\theta_b\cdot(cos^2\theta_B - sin^2\theta_B)}}{cos^2\theta_B - sin^2\theta_B} \tag{B.12}$$

Appendix C

3-D TDGL Matlab Code

It is composed of functions tdgl3d-v5LT, function tdgl3d-sub, and function der3d. tdgl3d-v5LT is a main TDGL file. It gets free energy variation from tdgl3d-sub in every time step. tdgl3d-sub calculates the free energy change in each iteration step. der3d is a function for calculating the 1st and 2nd order derivatives.

```
  function tdgl3d_v5LT
  % This is 3D TDGL program:

  test=0;

global a1;
global a2;
global a3;
global N;
global Nz;
global g1;
global g2;
global dd;
global Ext;

global Q11;
global Q12;
global Q13;
global Q14;
global Q21;
global Q22;
global Q23;
global Q24;
global Q31;
global Q32;
global Q33;
global Q41;
global Q42;
global Q44;
global Q55;
global Q56;
global Q65;
global Q66;
global energyplot

%Define Dimension N and iteration number IN
N=2^7;
Nz=2^2;
%number of total iteration
IN=5000;
iter=1;
% If energy plot is 0 do not calculate energy plot, if it is 1 it calculate energy status, it
need more memory
energyplot=0;
%If you want to see real space strain, then set it 1
real_strain=1;
%If you want to calculate displacement tehen set disp=1; otherwise set it 0
disp=1;
%Initial valvue
Px(1:N,1:N,1:Nz)=0;
Py(1:N,1:N,1:Nz)=0;
Pz(1:N,1:N,1:Nz)=0;
%random source(Random initial condition)
Pz(1:N,1:N,1:Nz)=(rand(N,N,Nz)-0.5)/10;
%This is initial condition for center nuclei is already there. when if 1==1, it will be on
if 1==0
for ii=1:N
   for jj=1:N
      R=N/15;
      if sqrt((N/2-ii)^2+(N/2-jj)^2)<R
         temp(ii,jj)=-0.55;
      else
         temp(ii,jj)=+0.55;
      end
   end
end
for kk=1:Nz
```

```
   Pz(1:N,1:N,kk)=temp;
end
clear temp;
end
%circle nucliation
FPx(1:N,1:N,1:Nz)=0;
FPy(1:N,1:N,1:Nz)=0;
FPz(1:N,1:N,1:Nz)=0;
dFx(1:N,1:N,1:Nz)=0;
dFy(1:N,1:N,1:Nz)=0;
dFz(1:N,1:N,1:Nz)=0;
sigx1(1:N,1:N,1:Nz)=0;
sigy1(1:N,1:N,1:Nz)=0;
sigz1(1:N,1:N,1:Nz)=0;
sigx2(1:N,1:N,1:Nz)=0;
sigy2(1:N,1:N,1:Nz)=0;
sigz2(1:N,1:N,1:Nz)=0;
sigx3(1:N,1:N,1:Nz)=0;
sigy3(1:N,1:N,1:Nz)=0;
sigz3(1:N,1:N,1:Nz)=0;
sigx4(1:N,1:N,1:Nz)=0;
sigy4(1:N,1:N,1:Nz)=0;
sigz4(1:N,1:N,1:Nz)=0;

if energyplot==1
   ETelastic(1:N,1:N,1:Nz)=0;
   alpa1(1:N,1:N,1:Nz)=0;
   alpa2(1:N,1:N,1:Nz)=0;
   alpa3(1:N,1:N,1:Nz)=0;
   beta1(1:N,1:N,1:Nz)=0;
   beta2(1:N,1:N,1:Nz)=0;
   beta3(1:N,1:N,1:Nz)=0;
   Etotal_old=0;
   Ep_old=0;
   Eg_old=0;
   Eh_old=0;
end
%This is displacement variable
if disp==1
   vkx(1:N,1:N,1:Nz)=0;
   vky(1:N,1:N,1:Nz)=0;
   vkz(1:N,1:N,1:Nz)=0;
   vx(1:N,1:N,1:Nz)=0;
   vy(1:N,1:N,1:Nz)=0;
   vz(1:N,1:N,1:Nz)=0;
end
%define constant mobility; and dd=grid space;g1 is isotropic gradient energy for in plane
%g2 is gradient energy for z direction
%Ext=external field
mobilityx=100*10^-17;
mobilityy=100*10^-17;
mobilityz=100*10^-12;
dd=10^-6;
g1=25*10^-5;
g2=40*10^-5;
Ext=-0*2*200*10^6;

%For LN di33=dielectric constant PSP=spontaneous polarization
%di33=30;
%PSP=0.75;
%For LT
di33=43.5;
PSP=0.55;
a1=1/(8.854*10^(-12)*di33);
a2=a1/PSP^2;
a3=0.00000001*10^9;
%Elastic C constant
```

```
C11=2.33*10^11*1;
C12=0.47*10^11*1;
C13=0.80*10^11*1;
C33=2.75*10^11*1;
C44=0.94*10^11*1;
C14=-0.11*10^11*1;
C66=0.93*10^11*1;
%This is original electrostrictive constant
q44=0.052*1;
q42=0.016*1;
q33=0.011*1;
q31=-0.0047*1;
q41=-q42;
q56=-2*q42;
q65=-q42;
%This is phenominological electrostrictive constant
Q11=C13*q31+C14*q41;
Q12=C13*q31+C13*q42;
Q13=C11*q31+C12*q31+C13*q33;
Q14=C11*q41+C12*q42+C14*q44;
Q21=C13*q31-C14*q41;
Q22=C13*q31-C14*q42;
Q23=C12*q31+C11*q31+C13*q33;
Q24=C12*q41+C11*q42-C14*q44;
Q31=C33*q31;
Q32=C33*q31;
Q33=C13*q31+C13*q31+C33*q33;
Q41=C44*q41;
Q42=C44*q42;
Q44=C14*q41-C14*q42+C44*q44;
Q55=C14*q65;
Q56=C44*q56;
Q65=C66*q65;
Q66=C14*q56;
%C dimension-->N/m^2
%Q dimension-->N*m^2/C^2
%a dimension-->N*m^6/C^4

P11(1:N,1:N,1:Nz)=0;
P21(1:N,1:N,1:Nz)=0;
P31(1:N,1:N,1:Nz)=0;
P12(1:N,1:N,1:Nz)=0;
P22(1:N,1:N,1:Nz)=0;
P32(1:N,1:N,1:Nz)=0;
P13(1:N,1:N,1:Nz)=0;
P23(1:N,1:N,1:Nz)=0;
P33(1:N,1:N,1:Nz)=0;

OMG11(1:N,1:N,1:Nz)=0;
OMG21(1:N,1:N,1:Nz)=0;
OMG31(1:N,1:N,1:Nz)=0;
OMG12(1:N,1:N,1:Nz)=0;
OMG22(1:N,1:N,1:Nz)=0;
OMG32(1:N,1:N,1:Nz)=0;
OMG13(1:N,1:N,1:Nz)=0;
OMG23(1:N,1:N,1:Nz)=0;
OMG33(1:N,1:N,1:Nz)=0;

Ak11(1:N,1:N,1:Nz)=0;
Ak12(1:N,1:N,1:Nz)=0;
Ak13(1:N,1:N,1:Nz)=0;
Ak21(1:N,1:N,1:Nz)=0; Ak22(1:N,1:N,1:Nz)=0;
Ak23(1:N,1:N,1:Nz)=0;
Ak31(1:N,1:N,1:Nz)=0;
Ak32(1:N,1:N,1:Nz)=0;
Ak33(1:N,1:N,1:Nz)=0;
```

```
Tk11(1:N,1:N,1:Nz)=0;
Tk12(1:N,1:N,1:Nz)=0;
Tk13(1:N,1:N,1:Nz)=0;
Tk22(1:N,1:N,1:Nz)=0;
Tk23(1:N,1:N,1:Nz)=0;
Tk33(1:N,1:N,1:Nz)=0;

%Define reciprocal grid
[y,x,z]=meshgrid(1:N,1:N,1:Nz);
fx=(2*pi*(x-1)/N-pi)/dd;
fy=(2*pi*(y-1)/N-pi)/dd;
fz=(2*pi*(z-1)/Nz-pi)/dd;
kx=fftshift(fx);
ky=fftshift(fy);
kz=fftshift(fz);
clear fx;
clear fy;
clear fz;
%normalize k vector
k(1:N,1:N,1:Nz)=sqrt(kx.^2+ky.^2+kz.^2);
%To prevent devide by 0
k(1,1,1)=1;
nx(1:N,1:N,1:Nz)=kx./k;
ny(1:N,1:N,1:Nz)=ky./k;
nz(1:N,1:N,1:Nz)=kz./k;
clear kx;
clear ky;
clear kz;

%Define OMG Matrix---> Green's function for reciprocal space strain energy
if (1==1)
ix=1:N;
ifx=(2*pi*(ix-1)/N-pi)/dd;
ikx=fftshift(ifx);
clear ifx;
for ii=1:N
   for jj=1:N
      for kk=1:Nz
         nxx=ikx(ii);
         nyy=ikx(jj);
         nzz=ikx(kk);

         if (ii*jj*kk~=1)
            nsize=sqrt(nxx.^2+nyy^2+nzz^2);
            nxx=nxx/nsize;
            nyy=nyy/nsize;
            nzz=nzz/nsize;

inv_OMG=[C11*nxx^2+C66*nyy^2+C44*nzz^2+2*C14*nzz*nyy,(C12+C66)*nxx*nyy+2*C14*nxx*nzz,(C13+C44)*
nxx*nzz+2*C14*nxx*nyy; ...
                (C12+C66)*nxx*nyy+2*C14*nxx*nzz,C66*nxx^2+C11*nyy^2+C44*nzz^2-
2*C14*nyy*nzz,(C13+C44)*nyy*nzz+C14*(nxx^2-nyy^2); ...
                (C13+C44)*nxx*nzz+2*C14*nxx*nyy,(C13+C44)*nyy*nzz+C14*(nxx^2-
nyy^2),C44*nxx^2+C44*nyy^2+C33*nzz^2];
         %input('inv_OMG')
         OMG=inv(inv_OMG);
         OMG11(ii,jj,kk)=OMG(1,1);
         OMG12(ii,jj,kk)=OMG(1,2);
         OMG13(ii,jj,kk)=OMG(1,3);
         OMG21(ii,jj,kk)=OMG(2,1);
         OMG22(ii,jj,kk)=OMG(2,2);
         OMG23(ii,jj,kk)=OMG(2,3);
         OMG31(ii,jj,kk)=OMG(3,1);
         OMG32(ii,jj,kk)=OMG(3,2);
         OMG33(ii,jj,kk)=OMG(3,3);
         end
      end
```

```
    end
end
OMG11(1,1,1)=OMG11(2,2,2);
OMG12(1,1,1)=OMG12(2,2,2);
OMG13(1,1,1)=OMG13(2,2,2);
OMG21(1,1,1)=OMG21(2,2,2);
OMG22(1,1,1)=OMG22(2,2,2);
 OMG23(1,1,1)=OMG23(2,2,2);
OMG31(1,1,1)=OMG31(2,2,2);
OMG32(1,1,1)=OMG32(2,2,2);
OMG33(1,1,1)=OMG33(2,2,2);
save('OMG11C14','OMG11');
save('OMG12C14','OMG12');
save('OMG13C14','OMG13');
save('OMG21C14','OMG21');
save('OMG22C14','OMG22');
save('OMG23C14','OMG23');
save('OMG31C14','OMG31');
save('OMG32C14','OMG32');
save('OMG33C14','OMG33');

else
load('OMG11C14','OMG11');
load('OMG12C14','OMG12');
load('OMG13C14','OMG13');
load('OMG21C14','OMG21');
load('OMG22C14','OMG22');
load('OMG23C14','OMG23');
load('OMG31C14','OMG31');
load('OMG32C14','OMG32');
load('OMG33C14','OMG33');
end

%This is starting of iteration
while (iter<=IN)
   %Turm off field!!!
   if (iter==300)
      Ext=50*10^6;
   end

   % Make arbitrary periodical P condition
  TM=(Px(N,:,:)+Px(1,:,:))/2;
  Px(N,:,:)=TM;
  Px(1,:,:)=TM;
  TM=(Px(:,N,:)+Px(:,1,:))/2;
  Px(:,N,:)=TM;
  Px(:,1,:)=TM;
  TM=(Px(:,:,Nz)+Px(:,:,1))/2;
  Px(:,:,Nz)=TM;
  Px(:,:,1)=TM;
  TM=(Py(N,:,:)+Py(1,:,:))/2;
  Py(N,:,:)=TM;
  Py(1,:,:)=TM;
  TM=(Py(:,N,:)+Py(:,1,:))/2;
  Py(:,N,:)=TM;
  Py(:,1,:)=TM;
  TM=(Py(:,:,Nz)+Py(:,:,1))/2;
  Py(:,:,Nz)=TM;
  Py(:,:,1)=TM;
  TM=(Pz(N,:,:)+Pz(1,:,:))/2;
  Pz(N,:,:)=TM;
  Pz(1,:,:)=TM;
  TM=(Pz(:,N,:)+Pz(:,1,:))/2;
  Pz(:,N,:)=TM;
  Pz(:,1,:)=TM;
  TM=(Pz(:,:,Nz)+Pz(:,:,1))/2;
  Pz(:,:,Nz)=TM;
```

```
  Pz(:,:,1)=TM;
%Define electro-strictive energy matrix Tkij in k space---> This is symetrical matrix
%First define real space and convert it to k space... if directly define in k space then I
first get Pz^2(r)-->FPz^2(k) or convolution
Tk11=Q11*Px.^2+Q12*Py.^2+Q13*Pz.^2+Q14*Py.*Pz;
Tk12=Q66*Px.*Py+Q65*Px.*Pz;
Tk13=Q56*Px.*Py+Q55*Px.*Pz;
Tk22=Q21*Px.^2+Q22*Py.^2+Q23*Pz.^2+Q24*Py.*Pz;
Tk23=Q41*Px.^2+Q42*Py.^2+Q44*Py.*Pz;
Tk33=Q31*Px.^2+Q32*Py.^2+Q33.*Pz.^2;
Tk11=fftn(Tk11);
Tk12=fftn(Tk12);
Tk13=fftn(Tk13); Tk22=fftn(Tk22);
Tk23=fftn(Tk23);
Tk33=fftn(Tk33);

%A--> OMG*Tk matrix
Ak11=OMG11.*Tk11+OMG12.*Tk12+OMG13.*Tk13;
Ak12=OMG21.*Tk11+OMG22.*Tk12+OMG23.*Tk13;
Ak13=OMG31.*Tk11+OMG32.*Tk12+OMG33.*Tk13;
Ak21=OMG11.*Tk12+OMG12.*Tk22+OMG13.*Tk23;
Ak22=OMG21.*Tk12+OMG22.*Tk22+OMG23.*Tk23;
Ak23=OMG31.*Tk12+OMG32.*Tk22+OMG33.*Tk23;
Ak31=OMG11.*Tk13+OMG12.*Tk23+OMG13.*Tk33;
Ak32=OMG21.*Tk13+OMG22.*Tk23+OMG23.*Tk33;
Ak33=OMG31.*Tk13+OMG32.*Tk23+OMG33.*Tk33;

%Define PI matrix
Pk11=nx.*nx.*Ak11+nx.*ny.*Ak21+nx.*nz.*Ak31;
Pk21=nx.*nx.*Ak12+nx.*ny.*Ak22+nx.*nz.*Ak32;
Pk31=nx.*nx.*Ak13+nx.*ny.*Ak23+nx.*nz.*Ak33;
Pk12=nx.*ny.*Ak11+ny.*ny.*Ak21+ny.*nz.*Ak31;
Pk22=nx.*ny.*Ak12+ny.*ny.*Ak22+ny.*nz.*Ak32;
Pk32=nx.*ny.*Ak13+ny.*ny.*Ak23+ny.*nz.*Ak33;
Pk13=nz.*nx.*Ak11+nz.*ny.*Ak21+nz.*nz.*Ak31;
Pk23=nz.*nx.*Ak12+nz.*ny.*Ak22+nz.*nz.*Ak32;
Pk33=nz.*nx.*Ak13+nz.*ny.*Ak23+nz.*nz.*Ak33;
%This is energy plot calculation routine for elastic and coupling part, in K space.
if energyplot==1
   gap=10;
   if(rem(iter,gap)==0)
   alpa1=conj(Tk11.*nx+Tk12.*ny+Tk13.*nz);
   alpa2=conj(Tk12.*nx+Tk22.*ny+Tk23.*nz);
   alpa3=conj(Tk12.*nx+Tk23.*ny+Tk33.*nz);
   beta1=OMG11.*alpa1+OMG12.*alpa2+OMG13.*alpa3;
   beta2=OMG21.*alpa1+OMG22.*alpa2+OMG23.*alpa3;
   beta3=OMG31.*alpa1+OMG32.*alpa2+OMG33.*alpa3;

   ETelastic=real((nx.*(Tk11.*beta1+Tk12.*beta2+Tk13.*beta3) ...
      +ny.*(Tk12.*beta1+Tk22.*beta2+Tk23.*beta3) ...
      +nz.*(Tk13.*beta1+Tk23.*beta2+Tk33.*beta3)));

  Eh=-sum(sum(sum(ETelastic)));
   end
end
%This is displacement calcuration loop in k space
if disp==0
   vkx=i*(OMG11.*nx.*(Tk11+Tk12+Tk13) ...
      +OMG12.*ny.*(Tk12+Tk22+Tk23) ...
      +OMG13.*nz.*(Tk13+Tk23+Tk33))./k;
   vky=i*(OMG21.*nx.*(Tk11+Tk12+Tk13) ...
      +OMG22.*ny.*(Tk12+Tk22+Tk23) ...
      +OMG23.*nz.*(Tk13+Tk23+Tk33))./k;
   vkz=i*(OMG31.*nx.*(Tk11+Tk12+Tk13) ...
      +OMG32.*ny.*(Tk12+Tk22+Tk23) ...
      +OMG33.*nz.*(Tk13+Tk23+Tk33))./k;
   vx=real(ifftn(vkx));
```

```
   vy=real(ifftn(vky));
   vz=real(ifftn(vkz));
   vt=sqrt(vx.^2+vy.^2);
   %This is real space strain calculation
   if real_strain==1
      [e1]=der3d(vx,1,1);
      [e2]=der3d(vy,2,1);
      [e3]=der3d(vz,3,1);
      [e4]=1/2*(der3d(vy,3,1)+der3d(vz,2,1));
      [e5]=1/2*(der3d(vz,1,1)+der3d(vx,3,1));
      [e6]=1/2*(der3d(vx,2,1)+der3d(vy,1,1));
      %Real space starin energy
      figure(100)
      surf(real(e1(:,:,Nz/2)));title(['strain xx(XY)
I=',num2str(iter)]);view(0,90);colorbar;shading interp;drawnow;axis tight;
      figure(101)
      surf(real(e2(:,:,Nz/2)));title(['strain yy(XY)
I=',num2str(iter)]);view(0,90);colorbar;shading interp;drawnow;axis tight;
      figure(102)
      surf(real(e3(:,:,Nz/2)));title(['strain zz(XY)
I=',num2str(iter)]);view(0,90);colorbar;shading interp;drawnow;axis tight;
      figure(103)
      surf(real(e4(:,:,Nz/2)));title(['strain yz(XY)
I=',num2str(iter)]);view(0,90);colorbar;shading interp;drawnow;axis tight;
      figure(104)
      surf(real(e5(:,:,Nz/2)));title(['strain xz(XY)
I=',num2str(iter)]);view(0,90);colorbar;shading interp;drawnow;axis tight;
      figure(105)
      surf(real(e6(:,:,Nz/2)));title(['strain xy(XY)
I=',num2str(iter)]);view(0,90);colorbar;shading interp;drawnow;axis tight;
      E_elastic=C11*e1.*e1+C11*e2.*e2+C33*e3.*e3+C44*e4.*e4+C44*e5.*e5+C66*e6.*e6 ...
         +2*C12*e1.*e2+2*C13*e1.*e3+2*C13*e2.*e3+2*C14*e1.*e4-2*C14*e2.*e4+2*C14*e5.*e6;
      E_coupling=Q11*e1.*Px.^2+Q12*e1.*Py.^2+Q13*e1.*Pz.^2+Q14*e1.*Py.*Pz ...
         +Q21*e2.*Px.^2+Q22*e2.*Py.^2+Q23*e2.*Pz.^2+Q24*e2.*Py.*Pz ...
         +Q31*e3.*Px.^2+Q32*e3.*Py.^2+Q33*e3.*Pz.^2 ...
         +Q41*e4.*Px.^2+Q42*e4.*Py.^2+Q44*e4.*Py.*Pz ...
         +Q55*e5.*Px.*Pz+Q56*e5.*Px.*Py ...
         +Q65*e6.*Px.*Pz+Q66*e6.*Px.*Py;

   end

end

%If Memory is required too much then I can use Pk P as same matrix
P11=ifftn(Pk11);
P21=ifftn(Pk21);
P31=ifftn(Pk31);
P12=ifftn(Pk12);
P22=ifftn(Pk22);
P32=ifftn(Pk32);
P13=ifftn(Pk13);
P23=ifftn(Pk23);
P33=ifftn(Pk33);

P11=2*real(P11);
P21=2*real(P21);
P31=2*real(P31);
P12=2*real(P12);
P22=2*real(P22);
P32=2*real(P32);
P13=2*real(P13);
P23=2*real(P23);
P33=2*real(P33);

%Enery calculation In real space
%This is real time evolution by using runge kunta method
[dFx,dFy,dFz,Eg]=tdgl3d_sub(Px,Py,Pz,nx,ny,nz,P11,P12,P13,P21,P22,P23,P31,P32,P33);
```

```
sigx1=-mobilityx*dFx;
sigy1=-mobilityy*dFy;
sigz1=-mobilityz*dFz;

[dFx,dFy,dFz,Eg]=tdgl3d_sub(Px+0.5*sigx1,Py+0.5*sigy1,Pz+0.5*sigz1,nx,ny,nz,P11,P12,P13,P21,P22
,P23,P31,P32,P33);
sigx2=-mobilityx*dFx;
sigy2=-mobilityy*dFy;
sigz2=-mobilityz*dFz;

[dFx,dFy,dFz,Eg]=tdgl3d_sub(Px+0.5*sigx2,Py+0.5*sigy2,Pz+0.5*sigz2,nx,ny,nz,P11,P12,P13,P21,P22
,P23,P31,P32,P33);
sigx3=-mobilityx*dFx;
sigy3=-mobilityy*dFy;
sizz3=-mobilityz*dFz;

[dFx,dFy,dFz,Eg]=tdgl3d_sub(Px+sigx3,Py+sigy3,Pz+sigz3,nx,ny,nz,P11,P12,P13,P21,P22,P23,P31,P32
,P33);
sigx4=-mobilityx*dFx;
sigy4=-mobilityy*dFy;
sigz4=-mobilityz*dFz;

Px=Px+(sigx1+2*sigx2+2*sigx3+sigx4)/6;
Py=Py+(sigy1+2*sigy2+2*sigy3+sigy4)/6;
Pz=Pz+(sigz1+2*sigz2+2*sigz3+sigz4)/6;

GPx=der3d(Px,1,1);
GPy=der3d(Py,2,1);

if(rem(iter,200)==0)
   figure(1)
surf(real(Pz(:,:,Nz/2)));title(['Pz(XY) I=',num2str(iter)]);view(0,90);shading
interp;colorbar;drawnow;axis tight;
end
if energyplot==1
   %This is energy calculation time gap.
   gap=10;
   if(rem(iter,gap)==0)
      Ep=sum(sum(sum(-a1*Pz.^2/2+a2*Pz.^4/4+a3*(Px.^2+Py.^2)/2)));
      Etotal=Ep+Eg+Eh;
      delta_Etotal=Etotal-Etotal_old;
      delta_Ep=Ep_old-Ep;
      delta_Eg=Eg_old-Eg;
      delta_Eh=Eh_old-Eh;
      Etotal_old=Etotal;
      Ep_old=Ep;
      Eg_old=Eg;
      Eh_old=Eh;
   end
end

if(rem(iter,5)==0)&(iter>290)
str=sprintf('outputP_%d',iter);
save(str,'Pz');
end

iter=iter+1;
clear figure;
end
```

```
function
[delta_Fx,delta_Fy,delta_Fz,Eg]=tdgl3d_sub(Pxx,Pyy,Pzz,nxx,nyy,nzz,PP11,PP12,PP13,PP21,PP22,PP2
3,PP31,PP32,PP33)

global a1;
global a2;
global a3;
global N;
global Nz;
global g1;
global g2;
global dd;
global Ext;

global Q11;
global Q12;
global Q13;
global Q14;
global Q21;
global Q22;
global Q23;
global Q24;
global Q31;
global Q32;
global Q33;
global Q41;
global Q42;
global Q44;
global Q55;
global Q56;
global Q65;
global Q66;
global energyplot
fold3_energy=g1*2500000000000;
fold6_energy=g1/500000000000000000000000;
%If dipole dipole interaction energy is required set dipole_energy=1
d_energy=0;
DDinteraction_energy_x=0;
DDinteraction_energy_y=0;
DDinteraction_energy_z=0;
%This is calculating dipole dipole interaction
if d_energy==1
   const1=10^5*10^12/8/pi/8.85/(2.2^2-1);

DDinteraction_energy_x=const1*2*real(ifftn(fftn(Pxx).*nxx.^2)+ifftn(fftn(Pyy).*nxx.*nyy)+ifftn(
fftn(Pzz).*nxx.*nzz));

DDinteraction_energy_y=const1*2*real(ifftn(fftn(Pyy).*nyy.^2)+ifftn(fftn(Pxx).*nxx.*nyy)+ifftn(
fftn(Pzz).*nyy.*nzz));

DDinteraction_energy_z=const1*2*real(ifftn(fftn(Pzz).*nzz.^2)+ifftn(fftn(Pxx).*nxx.*nzz)+ifftn(
fftn(Pyy).*nyy.*nzz));
end
%This is real space 3 fold gradient energy calculation data
if 1==1
   [FXX]=der3d(Pzz,1,2);
   [FYY]=der3d(Pzz,2,2);
   [FZZ]=der3d(Pzz,3,2);
   [FY,FX,FZ]=gradient(Pzz);
   AA=FX.*FY;
   BB=FX.^2-FY.^2;
   [AAY,AAX,AAZ]=gradient(AA);
   [BBY,BBX,BBZ]=gradient(BB);
   Gradient_energy=-5*g1*(FXX+FYY)*1-2*g2*FZZ*1 ...
      -fold3_energy*(12*AAX+6*BBY);
end
%This is real space 6 fold gradient energy calculation data
```

```
if 1==0
   [FX]=der3d(Pzz,1,1);
   [FY]=der3d(Pzz,2,1);
   [FXX]=der3d(Pzz,1,2);
   [FYY]=der3d(Pzz,2,2);
   [FZZ]=der3d(Pzz,3,2);
   [FYFX5]=der3d(Pzz,2,1);
   [FYFX5]=der3d(FYFX5.^5,2,1);
   [FXFX5]=der3d(Pzz,1,1);
   [FXFX5]=der3d(FXFX5.^5,1,1);
   [FXFX3Y2]=der3d(Pzz,1,1).^3.*der3d(Pzz,2,1).^2;
   [FXFX3Y2]=der3d(FXFX3Y2,1,1);
   [FYFX4Y]=der3d(Pzz,1,1).^4.*der3d(Pzz,2,1);
   [FYFX4Y]=der3d(FYFX4Y,2,1);
   [FXFXY4]=der3d(Pzz,1,1).*der3d(Pzz,2,1).^4;
   [FXFXY4]=der3d(FXFXY4,1,1);
   [FYFX2Y3]=der3d(Pzz,1,1).^2.*der3d(Pzz,2,1).^3;
   [FYFX2Y3]=der3d(FYFX2Y3,2,1);
   Gradient_energy=-2*g1*(FXX+FYY)*1-2*g2*FZZ*1 ...
      -fold6_energy*(12*FYFX5-12*FXFX5+120*FXFX3Y2+60*FYFX4Y-60*FXFXY4-120*FYFX2Y3);
end
clear A;
clear B;
Eg=0;
if energyplot==1
```

```
function DM=der3d(X,dm,od)


global dd;
%This is derivative function for dm direction dm=1,2,3 (x,y,z)
%X should be 3 Dimensional matrix
%order determined 1st or second derivative
dimN=size(X);
N=dimN(1);
Nz=dimN(3);
DM(1:N,1:N,1:Nz)=0;
temp1(1:N,1:N,1:Nz)=0;
temp2(1:N,1:N,1:Nz)=0;


% This is first derivative
if(od==1)
   if (dm==1)
      temp1(1:N-1,1:N,1:Nz)=X(2:N,1:N,1:Nz);
      temp1(N,1:N,1:Nz)=X(1,1:N,1:Nz);
      temp2(2:N,1:N,1:Nz)=X(1:N-1,1:N,1:Nz);
      temp2(1,1:N,1:Nz)=X(N,1:N,1:Nz);
      DM=(temp1-temp2)/dd/2;
   end
   if (dm==2)
      temp1(1:N,1:N-1,1:Nz)=X(1:N,2:N,1:Nz);
      temp1(1:N,N,1:Nz)=X(1:N,1,1:Nz);
    temp2(1:N,2:N,1:Nz)=X(1:N,1:N-1,1:Nz);
    temp2(1:N,1,1:Nz)=X(1:N,N,1:Nz);
    DM=(temp1-temp2)/dd/2;
   end
   if (dm==3)
      temp1(1:N,1:N,1:Nz-1)=X(1:N,1:N,2:Nz);
      temp1(1:N,1:N,Nz)=X(1:N,1:N,1);
      temp2(1:N,1:N,2:Nz)=X(1:N,1:N,1:Nz-1);
      temp2(1:N,1:N,1)=X(1:N,1:N,Nz);
      DM=(temp1-temp2)/dd/2;
   end
end


% This is second derivative
if(od==2)
   if (dm==1)
      temp1(1:N-1,1:N,1:Nz)=X(2:N,1:N,1:Nz);
      temp1(N,1:N,1:Nz)=X(1,1:N,1:Nz);
      temp2(2:N,1:N,1:Nz)=X(1:N-1,1:N,1:Nz);
         temp2(1,1:N,1:Nz)=X(N,1:N,1:Nz);
         DM=(temp1+temp2-2*X)/dd/dd;
   end
   if (dm==2)
      temp1(1:N,1:N-1,1:Nz)=X(1:N,2:N,1:Nz);
      temp1(1:N,N,1:Nz)=X(1:N,1,1:Nz);
         temp2(1:N,2:N,1:Nz)=X(1:N,1:N-1,1:Nz);
      temp2(1:N,1,1:Nz)=X(1:N,N,1:Nz);
      DM=(temp1+temp2-2*X)/dd/dd;
   end
   if (dm==3)
      temp1(1:N,1:N,1:Nz-1)=X(1:N,1:N,2:Nz);
      temp1(1:N,1:N,Nz)=X(1:N,1:N,1);
      temp2(1:N,1:N,2:Nz)=X(1:N,1:N,1:Nz-1);
      temp2(1:N,1:N,1)=X(1:N,1:N,Nz);
      DM=(temp1+temp2-2*X)/dd/dd;
   end
end
```

Appendix D

Transmission X-Ray Tracing Matlab Code

This is a Matlab code for transmission geometry X-ray tracing. Initial condition is the strain distribution inside the crystal. While X-ray beam propagates through a 500μm sample, it will absorbed and bent depending on the strain distribution.

```
function xray_eikonal5

%This is X-ray Eikonal Theory Program
%2L is lenth of calculation size of X
L=400*10^-6;
%dx is grid size
dx=1*10^-6;
%Number of grid
N=fix(2*L/dx)+1;
%Bragg angle
thetaB=29.2671*pi/180;
x(1:(N+2))=-L+dx*(-1:(N));
if(1==1)
   A=+0.5*10^-5;
   B=+1.5*10^-5;
   C=+0.5*10^-5;
   E=5*10^-7;
   a=1/(1*10^-6);
   b=1/(10*10^-6);
   c=1/(30*10^-6);
   e1=20*10^-6;
   e2=20*10^-6;
   e3=40*10^-6;
   D_temp1=+B*1/b*sqrt(pi)*erf((x-20*dx)*b);
   D_temp2=-C*1/c*sqrt(pi)*erf((x+20*dx)*c);
   D=A*log10(cosh(a*(x-0*dx)))/log10(exp(1))/a;
   D=0*(D_temp1+D_temp2+D);
   %This is dz/dx
   srotation=-E*(exp(-(x-250*dx).^2/e1^2)+exp(-(x+250*dx).^2/e2^2)-1.0*exp(-(x-
190*dx).^2/e1^2)-1.0*exp(-(x+190*dx).^2/e1^2));
   %This is initial strain
   strain=diff(D)/dx;
   figure(1000)
   plot(strain,'b');title('Strain');hold on;
   figure(1001)
   plot(srotation,'b');title('dz/dx');hold on;
   AD=srotation';
end
temp=diff(D);
%second derivative of displacement
ddD=diff(diff(D))/(dx)^2;
xx(1:N)=x(2:N+1);
N=length(xx);
%X-Ray input data
lamda=1.45315*10^-10;
%H vector mag
H=2*sin(thetaB)/lamda;
%For Sigma susceptibility H fourier component real part
susH=-0.12023*10^-4;
susO=0.24099*10^-4;
%For Sigma susceptibility H fourier component imaginary part
susiH=-0.79176*10^-6;
susiO=0.84288*10^-6;
C=1;
%For Pi susceptibility H fourier component real part
%susH=0.6275*10^-4;
AAA=lamda*sqrt(cos(thetaB)^2)/(C*sqrt(susH*susH));
%max(Beta) should much less than 1/AAA----> for Ray Theory
%figure(1)
%plot(x,D,'b.')
%figure(2)
%plot(xx,ddD,'b.')
%This is ray propagation part....
iternum=100;
deltaZ=500*10^-6/iternum;
%Set Initial Condition
%calcurate This For N source together   jj -->trace data saving start point
```

```
jj=401;
location(1:iternum)=0;
Dangle(1:iternum)=0;
I(1:iternum)=0;
start=1;
finish=N-0;
dnum=0;
Nd=finish-start+1;
Data(1:Nd,1:2)=0;
for kk=start:finish
%Set Initial Condition
%Asymmetric ratio and asymmetric angle da
da=strain;
Gamma=cos(da-thetaB)/cos(da+thetaB);
GammaH=cos(da-thetaB);
GammaO=cos(da+thetaB);
SigmaOS=C*sqrt(abs(Gamma)*susH^2)/sin(2*thetaB);
deltaoff=-susO*(1-Gamma)/2/sin(2*thetaB)*0;
%Deviation angle theta
deltaT=-strain(kk)*tan(thetaB);
%deltaT=deltaT-0.0*10^-5;
deltaT=srotation(kk);
%deltaT=+0*10^-6;
dev_P=(deltaT-deltaoff)/SigmaOS;
Xo=1/lamda/2/sqrt(abs(Gamma))*sqrt(susH^2)*(dev_P+sqrt(dev_P^2+1));
Xh=1/lamda^2*susH^2/4/Xo;
mu0=36445;
mu=mu0*(1-abs(susiH/susiO)/sqrt(1+dev_P^2));
Eta=dev_P+sqrt(dev_P^2+1);
Eta2=dev_P-sqrt(dev_P^2+1);
Int0=1;
Int_Obeam=Int0*(Eta2)/(Eta2-Eta);
Int_Hbeam=Int0*(Eta2*Eta)/(Eta2-Eta);
Intensity=sqrt(Int_Obeam+Int_Hbeam);
   Z=0;
   dnum=dnum+1;
   startX=xx(kk);
   Beta=H*sin(thetaB)^2/cos(thetaB)*lamda/C/susH*ddD(kk);
   locationX=startX;
   AM=Eta-1/Eta;
for ii=1:iternum
   Z=Z+deltaZ;
   %Update AM parameter
   AM=AM-2*Beta*deltaZ;
   %Update Eta
   Eta=((AM-sqrt(AM^2+4))/2);
   %Update Alpha
   Alpha=atan((1-abs(Eta)^2)/(1+abs(Eta)^2)*tan(thetaB));
   %Update X location
   locationX=locationX+deltaZ*tan(Alpha);
   if(kk==jj)
   location(ii)=locationX;
   Dangle(ii)=Alpha;
   I(ii)=Intensity;
   end
   %Get discritized locationX coordinate number and iterpolation ddD value
   tnuma=fix((locationX+L)/dx)+1;
   if(tnuma<N-1)&(tnuma>2)
      iterp_ddD=(ddD(tnuma+1)*(locationX-xx(tnuma))+ddD(tnuma)*(xx(tnuma+1)-locationX))/dx;
   else
      iterp_ddD=0;
   end
   %Update Beta
   Beta=H*sin(thetaB)^2/cos(thetaB)*lamda/C/susH*iterp_ddD;
   %Update deviation parameter dev_P and absorption coefficient
   dev_P=(Eta^2-1)/(2*Eta);
   mu=mu0*(1-abs(susiH/susiO)/sqrt(1+dev_P^2));
```

```
   %Int_Obeam=Intensity;

   %Intensity=(Int_Obeam^(1/2)+Int_Hbeam^(1/2))^2;
   %mu=mu0*(1-0.8/sqrt(1+dev_P^2));
   %Intensity=Intensity*exp(-mu*deltaZ/cos(thetaB));
   dI=Intensity*(-mu0/cos(thetaB)*deltaZ+mu0/cos(thetaB)*abs(susiH/susiO)*sqrt(1-
tan(Alpha)^2/tan(thetaB)^2)*deltaZ);
   Intensity=Intensity+dI;
end
Data(dnum,1)=locationX;
Data(dnum,2)=Intensity;
Data(dnum,3)=Eta;
Data(dnum,4)=Beta;
Data(dnum,5)=mu;
Data(dnum,6)=dev_P;
end
figure(3)
plot((1:iternum)*deltaZ,location,'b.');title('ray');hold on;
figure(4)
plot((1:iternum)*deltaZ,Dangle,'b.');title('Eta');hold on;
ID1=interp(Data(:,1),30);
ID2=interp(Data(:,2),30);
ID3=interp(Data(:,3),30);
figure(5)
plot(Data(:,6),'k-');title('Dev_P');;hold on;
figure(6)
plot(ID1,'b-');title('location');;hold on;
figure(7)
plot(ID2,'b-');title('Intensity');;hold on;
figure(8)
plot(ID3,'b-');title('Eta');;hold on;
figure(9)
plot(Data(:,4),'b-');title('Beta');;hold on;
figure(10)
plot(Data(:,5)/mu0,'b-');title('mu/mu0');;hold on;
I(iternum)

%Now, calculate Obeam, and Hbeam
Obeam=(ID2.^2./(1+ID3.^4+2*ID3.^2*cos(2*thetaB))).^(1/4);
Hbeam=ID3.*Obeam;
figure(11)
plot((Obeam).^2,'b-');title('Zero beam');;hold on;
figure(11)
plot((Hbeam).^2,'b-');title('H beam');;hold on;
NNN=length(ID1);
LL=L;
ddx=dx/1;
ID11=ddx*round(ID1/ddx);
MM=2*LL/ddx+1;
%#=(xv+L)/ddx+1
%xv=-L+ddx*(#-1)
%MM is max #
MI1(1:MM)=0;
TObeam(1:MM)=0;
THbeam(1:MM)=0;
%MI2(1:MM)=0;
for ii=1:NNN
   DNN=fix((ID11(ii)+LL+10^-15)/ddx)+1;
   if(DNN>0)&(DNN<=MM)
      MI1(DNN)=MI1(DNN)+ID2(ii);
      TObeam(DNN)=TObeam(DNN)+Obeam(ii)^2;
      THbeam(DNN)=THbeam(DNN)+Hbeam(ii)^2;
      %MI2(DNN)=MI2(DNN)+1;
   end

end
figure(34)
```

```
plot(1:MM,THbeam,'g.-');;hold on;
BD=THbeam';
save('data1','AD','-ascii');
save('data2','BD','-ascii');
```

Appendix E

3-D Fast Fourier Transform Beam Propagation Method (FFT-BPM) Matlab Code

This is a Matlab based 3D FFT-BPM code. Initial beam will propagate through a 500μm thickness crystal.

```
function bpm3D_L5
%This can read fdtdtobpm data as input field.....set AA=1 if you want to FDTD data.
%This is for 3D anisotropic FFT-BPM code.
%This is only for vy component
%This is new index profile
%increase dx,dz two times larger than bpm3D...to propagate 500um
AA=1;
%Number of grid
N=2^11;%even number
%low index and high index value
ns=2.288;
nf=2.287;
%nf=2.288;
nave=(ns+nf)/2;
linep(1:N)=0;
loopnum=10;
maxiterations=10000;
%nave=ns;
%wavelength
lamda=0.6*10^-6;
%calculation domain size
cladwidth=N*0.2*10^-6;
%step for propagation direction
dz=0.05*10^-6;
%spatial grid size
dx=(cladwidth/N);
dc=fix(N/2);
Radius=1.*10^-6;
Radius=fix(Radius/dx);
%index distribution data
ny(1:N,1:N)=ns;
%From k space coordinate
[x,y]=meshgrid(1:N,1:N);
fx=2*pi/cladwidth*(x-1)-pi/cladwidth*N;
fy=2*pi/cladwidth*(y-1)-pi/cladwidth*N;
kx=fftshift(fx);
ky=fftshift(fy);
clear fx;
clear fy;
%%%%%%%%%%%%%%%%%%%%%%%%%%%%%%%%%%%%%%%%%%%%%%%%%%%%%%%%%%%%
%This is main index profile
wt1=30/2;
offs=25;
t(1:N)=0;
t(1:N)=(1:N)-(N+1)/2-offs;
ny_temp1(1:N)=nf+(tanh(t(1:N)/wt1)+1)/2*(ns-nf);
%This is small additional step profile
stesize=60*10^-4;
wt2=2;
ny_temp2(1:N)=stesize*(exp(-(t(1:N)+3).^2/wt2)-exp(-(t(1:N)-2).^2/wt2));
ny_temp2=ny_temp1+ny_temp2;
for jjj=1:N
ny(1:N,jjj)=ny_temp2(1:N)';
end
%space coordinate
x=cladwidth/N*x-cladwidth/2;
y=cladwidth/N*y-cladwidth/2;
od(1:N,1:N)=1;
atten=1;
aper=80;%percentage of real area outside is obsorbing boundary
aper=round(N*aper/100);
num1=N/2-fix(aper/2);
num2=N/2-fix((aper+1)/2);
iterations=0;
k0=2*pi/lamda;
%BOundary aborption
start=aper+num1;
```

```
for ii=1:N-1
   for jj=1:num1
      if(ii>=jj)&(ii<=-jj+N)
         od(ii,jj)=1-((exp(-(jj-num1)/num1)-1)/(exp(1)-1)).^2;
      end
      if(ii<=jj+start)&(ii>=-jj-start+N)
         od(ii,jj+start)=1-((exp(((start+jj)-(start))/num2)-1)/(exp(1)-1)).^2;
      end
      if(jj<=ii)&(ii<=-jj+N)
         od(jj,ii)=1-((exp(-(jj-num1)/num1)-1)/(exp(1)-1)).^2;
      end
      if(ii<=jj+start)&(ii>=-jj-start+N)
         od(jj+start,ii)=1-((exp(((start+jj)-(start))/num2)-1)/(exp(1)-1)).^2;
      end
   end
end
od=od*atten;
temp(1:N,1:N)=0;
temp=od(1:N,1:N);
clear od;
od=temp;
clear temp;
vy(1:N,1:N)=0;
clear IFvy;
clear Fvy;

%Ideal source
for ii=1:N
   for jj=1:N
      RR=sqrt((1*10^-6)^2+((ii-N/2-1)*70*10^-9)^2+((jj-N/2-1)*70*10^-9)^2  );
      PP=2*pi/lamda*(RR-1*10^-6);
      vy(ii,jj)=1/RR^2*exp(-i*PP);
   end
end
vy=fftshift(vy);
AAA=sign(max(0,nave^2*k0^2-kx.^2-ky.^2));
phase1=AAA.*exp(i*dz*(kx.^2+ky.^2)./(nave*k0+sqrt(max(0,nave^2*k0^2-kx.^2-ky.^2))));
phase2y=exp(-(i*(ny-nave)*k0)*dz).*od;;
phase2y=fftshift(phase2y);
distance=0;
while iterations<maxiterations
   for loop=1:loopnum
      vy=ifft2(fft2(vy).*phase1).*phase2y;
      iterations=iterations+1;
   end
   %iterations

   if(rem(iterations,loopnum*10000)==0)
   distance=distance+1;
   end
   if(rem(iterations,10000)==0)&(iterations>0)
   str=sprintf('vyL3_5_%d',iterations);
   save(str,'vy');
   end
end
str=sprintf('nyL3_5');
save(str,'ny');
clear all;
```

Vita

Sungwon Kim was born in Republic of Korea on July 21, 1972. In 1997, he received the B.S. degree from Department of Ceramic Engineering at Yonsei University in Seoul, Korea. In 1999, he earned his Master's degree in Material Science and Engineering at Korea Advanced Institute of Science and Technology. He enrolled in the Ph.D. program in the Department of Intercollege Graduate Program in Materials at the Pennsylvania State University in 1999. His thesis work was in the area of nano scale characterization of ferroelectric crystals, and nano photonics.